# Optical and Radar Wind Comparisons in the Mesosphere and Lower Thermosphere

A thesis
presented in partial fulfilment
of the requirements for the degree

of

Doctor of Philosophy

in the

University of Canterbury,
Christchurch, New Zealand.

by
Steven Michael Smith

December, 1996

**To my Father and Mother**

# Abstract

This project involved the comparison of horizontal winds in the upper mesosphere at 80–105 km which were obtained by two different ground-based techniques located in Canterbury. Optical Doppler winds were derived from night time observations of the mesospheric 557.7 nm airglow emission near 95 km (FWHM intensity ~10-12 km) using a Fabry-Perot Spectrometer (FPS) during the period February 1991 to July 1994. These were compared to simultaneous radar winds obtained using a partial-reflection MF (2.4 MHz) wind–profiling radar. The comparisons were made on 103 nights considered suitable by exhibiting no cloud and low magnetic activity (low $K_p$) in order to eliminate the possibility of auroral contamination in the FPS measurements.

The results of the FPS/radar wind comparisons were of limited success due to the significant effect of RF noise associated with the radar wind measurements. The meridional optical/radar wind comparisons produced more consistent results than the zonal wind comparisons.

The distribution of daily mean radar wind vectors for all 103 days was aligned perpendicular to the direction of the magnetic meridian. This indicates that the radar winds at 85–105 km are possibly under partial geomagnetic control.

The mean height of best agreement from the cross-correlations between the night time FPS and radar hourly mean winds was 95.8 km with a standard deviation of 6.4 km. This height is agrees closely with the average height of 95.2 km obtained from studies of (satellite) WINDII 557.7 nm emission data. In a second comparison of simultaneous hourly FPS and radar winds, observations averaged over several nights during March/April 1993 were compared with a mean 557.7 nm emission height profile at 44°S from WINDII data for March/April. There was good agreement between the FPS and radar hourly winds height in the 88–96 km height region, with best agreement at 92 km.

In an alternative, best agreement between the comparison of phase of the semi-diurnal tide fitted to the optical and radar winds was found to occur in the 100–105 km height region.

The amplitudes of the semi-diurnal tide as exhibited in the optical and radar wind fields were investigated and the optical tidal amplitudes were generally larger than the corresponding radar amplitudes. The median optical/radar semi-diurnal amplitude at a height of 95 km was 1.4 with a lower and upper quartile values of 1.0 and 2.5, respectively. The amplitude discrepancy was largest near 95 km.

# Contents

# List of Figures

# List of Tables

# Chapter 1

# 557.7 nm Airglow

## 1.1 Introduction

The dynamics of the 80–100 km region of the Earth's atmosphere are poorly understood compared to other regions. Information about the dynamics of this region has primarily been obtained since the 1950's by radar observations of the drifts of meteor trails, from partial reflections and by rocket flights. Over the last two decades optical observations using Fabry-Perot spectrometers (FPS) (Hernandez 1976, Cogger et al. 1985, Lloyd et al. 1990, Manson et al. 1991, Phillips et al. 1994), Michelson interferometers (Weins et al. 1988, Shepherd et al. 1993a, Fauliot et al. 1995) and, more recently, lidars (Thomas et al. 1977) have increasingly been employed. Previous comparative studies of optical/radar winds have been made in the northern hemisphere using FPS and meteor radar winds (Hernandez and Roper 1979) and FPS and medium-frequency (MF) partial reflection radar winds (Lloyd et al. 1990, Manson et al. 1991 and Phillips et al. 1994). In the southern hemisphere, FPS/MF radar comparisons have been made by Hernandez et al. (1996).

This project involves the determination and comparison of horizontal winds in the mesosphere and lower thermosphere (MALT) which were obtained by two different techniques. Horizontal winds were derived from night time observations of the Doppler shift of the mesospheric 557.7 nm airglow emission using a Fabry-Perot spectrometer (FPS) during the period February 1991 to July 1994.

The FPS observations were made on 103 clear nights with low magnetic activity in order to eliminate the possibility of auroral contamination. Simultaneous radar winds were obtained using an MF partial-reflection (PR) drifts radar. Both instruments shared a similar sampling volume, having a horizontal separation of only 60–70 km.

The FPS and radar techniques measure winds with different methods and time scales. The radar winds are derived from vertical probings from 80 to 105 km which take about 80 seconds to complete. The radar probes an elliptical area aligned in the EW direction

48×37 km in horizontal extent at 95–100 km. The heights of the radar winds are obtained by gating the received partial reflections signals in 1 km intervals. However, the transmitter pulse width at half-power (FWHP) is 4.5 km and, thus, the radar winds are a weighted mean over this distance.

The neutral optical winds were derived from passive sampling observations of the Doppler shift of the 557.7 nm layer each with an integration time of 10–15 minutes. The sampling volume is a cylinder approximately 30 km long and 3 km in diameter in the sampling region. The observation period of the optical winds during the night varied from about 7 hours in the summer to about 14 hours in the winter. Various studies indicate that the 557.7 nm emission near Mt. John, New Zealand is centred near 95 km (Hernandez et al. 1995) with a FWHM emission thickness of about 12 km (Shepherd et al. 1995). The resulting optical winds are therefore a weighted mean over this height interval.

The layout of this thesis is as follows. Chapter 1 is an introduction into what is generally accepted about the 557.7 nm night airglow. Its morphology and diurnal and seasonal behaviour is reviewed as well as the relevant photochemistry. The horizontal and vertical structure of the emission is discussed from what is currently known from rocket and satellite observations. Solar and geomagnetic effects are also covered. Finally, previous optical/radar wind comparison studies, similar to this present one, are reviewed. Chapter 2 describes the observation and theory of tides and gravity waves in the MALT region.

The principles used to obtain the horizontal optical winds from night time airglow observations are dealt with in Chapter 3. The FPS at Mt. John and its operation are also described. Chapter 4 details the principles used to derive the horizontal radar winds using an MF partial reflection radar. The operation of the MF radar at Birdlings Flat is then described. In Chapter 5, the reduction of the raw optical data into horizontal winds and the subsequent analysis of the optical and radar winds, both separately and for comparative purposes are described. The quality of the data sets is also compared. The optical and radar wind results are presented and discussed separately in Chapters 6 and 7, respectively, while Chapter 8 contains the results and discussion of the optical/radar wind comparison. Chapter 9 presents the conclusions of the results obtained in this project.

## 1.2 The Atmosphere

The vertical structure of the Earths' atmosphere can be divided according to the predominant physical conditions and processes. In terms of temperature, the Earth's neutral atmosphere can be divided into four main height regions which are shown in Figure 1.1. The region known as the mesosphere extends from about 50 km to 90 km. In this region the temperature decreases with height from ~300 K at 50 km to ~150K at 90 km. Near 90 km

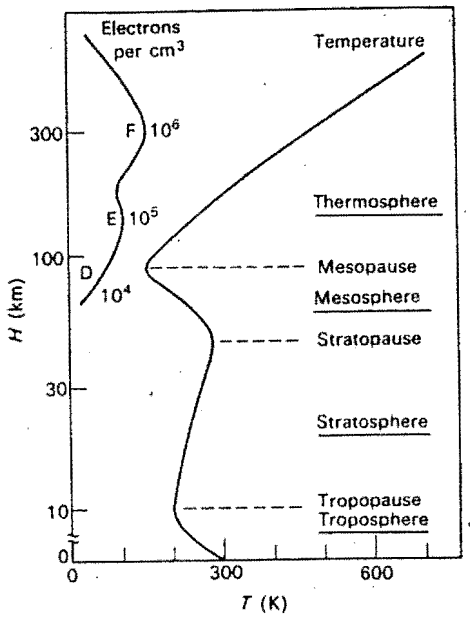


Figure 1.1: The atmospheric regions divided into the temperature and ionospheric regimes (from McEwan and Phillips 1975). The mesospheric 557.7 nm emission originates from 95–100 km.

the temperature gradient changes sign and the temperature begins to increase with increasing height. The height at which this transition occurs is known as the mesopause. In the region above the mesopause the temperature increases rapidly with height. This region is known as the lower thermosphere.

Since the upper atmosphere from about 60 to 800 km contains significant amounts of free electrons and ions it is also called the ionosphere. It can be classified arbitrarily into height regions according to the dominant ionisation processes and species occurring there. Direct evidence of its existence was obtained by Appleton and Barnett (1925). The ionosphere consists of three main regions (see Figure 1.1):

1. The D region: 60 $\sim$ 95 km
2. The E region: 95 $\sim$ 140 km
3. The F region: above $\sim$ 140 km.

Different photo-ionisation and photochemical processes govern each of these regions. Free electrons are produced mainly by solar photo-ionisation of NO at 60–90 km (D region) and of $O_2$ above 90 km (E region). The amount of ionisation, and hence the electronic density, is strongly diurnal. In the E region, the electronic density is typically $10^{11}$ $m^{-3}$ during the day and drops to $5\times10^{9}$ $m^{-3}$ at night. A relatively slow recombination coefficient ($10^{-13}$ – $10^{-14}$ $m^3s^{-1}$) means that the amount of E region ionisation is significantly reduced (by $\sim$100$\times$) but does it not entirely disappear at night.

The D region is largely absent at night. Because of this electron density fluctuation, there is a marked diurnal variation in the quantity and quality of the radar data from the 80–100 km region. At night, the S/N and yield of the radar wind data are both significantly reduced. This occurs because the reduction in D region absorption allows RF signals to propagate over large distances and therefore cause interference. During the daytime, absorption by the D region considerably weakens such signals. In addition to the dominant diurnal variation, the electronic density can also be quite variable from day to day.

In terms of dynamics, turbulent mixing is the dominant mixing process occurring below about ~100 km. Above ~100 km, as the number density of the various atmospheric species continues to decrease exponentially, diffusive separation becomes the dominant mixing process. This transition zone between mixing processes at about 100 km is known as the turbopause.

## 1.3 557.7 nm Emission

Airglow emission at 557.7 nm occurs due to the radiative de-excitation of neutral atomic oxygen in the 90 to 105 km height region by the forbidden transition $^1D_2$–$^1S_0$. It originates from a relatively narrow height region (mean emission FWHM of ~10 km) centred near 95 km (O'Brien et al. 1965, Donahue et al 1973, Wasser and Donahue 1979, Thomas and Young 1981, Ogawa et al. 1987, Shepherd et al. 1995, Ward et al. 1995, Hernandez et al. 1995). The emission layer's relatively small vertical thickness makes it an ideal tracer element of neutral wind motion at a height traditionally difficult to investigate.

The Barth mechanism (Barth 1964, Slanger and Black 1977, Bates 1979, 1990, 1992, Witt et al. 1979, Thomas 1981, Greer et al. 1986) is generally accepted is the major progenitor of 557.7 nm emission. This mechanism is a two-step process involving a three-body association:

$$O + O + M \rightarrow O_2^* + M \tag{1.1}$$

where M is any atomic or molecular species, and then energy transfer via collisional de-excitation (Witt et al. 1979) to produce O($^1$S)

$$O_2^* + O(^3P) \rightarrow O_2 + O(^1S) \tag{1.2}$$

The $O_2^*$ molecule may also be collisionally de-excited by other atomic or molecular species

$$O_2^* + M \rightarrow O_2 + M \tag{1.3}$$

or radiatively de-excite via

$$O_2^* \rightarrow O_2 + h\nu \qquad \text{(Chamberlain Bands)} \tag{1.4}$$

or via the Atmospheric Bands of $O_2$ which consist of the R and P branches between 860-870 nm (Chamberlain 1961).

The final stage involves radiative de-excitation by the $O(^1S)$ atom:

$$O(^1S) \rightarrow O(^1D_2) + h\nu(557.7\text{nm}) \tag{1.5}$$

In the thermosphere neutral O atoms are produced by the photodissociation of $O_2$. The O atoms produced slowly diffuse downwards to below 100 km where they are removed via the Barth reaction. This reaction is very effective in this height region because it coincides with the maximum concentration of neutral O and because the $O(^1S_0)$ production rate is proportional to the square of the number density of atomic oxygen. Despite the downward diffusion process, the thermospheric O concentration remains relatively constant because the diffusion rate is slow compared to the diurnal period (Rees 1989).

Chapman (1931) first proposed a three-body association reaction as a production mechanism for the 557.7 nm emission. However, in-situ measurements from rocket studies have led to refinements in the theory of the production and quenching coefficient rates of the various atomic and molecular species involved in 557.7 nm emission production (Thomas et al. 1979, Witt et al. 1979, Greer et al. 1986). As a result, this reaction has been discounted as the major production mechanism of 557.7 nm emission. Bates (1979) argues that the Chapman reaction is also too slow to produce the typical observed 557.7 nm emission rate.

The airglow emission rate is usually measured in units of Rayleighs. One Rayleigh (R) = $4\pi$I where the intensity, I, is in units of $10^6$ quanta cm$^{-2}$ s$^{-1}$ sterad$^{-1}$ (Hunten et al. 1956).

The 557.7 nm emission line is the brightest in the visible region of the airglow spectrum with typical emission intensities of 150–250 R (Chamberlain 1961, Silverman 1970). This is approximately one-tenth of the human vision threshold (Chamberlain 1961). The 557.7 nm line is therefore very useful for airglow studies as it is easily identified and compatible with the sensitivity bandwidth of most detectors.

Quenching of $O(^1S_0)$ atoms in the 95–100 km is an important removal mechanism and is predominately due to collisions with $O(^3P)$ atoms (Petitdidier and Teitelbaum 1979, Wasser and Donahue 1979) and $O_2$ (Thomas 1981) molecules. The sharp drop-off in 557.7 nm emission below 95 km, as found from rocket studies (O'Brien et al. 1965, Baker and Waddoups 1967, Offerman and Drescher 1973, Thomas 1981, Thomas and Young 1981) is a consequence of the rapid increase in the collisional frequency and number density of these

species with decreasing height and the importance of collisional de-activation of these two species. A small amount of $O(^1S_0)$ quenching is also possibly due to $N_2$ (Thomas 1981).

The radiative lifetime of the $O(^1S_0)$ state is relatively long ($\tau \sim 0.74$ s) compared to the collisional frequency in the 95–100 km region ($\sim 3500\ s^{-1}$) (Benedetti-Michelangeli et al. 1974). Therefore the O atoms are thermalised before emitting.

### 1.3.1 Vertical Distribution of 557.7 nm Emission

Rocket flights have been very useful in the direct determination of the vertical structure of 557.7 nm emission and they have revealed clear evidence of vertical structure ranging from small-scale sizes ($\sim$ few km) (Thomas and Young 1981, for example) up to the two distinct layers in the E and F regions (Gulledge et al. 1968). However, such flights are expensive and not very frequent. Space-based orbiting platforms are now increasingly being used to study the 557.7 nm layer (Donahue et al. 1973, Hays et at. 1993, Shepherd et al. 1993a,b, 1995, Ward et al. 1995).

Table 1.1 shows the results from several rocket flights and space platforms. The majority of the rocket launches occurred before local midnight at around 21:00–22:00 hours LT. From Table 1.1, the mean height of the mid-latitude emission profiles (30°–60°) is 96.3 km with a standard deviation of 2.3 km. The mean vertical thickness (FWHM) is 9.5 with a standard deviation of 4.8 km. The heights of any sub-maxima (denoted sub) present were not used in this determination.

Rocket and satellite measurements indicate that the mid-latitude 557.7 nm emission rate is typically $\sim$150 photons $cm^{-3}s^{-1}$ and peaks near 95 km (Thomas and Young 1981, Shepherd et al. 1995, Hernandez et al. 1995). The emission profile has a half-intensity width of about 12 km (Shepherd et al. 1995). Above 115 km, the 557.7 nm emission rate is less than 20 photons $cm^{-3}s^{-1}$ (Thomas and Young 1981, Shepherd et al. 1995).

Thomas and Young (1981) surveyed the vertical profile of mid-latitude 557.7 nm emission in the 80–120 km region using data obtained from a rocket flight. The emission extended from 90 to 105 km and peaked at 94–95 km. Markedly different vertical emission profiles were obtained during the ascent and descent phases of the flight (see Figure 1.2). The ascent profile has relatively smooth variation to a peak and a high-altitude tail whereas the descent profile is much broader with two sub-peaks at 93 and 95 km. The horizontal separation of the ascent and descent portions of the flight was not indicated and so the differences may be a combination of spatial and temporal variations in the 557.7 nm emission.

The only rocket flight conducted in the southern hemisphere known to the author was by Armstrong and Best (1968). Despite severe technical problems encountered during the flight, the height of maximum 557.7 nm emission was estimated as 94 km, which is consistent

| Date | Lat | LT | UT | Height Max | FWHM | Reference |
|---|---|---|---|---|---|---|
| 12-12-55 | 32N | 22:00 | | 97 (1) | 10 | Packer 1961 |
| 5-7-56 | " | 00:50 | | 97 (1) | 6 | " |
| 28-3-57 | " | 21:25 | | 99 (1) | 14 | " |
| 6-11-59 | " | 00:25 | | 97 (1) | 14 | " |
| 9-7-64 | 38N | 21:15 | 04:15 | 94.5 (0.3) | 6 | O'Brien et al. 1965 |
| 1-12-64 | 32N | 01:15 | 06:15 | 95 (4) | 26 (4) | Hennes and Dunkelman 1966 |
| 22-10-65 | 32N | 22:30 | | 95 (1) | 6 (up) | Gulledge et al. 1965 |
| 28-4-66 | 32N | 20:49 | | 102 (5) | 12 | Baker and Waddoups 1967, 1968 |
| | | | | 94 | - | Best and Armstrong 1968 |
| 21/22-5-69 | 22N | 21:37 | 03:00 | 99 (1) | 6 | Dandekar and Turtle 1971 |
| 8-69/4-70 | | var | var | 97 (2) | | Donahue et al 1973 |
| " | | var | var | (95-110 with lat) | | Wasser and Donahue 1979 |
| 13-10-70 | 39N | 02:08 | | 97.5 (0.3) | 6 | Offerman and Drescher 1973 |
| 1-4-74 | 57N | 22:37 | 22:37 | 97.5 (0.5) (main) (up)<br>92.0 (0.5) (sub)<br>98.0 (0.5) (sub) (down)<br>92.5 (0.5) (main) | | Dickinson et al. 1974 |
| 7-3-75 | 68N | 01:23 | 00:23 | 97.0 (0.5) | 11.5 | Witt et al. 1979 |
| 9-9075 | 57N | 00:56 | 00:56 | 96.5 (1.0) | 5 | Thomas et al. 1979 |
| 11-7-77 | 32N | 23:45 | | 94.5 (0.5) | 5.5 (up) | Thomas and Young 1981 |
| | | | | 95.0 (1)<br>(subs at 95 and 93 km) | 7 (down) | Thomas 1981 |
| 23-3-82 | 57N | 21:27 | 21:27 | 98.0 (0.5) | 7 | Greer et al. 1986 |
| | | 22:58 | 22:58 | 96.5 (0.5) | 8 | |
| | | 23:13 | 23:13 | 97.0 (0.5) | 7.5 | |
| 3/4-77/80 | var | var | | 97.0 (0.5) | 8 | Yee and Abreu 1987 |
| 1-12-83 | 47.5S | 22:25 | 22:25 | 89 (2) | | Swenson et al. 1989 |
| 2-12-83 | 23S | | 22:00 | 98 (1) | 13 | Torr et al. 1985 |
| 5-12-83 | 4S | 20:10 | 02:10 | 97 (2) | | Swenson et al. 1989 |
| | 14S | 20:14 | 02:14 | 92 (2) | | |
| 24-8-81 | 31N | 21:00 | 12:00 | 96 (1) | 9 | Ogawa et al. 1987 |
| 6-9-86 | 31N | 22:00 | 13:00 | 95.5 (1.0) | 8 | Kita et al. 1988 |
| 12-12-85 | 6S | 23:59 | 01:59 | 97 (1) | 6 (up) | Gobbi et al 1992 |
| | | | | 95 (1) | 7 (down) | |
| 31-10-86 | 6S | 21:30 | 23:30 | 97.5 1.0 | 8 | Gobbi et al 1992 |
| 2-10-91 | 8N | 04:57 | 18:57 | 98.0 (1.0) | 12 | Shepherd et al. 1993a |
| 30-10-93 | 30S | 22:35 | 10:35 | 93.0 (1.0) | 12 | Ward et al. 1995 |
| 1992-93 | 43S | var | var | 95.2 (1.6) | | Hernandez et al. 1995 |
| 03/04-93 | 40S | var | var | 93 (1) | 11 | Shepherd et al. 1995 |

Table 1.1: Various rocket and satellite measurements of the 557.7 nm emission height. Known uncertainties are shown in brackets.

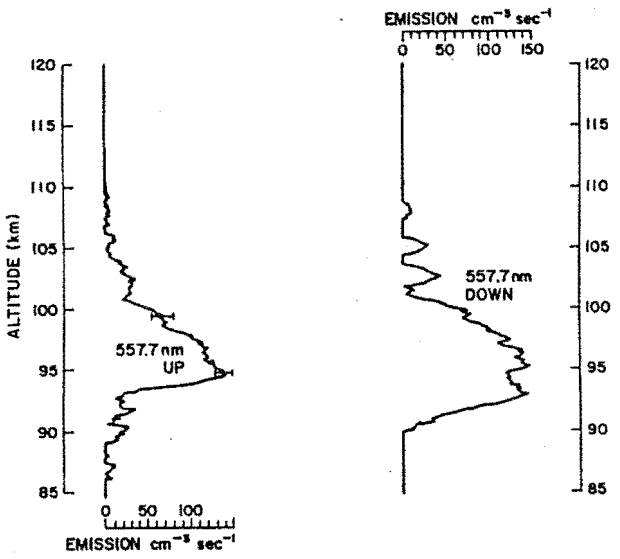


Figure 1.2: Vertical profiles of 557.7 nm emission near 95 km as obtained during a rocket flight illustrating variations in the vertical profile between the ascent and descent stages (from Thomas and Young 1981).

with the results obtained in the northern hemisphere.

There have been several reports of variations in the height of the 557.7 nm emission layer from space-based platforms. Swenson et al. (1989), using Shuttle-based limb measurements made at 22:25 LT in early December, reported the height of the 557.7 nm emission maximum, along a orbital flight path centred at about 45°S, to occur near 90 km. Any possible distortions in the imaging system were minimised and field stars were used as reference markers enabling the true horizon to be determined in the frame (Swenson et al. 1989).

The height of the emission layer above the region of Mt. John, New Zealand, was recently determined by Hernandez et al. (1995) using observations made by the Wind Imaging Interferometer (WINDII) aboard the Upper Atmosphere Research Satellite (UARS) (Shepherd et al. 1993a). The WINDII obtains winds, temperatures and emission rates from various species in the upper atmosphere. During 1992–1993, 32 passes were made over the region; the 557.7 nm emission profile was found to occur at an average height of 95.2 km with a standard deviation of 1.6 km. An apparent seasonal variation in the height of the emission maximum of up to 5 km was also indicated with lower heights occurring during autumn (Hernandez et al. 1995). Hernandez et al. (1995) found no evidence of the emission layer occurring at heights less than about 93–95 km during the summer months.

Donahue et al. (1973) and Wasser and Donahue (1979), using photometric satellite data of 557.7 nm emission originating from 80–120 km, reported that a large amount of vertical structure is exhibited in 557.7 nm emission. The layer heights were determined to

within 1–2 km. There were also marked variations in the vertical gradient of emission rate with altitude. The altitude of maximum emission was found to vary between 95 to 110 km with the average height at about 97±2 km with the width of the layer typically being ~8 km. They also found that the altitude of maximum emission was lower within about $10^o$ latitude of the equator compared to higher latitudes.

Similarly, Yee and Abreu (1987) investigated 557.7 nm MALT emission using a satellite-based photometer during a solar maximum period. Their results indicated that the emission extended from 90 to 102 km with a peak at 96.5±1 km and a half-intensity width of about 8 km.

### 1.3.2 F Region 557.7 nm Emission

There is a small contribution of 557.7 nm emission from a broad faint layer centred near 250 km in the F region which arises due to the dissociative recombination of $O_2{}^+$ (Biondi and Feibelman 1968, Gulledge et al. 1968, Hernandez 1971, Thomas and Donahue 1972, Cogger and Anger 1973). This reaction may be described by

$$O_2^+ + e \rightarrow O_2^* \rightarrow O + O + K.E. \tag{1.6}$$

The $O_2^*$ represents the repulsive state of the neutral oxygen molecule. This intermediate state dissociates into two atoms of oxygen, one or both of which may be in the ground state or in the excited metastable states, O($^1$S) or O($^1$D). This reaction has two main O($^1$S) production channels:

$$O_2^* \rightarrow O(^1S_0) + O(^1D) + 0.83eV \tag{1.7}$$

$$\rightarrow O(^1S_0) + O(^3P) + 2.79eV \tag{1.8}$$

Less than 10% of the atomic oxygen produced via this reaction is in the excited O($^1$S) state (Rees 1989). The first channel is favoured over the second (Killeen and Hays 1981, 1983) by a factor of 4.

The F region 557.7 nm emission is only partially thermalised (Hernandez 1971, Killeen and Hays 1983) resulting in a broad line-profile. This excess energy is exhibited as translational motion of the centre of mass system of the two product O atoms. The resulting measured profile would therefore consist of a composite of three profiles; one due to thermalised 557.7 nm emission originating from near 95 km and two non-thermalised profiles due to 557.7 nm emission originating from the F region via the two production channels.

The F region component contributes less than 20% to the total 557.7 nm emission (Jacka 1984). By increasing the resolution of the FPS the contribution by this component can

be rendered negligible. The increased resolution can be achieved by employing a larger etalon gap distance and, as a result, the broader emission line profile of the F region component will be washed out by the overlap of the spectral orders of the interferometer (Hernandez 1971).

### 1.3.3 Horizontal Structure

A wide range of horizontal scale-sizes ranging from 10–$10^3$ km has been observed in the 557.7 nm emission. Photometric imaging of the emission indicates that it frequently exhibits patchiness and wave-like structure (Peterson and Kieffaber 1973, Moreels and Herse 1977, Herse et al. 1980, Armstrong 1982, 1986, Taylor et al. 1987, 1991, 1995, Taylor and Hapgood 1990), the latter being attributed to gravity wave activity. Other indirect investigations, such as spaced and field-scanning photometers have observed variations in airglow emission rate which are also consistent with wave-like structure (Freund and Jacka 1979, Takahashi et al. 1979, 1985, Meek and Manson 1983). Freund and Jacka (1979) reported variations with periods of tens of minutes dominating photometric measurements of 557.7 nm emission and attributed these to gravity waves propagating through the emission layer with horizontal phase velocities of 50–100 $ms^{-1}$. A similar study was made by Meek and Manson (1983) who reported similar intensity variations with periods of 15–20 minutes superimposed on variations with periods of several hours. The former variations were attributed to gravity waves propagating through the emission layer and producing intensity fluctuations. Direct imaging of the 557.7 nm emission using a low-light TV system (Taylor et al. 1987, 1988, 1990, 1991, 1993, Taylor and Garcia, 1995) reveals wave-like structure indicative of short-period gravity waves with horizontal wavelengths of ~30 km and periods of 10–20 minutes. For example, Taylor et al. (1987) reported horizontal emission structure with a period of about 21 minutes and a horizontal wavelength of 7 km. Spectral analysis by Taylor et al. (1991) indicated wave-like structure with a horizontal wavelength of about 23 km occurring in the OH emission layer near 90 km with a period of about 15 minutes. Finally, Taylor and Garcia (1995) reported wave structure in 557.7 nm images with periods of 12–29 minutes and exhibiting horizontal wavelengths of 30–70 km. Armstrong (1982) reported photographic evidence of a wave of period 57 minutes and a horizontal wavelength of 244 km in 557.7 nm emission during one night of observations.

Large-scale horizontal structure in 557.7 nm emission of about 2500 km was reported by Roach et al. in 1958 from ground-based observations. More recently, planetary-scale horizontal variations have been observed from various space platforms (Yee and Abreu 1987, Swenson et al. 1989, Shepherd et al. 1993b, 1995). Yee and Abreu (1987), used photometric satellite 557.7 nm emission measurements and reported horizontal wave-like variations with periods of 10–12 hours. The variations consisted of a broad post-sunset maximum centred

at about 21:00 hours local time (LT) followed by a narrow post-midnight minimum centred at about 02:00 hours LT and was attributed to solar semi-diurnal tidal activity which is, in general, similar to the behaviour reported by Petitdidier and Teitelbaum (1977). Due to the large amplitude of the observed intensity variations it was suggested that dynamics, and not photochemistry, was responsible for the intensity variations (Yee and Abreu 1987).

### 1.3.4 Diurnal and Seasonal Variations

There is considerable variation in 557.7 nm emission intensities from night to night. Several workers using relatively large datasets report that an emission maximum in 557.7 nm emission occurs during the middle of the night at temperate latitudes (Barbier 1959, Christophe-Glaume 1965, Brenton and Silverman 1970). These diurnal variations were also found to vary seasonally. A maximum in intensity occurs near midnight during the months of November to March with the remaining months having less marked diurnal variations. During May to August, however, an intensity maximum did occur which gradually progressed from the beginning of the night to the end of the night during this period. Petitdidier and Teitelbaum (1977) reported that the action of the semi-diurnal tide governed the diurnal variation in the 557.7 nm emission intensity at mid-latitudes. In the southern hemisphere, Neff (1965) made zenith 557.7 nm emission measurements at Christchurch, New Zealand (43°S) during 1962–64 and reported that the mean 557.7 nm intensity during the night reached a maximum at midnight during late summer through to early winter. For the remaining months, he found no regular diurnal variation.

Green-line 557.7 nm airglow exhibits latitudinal intensity variations with maxima occurring in the mid-latitudes near $\pm 40^{o}$ (Christophe-Glaume 1965, Donahue et al. 1973, Cogger et al. 1981, Shepherd et al. 1993, 1995 and Ward et al. 1995). This latitudinal maximum, however, is variable from night to night. Christophe-Glaume (1965) used data from several stations and found that latitudinal maximum intensity was a function of dip (rather than geographic) latitude and also that seasonal latitudinal variations were due to geomagnetic latitude.

Donahue et al. (1973), using photometric satellite data of 557.7 nm emission originating from 80 to 120 km in height, reported a semi-annual variation in 557.7 nm emission intensity of up to a factor of 2 between the latitudes 40 and 60°. Large emission intensity maxima occurred during the winter followed by large minima during the summer. Large asymmetries in the 557.7 nm emission intensity between the hemispheres were also observed during April and October. Vertical transport was suggested as the mechanism to explain this behaviour.

Cogger et al. (1981) reported large emission fluctuations of up to a factor of 2 from

day to day, using 32,000 limb observations from the ISIS-2 satellite, obtained between April 1971 and December 1972. The mean mid-latitude emission rate was ~175 R. A semi-annual emission variation was also found with maxima occurring during mid-April and mid-October which accounted for 20% of the mean emission rate. Globally there was a marked hemispherical asymmetry with a large emission peak occurring near 35° in the winter hemisphere and a smaller emission peak occurring near 25° in the corresponding summer hemisphere. The difference in the sizes between the two solstice peaks was attributed to seasonal differences in emission. Seasonal changes in circulation and turbulence were suggested as the cause of the observed seasonal variations.

A seasonal maximum in 557.7 nm emission intensity is found to occur near the autumnal equinox. Roach (1955) found a maximum in 557.7 nm intensity during October at Fritz Peak. Ward and Silverman (1962) found a similar result together with another maximum near the vernal equinox as did Armstrong (1968) in the southern hemisphere who, using FPS measurements, found a maximum occurring during April. When nights of low magnetic activity, as determined from the planetary index $K_p$, were selected the seasonal variation in intensity was found to occur in phase with variations in the 557.7 nm emission temperature. The possibility of auroral 557.7 nm emission was minimised when nights of low magnetic activity were investigated. Hernandez and Silverman (1964) re-analysed data obtained by Rayleigh during 1925-27 in Australia (Rayleigh 1928). A maximum in 557.7 nm intensity during April was clearly evident from the monthly mean intensity measurements.

Also in the southern hemisphere, Neff (1965) reported that intensity maxima in 557.7 nm emission occurred during late April-early May (late autumnal equinox) and also during November and December (early summer). A minimum in intensity occurred from late May through to late October (winter). These he compared to observations made at a similar latitude in France in the northern hemisphere and found "seasonally coincident" behaviour in the annual variations of 557.7 nm emission intensity between the hemispheres.

### 1.3.5 Solar and Geomagnetic Activity

Auroral activity at mid-latitudes arises mainly due to energetic particles from the magnetosphere entering the upper atmosphere (Chamberlain 1961, Hargreaves 1992) during periods of moderate to high geomagnetic activity. This activity will result in an increase in the measured 557.7 nm emission intensity at a mid-latitude site.

The majority of auroral 557.7 nm emission results from energy transfer between $N_2$ molecules and $O(^3P)$ atoms (Sharp and Torr 1979, McDade and LLewellyn 1984, Vallance Jones et al. 1985, Rees 1989). Secondary electron impact on $O(^3P)$ atoms and impact dissociation of $O_2$ molecules by primary electrons also provide a small contribution (Rees

1989).

The level of geomagnetic activity is determined from the value of the 3-hour planetary geomagnetic index, $K_p$. This index is a world-wide measurement of the amount of magnetic disturbance. The $K_p$ index scale is quasi-logarithmic and ranges from 0 (very quiet) to 9 (very disturbed).

At mid-latitudes, there is a clear dependence between 557.7 nm emission intensity and magnetic activity. However, this dependence occurs above a threshold magnetic activity, usually measured in $K_p$, with the intensity of emission then increasing with increased $K_p$ (Roach 1960, Silverman et al. 1962, Sanford 1959, 1964). The threshold is determined by the latitude of the station. Sanford (1959, 1964) reported little or no dependence of 557.7 nm emission intensity with magnetic activity for local K values less than about 5 but for higher values there was a clear dependence of increasing intensity of 557.7 nm emission with increasing local K index. He used a spectrograph to investigate the absolute 557.7 nm emission intensity at Invercargill, New Zealand (51°S geomag.) from August 1957 to January 1958. Observations were made towards the north and the south at various zenith angles from 45° to 70°. For both directions the 557.7 nm emission intensity was found to increase with increasing local K index especially for $K \geq 5$. The 557.7 emission intensity increased by over an order of magnitude as $K_p$ increased from 0 (quiet) to 9 (stormy). This increase was much larger than that found at similar northern latitudes such as Fritz Peak (49°N geomag.) and Rapid City (53°N geomag.). Corrections were made for reciprocity failure of the emulsion on spectrographic plates due to the large exposure times (1–5 hours) (Sanford 1964). An all-sky camera was also used in conjunction with the spectrographic observations to determine the occurrence of aurora. In the observations to the north no aurora were observed at $K_p < 8$ whereas to the south a few aurora were observed at $K_p = 2$. Figure 1.3 shows the mean zenith 557.7 nm emission intensity as a function of local K-index for several stations (Sanford 1964).

From a comparative study of 557.7 nm emission intensity data obtained from auroral and sub-auroral stations Roach (1960), Roach and Rees (1960) and Roach et al. 1960 found that 557.7 nm intensity increased with magnetic activity measured by $K_p$. More specifically, an increase in $K_p$ resulted in an increase between the night's minimum and maximum 557.7 nm emission intensity for the night. Roach (1960) called this phenomenon intensity spread. For a given amount of magnetic activity the minimum increased only slightly whereas the maximum would increase markedly. This behaviour was more pronounced at high-latitudes (College 65°N geomag.) near the auroral zone than at mid-latitude stations. The relationship observed by Sanford (1964) is consistent with these results despite his use of local K indices as opposed to $K_p$.

McCaulley et al. (1960) found a positive correlation between the horizontal magnetic

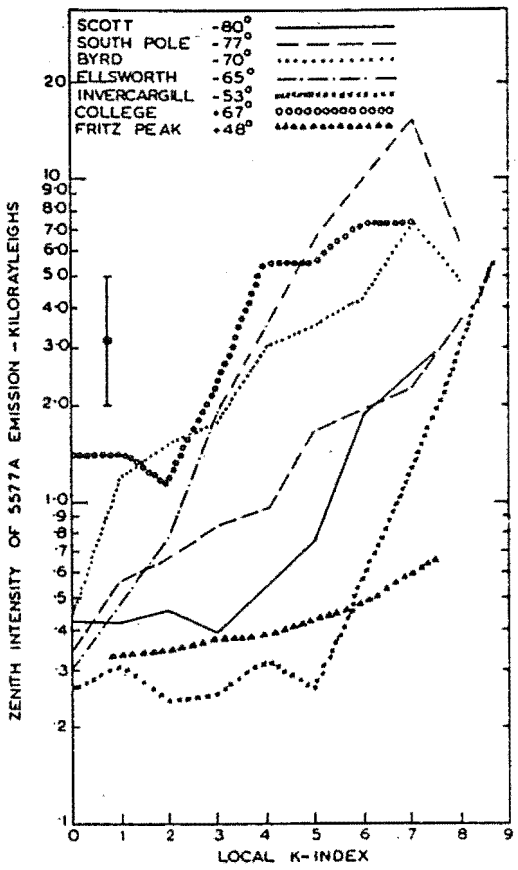


Figure 1.3: Mean zenith 557.7 nm emission intensity as a function of local K-index at several stations including Invercargill (Sanford 1964).

intensity, H, and 557.7 nm emission intensity up to naked eye intensity. Hourly values of the 557.7 nm zenith emission intensity at Fritz Peak were compared to the relative change in H, $\Delta$H, from quiescent conditions over the corresponding hourly period. The horizontal magnetic intensity is more discriminating than the $K_p$ index because, unlike $K_p$, it can be defined over a period of less than three hours. $K_p$ is also a measure of the variability of H. Hence if H is relatively constant but large compared to quiescent conditions ($\Delta H = 0$) then $K_p$ will be low (McCaulley et al. 1960). An increase in 557.7 nm emission intensity of 5–10% within 1 hour after a sudden storm commencement has been reported by Christophe-Glaume (1965) and Silverman and Bellew (1965). Dandekar and Silverman (1964) found strong evidence of 557.7 nm emission enhancement on nights following solar flare activity. This can be attributed to the increased production of atomic oxygen as a result of the increased UV flux.

Rosenberg and Zimmerman (1967) compared over seven years of 557.7 nm zenith photometric intensity measurements from 33°N with two coincident solar activity indices: 10.7 cm solar flux level and Zurich relative sunspot number. A significant positive correlation was found between the airglow intensity and both the solar activity indices with a higher correlation found between the 10.7 cm solar flux and 557.7 nm intensity. The total observation period was comparable to one solar cycle and the data was grouped accordingly. The highest correlation between 557.7 nm airglow intensity and solar activity occurred mid-

way between solar maximum and minimum. Brenton and Silverman (1970) found that short term ($\sim$ hours) variations in 557.7 nm emission intensity exhibited no statistically significant dependence on the sunspot cycle.

Studies indicate that the 557.7 nm emission intensity increases when the levels of solar activity increases (Dandekar and Silverman 1964, Rosenburg and Zimmerman 1967). In the mid-latitudes, 557.7 nm emission intensity increases when the level of geomagnetic activity, measured using the planetary $K_p$ index, increases above a certain threshold, which is determined by the latitude of the station (Roach 1960, Silverman et al. 1962, Sanford 1959, 1964). Sanford (1959, 1964) determined the threshold level to be near the local K value of 5 for the South Island of New Zealand. In the present study, the selection of nights during which $K_p \leq 3$ will minimise the possibility of contamination by auroral 557.7 nm emission.

## 1.4 FPS/MF Radar Comparison Studies

Comparisons between radar and optical winds are not common. The first major comparison study of radar and optical winds was made by Hernandez and Roper (1979) who compared meteor radar winds measured near Atlanta, Georgia with 557.7 nm airglow winds obtained by FPS observations at Fritz Peak, Colorado over 1000 km away. Both observations were undertaken during the period August 1974 to November 1975. To minimise the sampling differences between the two data sets the meteor winds were weighted with an airglow profile and the optical winds were grouped into hourly mean bins. Despite the large spatial separation of the two stations, the mean wind motions of the two data sets generally followed each other. There were magnitude differences in the meridional winds but these were attributed to the smoothing which was inherent in the determination of the meteor winds.

The first comparative study of MF partial-reflection radar winds using the spaced antenna method and FPS Doppler wind of nighttime 557.7 nm emission was made by Lloyd et al. (1990) at Saskatoon (61°N). The study involved comparing night time hourly mean radar winds from the 80–110 km height region and FPS 557.7 nm Doppler winds during 9 nights. The wind comparisons were made with the assumptions that the height and vertical profile of the 557.7 nm emission layer were diurnally and seasonally constant. Because of the latitude of the site, auroral 557.7 nm emission was carefully monitored and only magnetically quiet days were used. The individual night comparisons were made difficult due to the low S/N and yield of radar wind values at night time. The low S/N of the echoes resulted in a low yield of radar wind values ( 2–3 $hr^{-1}$ in the 90–100 km region at night). Four-day mean winds over a height range of 9 km were also used to increase the amount of hourly mean radar wind values for the comparison. The 4-day mean winds also minimised the presence of incoherent sources such as gravity waves.

The wind fields of both sets of winds were dominated by a semi-diurnal tidal variation but the radar winds were more scattered, especially above about 95 km. A 12-hour cosine and a constant were fitted to the FPS east- and north-pointing wind measurements using the least squares method. The radar wind fit included a 24-hour component unlike the FPS winds.

There was relatively good agreement between the tidal fits especially in the amplitudes. There were occasional differences in phase of up to 2 hours between the two wind fields which were attributed to gaps in the night time radar wind data or modulation of the FPS wind field by the 24-hour diurnal tide.

Manson et al. (1991) followed up this study using radar winds from the 75–110 km height region obtained with a new phase-coherent system at the same site. This improved the S/N and yield of the radar wind data. Like the optical/radar wind comparisons by Lloyd et al. (1990) the height of 557.7 nm emission layer was assumed to be both diurnally and seasonally stable, as were the radar winds.

Thirteen individual nights of FPS winds (during September 1988 to February 1989) were compared with the corresponding hourly mean radar winds. Both sets of winds were dominated by a 12-hour variation and excellent agreement was reported between the two wind vector fields and the 12-hour tidal fits with the height region of best agreement being 96–102 km. There were, however, differences between the phases of the optical and radar winds at the height of maximum agreement from night to night. The mean radar/FPS semi-diurnal phase difference was 0.5 hours with a range of 0–2 hours (Manson et al. 1991). There were also differences in the amplitude of the semi-diurnal tide as measured by the FPS and radar of 5–20 $ms^{-1}$ with a mean of 5 $ms^{-1}$. The discrepancies in the FPS/radar winds were attributed to differences in the lengths of the data sets and low night time yields of radar winds which resulted in large random errors in the hourly mean radar winds. Group retardation was assumed to be negligible (less than 1 km) during the night (Manson et al. 1991). Differences in the optical and radar wind fields did occur and these were suggested to be due to gravity wave activity.

Phillips et al. (1994) compared 200 days from four years' simultaneous MF radar and FPS 557.7 nm winds obtained during April 1988 - February 1992. The MF radar was the same phase-coherent system used by Manson et al. (1991). Despite this system however the night time radar wind yield was still low and real-time comparisons were often poor. So for the optical/radar comparison the entire four years' radar wind data was bin-averaged according to month and hour to form monthly-mean diurnal averages. The FPS wind data was similarly treated. This procedure was done in order to reduce the large random errors associated with the nighttime radar winds but the optical/radar comparisons are not then strictly simultaneous. The study involved selected nights with $A_p<10$ in order to minimise

auroral 557.7 nm emission contamination.

Best agreement between the mean radar and optical winds was found at 97 km which is consistent with the results of rocket flights. Despite the similarities between the two wind sets differences of 0–2 hours in the phase of the semi-diurnal tide between the optical and radar winds did occur. There were also differences found between the fitted semi-diurnal tidal amplitudes with radar/FPS amplitude ratios at 103 km of 0.8 (zonal) and 0.9 (meridional). It was suggested that differences between the optical and radar wind field may arise due to the sampling of differing phases of a gravity wave between opposite observing directions. The optical observing area had a diameter of 350 km compared to 50 km for the radar.

The Saskatoon optical/radar comparison studies of Lloyd et al. (1990), Manson et al. (1991) and Phillips et al. (1994) all reported that the paucity of night time radar winds resulted in poor results from real-time comparisons. The reason being the mutual exclusivity of the two techniques' data acquisition rate (Phillips et al. 1994). For these three studies 557.7 nm auroral contamination due to the high magnetic and geographic latitude of the measurements appeared to be a frequent problem in obtaining reliable FPS wind measurements.

One study in which large discrepancies were observed between FPS and partial reflection drifts radar winds was the Arecibo Initiative in Dynamics of the Atmosphere (AIDA) campaign which was held over several days in April 1989 (Hines et al. 1993). This was a comparative multi-instrument study of the validity of the MF radar technique used to determine MALT winds. One part of the initiative was the comparison of optical winds derived from FPS observations of the 557.7 nm nightglow with simultaneous radar winds obtained from a nearby Imaging Doppler interferometer (IDI) (3.175 MHz). The optical/radar comparisons were made during two nights in April 1989 (Hines et al. 1993).

The IDI technique is related to the radar system used in this present project but involves an array of coherent receivers which record phase as well as amplitude information to obtain directional information on the drift motion. Comparisons were made between individual FPS and radar wind vectors averaged over 21 minutes. Little consistency was found between radar and optical wind vectors during both nights and the authors expressed doubt that the motions measured by the radar were in fact due to neutral wind motion. It was suggested that the radar/FPS winds discrepancies occurred because the radar was measuring the horizontal phase velocities of gravity waves propagating through the 90–100 km region and the validity of the partial reflection winds technique in this region was questioned.

The IDI radar wind data were also compared with data obtained from an incoherent scatter radar (ISR). The sampling rate of each technique was different. The IDI data were obtained from three 25-minute sampling intervals whereas ISR data were obtained from a 2 hour sampling interval (Briggs pers. comm.) Re-evaluation of the acceptance criteria used

to derive horizontal wind velocities from the IDI measurements in the study of Hines et al. (1993) was performed by Turek et al. (1995). His results indicated that the differences of $\sim$40 ms$^{-1}$ that were exhibited between the IDI and ISR winds above 80 km were not as large as originally thought. In fact, the IDI and ISR wind differences were typically only $\sim$10 ms$^{-1}$ for heights up to about 95 km. The original radar data was also used to derive horizontal winds using the FCA procedure (see Chapter 4) and these winds were also compared to the winds derived using the IDI technique. Both wind sets were found to be almost identical within the uncertainties of the wind values.

# Chapter 2

# Tides and Gravity Waves

## 2.1 Atmospheric Tides

Solar tides are forced thermal oscillations of density, wind velocity and temperature, etc driven by insolation absorption by ozone ($O_3$) and tropospheric water vapour ($H_20$) (Chapman and Lindzen 1970, Lindzen and Hong 1974, Forbes 1982a, b, Forbes and Garrett, 1978, 1979, Walterscheid et al. 1980). As the Earth rotates, the sun appears to move westwards and, as a consequence, so does the perturbation region of maximum heating. Tides produced in this way are known as migrating tides and the period of oscillation is the same as the forcing period. The solar heating cycle is diurnal and the perturbation function has the form of a truncated sinusoid. As a result, harmonics with periods of 12, 8, 6 hours, etc also occur.

In the southern hemisphere, tidally-driven horizontal wind vectors exhibit an anti-clockwise rotation when viewed from above. The zonal component in general leads the meridional by 90°. This holds for all the important semi-diurnal and diurnal modes at 44°S (Smith 1981). The phase of the zonal (meridional) component of the tide is usually defined as the local time of maximum eastward (northward) wind.

Several modes of oscillation are possible and these are designated by the parameter (m,n). The zonal wavenumber, m, indicates the number of cycles per day (m=2 for the semi-diurnal tide). The number of nodes between the poles is equal to the quantity (n–m), excluding those at the poles themselves. For example, the (2,4) mode is semi-diurnal and possesses 2 nodes between the poles. Because solar heating is greatest in the equatorial region, tidal modes with antinodes at the equator are generated in preference to those without. Symmetric modes are those modes which are symmetrical between hemispheres and where n is even. Antisymmetric modes are antisymmetrical between hemispheres and n is odd.

A mode may or may not propagate vertically. For a vertically propagating mode, the phase varies with height and a vertical wavelength, $\lambda_z$, may be defined as the vertical

distance over which the phase of the tidal oscillation varies by $2\pi$. The mode determines the size of $\lambda_z$ and, in general, the higher the order of the mode, the smaller is $\lambda_z$. For example, the (2,2) and (2,4) modes have vertical wavelengths of 170 km and 41 km, respectively, at 100 km. Hernandez et al. (1995), using FPS wind measurements obtained above Mt. John, reported the vertical wavelength of the semi-diurnal tide to range from 25 to 50 km during the year. During the autumn equinox the semi-diurnal tide was reported to exhibit vertical wavelengths of $\sim$100 km and this was attributed to an enhancement of the (2,3) mode.

A single upwardly propagating semi-diurnal tidal mode will exhibit a constant change in wind phase, with the time of maximum wind decreasing with increasing height. A tidal mode with a constant phase at all heights is known as an evanescent mode and does not propagate vertically. In general, a number of modes, each with a different vertical wavelength, may be present and so the vertical tidal behaviour will be rather complicated and the sense of rotation may even reverse. Changes in the reflection characteristics of the region, such as due to density and temperature changes, are also important. A reflected mode may propagate downwards and thus alter the apparent modal content in the region (Fellous et al. 1974, 1975).

In the mid-latitude MALT, the solar semi-diurnal tide is the dominant tidal oscillation, exhibiting an amplitude of typically 15–30 $ms^{-1}$ (Chapman and Lindzen 1970, Smith 1981, Manson et al. 1985, 1989). The $O_3$ and $H_2O$ heating rates vary seasonally and latitudinally but on average the $O_3$ maximum is centred at 50 km with a FWHM of about 20 km. The semi-diurnal heating rate for $H_20$ is greatest near ground level and decreases with increasing height (Forbes and Garrett 1979). The broad height range of the $O_3$ excitation region causes short vertical wavelength modes ($\lambda_z\sim$30–40 km), such as (2,5) or (2,6), to experience destructive interference. Tidal modes with large vertical wavelengths, such as the (2,2) mode, are therefore excited preferentially. Forbes (1982b) showed that the (2,2) mode is associated with the majority of the $O_3$ and $H_2O$ heating and that there is less than 20% seasonal variation in the heating rate (Forbes 1982b). The heating rates associated with higher modes such as the (2,4) and (2,5) modes vary seasonally by 25–100% (Forbes 1982b). Diurnal modes arising from $O_3$ excitation tend to have small vertical wavelengths and are thus very weak in the mid-latitude MALT, but the (1,1) mode is strong near the equator because of the excitation due to tropospheric water vapour (Forbes 1982b).

Classical tidal theory suggests that the amplitude of the tidal perturbation will increase exponentially with increasing height as a result of the reduction in the atmospheric density and the constancy of the wave's energy flux. However, in practice, the amplitude of the tide is significantly reduced by eddy diffusion (Forbes 1982b) and by the generation of turbulence by the wave (Vincent and Stubbs 1977, Manson et al. 1979, Hodges 1979). The amplitudes of the higher order modes such as (2,4) and (2,5) are significantly affected by

eddy diffusion above 100 km, which increases exponentially above this region and limits the exponential growth of the tidal amplitudes with increasing height (Forbes 1982b).

Although the (2,2) mode is the dominant mode of excitation, the (2,4) mode ($\lambda_z \sim 40$ km) is the dominant mode exhibited during the majority of the year in the 80–110 km region (Lindzen and Hong 1974). The (2,4) and higher modes tend to be dominant because of mode coupling between the (2,2) and (2,3) modes due to the presence of vertically varying background winds and meridional temperature gradients (Lindzen and Hong 1974, Forbes and Garrett 1978, Forbes 1982). Lindzen and Hong (1974) showed that a vertically-varying background wind will produce coupling between the (2,2) and higher modes and will result in an enhancement of the (2,4) mode by a factor of two. The modes excited through mode coupling are also therefore sensitive to zonal wind changes.

Forbes and Garrett (1978), Walterscheid et al. (1980) and Forbes (1982b) progressively used improved heating rate estimates and reported similar findings including a 50% enhancement of the amplitude of the (2,4) mode above 70 km (Walterscheid et al. 1980). Forbes (1982b) included anti-symmetric Hough components in the model and obtained improved agreement between the model and observed tidal parameters for the 80–100 km region. For example, the observed semi-diurnal tidal amplitude at 95 km during the summer time is 10–20 $ms^{-1}$ and the model predicted 15–40 $ms^{-1}$ (Forbes 1982b). During the winter, the observed amplitude is 10–40 $ms^{-1}$ and the model predicted 20–50 $ms^{-1}$ (Forbes 1982b). The results showed that, as a result of mode coupling, the vertical wavelength of the semi-diurnal tide will be shorter than expected due to contributions from higher-order modes.

The specific tidal structure near 95 km is sensitive to variations in the thermal excitation, background zonal mean wind and the meridional temperature gradient (Lindzen and Hong 1974, Forbes and Garrett 1978, 1979, Walterscheid et al. 1980, Forbes 1982b) and only a small variation in the background wind is necessary to produce a large change in the modal content at this region. Changes of ~1–2 hours in the relative phases of the component modes are expected to produce considerable phase variations in the observed daily semi-diurnal phase at any particular height in the MALT and the (2,4) mode is significantly affected by mode coupling (Forbes 1982b).

Studies indicate that there is a strong seasonal variation exhibited by the phase and amplitude of the semi-diurnal tide. The phase variation within a particular season is typically 3 hours (Forbes 1982b) which is consistent with the results of radar studies such as those by Manson et al. (1985, 1989). These studies also indicate that a rapid transition in the semi-diurnal phase occurs during the spring and autumn equinoxes (Smith 1981, Manson et al. 1985, 1989). During the months after the autumn equinox through to the spring equinox, the semi-diurnal phase exhibits a steady retardation of 5–6 hours.

The observed seasonal phase changes can be explained in terms of seasonal variations

in the contribution from large-amplitude antisymmetric modes which result from seasonal changes in the heating rates. However, there are seasonal variations in background winds and meridional temperature gradients which may also contribute. Lindzen and Hong (1974) suggested that the seasonal variations were due to the excitation of antisymmetric modes by background winds through mode coupling with symmetric modes. Lindzen (1976) noted that hemispherical differences in the background winds could give rise to differences in the modal composition between summer and winter or spring and autumn. Forbes and Garrett (1978) considered the relative importance of higher order modes at the equinoxes. Similarly, Walterscheid et al. (1980) predicted the dominance of the symmetric modes (2,2) and (2,4) at the solstices and that the presence of antisymmetric modes, such as (2,3), during the equinox were likely because of the latitudinal structure of $O_3$ during this time which would enhance the generation of such modes. Walterscheid et al. (1980) also concluded that modes of short vertical wavelength would be more important in winter, and that the abrupt phase change at equinox may be due to hemispherical circulation differences.

Marked differences in the diurnal and semi-diurnal tidal structure between the northern and southern hemispheres have been reported by Aso and Vincent (1982) and Vincent et al. (1989). This behaviour was attributed to the presence of anti-symmetric modes. During the equinoxes antisymmetric modes are excited as a result of a decrease in the amount of ozone in the southern hemisphere due to northward transport.

## 2.2 Gravity Waves

Gravity waves are buoyancy oscillations in density, wind velocity and temperature, etc, that occur and propagate in the Earth's atmosphere. The gravity waves observed in the MALT originate predominantly from the lower atmosphere as a result of tropospheric storms and fronts (Freund and Jacka 1979, Taylor and Hapgood 1988) and from the interaction of prevailing winds with local orography, such as mountain ranges (Gerbier and Berenger 1961).

If one assumes an inviscid, horizontally stratified atmosphere, a parcel of air, if displaced vertically, will oscillate. The restoring force is provided by the buoyancy of the parcel. When the restoring force is entirely due to buoyancy the waves are called internal gravity waves. In practice, the restoring force is a combination of buoyancy, the pressure change due to compression of the medium and the Earth's rotation and it is assumed that the perturbation quantities vary exponentially with height. The horizontal velocity variations will have the form

$$u' = u_0 \exp(\frac{z}{2H}) \exp[i(\omega t - k_x x - k_y y - k_z z)] \tag{2.1}$$

where $k_x$, $k_y$ and $k_z$ are the wavenumbers in the horizontal (x and y) and vertical

(z) directions, respectively, $u_0$ is a constant with dimensions of velocity.

The horizontal and vertical perturbation velocities, u′ and w′, are related to the horizontal and vertical wavelengths of the perturbation through

$$\frac{\mathrm{u}'}{\mathrm{w}'} = -\frac{\lambda_x}{\lambda_z} \tag{2.2}$$

The upper-frequency limit to buoyancy oscillations in the atmosphere is the Brunt-Vaisala frequency, $f_b$. It is the natural frequency of oscillation in the Earth's atmosphere and is determined by

$$f_b^2 = \frac{1}{4\pi^2}\frac{g}{T}\left(\frac{\partial T}{\partial z} + \frac{g}{C_p}\right) \tag{2.3}$$

where T is temperature, g the acceleration due to gravity and $C_p$ is the specific heat capacity at constant pressure. In the MALT, the Brunt-Vaisala frequency corresponds to an oscillation period of about 5 minutes.

For waves with periods of several hours, the Coriolis force due to the Earth's rotation becomes important. The Coriolis force acts perpendicular to the velocity vector. Such long-period gravity waves are called inertio-gravity waves and the zonal and meridional perturbation velocities are related by

$$v' = -\frac{if}{\omega}u' \tag{2.4}$$

where $\mathrm{i} = \sqrt{-1}$.

Displaced parcels of air trace out an ellipse which is inclined to the horizontal plane and which is perpendicular to the direction of the phase propagation. As the period of the wave increases, the particle trajectories become more circular and the velocity vectors become more horizontal.

The upper limit of the period of inertio-gravity wave oscillation is determined by the inertial frequency or Coriolis parameter $f$. This parameter is latitude-dependent and has the form

$$f = 2\Omega\sin\theta \tag{2.5}$$

where $\Omega = 7.3\times10^{-5}$rad s$^{-1}$ is the Earth's angular rotation velocity and $\theta$ is the latitude. At Birdlings Flat (44°S) the inertial frequency is $10^{-4}$rad s$^{-1}$ which corresponds to a period of 17.3 hours.

For gravity waves of frequency $\omega$ and vertical and horizontal wavenumbers, $k_z$ and $k_x$, respectively, the dispersion relation in a rotating plane is

$$k_z^2 = \frac{\omega_b^2 k_x^2}{\omega^2 - f^2} - \frac{1}{4H^2} \tag{2.6}$$

where $\omega_b$ is the Vaisala-Brunt angular frequency and H is the atmospheric scale height (~8 km). Vertical propagation of the gravity wave is possible only if $k_z^2 > 0$ and $f < \omega < \omega_b$. Tides are a special case of inertio-gravity waves.

Several workers (Noxon 1978, Frederick 1979, Hatfield et al. 1981, Gardner and Shelton 1985, Hines and Tarasick 1987, Tarasick and Hines 1990 and Walterscheid et al. 1987, for example) have investigated the effects of gravity wave propagation upon airglow layers, especially the OH and $O_2$ night airglow emissions. Frederick (1979) showed that atomic oxygen density variations in the MALT, of up to 10 km in the vertical direction, were possible under the influence of a gravity wave with a horizontal wavelength of 200 km and a vertical wavelength of 20 km. Similar findings with regard to vertical emission profile variations were found by Hatfield et al. (1981) and Gardner and Shelton (1985) who investigated gravity-wave effects on OH night airglow and neutral sodium layer emission intensities, respectively.

Turbulence below the level of the turbopause (~110-120 km) appears to be mainly associated with gravity wave breaking action (Fritts and Rastogi 1985, Fritts 1990). The amplitude of a gravity wave propagating vertically upwards in the MALT increases exponentially in order to conserve the energy flux of the wave (i.e amplitude $\sim \exp(\frac{z}{2H})$). This is because the amplitude is proportional to the square root of the density of the surrounding medium ($\rho^{1/2}$) which, itself, decreases with increasing height. The exponential rate of increase with height in the amplitude of gravity waves in the MALT has been found to be less than expected (Reid and Vincent 1986). This behaviour has been attributed to a damping or saturation mechanism which limits the growth of the gravity wave amplitudes with height (Lindzen 1981, Fritts 1984). Gravity wave saturation has been found to be an important mechanism in the dynamics of the MALT region (Fritts 1984, 1989).

Lindzen (1981) showed that, as the amplitude of the wave increases, non-linear effects become important and the wave becomes unstable, or saturated, and eventually breaks depositing its momentum into the region to produce turbulence and heating (Fritts and Rastogi 1985).

Hines (1968) earlier showed that such interactions between gravity waves and the prevailing wind may occur at so-called critical levels where the wave's phase speed and the mean wind speed are equal. The presence of a background mean wind of velocity, u, can therefore determine the amount of gravity wave saturation that will occur. When a gravity wave of phase velocity c, producing a perturbation velocity u', enters a region in which the total velocity u' + u > c, the wave will experience convective instability and the amplitude

growth of the wave will be restricted so that $|u'| \leq |c-u|$. The wave's momentum is therefore transferred into the medium which, in turn, results in an acceleration or deceleration of mean flow towards the phase speed of the wave. If the direction of propagation of the gravity wave and the mean wind flow are co-directional then the mean wind will be accelerated towards the phase speed of the gravity wave. However, if the wave propagation is oppositely-directed to the mean wind, wave breaking may occur. The addition of the wave momentum into the medium would then result in a reversal of the direction of the mean wind. The process of gravity wave saturation in the MALT therefore provides a mechanism for momentum transfer into this region, resulting in local heating and/or changes in the magnitude or directions of the prevailing wind (Hines et al. 1968).

# Chapter 3

# Optical Doppler Winds and the Mt. John Fabry-Perot Spectrometer

## 3.1 The Fabry-Perot Spectrometer

### 3.1.1 General Principles

The Fabry-Perot spectrometer (FPS) (Fabry and Perot 1896, 1897) was first used in airglow studies by Babcock in 1923, to determine the kinetic temperature of the 557.7 nm emission layer. The routine determination of MALT winds and temperatures by optical means is a relatively recent technique, beginning in the 1960's (Armstrong 1968). Fully-automatic FPS's are now employed throughout the world (Hernandez 1980, Jacka 1984) and the technique of deriving horizontal line-of-sight Doppler winds will be described later in this chapter.

There are several excellent books available dealing with the theory and operation of Fabry-Perot spectrometers (Hernandez 1986, Vaughan 1989 and Hariharan 1992, for example) so only a brief description will be given here.

The FPS operates on the principle of interference due to multiple reflections of light between two (or more) flat parallel, highly–reflecting surfaces. Figure 3.1 illustrates the principle. Two reflecting surfaces, in a medium of refractive index, $\mu$, are separated by distance, d. Monochromatic light waves of wavelength $\lambda$, are incident to the surfaces at an angle $\theta$ to the normal. Multiple reflections of each incident light wave occurs within the gap with each successive reflection introducing an extra path difference. This results a phase difference, $\phi$, between adjacent light waves which can be described by

$$\phi = \frac{4\pi\mu d cos\theta}{\lambda} \tag{3.1}$$

In the case of transmission, constructive interference will occur when $\phi$ has integral values of $2\pi$ (i.e. $\phi = 2\pi m$), where $m$ is the order of interference. This corresponds to the condition

$$m\lambda = 2\mu d cos\theta \tag{3.2}$$

The resultant transmitted intensity distribution is a concentric set of alternating light and dark fringes. The fringes are loci of constant phase and the distribution is known as the Airy intensity distribution formula for transmission, $I_t(\phi)$ (Tolansky 1948).

$$I_t(\phi) = \frac{T^2}{(1-R)^2}[1 + \frac{4R}{(1-R)^2}\sin^2\frac{\phi}{2}]^{-1} \tag{3.3}$$

where R and T are the reflection and transmission amplitude coefficients of the etalon, respectively. By definition, R + T + A = 1, where A is the coefficient due to scattering or absorption.

The form of the transmission Airy formula, for various values of R, is shown in Figure 3.2. It is clear that increasing the reflection coefficient of the plates decreases the width of the fringes. The reflection coefficient at 557.7 nm of the etalon at Mt. John was determined to be 79.4% using the technique described by Giacomo (1952) (Hernandez and Smith pers. comm.) (see Appendix A).

The width of the fringes is defined as the fringe-width where the intensity is equal to half its maximum value, known as the Full Width at Half-Maximum (FWHM). The free spectral range (FSR) is defined as the change in wavelength required in order to alter the spectral order by 1 when the etalon spacing is fixed. The finesse, F, of the fringes is usually defined as the ratio of the FSR to the FWHM. The finesse is therefore dependent on the reflectivity of the surfaces and hence this ratio is also known as the reflectivity finesse of the etalon and can be described approximately by

$$F = \frac{\pi\sqrt{R}}{1-R} \tag{3.4}$$

The range of wavelengths corresponding to the FWHM, $\lambda_{FWHM}$, is known as the resolving limit of the FPS and is described approximately by the ratio of the free spectral range to the finesse as

$$\Delta\lambda_{FWHM} = \frac{(1-R)\lambda^2}{2\pi d\sqrt{R}} \tag{3.5}$$

The corresponding resolving power is defined as

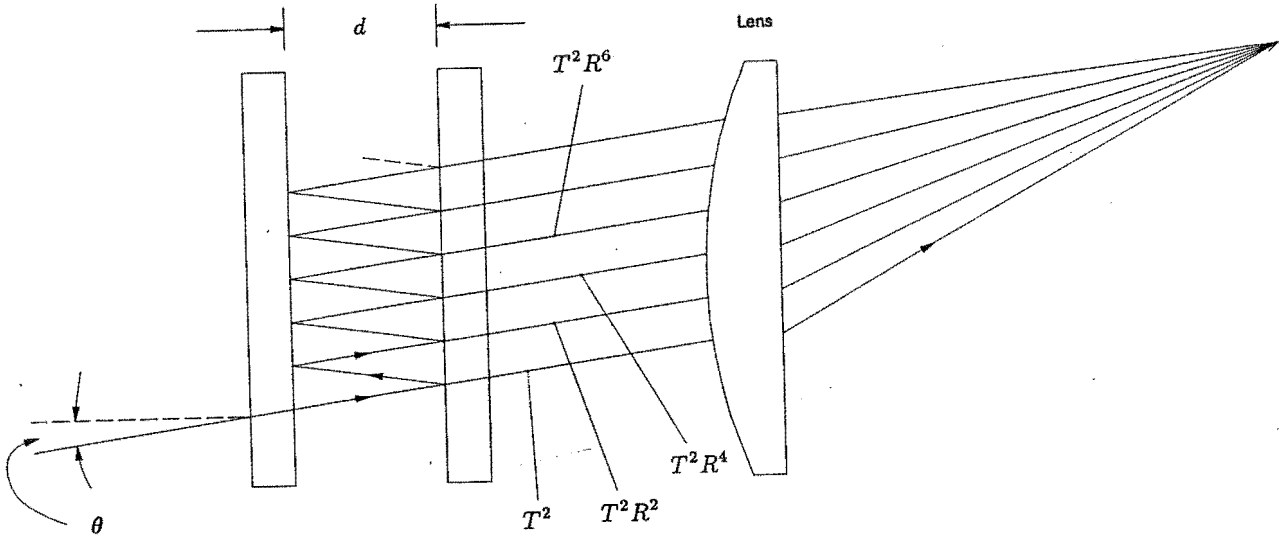


Figure 3.1: A schematic diagram of the basic arrangement in an FPS etalon. Incident light entering the etalon from the left undergoes multiple reflections within the etalon gap, d. The resulting fringes are focussed onto a screen by a field lens.

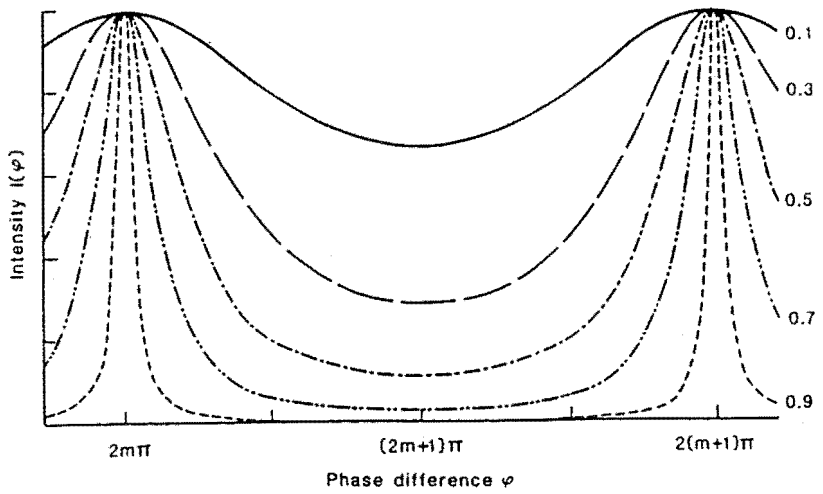


Figure 3.2: The Airy transmission function for several values of reflection coefficients. The distance between successive orders corresponds to a phase difference of $2\pi$ and is known as the free spectral range (FSR) (from Hariharan 1992).

$$R_p = \frac{\lambda}{\Delta\lambda_{FWHM}} \tag{3.6}$$

For the FPS etalon at Mt. John: $\Delta\lambda_{FWHM} = 1.8\times10^{-12}$ m or 1.8 pm, and $R_p = 3.1\times10^5$ at 557.7 nm.

## 3.2 The Mount John Fabry-Perot Spectrometer

### 3.2.1 FPS Wind Measurements

A high-resolution Fabry-Perot spectrometer (FPS) was employed to determine the horizontal winds in the MALT region near 95 km from line-of-sight Doppler measurements of the atmospheric 557.7 nm night emission. The instrument was provided by G. Hernandez and R. W. Smith of the Universities of Washington (Seattle) and Alaska (Fairbanks), respectively, and is sited at Mt. John Observatory, Lake Tekapo in the South Island of New Zealand (43.986° S, 170.465° E geographic) at an altitude of 1000 m above sea level. The location of the FPS, together with the MF radar also used in this project, is shown in Figure 3.3. The FPS is fully autonomous with both data acquisition and instrument operation controlled by a dedicated PC/AT computer. Regular maintenance trips to the Observatory were undertaken in order to ensure the health of the instrument and to retrieve the data.

The FPS is a passive sampling instrument which obliquely samples the airglow emission along the line of sight at an elevation of 20° above the horizon. The emission, recorded as interference fringes by the FPS, provides a tracer of the neutral wind motion within the emission layer allowing horizontal line-of-sight wind velocities to be determined from the Doppler-shifted fringe records. The general observing geometry is shown in Figure 3.4. A repeating sequence of measurements in the direction of the four cardinal points (N, E, S and W) plus zenith is employed during the night. Each individual measurement takes 10–15 minutes and hence approximately 45–70 minutes are required to complete one cycle. This was dependent on the brightness of the OH emission which was simultaneously measured with the 557.7 nm and dictated the sampling time (see section 3.2.6). Hence, each raw wind record is effectively time-averaged over 10–15 minutes allowing a good signal-to-noise ratio (S/N) to be obtained for the data. It does, however, limit the time resolution of the measurements in any one particular direction to ~60 minutes.

The FPS obtains measurements when the sun is 9° below the horizon (end of civil twilight). The night time measurement period varied seasonally from ~7 hours during the summer to ~14 hours during the winter.

The field of view of the FPS is approximately 0.25° (half the width of full-moon), defining a sampling spot size diameter of 1.2 km at a height of 97 km in the zenith or 3.2 km

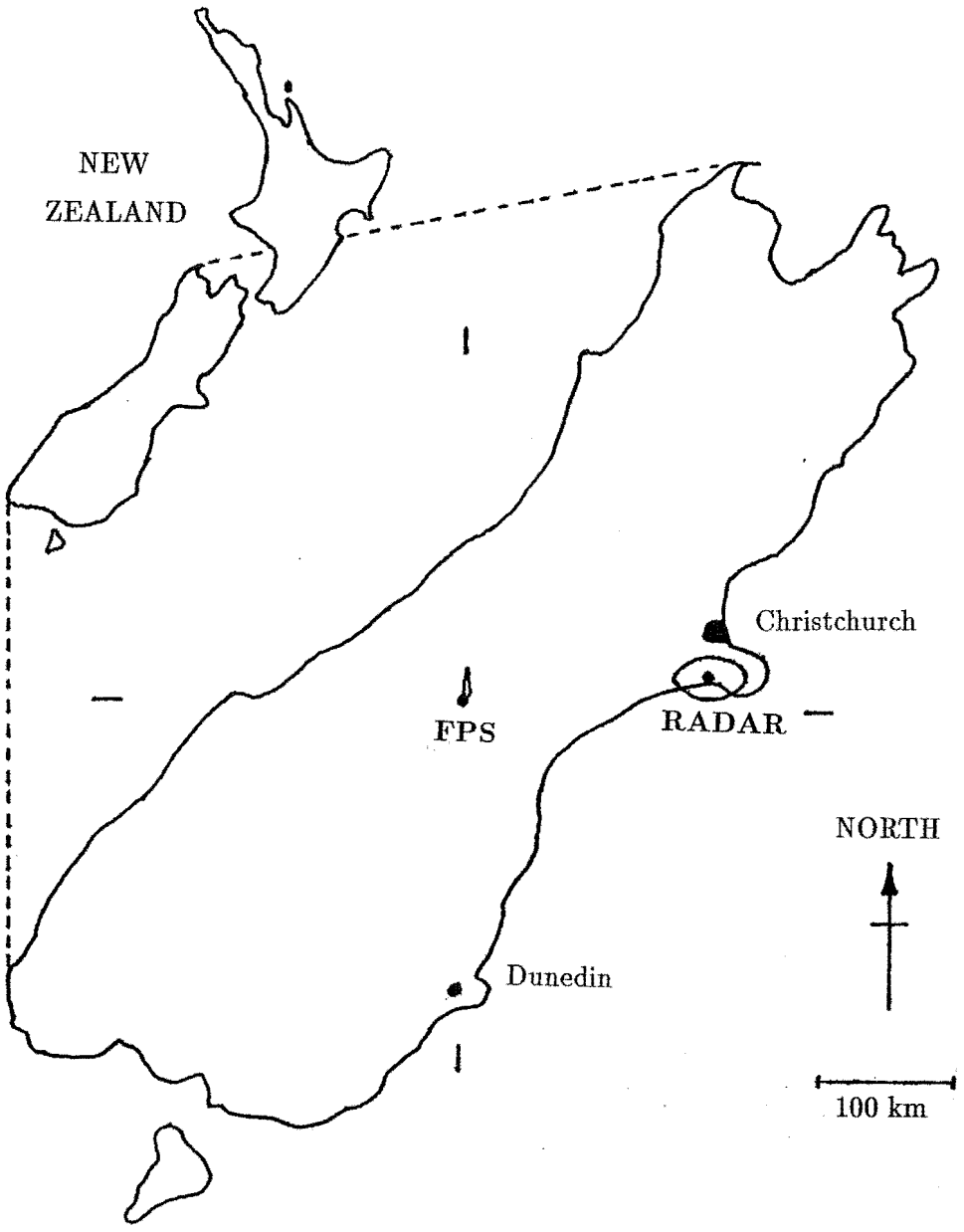


Figure 3.3: The relative geographic locations of the FPS and radar. The short bars in the cardinal directions ~250 km from the FPS location are the horizontal sampling regions of the FPS. The radar elliptical sampling beam is also shown.

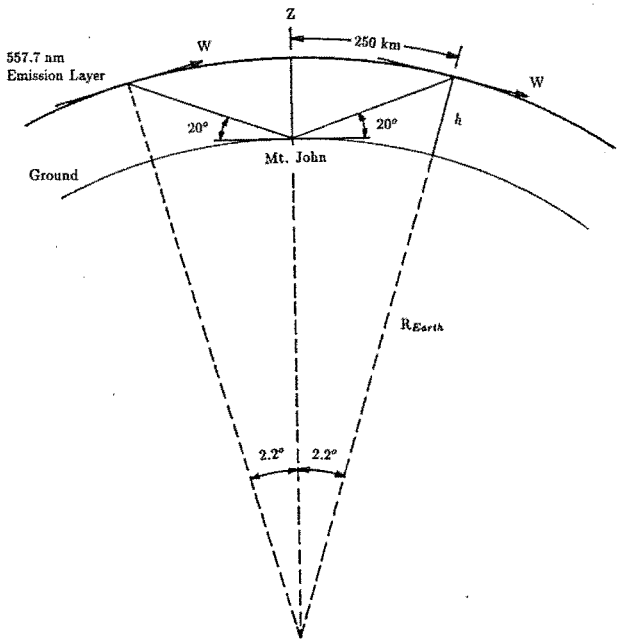


Figure 3.4: The observing geometry (not to scale) of the FPS used to determine the neutral wind motion due to 557.7 nm emission.

at an elevation of 20°. The 557.7 nm layer width at one-half emission (FWHM) is typically ~10–12 km (O'Brien et al. 1965, Donahue et al. 1973, Thomas and Young 1981, Shepherd et al. 1995, Ward et al. 1995) so the sampled volume in the line-of-sight is a narrow pencil ~3 km in diameter and ~30 km in length. The sampled 557.7 nm airglow volumes for two opposite directions, eg. north and south, are separated by ~500 km.

The FPS records the total emission along the line of sight so no height information about the vertical distribution of the 557.7 nm emission is available. The measurements are therefore a weighted distribution of the emission along the instrumental line of sight.

The emission layer is assumed to occur at a constant height and be horizontally and temporally homogeneous. The neutral wind is assumed to move horizontally within the emission layer and is derived from the Doppler shift of the fringes. The line of sight wind motion is converted to a horizontal wind. Because the emission originates from a neutral species, the FPS winds are not expected to be affected by the geomagnetic field.

Vertical motion within the layer is assumed to be negligible or, at the very least, significantly smaller than the uncertainty of the derived horizontal wind. This is assumption is generally correct for periods of low geomagnetic activity ($K_p<3$) at mid-latitudes in the MALT (Hernandez 1980, Rees et al. 1989, Price et al. 1995). For this project, the mean night time vertical velocity is assumed to be zero and the measured fringe profiles obtained in the zenith during the night are used as the zero wavelength reference for the Doppler shifts of the azimuth observations.

The error in the assumption of zero vertical velocity can be estimated from the

standard deviation of the night's zenith-pointing winds. During a typical night, the standard deviation of the raw zenith wind velocities was ~5–7 $ms^{-1}$. The error in the optical winds measured in this project was typically 10–12 $ms^{-1}$. In-situ measurements obtained by radar tracking radar-reflective foil which had been injected into the region by a rocket were made during the DYANA campaign during January–March 1990 (Widdell et al. 1994). The results indicated that vertical velocities near 95 km were typically about 4 $ms^{-1}$. Velocities of 6 $ms^{-1}$ were occasionally reported. These results are similar to the FPS vertical velocities measured in this present project.

For the comparison with the MF radar winds, measurements made during clear nights with low geomagnetic activity ($K_p$<3) were selected; the selection of such nights is described further in Chapter 5.

The line-of-sight integration of the 557.7 nm emission results in the contribution from two distinct components of emission comprising the observed line profile; namely, emission from 95–100 km in the MALT in which this study is concerned, and emission from near 250 km in the F region. The etalon gap of 20 mm was chosen in order to filter out the majority of the F region 557.7 nm contribution (Hernandez 1971, 1976, 1980, Hernandez and Killeen 1989, Hines et al. 1993). The F region component is hotter than the MALT component and so exhibits a broader emission line profile. By increasing the resolution of the instrument the F region component will be washed out as a result of the overlap of spectral orders by the interferometer. The increased resolution is achieved by increasing the distance between the optical flats of the etalon.

The meteorological sign convention is used to describe the wind velocities in this project. Eastward and northward winds are denoted as positive and westward and southward winds are denoted as negative. The choice of the appropriate sign for the optical wind directions was checked several times during the course of this project and the derivation procedure is described in the Appendix A. The time of observation of the raw FPS measurements is the central time of the measurement in UT.

Figure 3.5 is a schematic diagram of the FPS showing its mode of operation and major parts. Airglow emission is directed down into the FPS room by a periscope mirror assembly on the roof of the observatory building. The movements of the periscope mirror are controlled by the computer, together with a shutter-mechanism. The emission passes through the etalon and the resultant interference fringes are directed, via a dichroic mirror, to one of two data channels where photomultiplier tubes (PMTs) detect the light intensity. Prior to entry to the PMTs, the emission passes through narrow-band interference filters. The emission detected by the PMTs is amplified and summed for each incremental step of the scan (1/256 of scan or 1/32 s) and then written to the computer memory. Several successive scans are made at one particular direction and coherently added. The fringe spectra are

appropriately scaled and displayed in real time during aquisition on the computer. Once the S/N of the fringe record reaches a pre-determined count the record is stored on the computer's hard disc for analysis. The two data channels simultaneously produce two different fringe records from different emission wavelengths. The following sections provided a more detailed description of the various components and systems of the FPS.

### 3.2.2 The Etalon

The FPS consists of a self-aligning quartz etalon (Hernandez and Mills 1973) with a clear aperture of 152 mm and and an air gap of 20 mm. The etalon is scanned electro-mechanically using stacks of piezoelectric crystals arranged between the two optical flats. The etalon scanning operation is controlled by an electronic servo system, clocked by a 1024 Hz oscillator and independent of the computer. The servo system scans the spectrum every 9 seconds (8 s etalon scan plus 1 s flyback time) and controls the alignment and stability of the instrument. The servo system operates continuously, even during the daytime when data aquisition has ended. During night-time operation, computer control and the data aquisition rate are controlled by a 32 Hz signal which is derived from the oscillator.

The etalon is a re-entrant type. This is one in which the lower optical flat, which has a smaller diameter than the upper flat and is mobile during scanning, lies "inside" the spacers separating it from the upper flat (see Figure 3.5). The inside surfaces of the two flats are parallel and smooth to within $\lambda/200$ (Hg test lamp $\lambda$=546.1 nm during etalon production). Each flat is about 35 mm in thickness and the outside optical surfaces are wedged at an angle of $30'$ in order to remove unwanted ghost fringes due to multiple reflections. The etalon temperature was maintained at a constant 24°C through the use of a heater controller unit and a heater blanket wrapped around the etalon cap. This is monitored with a temperature sensor. An air conditioning unit within the instrument room maintains the room at a temperature of about 19–20°C.

Both the scanning and re-entrant stacks are connected via a feedback system which constantly monitors the parallelism and stability of the etalon gap. The two etalon flats were contact-glued to two sets of three stacks of piezoelectric material. The piezoelectric material is a modified lead zirconate titanate ceramic called PZT-8 and is produced by Vernitron Corp., USA. Each individual stack consisted of six washer-shaped discs of piezoelectric material, each 2 mm thick, which were cemented together with epoxy glue and wired in parallel. These were set at $120^o$ intervals around the periphery of the plates. The second set was set around the periphery also. A set of three Cervit spacers were epoxied to the outside set in order to give the nominal gap distance of 20 mm. The spacers had coefficients of expansion which were well-matched with the piezoelectric stacks, allowing the gap to remain constant, during

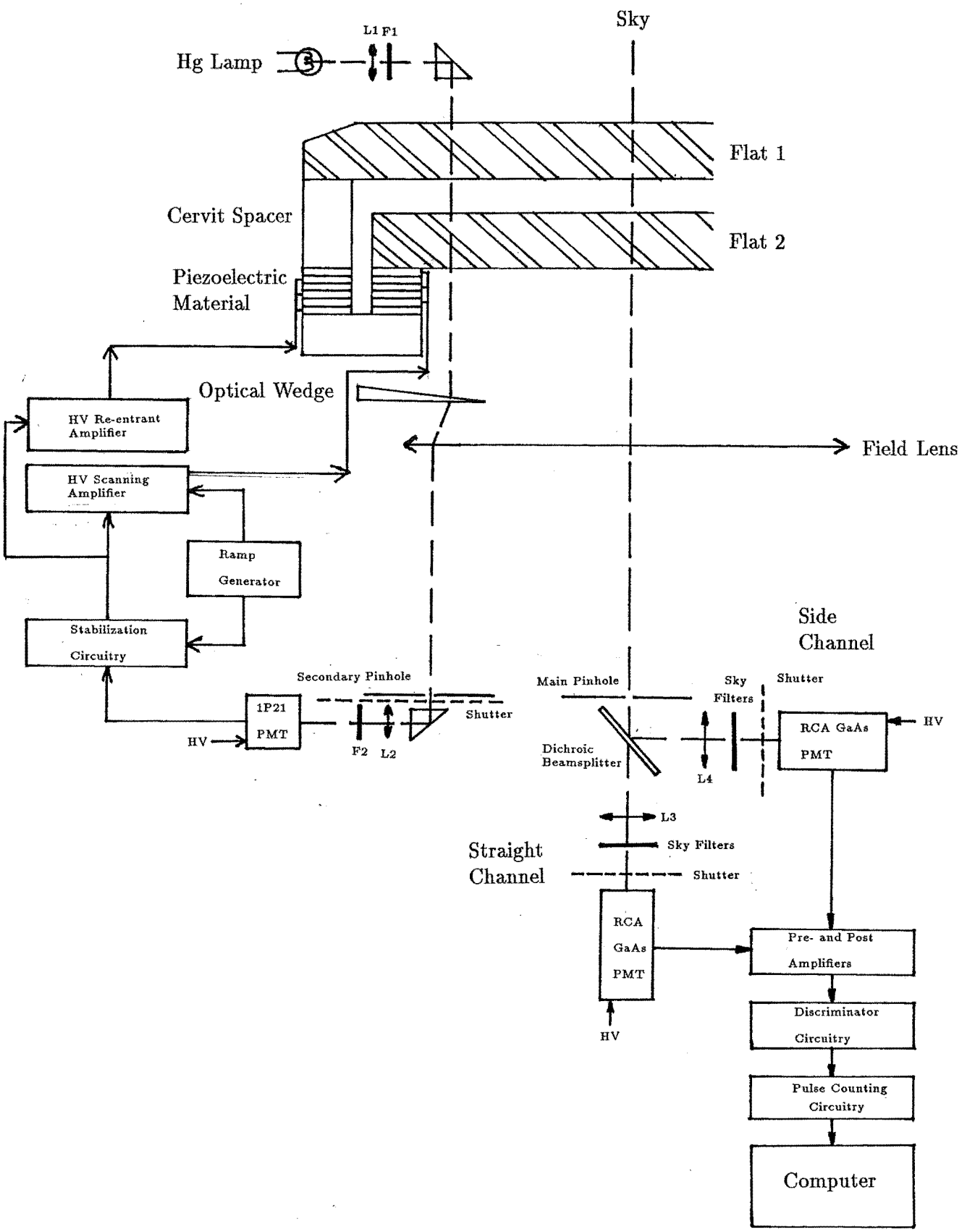


Figure 3.5: Schematic diagram (not to scale) showing the major components of the FPS. The stability and parallelism of the etalon is maintained by the feedback system on the left side of the diagram. The data acquisition system is on the right hand side of the diagram and is aligned with the central optical axis of the etalon.

expansion or contraction due to temperature variations. The bottom of each piezoelectric stack was cemented to a quartz base to further provide both mechanical and thermal stability. During normal operation the etalon voltage was scanned from approximately 250 to 750 V. The plate separation change for this voltage range was 1.8 $\mu$m and resulted in the sampling of over three orders at 557.7 nm.

Prior to September 1991, the inside set of posts was used to scan the gap and the outer set of posts was used as to maintain the stability of the gap. A positive voltage ramp was applied to the inside set of piezoelectric stacks and, as a result, the gap distance increased during the scanning. During 1991, it was found that one of the piezoelectric stacks responsible for the scanning operation was deteriorating. The deterioration affected the instrument's ability to maintain parallelism of the etalon during scanning, especially during large and rapid atmospheric pressure changes, such as the passage of a frontal system over the site. In particular, the scanning voltage range required for one of the scanning stacks had increased from about 500 V, at the time of installation in November 1990, to almost 950 V in September 1991. This caused the etalon to frequently lose alignment.

In September 1991, the functions of the two sets of piezoelectric stacks were interchanged. The positive voltage ramp is now applied to the outer set of piezoelectric stacks and the etalon gap distance now decreases during the scan. The interchange removed the deterioration since the re-entrant stack does not scan but is used to keep the etalon gap constant during external variations in temperature and pressure.

The scanning behaviour of piezoelectric material with regard to FPS instruments has been described by Hernandez (1978) and its use has been reviewed by Vaughan (1989). A voltage applied to piezoelectric material induces a strain on the material which causes it to increase in length parallel to the direction of the applied voltage. The incremental increase in length with increasing applied voltage is not an exact linear relationship. This is due to the nature of piezoelectric material and the physical construction of the material used between the etalon plates. The result of the non-linear behaviour was to produce unequal spacing between adjacent FPS fringe peaks such that the maxima of each subsequent order would occur closer and closer together. The effect of the non-linear scanning behaviour on the FPS fringe data was minimised during the data reduction stage and is described in chapter 5.

### 3.2.3 Piezoelectric Scanning - Stability and Parallelism

Several electronic units drive the etalon scanning operation and ensure the parallelism and stability of the gap with respect to a reference wavelength during the scanning process. The design is based upon that described by Hernandez and Mills (1973).

### Ramp Generator

The ramp generator controls the servo process of scanning the etalon. It is the main driver of the etalon scanning operation and produces the scanning voltage waveform. The voltage waveform is an analog linear sawtooth from 0 to 10 VDC. It is produced by an up/down digital counter which is clocked by a very stable 1024 Hz oscillator. The digital output from the counter is converted to an analog signal via a stabilised ten-bit D-to-A converter. The scan is divided into 256 steps, or bins, to match the rate of data acquisition (32Hz) by the compute from the oscillator. The generator also produces gating pulses at the beginning and end of the ramp, as well as gate pulses at two arbitrary positions along the ramps, to synchronise each of the three scanning stacks. The positions of the two gate pulse markers along the ramp can be set on the front panel of the electronics rack. The ramp waveform is then sent to the Self-Aligning Unit (SAU), which will be discussed next.

### Self-Aligning Unit (SAU)

The Self-Aligning Unit (SAU) is a feedback system containing six gated integrators and smoothing circuitry used to maintain the parallelism of the etalon and simultaneously maintain stability of the gap with respect to a reference wavelength (546.1 nm). It is powered by a low-voltage 5V, 3A supply. A sawtooth linear ramp signal, originating from the ramp generator, is divided into three equal and independent signals by the SAU. These are passed to the high-voltage (HV) amplifiers where they are amplified to a voltage sufficient to drive the piezoelectric stacks. A single high-voltage supply of 60 mA at 1100–1200 VDC (depending on the load) supplies both the scanning and the re-entrant amplifiers. The linearity of the HV amplifiers driving the piezoelectric scanning crystals was checked and was not found to contribute to the non-linearity of the scanning. Figure 3.6 is a schematic diagram of the stabilising circuitry for one channel (Hernandez and Mills 1973).

Three Hg (546.1 nm) discharge lamps (Type 11SC-2) are arranged above the etalon, at 120° intervals around its edge. This wavelength was chosen because it is within the high reflectivity region of the etalon coatings. The 564.1 nm emission from the three Hg lamps is pre-filtered using 5–6 $\AA$ nominal bandwidth filters centred on 564.1 nm with a rejection factor at 557.7 nm of $10^3$ (Hernandez pers. comm.). The lamps shine directly through the etalon and form fringes on three subsidiary pinholes. To reach these pinholes, the Hg light is deviated 70 mm away from the main axis of the FPS, and hence the main pinhole, by three small wedge prisms (one for each lamp) (see Figure 3.5). The fringes are then filtered and focussed onto three 1P-21 photomultipliers. The signal from the 1P-21's (~few hundred pA) is then passed through a current-to-voltage pre-amplifier (one for each PMT) and converted to a more usable voltage (~1 V). The signal is then sent to the first stage of the SAU where

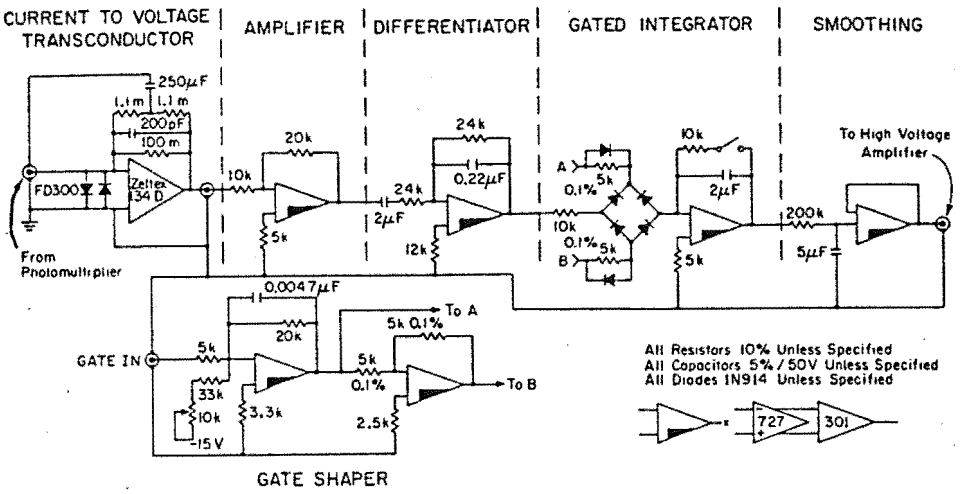


Figure 3.6: Schematic diagram of the SAU circuitry for one channel, i.e. from one 1P21 PMT. Elements responsible for housekeeping duties such as compensators, meters, etc are omitted for clarity (From Hernandez and Mills 1973).

it is AC-coupled (since it is the phase of the signals from the 1P-21's due to the fringes that is required). The signal then passes through another amplifier and a broad-band low-pass filter.

Between the amplification and filtering stages the phases of the three signals are time-synchronised to within 0.1% (Hernandez and Mills 1973). The initial phase differences are due to different RC time constants of the circuits dealing with each of the three signals. Differences in the individual componentry tolerances results in time shifts between the theoretically–equal signals. Three circuits, one for each signal, are employed to allow the time constants to be equalised by introducing a time delay into each of the three channels. This involves the placement of three light-emitting diodes (LED's) in the three 1P-21 tube holders. The three LED's are connected in series. A triangular-shaped signal with a frequency of about 0.25 Hz is generated by an LED driver circuit in the SAU and is sent to the LEDs. The LED driver circuit is not synchronised to the ramp signal. The SAU provides a trigger signal to allow an oscilloscope to be used for diagnostics.

The three time-synchronised signals are then differentiated so that zero-crossings are obtained where peaks in the signal occur. This differentiated signal is then transferred via a field-effect transistor (FET) switch to the gated integrators. The gate is fixed relative to the beginning of the voltage ramp cycle and is produced via a digital comparator by the ramp generator. The gate width is less than 1/256 of the total scan time, being narrow and fast enough to provide corrections to parallelism of the etalon flats to within $\lambda/200$ with

negligible overshoot. It is theoretically able to improve upon this value (Hernandez and Mills 1973) but in practice it is limited by the surface accuracy of the etalon flats.

Three orders of the Hg 546.1 nm line are scanned during each 8–second scan. The first gate provides the parallelism and stability of the etalon gap. The second gate is used to equalise the gain of the HV amplifier scanning the piezoelectric stacks.

The location of the fringe maxima is determined by the zero-crossings of the derivative of the signal relative to a gate signal once every ramp cycle. The integrator voltage that is obtained possesses a polarity and a magnitude which corresponds to the relative time displacements between the zero-crossing and the gate; and it is proportional to the displacement. During every ramp cycle, the integrator voltage level decreases until the gate coincides with the zero-crossing. At this point, the voltage stabilises and the etalon is locked onto the Hg fringes and alignment is achieved.

The integrators, in a sense, act as a long-term memory of the zero-crossing displacements, and hence the fringe peak position. The integrator output biases the HV amplifier and delivers a correction signal to the piezoelectric stacks such that the time difference is reduced.

The output from the integrators is fed into a low-pass ($t_c$=20s) RC filter. The smoothing removes transients due to electrical noise or vibrations and also it reduces the amount of spiking due to the actual gating process of the integrator. The smoothed output of the integrator is then applied as a bias correction signal to the three separate sections of the scanning HV amplifier (the three channels, one for each scanning stack, are fed into the three top meters on the front panel of the SAU) with the polarity from each applied so that the gate/zero-crossing time difference is reduced and self-correction occurs.

Similar treatment is made in the case of the second gate. The three sets of smoothed integrator voltages drive the LED-photoconductor combinations so as to alter the gain of the HV scanning ramp. This forces the second zero-crossings and the second gates of the three piezoelectric stacks to coincide so that the etalon is parallel at both gates 1 and 2.

A quantitative measurement of the stability of the FPS etalon was obtained using a frequency-stabilised 632.8 nm HeNe laser. The laser emission profiles were recorded every hour during the daytime. Figure 3.7 shows the corresponding velocities derived from the laser fringe profiles for 4 March 1994, a typical day. The uncertainties associated with these values are the uncertainty of fit values of the fringe peak positions. The distribution is centred about zero and has a standard deviation of 4.9 $ms^{-1}$. The variation from zero is a combination of the etalon stability and the stability of the laser frequency. Typically, the zenith velocity distribution during the night, the mean value of which is used as the zero velocity reference, has a standard deviation of 5–7 $ms^{-1}$, which is less than the uncertainty in the determined optical wind values, about 10–12 $ms^{-1}$. Hence any variations in the fringe peak positions

due to variations in the stability of the etalon gap were less than the uncertainty of the wind velocity measurements.

### 3.2.4 Filter System

The FPS has two identical automatic filter changers in both channels. The position of each is controlled by the computer controller which is run by a batch data file. Each filter changer holds two different narrow-band interference filters and is driven by a stepping motor and a lead screw. The stop positions are determined by limit switches. The position of each is controlled by the computer controller, which is also run by the batch file.

Channel 1 or the straight channel (the channel with the PMT directly along the major axis of the FPS) houses the 840.0 and 630.0 nm filters. Channel 2 or the side channel (the channel with the PMT perpendicular to the major axis of the FPS) houses the 632.8 and 557.7 nm filters. In addition, either of the filter changers may be removed and a single-colour filter holder may be used. The batch data file can be altered to allow for this mode of operation. The 632.8 nm HeNe laser filter is located in the side channel because of the high relative intensity of the laser source and to allow for effective use of the remaining filter positions.

Narrow-band interference filters were employed to isolate each emission for detection and recording. The nominal bandwidth of the 557.7 nm filters was 4–5 $\AA$ (Hernadez pers. comm.). The 840.0 nm filter has a nominal bandpass of 4–5 $\AA$ and the 632.8 nm filter, for the laser calibration measurements, has a nominal bandpass of about 10 $\AA$ (Hernandez pers. comm.).

The narrow bandwidths of the filters therefore isolated each emission and no Hg lamp emission leakage is detectable at any of the observation wavelengths. Furthermore, the Hg lamp filters reject emission at the wavelength of 557.7 nm by a factor of $10^3$ (Hernandez pers. comm.), so the amount of 557.7 nm emission entering the SAU system was negligible.

Heater controller units maintain the filters at a temperature of approximately 25°C using a heater element and a thermistor which are located in each of the two filter holder housings adjoining the PMTs.

The throughput of each filter was optimised by adjusting the filter tilt angle with respect to the incident beam in order to maximise the emission count rate. This process was performed periodically and it was repeated several times for each filter in order to average out any external variations in the emission. Prior to this operation, the fringe pattern was also checked for alignment on the PMT photocathode in order to give the maximum count rate.

The filters were generally replaced during January of each year or when required.

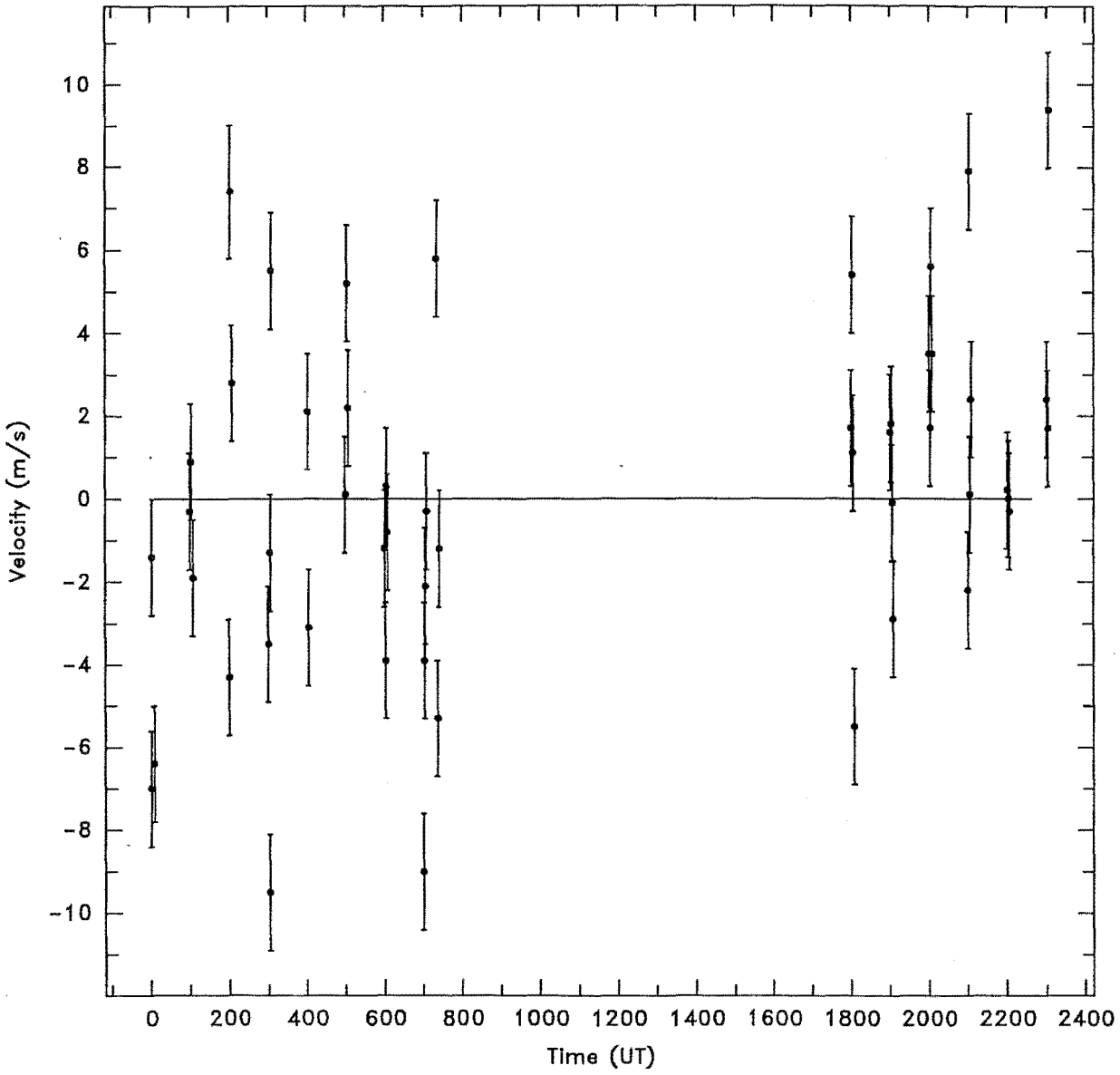


Figure 3.7: The corresponding velocities derived from the 632.8 nm HeNe laser fringe profiles for 4 March 1994 illustrates that the FPS exhibits a stability of between 5-7 $ms^{-1}$. The standard deviation of the raw measurements for the night is 4.9 $ms^{-1}$.

### Main Lens

A 152 mm diameter achromatic lens with a focal length of 629 mm is positioned between the etalon housing and the main pinhole. This lens focuses the sky emission fringes onto the main pinhole. During 1991, the original lens was found to be severely astigmatic, resulting in significantly asymmetric fringe profiles. A replacement lens was installed in September 1991 which eliminated the astigmatism.

### Main Pinhole

The main pinhole is an accurately-machined hole in a screen, onto which the interference fringes are focussed. The rectangular-shaped screens can be removed to allow different sizes of pinholes to be used. During this project, several different-sized pinholes ranging from 27.0 to 57.0 mK were used to optimise the data records (A milli-Kayser (mK) is a unit of inverse length. eg. 57 mK = $57 \times 10^{-3}$ $cm^{-1}$ or $57 \times 10^{-3}$ wavenumbers). The periods during which each size were used are given in Appendix A.

### Dichroic Mirror

A magenta dichroic mirror, positioned below the main pinhole and set at $45^o$ to the major axis of the FPS, is used to direct the emission into the two PMTs by acting as a beam-splitter (see Figure 3.5). The placement of the filters in either channel was determined by the measuring the count rate with each filter sited in either Channel 1 or 2. The final filter positions were then chosen to optimise the count rate.

## 3.2.5 Signal Detection

The detection system of the FPS consisted of two Peltier-cooled RCA C31034 GaAs photomultiplier tube (PMTs), one for each channel, connected to amplifiers and pulse-counters. The PMTs are powered by a 0.5 mA supply set at 1460 VDC. The Peltier elements are powered from an independent low-voltage source. An alcohol-water mixture is pumped around a closed circuit through both PMT housings via a chiller to maintain them at $\sim 5^oC$.

From the PMTs, the signal pulses are pre-amplified using a charge-to-voltage pre-amplifier. They then pass into the main amplifier, the gain of which was adjusted until the majority of pulses peaked at 6 V amplitude. The pulses are then transferred into a window-type discriminator. This is one in which an upper and a lower level can be set. The lower level is set to about 2 V to eliminate noise pulses. The upper level is set at 8 V above the lower level. This allowed for the transmission of large amplitude pulses without excessive clipping of the pulses. From the discriminator, the pulses are fed into the pulse-counting circuitry used by the computer.

### 3.2.6 Periscope and Shutter

The periscope is physically separate from the FPS and is fixed to the observatory roof. It consists of a plane mirror which directs the airglow emission, from $20^o$ above the horizon and from the zenith, down onto the FPS etalon. For the zenith observations, the mirror is moved out of the optical axis of the instrument to allow the etalon itself to directly collect the vertically incident airglow emission. The pointing accuracy of the periscope mirror is within $\pm 2.5^o$.

The periscope is not fully computer-controlled in the strict sense. The computer initially registers that a direction change should take place. The computer interface then dictates the direction which the mirror would point. The mirror then moves to that direction. Finally, the computer reads the new direction and adjust its internal direction reading accordingly.

The periscope apparatus is enclosed in a windowed weatherproof box measuring approximately 1.0 m $\times$ 0.5 m by 1.0 m deep. A 30 cm steel flue directs the light from the periscope down through the roof into the room housing the FPS. This flue ends at the ceiling where the shutter is housed. The shutter is essentially a movable slide connected to a computer-controlled stall motor.

During the first two years of operation, the periscope apparatus frequently locked up the computer, and hence the FPS operation. This required the instrument to be manually re-booted. This recurrent problem was eliminated during 1992, when the periscope's computer interface was re-designed.

### 3.2.7 Computer Control and Data Acquisition

#### Hardware

The FPS is automatically-controlled by a COMPAQ 286e AT computer running a batch program. This machine contains an Intel 80286 CPU chip and a 80287 math co-processor chip. It has 1 MB of RAM and a 42 MB hard-disc. The machine accepts 1.2 MB 5 1/2" floppy-discs and also 40 MB tape cartridges for data archiving. The machine will automatically re-boot the FPS program if there is a power-cut.

#### Software

The software responsible for the FPS operation was written in Ryan-McFarland Fortran (IBM Professional Fortran) by J. Baldridge and R.W. Smith (Hernandez and Smith pers. comm.). It is designed to interface with the servo-controlled FPS without affecting it optically or mechanically. The main program and a complement of subroutines control the

acquisition, display and archiving of the data (Hernandez and Smith pers. comm.). The program also enables the instrument to be monitored remotely from Christchurch and the United States. A subroutine is responsible for the calculation of the start and stop times of the instrument data taking through the determination of the sun's distance below the horizon during the year. A photo-resistive circuit is employed as a back-up, to ensure that the shutter closes at the end of the night's observing, and remain so during the day, in order to protect the light-sensitive PMTs.

The observation sequence is governed by a batch data file. This contains information on the filters to be used, count and background acceptance criteria, the sequence of directions, etc which the program requires to run the instrument and correctly record the data.

### Data Acquisition, Computation and Display

The FPS operation program accepts data signals from the ramp generator and interrupts are employed in the program to record the incoming data. The program also displays the resulting fringes and performs various calculations and housekeeping tasks during gaps in the data recording. Remote access via a modem is also available and this allows the progress and health of the instrument to be routinely monitored from anywhere. Various parameters can be quickly and easily determined and altered remotely such as the start and stop times, the count and background acceptance criteria, as well as the filters being used.

An interrupt routine reads in the two sets of photon counts, the temperature and voltage sensors, etc via a parallel data input port, at a rate of 32 Hz, which is governed by two sets of pulses from the ramp generator. During each scan, the two sets of photon counts, each scan consisting of 256 bins of counts, are stored in buffers which are accessed through a Scientific Solutions parallel port board. When a scan is completed, the two set of counts are added to the previous scans in the memory, and the housekeeping data, such as temperature and voltage measurements, are updated and re-displayed.

Equidistant equal-noise sampling (Hernandez 1986) is the method used to record the airglow emission. The measurement of the emission using this method is independent of the emission rate and so it minimises the effect of possible intrinsic emission variations during the measurement. It also allows for an arbitrary S/N ratio to be obtained for all the measurements.

The method relies on reaching a pre-selected number of counts and allows for a specified number of background noise counts in the following way. Pre-selected values for the total count TC, and background count per scan B, are initially entered into the batch file, which is read by the FPS operating program. During the night-time operation, if, at some particular time the total number of scans is N and the total number of counts is T, then the

instantaneous adjusted (for background noise) total count number, AC will be:

$$AC = T - NB \tag{3.7}$$

At the end of each scan, if AC is greater than the pre-selected total count number, TC, the fringe record is written onto the hard disk. For example, if the pre-selected total count TC is 20000 and the background count number per scan is 50. Consider that, after 51 scans, the total counts T obtained is say, 21000, then the adjusted total count number AC is 18450 counts. If after 52 scans, T = 23000 counts then AC = 20400 counts. Since AC > TC, the criterion is satisfied and the data is written onto the hard-disk. The FPS then changes to the next direction determined by the batch file. At the end of the night's operation, the night's data is written onto 40 MB magnetic tape for subsequent retrieval and analysis. The size of a night's data file depends upon the meteorological conditions and the intensity of the emission, but is usually between 100–800 kB.

### 3.2.8 Uninterruptible Power Supply

The FPS, together with all of its attendant support systems, draws approximately 2 kW. The whole system is protected from power spikes and temporary losses and cuts in supply by an Uninterruptible Power Supply (UPS). The UPS contains batteries which are charged during periods of normal running. During a power loss they can provide 1 kVA of power for about 20 minutes.

# Chapter 4

# Partial Reflection Winds and the Birdlings Flat Radar

## 4.1 Radio Wave Scattering

There many texts available on the subject of radio wave scattering, such as Budden (1985) and Davies (1992). This discussion will be confined to vertical (normal) incidence.

Free electrons in the ionosphere interact and oscillate with the electric field of an incident radio wave. The natural frequency of oscillation of the electrons is known as the plasma frequency $\omega_p$, and it is proportional to the square root of the number density of electrons (Davies 1992); namely

$$\omega_{\mathrm{p}} = \sqrt{\frac{\mathrm{Ne}^2}{\epsilon_0 \mathrm{m_e}}} \tag{4.1}$$

where $N$ is the electronic number density, $e$ the electronic charge, $m_e$ the electronic mass and $\epsilon_0$ the permittivity of free space.

The number density of electrons generally increases with height in this region and hence, so does the plasma frequency. The maximum plasma frequency corresponding to a particular ionospheric region is known as the critical frequency. If the probing frequency of a radio wave is higher than the critical frequency, the wave will penetrate the layer and proceed to higher altitudes. If the probing frequency is equal to the plasma frequency the radio wave will be totally reflected. The plasma frequency at 95–100 km is ~1 MHz, which is comparable to the MF probing frequency.

In a slowly varying ionospheric medium, reflection of a radio wave will occur when the term $\frac{1}{n}\frac{dn}{dz}$ (Budden 1985) gets large, i.e. when $n \longrightarrow 0$, in which case total reflection occurs, and when $\frac{dn}{dz}$ gets large, and partial reflection occurs (Budden 1985).

The Appleton-Hartree (A-H) equation (Appleton 1927; Hartree 1931) describes the

refractive index, $n$, of a birefringent-refringent plasma medium, such as the ionosphere.

$$n^2 = 1 - \frac{X}{1 - iZ - \frac{Y_T^2}{2(1-X-iZ)} \pm \sqrt{\frac{Y_T^4}{4(1-X-iZ)^2} + Y_L^2}} \tag{4.2}$$

where $X = (\omega_p/\omega)^2$, $Y_L = \omega_{HL}/\omega$, $Y_T = \omega_{HT}/\omega$, $Z = \nu/\omega$ and $\omega_H = 2\pi f_H$ and is known as the angular gyromagnetic frequency (see Equation (4.3) below). The subscripts T and L denote the longitudinal and transverse components of the geomagnetic field with respect to the direction of the propagation of the electromagnetic wave.

The refractive index is, in general, a complex quantity of the form $n = \mu - i\chi$ and the A-H equation can be approximated depending on the dominant parameters occurring in each region of height.

The motion of a charged particle in the presence of a magnetic field is influenced by the Lorentz force in the direction perpendicular to both the velocity vector and the magnetic field. The projection of the particle's motion in the plane perpendicular to the magnetic field is circular and the frequency of this gyration is called the gyromagnetic frequency $f_H$ and is defined as

$$f_H = \frac{e}{2\pi mB} \tag{4.3}$$

where $m$ is the particle mass and B is the magnetic field.

Below about 95 km, collisions between free electrons and neutrals are important, however the influence of the geomagnetic field can be considered negligible. Thus, the A-H equation can be approximated to

$$n^2 = 1 - \frac{\omega_p^2}{\omega^2} \frac{1}{1 - i\frac{\nu}{\omega}} \tag{4.4}$$

where $\nu$ corresponds to the electron-neutral collision frequency. This parameter depends on the number densities of electrons and neutrals and it varies rapidly with height, as well as temporally. In this height region, non-deviative absorption (discussed later) of the radio wave will occur and this will be greatest when $\nu$ is comparable to the probing frequency.

When a radio wave of encounters a region where the wave frequency approaches the plasma frequency the magnitudes of the group and phase velocities of the wave diverge. The group velocity slows down and the wave is reflected. Total reflection of the wave will occur when the real part of the refractive index $\mu = 0$. When collisions are included in the refractive index calculation the reflection process becomes more complicated and requires a study of processes in the complex plane (Budden 1985). It also requires that the height be considered as a complex variable (Budden 1985).

At heights above 95–100 km, $\nu$ is very small compared to the probing frequency ($\nu$~100 kHz at 100 km (Davies 1966)) and so can be neglected, i.e. Z = 0. The geomagnetic field however becomes important. The refractive index becomes a purely real quantity i.e. $n = \mu$, and the A-H equation will contain terms involving the longitudinal and transverse components of the electron gyrofrequency with respect to the geomagnetic field.

In the presence of the geomagnetic field, the refractive index is double–valued. Upon entering the ionosphere, a linearly polarised radio wave will decompose into two characteristic modes of propagation, the ordinary, o, and the extraordinary, x, modes. The o and x modes will be two elliptically–polarised waves rotating in opposite directions.

The propagation paths of the two modes may differ considerably, with the total reflection points of each mode differing by over 50 km, horizontally and vertically (Davies 1992). Differences in the refractive indices or in the ray paths will cause the o and x waves to rotate differentially. If the difference in phase path is a linear function of time then a linear receiving array, such as at Birdlings Flat, will observe a sinusoidal fading behaviour.

The amount of non-deviative absorption is proportional to the product of the electron-neutral collision frequency and the electron number density, which is greatest at 70–80 km in the D region. Non-deviative absorption occurs when $\mu$ is close to 1 and the product $N\nu$ is large. The ray path is unaltered by this type of absorption. If the phase propagation of the wave is assumed to be parallel to the geomagnetic field (quasi-longitudinal (QL) approximation) then the non-deviative absorption coefficient $\kappa$, can be approximated to (Davies 1992)

$$\kappa \approx \frac{e^2}{2\epsilon_0 mc} \frac{N\nu}{(\omega \pm \omega_{HL})^2 + \nu^2} \tag{4.5}$$

where $\kappa$ corresponds to the imaginary part of the refractive index since $\kappa = \chi\omega/c$.

The o and x modes correspond to the + and − signs, respectively. The x mode experiences more absorption than the o mode, because the minus sign results in a smaller–valued denominator in Equation (4.5). This is especially true during the daytime, so the amplitude ratio of the x and o modes, $A_x/A_o$, is usually much smaller than unity. The diffraction pattern sampled by the spaced receivers on the ground (discussed later in this chapter) during the daytime is therefore due predominantly to o mode propagation. At night, in the absence of the D region, it is possible that the $A_x/A_o$ ratio is higher. If this arises then interference between the two modes may occur, resulting in polarisation fading. The interference will alter the diffraction pattern as it moves across the receiving array and cause erroneous wind measurements.

Polarisation fading may occur when the amplitudes of the o and x modes are comparable. Random path differences in the o and x mode partial reflection points would be

| | Number Density ($m^{-3}$) | |
|---|---|---|
| | Noon | Midnight |
| Summer | $2.3 \times 10^9$ | $3.8 \times 10^8$ |
| Winter | $3.5 \times 10^9$ | $4.0 \times 10^8$ |

Table 4.1: Typical midday and midnight electron number densities at a height of 95 km above Birdlings Flat during mid-winter and mid-summer (von Biel pers. comm.).

| | Noon | ($m^{-1}$) | Midnight | ($m^{-1}$) |
|---|---|---|---|---|
| | $\kappa_o$ | $\kappa_x$ | $\kappa_o$ | $\kappa_x$ |
| Summer | $1.22 \times 10^{-6}$ | $1.77 \times 10^{-5}$ | $2.02 \times 10^{-7}$ | $2.92 \times 10^{-6}$ |
| Winter | $1.47 \times 10^{-6}$ | $2.13 \times 10^{-5}$ | $1.68 \times 10^{-7}$ | $2.43 \times 10^{-6}$ |

Table 4.2: Non-deviative absorption coefficients for the o and x modes corresponding to the electron densities during summer and winter at 95 km in Table 4.1.

expected to produce a low correlation (~0.3 or less) between phases of the two modes. The level of polarisation fading can be estimated by determining the difference in the level of absorption which occurs during the day and night.

The $A_x/A_o$ ratio is routinely determined with a radar polarimeter sited at Birdlings Flat and operated by Dr. H.A. von Biel (1992) of the Department of Physics and Astronomy, UoC. This instrument measures the ordinary and extra-ordinary components of the reflected radar pulse (von Biel 1992). A quantitative estimate of $A_x/A_o$ can be made by estimating the diurnal variation in the level of absorption of each mode, using Equation (4.5), and the typical midday and midnight electron number densities at a height of 95 km above Birdlings Flat during mid-winter and mid-summer. These values are listed in Table 4.1 (von Biel pers. comm.) and although they are typical, daily variations of 2–5 times may frequently occur. It can also be seen from table 4.1 that the diurnal variation in the electron density at 95 km is about one order of magnitude. The collisional frequencies associated with the summer and winter data in Table 4.1 were 57500 $s^{-1}$ and 45500 $s^{-1}$, respectively, and were obtained from experimental data (von Biel pers. comm.). The values of $\omega$ and $\omega_{HL}$ are $1.5 \times 10^7$ $rads^{-1}$ and $8.8 \times 10^6$ $rads^{-1}$, respectively.

Table 4.2 shows the resulting non-deviative absorption coefficients ($\kappa_o$ and $\kappa_x$ corresponds to the o and x modes, respectively) derived from the electron densities in Table 4.1 using Equation (4.5).

The $A_x/A_o$ ratios can be determined using the equation (Davies 1992)

$$\frac{A_x}{A_o} = \frac{\rho_x}{\rho_o} exp[-2 \int_0^h (\kappa_x - \kappa_o) dh] \tag{4.6}$$

where $\rho_o$ and $\rho_x$ are the reflection coefficients for the o and x modes, respectively. To a first approximation, the ionosphere can be considered to be a slab of ionisation with a vertical thickness, h, of 10 km. For each season, one day and one night $A_x/A_o$ ratio value will be obtained. The ratio of the day and night $A_x/A_o$ ratios will indicate the change in the relative absorption of the two modes between day and this may be obtained by the ratio

$$\frac{exp[-2\int_0^h(\kappa_x-\kappa_o)dh]_{day}}{exp[-2\int_0^h(\kappa_x-\kappa_o)dh]_{night}} \tag{4.7}$$

From Equation (4.7), the day/night ratio of the $A_x/A_o$ ratio is found to be 0.76 for the summer and 0.67 for the winter. During the summer time, this indicates that the night time $A_x/A_o$ ratio is only about 25% higher than the daytime ratio. During the winter, time the night time $A_x/A_o$ ratio is higher than the daytime ratio by about one-third. This model, the slab approximation is a very crude model and provides only a rough estimate of the change in the $A_x/A_o$ ratio from day to night. Belrose (1970) directly measured the relative amplitudes of $A_x$ and $A_o$ in the 60–90 km height region, at height intervals of 2 km, using a probing frequency of 2.66 MHz. He reported the $A_x/A_o$ ratio at 95 km to be typically $\sim$0.2 or less during the daytime (see Figure 4.1). At Birdlings Flat, the $A_x/A_o$ ratio above 90 km during both day and night time conditions has been reported to be near zero (von Biel pers. comm.). So the polarisation fading will not be expected to affect the radar wind measurements.

During both the day and the night, since the x mode is almost entirely absorbed (von Biel pers. comm.), the resulting signal echo received by the BF receivers will be a circularly polarised o wave. At night, the absence of the D region will enable RF noise to propagate over large distances with little absorption. This noise will interfere with the partial reflection signal.

Measurements of the worldwide distribution of atmospheric RF noise (CCIR 1988) indicate that the level of noise power at 2.4 MHz in the summer in the vicinity of Birdlings Flat during 12:00–16:00 local time is approximately 22 dB (Davies 1992). This value is consistent with the 20–25 dB increase in RF noise power during the night which is observed at Birdlings Flat during the summer from N40 measurements (discussed in chapter 5).

Partial reflection occurs as a result of backscatter from fluctuations in the refractive index caused by electron density variations in the ionospheric medium. The fraction of backscattered power to total power is the square of the amplitude reflection coefficient. In the 80–105 km height region, the power reflection coefficient is typically $10^{-3} - 10^{-5}$ (Hocking 1979).

At MF frequencies, where $\omega_p$ and $\nu$ are important, the relationship between the electron density gradient and the scattered echo strength is complicated but in general the

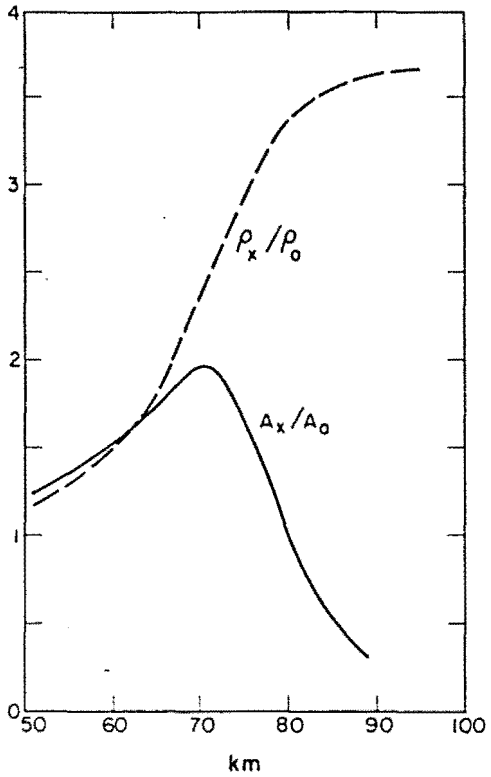


Figure 4.1: Height variation of the measured daytime $A_x/A_o$ and $R_x/R_o$ ratios during the daytime at 2.66 MHz (from Belrose 1970). The height variation at night is also similar (von Biel pers. comm.).

scattered signal strength is found to be proportional to the electron density gradient. At these frequencies, the QL approximation may be used ($Y_T = 0$ and $Y = Y_L$) and the A-H is simplified to (Davies 1992)

$$n^2 = 1 - \frac{X}{1 - iZ \pm Y} \tag{4.8}$$

A refractive index gradient of about $2\times10^{-5}$ over a vertical distance of $\lambda/2$ is required to produce a typical echo and this requires a change in the electron density of only about 2 $cm^{-3}$ (Gardner and Pawsey 1953). Manson et al. (1969) reported that an electron density variation of 1–18% was required to produce a typical return. These variations can range from steep gradients, due to sharply-bounded irregularities, to quasi-isotropic regions with scale-sizes comparable to the probing wavelength ($\lambda$ = 125 m) (Fraser 1984).

Bragg scattering occurs from structures with vertical depth scales of $\sim\lambda/2$ and which are much smaller than a (horizontal) Fresnel zone. This is generally the main type of scattering from the 80–100 km region and produces randomly-varying phase and amplitude echoes. It is believed to originate from small-scale irregularities generated by turbulence (Hocking 1985, 1988a).

Fresnel reflection, including specular reflection, is a scattering process which occurs when the horizontal scale of the scattering structures is comparable with the Fresnel zone size. In the 80–100 km region, the first Fresnel zone is 2–2.5 km in size which is much larger than the scale-size responsible for Bragg scattering. Fresnel reflection generally produces stronger and more coherent echoes than Bragg scattering, with rapid fluctuations in signal strength (Hocking 1979, Hocking and Vincent 1982). It is claimed to be the dominant scattering process in the MALT below about 80 km (Briggs and Vincent 1973) and is associated with thin, horizontally stratified ionisation which possess sharp gradients in refractive index (Briggs and Vincent 1973). It is also strongly directional; inferring that there is only one dominant reflection point.

Fresnel scatter is a variation on the process of Fresnel reflection and is the result of multiple Fresnel reflecting layers simultaneously occurring within the radar volume (Hocking and Vincent 1982). Distortions of the stratification, such as due to wave motion, may lead to multiple specular reflections which mutually interfere to produce quasi-randomly varying echoes and so mimic incoherent backscatter. If the radar volume is increased, the signal strength also increases. This is because more scatterers are probed, unlike Fresnel reflection from a flat reflecting layer.

In practice, a combination of these types of partial reflection backscatter is expected from the MALT region.

Partial reflection backscatter may be isotropic or anisotropic, depending on the

nature of the scattering mechanism or structures which are responsible (Briggs and Vincent 1973). Isotropic backscatter occurs uniformly in all directions. It is characterised by signal echoes whose phase and amplitude vary randomly with time, i.e. it is incoherent. It is usually produced by small scale variations in the refractive index. Anisotropic backscatter exhibits directionality or aspect sensitivity. Such backscatter tends to be coherent, that is, the amplitude and phase vary smoothly with time. Single specular reflectors tend to scatter anisotropically. Stratified ionisation, such as Sporadic-E (discussed later in section 4.1.2), for example, produces strong specular reflections which are exhibited as coherent backscatter.

The aspect sensitivity of partial reflection backscatter is generally found to be altitude-dependent (Fraser and Vincent 1970, Fritts 1984, 1989, Hocking 1988a, Hines 1991) which indicates that the nature of the scatterers is also altitude-dependent. Isotropic scattering is dominant above 80 km and anisotropic scattering is dominant below 80 km. Briggs and Vincent (1973) reported off-angle scattering of $\leq 10^o$ from irregularities below 80 km indicating specular reflection from thin stratified irregularities with horizontal scale sizes of several kilometres and vertical scales sizes of $\lambda/2$ or less. Similar findings were reported by Vincent and Belrose (1978) and Hocking (1979). Above 80 km, the backscatter was found to be more isotropic with frequent off-angle returns of up to 15–20$^o$ (Vincent and Belrose 1978). It was suggested that isotropic scattering from centres of turbulence was the main contributor to the returns from above 80 km.

### 4.1.1 Partial Reflection Radar Wind Determination and Full Correlation Analysis

The partial-reflection (PR) spaced-antenna method enables the ionosphere to be continuously monitored in the 60 to 100 km height region. The MF radar probes the MALT region by sending short, high-powered radio pulses vertically into the MALT. An array of ground-based antennas detects and records the back-scattered Fresnel echoes, each of which are similar in form, but shifted in time due to the relative spatial displacements of the antennas.

Because of its simplicity and low cost the MF radar and the spaced antenna method has been developed and used extensively over several decades to probe the upper atmosphere initially utilising total reflection (Mitra 1949, Briggs and Spencer 1954) and subsequently partial reflection (Fraser 1965, 1968). There are several MF spaced antenna partial reflection radar stations currently in operation throughout the world and several excellent review papers exist which describe the method (Briggs et al. 1950, Kent 1970, Briggs 1977, 1984, 1993, Gregory et al. 1979, Hocking 1983, Fraser 1984, 1989, Hocking et al. 1989).

At each antenna, the signal amplitude of the back-scattered pulse is observed to

fluctuate temporally and this is known as fading. The fading records are analysed using the Full Correlation Analysis (FCA) technique (Briggs et al. 1950, Brown and Chapman 1972, Briggs 1984). Both methods are similar and produce very similar results. The Brown and Chapman algorithm is used at Birdlings Flat for historical reasons and it differs from the Briggs method in that it uses one side of the array triangle as a baseline to calculate the apparent velocity. The true velocity is determined by employing the characteristic ellipse to correct the apparent velocity. Unlike the Briggs method, the Brown and Chapman algorithm gives no error estimates for the derived parameters. The computer code was written by Dr. G.J. Fraser.

Consider two spaced receiving antennas i and j which are separated by $\epsilon_{ij}$ and $\eta_{ij}$ in the x- and y-directions, respectively. The cross-correlation function between the two antennas can be described as

$$\rho(\epsilon,\eta,\tau) = \frac{< f(x,y,t) \cdot f(x+\epsilon, y+\eta, t+\tau) >}{<\mid f(x,y,t)^2 \mid>} \tag{4.9}$$

The line joining the points in the diffraction pattern which are responsible for the maxima in the signal strength recorded at each of the receiving antennas is known as the "line of maxima". This "line" is assumed to be aligned perpendicular to the direction of drift. If random motions within the diffraction pattern are assumed to be small then the apparent drift velocity can be derived from the time lag of the maximum of the cross-correlation function between each pair of spaced receivers. Figure 4.2 shows the schematic forms of the auto- and cross-correlations due to the drift motion of a diffraction pattern across two spaced receiving antennas. Several parameters associated with the functions are also shown. The maximum of the cross-correlation function between an antenna pair occurs at a time shift $\tau'_{ij}$ and corresponds to the drift time between the two receivers. The fading time, denoted as $\tau_{fad}$, is the time taken for the auto-correlation function of an antenna to fall to a value of 0.5.

The assumption of ergodicity (Briggs et al. 1950, Briggs 1984) is made, which means that the time average between two fixed receivers at points $\epsilon$ and $\eta$ produces the same results as taking averages over all points between $\epsilon$ and $\eta$. This means that the spatial and temporal cross-correlation functions are of similar functional form. The FCA procedure also makes this assumption (Briggs 1994). Furthermore, it also means that the auto-correlation functions have the same functional form as the cross-correlation functions between each antenna pair.

Random changes within the diffraction pattern, as it drifts over the array, tend to result in an over-estimation of the drift velocity. This is because random changes which occur in the direction of drift will produce a higher correlation at a shorter time lag than for the case when no random changes occur. Random changes which occur in the direction

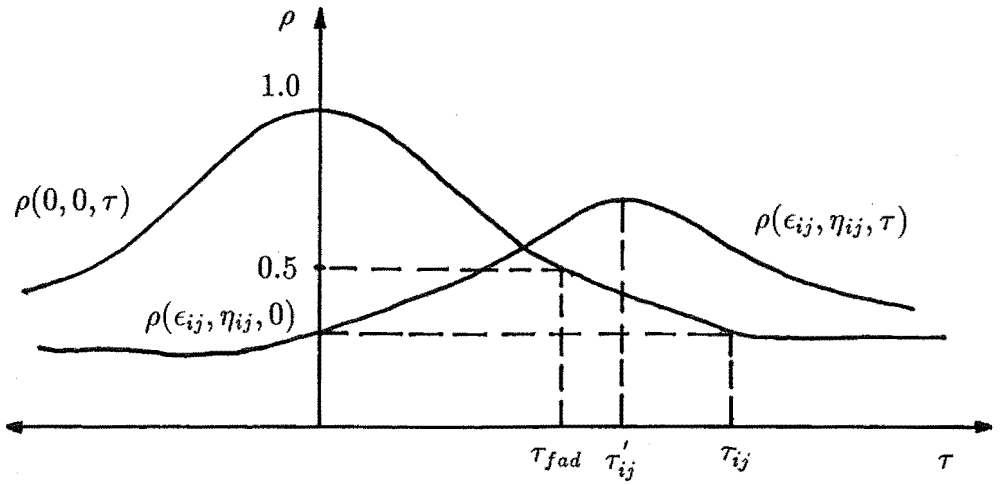


Figure 4.2: The typical form of the auto- and cross-correlation functions associated with a pair of spaced receivers.

opposite to the drift will produce a lower correlation at longer time lags because of the longer evolution time of the random changes in this direction. The correlation functions are therefore biased to smaller time-lags, resulting in an overestimation in the drift velocity. Overall, any random changes within the diffraction pattern tend to reduce the maximum value of the cross-correlation function in the drift direction (Briggs et al. 1950). In addition to random changes, anisotropy of the diffraction pattern results in an underestimation of the drift velocity (Phillips and Spencer 1955). If the pattern is elongated, the time delays between each antenna pair associated with the drift motion will not accurately reflect the motion. The drift velocity will be biased in the direction which is perpendicular to the elongation (Phillips and Spencer 1955). FCA accounts for the effects of random changes and pattern anisotropy by matching the temporal and spatial correlation functions of the diffraction pattern.

On the ground, the contours of equal correlation for an isotropic pattern are circular and are centred at the origin at zero time shift. At this time shift, the cross-correlation function provides a measure of the spatial correlation function. For a general anisotropic pattern, the correlation contours are described by a family of ellipses in ($\epsilon$,$\eta$)-space centred on the origin and are of the form

$$\rho(\epsilon, \eta) = \rho(A\epsilon^2 + B\eta^2 + 2H\epsilon\eta) \tag{4.10}$$

The correlation ellipse for which $\rho = 0.5$ is called the characteristic ellipse and it is a measure of the scale-size of the irregularities. A temporal axis orthogonal to the spatial axes $\epsilon$ and $\eta$ can be added to produce a family of ellipsoidal surfaces of equal correlation in

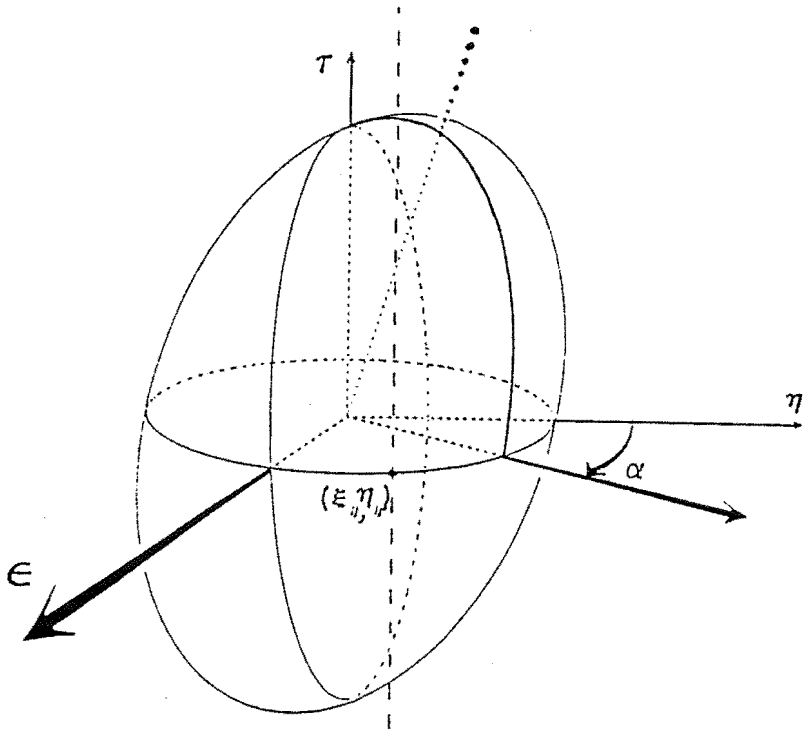


Figure 4.3: The characteristic ellipsoid surface of equal correlation in ($\epsilon$,$\eta$,$\tau$)-space (from Brown 1992).

($\epsilon$,$\eta$,$\tau$)-space. This has the form

$$\rho(\epsilon, \eta, \tau) = \rho(A\epsilon^2 + B\eta^2 + C\tau^2 + 2H\epsilon\eta) \tag{4.11}$$

and is shown in Figure 4.3.

If there is no overall drift motion the ellipsoidal surfaces will be vertical. Drift motion causes the ellipsoidal surfaces to tilt away from the temporal ($\tau$) axis and the form of the Equation (4.11), describing the surfaces, acquires two extra terms which are products of both the temporal and spatial terms. The inverse of the slope of the tilt describes the magnitude of the drift velocity and the direction of the tilt away from the temporal axis describes the direction of the drift motion. The coefficient associated with the temporal variable $\tau$ is also altered because the motion alters the fading time and so the width of the auto-correlation function is also altered. The auto-correlation function itself now can be described by

$$\rho(\epsilon, \eta, \tau) = \rho(A\epsilon^2 + B\eta^2 + C\tau^2 + 2F\epsilon\tau + 2G\eta\tau + 2H\epsilon\eta) \tag{4.12}$$

Using FCA, the coefficients A, B, C, F, G and H can be derived from the records of an array of three or more antenna to fully describe the motion and characteristics of the diffraction pattern and hence the irregularities.

The auto-correlation function describes the correlation of the time series with itself over several time lags. Uncorrelated high-frequency RF noise and interference usually causes a spike to occur in the auto-correlation function at zero lag. This effect is removed by a procedure known as "de-spiking" (Goldstein 1951) which involves fitting a parabola or Gaussian function to the time lags of the auto-correlation function on either side of zero-lag but not including it. After de-spiking the three auto-correlation functions are averaged together. The interpolated auto-correlation maximum at zero lag provides a measure of the signal level.The value of the non-interpolated minus the interpolated auto-correlation maxima at zero lag provides a measure of the noise level. The signal-to-noise ratio (S/N) of the time series can thus be obtained. A spike may also occur at zero lag in the cross-correlation functions if the RF noise or interference is correlated between the antenna pairs.

For a pair of antennas i and j which are separated by $\epsilon_{ij}$ and $\eta_{ij}$ in the x- and y-directions, respectively, the cross-correlation function is of the form

$$\rho(\epsilon_{ij}, \eta_{ij}, \tau_{ij}) = \rho(A\epsilon_{ij}^2 + B\eta_{ij}^2 + C\tau_{ij}^2 + 2F\epsilon_{ij}\tau_{ij} + 2G\eta_{ij}\tau_{ij} + 2H\epsilon_{ij}\eta_{ij}) \tag{4.13}$$

This function fully describes the spatial and temporal relationship between the spaced receivers. The maximum value of the function occurs at a time shift of $\tau_{ij}^{'}$ when $\frac{\partial \rho}{\partial \tau_{ij}} = 0$. This results in

$$\tau_{ij}^{'} = -\frac{F}{C}\epsilon_{ij} - \frac{G}{C}\eta_{ij} \tag{4.14}$$

The values of $\tau_{ij}^{'}$ can be determined from the cross-correlation functions for each of the three antenna pairs to produce a set of three simultaneous equations from which the coefficients F/C and G/C can easily be determined. The magnitude and direction of the apparent wind velocity, which assumes an isotropic, time-invariant pattern, can be estimated using these coefficients.

At zero time shift the value of the cross-correlation function between each antenna pair is $\rho(\epsilon_{ij},\eta_{ij},0)$. The mean auto-correlation function of all three antennas has the same value at a time shift of $\tau_{ij}$. Hence $\rho(\epsilon_{ij},\eta_{ij},0) = \rho(0,0,\tau_{ij},)$ and so Equation (4.13) becomes

$$\rho(C\tau_{ij}^2) = \rho(A\epsilon_{ij}^2 + B\eta_{ij}^2 + 2H\epsilon_{ij}\eta_{ij}) \tag{4.15}$$

This equation can be rearranged to find $\tau_{ij}^2$

$$\tau_{ij}^2 = \frac{A}{C}\epsilon_{ij}^2 + \frac{B}{C}\eta_{ij}^2 + \frac{2H}{C}\epsilon_{ij}\eta_{ij} \tag{4.16}$$

and the coefficients A/C, B/C and 2H/C can be determined by solving the set of three simultaneous equations.

To determine the true drift velocity, the ellipsoidal correlation surfaces observed on the ground by the stationary array are compared to those seen by an observer moving along with the drift motion. The coordinate system in the frame of the moving observer will be $\epsilon'$ = $\epsilon$ - $V_x\tau$ and $\eta'$ = $\eta$ - $V_y\tau$. To this observer the pattern will only change randomly and the correlation surfaces will have no tilt because of their common motion with the pattern.

In the stationary frame, the correlation surfaces can therefore be described as

$$\rho(\epsilon,\eta,\tau) = \rho(A[\epsilon - V_x\tau]^2 + B[\eta - V_y\tau]^2 + K\tau^2 + 2H[\epsilon - V_x\tau][\eta - V_y\tau]) \tag{4.17}$$

which is of similar form to Equation (4.13). To find the eastward and northward components $V_x$ and $V_y$ of the true drift velocity $\mathbf{V}$, one equates the coefficients of $\epsilon\tau$ and $\eta\tau$ to give

$$AV_x + HV_y = -F \tag{4.18}$$

$$BV_y + HV_x = -G \tag{4.19}$$

If Equations (4.18) and (4.19) are divided by C, then all the coefficients are known and so $V_x$ and $V_y$, and hence the true velocity $\mathbf{V}$, can be determined by solving them simultaneously. The drift speed V, and the direction $\phi$, are related to the velocity components by

$$\mathbf{V} = \sqrt{V_x^2 + V_y^2} \tag{4.20}$$

$$\phi = \tan^{-1}(\frac{V_x}{V_y}) \tag{4.21}$$

Other parameters, such as the spatial scale-sizes and lifetimes of the irregularities, can also be derived from the FCA procedure. These are described in Appendix C.

### 4.1.2 Electrodynamic Effects

The partial reflection radar winds are derived from the scattering from electron density variations so it is important to consider any electrodynamic effects due to the geomagnetic field $\mathbf{B}$, and any electric fields present, on the motion of the ionisation irregularities. Above 95–100 km, electrodynamic effects become important because of (i) the decreasing collision frequency with height and (ii) the increasing conductivity of the region with height. The latter is evidenced by the existence of sporadic-E (discussed in the next section) and the dynamo region near 120 km.

In the 80–105 km region, the collision frequency is larger than the gyrofrequency for ions but is less for electrons i.e. $\nu_{ni} > f_{Hi}$, $\nu_{ne} < f_{He}$. In fact, the ratio of $\nu_{ne}/f_{He}$ is $\sim 1$ at 75 km whereas $\nu_{ni}/f_{Hi}$ is $\sim 1$ at 130 km (Kelley 1989). Hence, the mean velocities of the positive ions and electrons in the 80–105 km height region will be expected to be different.

At 95 km, $\nu_{ni}$ is of the order of 2000 $s^{-1}$ (Johnson 1961) which is about 200 times higher than $f_{Hi}$. The motion of the ions will therefore be dominated by collisions so the ions will tend to move along with the neutral wind. For electrons at 95 km, $\nu_e$ is less than $f_{He}$ by a factor of over 100 (Johnson 1961) and consequently the motion of the electrons will be expected to be magnetically controlled. The resulting separation of the ions and electrons will produce an electrostatic field. The electrons, being more mobile than the ions, especially in the direction parallel to the geomagnetic field, will tend to move towards the ions in order to neutralise the field. Electron motion in the meridional direction will be largely unaffected by the geomagnetic field because the electrons will move along the field lines producing a field-aligned component of drift. Zonal neutral wind motion will cause electron drift $(\mathbf{E} \times \mathbf{B}) / \mathbf{B}^2$, which is perpendicular to both $\mathbf{B}$ and any electric field $\mathbf{E}$ present, and inclined out of the plane of the neutral wind motion (Rishbeth and Garriott 1969).

The effect of turbulence, which is believed to occur almost constantly above 80 km, is also an important factor governing the plasma dynamics in this region. Turbulence, most probably generated by gravity wave activity, is considered to be the main mechanism for the production of ionisation irregularities in the MALT above 80 km (Hocking 1979, Hocking and Vincent 1982, Fraser and Khan 1990). Such regions of turbulence are considered to move along with the neutral wind (Hines 1991) because the turbulence is believed to originate from the breaking of gravity waves which have reached a height where their phase speed and the mean wind speed are equal (Hines (1968), Fritts (1984), as discussed in chapter 2). The turbulence produces irregularities which become polarised, each is held together by an electric field set up by the charge separation of ions and electrons (Villars and Fesbach 1963, Tsedelina 1965, Kato and Matsushita 1968, Beer 1974, Briggs 1977). Villars and Feshbach (1963) reported that the geomagnetic field would have no effect on the motion of the ionisation irregularities at heights below 100 km and that the irregularities will move along with the neutral wind. Above 100 km, they concluded that there would be little geomagnetic control even up to 120 km. Similarly, Tsedelina (1965) reported that isotropic irregularities originating from turbulence within the entire E region are subject to turbulent control and moved along with the neutral wind. However, if turbulence is present up to 120 km, it does not explain the frequent occurrence, especially during the daytime in summer, of the occurrence of sporadic-E ionisation in this height region. The action of turbulence would tend to disintegrate these irregularities, or prevent their formation in the 100–120 km height region, but they can occur and remain for several hours (Derblom 1981, Whitehead 1989).

Departures of the irregularities from the neutral wind motion may be expected if the turbulence was either not present or generated by one or more large-scale waves propagating in different directions. One might then expect to observe the apparent motion of the resulting interference patterns due to the propagation of the waves. However, Hines (1968, 1991) suggested that the motion of these interference patterns would be small ($\sim$3 ms$^{-1}$) compared to the motion due to the wind.

Several workers have made comparisons between partial reflection radar winds and other techniques on various time scales. Fraser and Kochanski (1970) reported comparisons of seasonal averages of BF radar wind measurements from the 65–110 km height region with meteor wind measurements made in Australia and chemical release trails obtained from 20 rocket soundings made in the United States. As well as originating from different hemispheres, the data sets differed in the actual measurement periods and durations and in the data density with altitude (Fraser and Kochanski 1970).

The BF radar wind profiles were consistent with the meteor wind profiles but there were differences of up to 10 ms$^{-1}$ in the 80–90 km height region. It was noted that the meteor wind profiles were "computationally unstable" near 75 and 105 km, the upper and lower bounds of the profiles (Fraser and Kochanski 1970).

The general shape of the BF radar and rocket measurement height wind profiles were similar but BF radar wind profile was shifted $\sim$5-8 km lower in height than the rocket measurements and so differences in wind direction were exhibited between 90–100 km. Differences in wind magnitude of up to 20–30 ms$^{-1}$ were also typical above 90 km. The systematic height difference can be explained by the different hemispheres of origin of the two wind data sets, as well as the different years of measurement. When the systematic height discrepancy was removed, the rms wind differences were $\sim$8–10 ms$^{-1}$. In general, the results were consistent with the interpretation that the BF radar measured neutral wind motion (Fraser and Kochanski 1970).

Vincent et al. (1977) compared neutral wind measurements in the 60–90 km height region determined from a partial-reflection MF radar and from rocket-ejected falling spheres and dropsondes. It was reported that two wind sets agreed very well in both magnitude and direction (Vincent et al. 1977).

Gonzalez et al. (1994) reported the results of simultaneous comparisons of between 70–110 km winds derived from in-situ measurements of foil chaff motion during eight rocket flights and a ground-based MF partial-reflection radar sited 105 km away during the 1990 DYANA campaign during January and February. Thirty-minute MF radar wind vectors centred on the launch times were compared with the foil chaff wind measurements. The two sets of winds were generally similar in magnitude and direction but there were occasional differences of over 60–80 ms$^{-1}$ in magnitude and 180° in direction. The low yield of night-

time MF radar winds, due to the low night time S/N ratio, and the 150 km separation of the two experiments was given as reasons for the discrepancies. In addition to this, only three of the rockets provided wind data above 90 km. In order to compensate for the low yield of radar winds the median radar and rocket wind profiles were derived for the entire period. The mean radar/rocket wind magnitude ratio for the 18 heights was 0.78 $\pm$ 0.1 and the mean direction difference was -16$^o$ $\pm$ 10$^o$ (Gonzalez et al. 1994). Tidal variability over the entire observing period was also suggested as the reason for the difference in the mean wind directions.

The results of these studies appear to indicate that for heights up to about 95–100 km, the ionisation irregularities will in general move along with the neutral wind and that the radar winds are measuring the neutral wind flow.

Evidence of magnetic control of partial drifts radar winds above 100 km has been reported by Stubbs (1977). The ground patterns of the characteristic ellipse associated with radar winds above 100 km exhibited a tendency to be aligned along the magnetic meridian. It was suggested that the directions of the mean winds may have been a contributing factor to this result.

It is possible that the radar winds, especially those from above 95–100 km, may be affected by an interaction between the ionisation and the geomagnetic field. The free electrons would tend to move along the geomagnetic field lines i.e. $\sim$26$^o$ from the meridional direction. As a result, the meridional optical/radar winds would tend to agree more often than the zonal winds.

At heights of 95 km or more, the effect of the increased ionisation number density results in a significant reduction in the group velocity of the radio pulse prior to being reflected. The virtual height is the apparent height of reflection as recorded on the ground and it is always equal to or greater than than the true height of reflection. If greater, then the radio wave has undergone pulse retardation due to a slowing of the wave through the ionospheric medium. The amount of pulse retardation is dependent upon the vertical electron density profile and the geomagnetic field. Fraser and Kochanski (1970) determined the amount of pulse retardation associated with the height of the BF radar winds under various conditions using the group refractive index as described by Shinn and Whale (1952). The E region electron density height profiles were assumed to be an $\alpha$-Chapman layer and electron collisions were ignored (Fraser and Kochanski 1970).

Fraser and Kochanski (1970) reported that the amount of pulse retardation at 100 km was less than 1 km during the daytime during the winter but could be as high as 5 km at 100 km during the summer daytime. The BF transmitter pulse width is 4.5 km and so the apparent height of the winds can be assumed to originate within one pulse width of their true height (Fraser and Kochanski 1970). The reduction in the ambient ionisation in the MALT

region at night means that the amount of pulse retardation was less than 1 km for heights investigated in this project and consequently, could be neglected. Namboothiri et al. (1993) studied pulse retardation at times of solar maximum and minimum and reported that the effect of pulse retardation on the apparent heights of radar winds was negligible during both periods in winter. During summer months, the height of radar winds may be overestimated above 95 km during solar maximum and above 97 km during solar minimum (Namboothiri et al. 1993).

### 4.1.3 Sporadic-E Ionisation and Radar Winds

Sporadic-E ($E_s$) is an ionisation irregularity which frequently occurs in the 95–110 km height region of the E region. It is believed to originate from the compression of positive metallic ions of meteoric origin by neutral wind shears which occur in this region. It is characterised by very thin ($\sim$1–2 km), dense stratified layers of ionisation of up to 100$\times$ the ambient E region electron density. Although $E_s$ can be highly variable in time and space there are clear patterns of diurnal, seasonal and latitudinal behaviour. Several excellent reviews are available on the subject (Smith and Matsushita 1962, Whitehead 1970, 1972, 1989 and Derblom 1981).

The geomagnetic field is an important factor in the formation of $E_s$ ionisation and the wind shear theory is the most widely accepted theory of mid-latitude $E_s$ production (Dungey 1959, Whitehead 1961, 1970, 1989, Axford 1963, Hines 1964). Consider a neutral zonal wind blowing in the 110–120 km region. In this region, the ions tend to be dragged along by the zonal wind due to collisional interaction. The electrons are under magnetic control and so tend to be left behind. The ion flow is acted upon by the Lorentz force which causes the ions to have a velocity component which is perpendicular to both the magnetic field and the neutral wind flow. The separation of the positive ions and electrons results in the setup of an electrostatic field (Briggs 1977, Rishbeth and Walker 1982). Under the influence of this field the electrons tend to follow the ions, which renders the entire layer essentially neutral. A zonal wind shear consisting of westward flow above and eastward flow below will tend to produce an accumulation of positive ions within the node of the shear because the ions will move upwards (downwards) due to an eastward (westward) wind (see figure 4.4).

$E_s$ ionisation is frequently observed to descend in height from $\sim$120 km to $\sim$100 km, or so, over a period of several hours (Axford 1963, Chimonas and Axford 1968, Smith 1989) at a rate of $\sim$1–3 $ms^{-1}$ (Whitehead 1989). The lifetimes of the metallic ions are long (T $\sim$ hours) (Axford 1963, Brown 1973, Whitehead 1989) and so $E_s$ layers near 100 km may remain for several hours without the effects of diffusive turbulence destroying the layer (Chi-

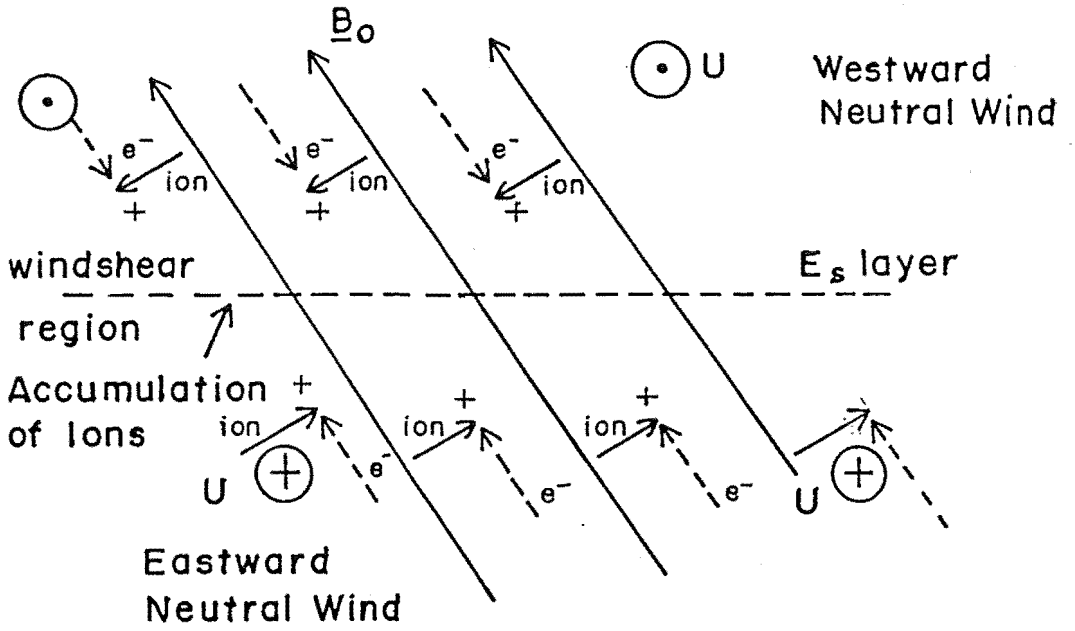


Figure 4.4: Formation of $E_s$ ionisation due to an east-west wind shear (From Smith 1989).

monas 1974). The presence of $E_s$ ionisation near 100 km therefore does not necessarily mean that the dynamics of the scattering electrons in this lower height region are geomagnetically dominated. Since the electrons tend to follow the ion motion, as a result of the electric field set up by the wind shear, they are not constrained by the geomagnetic field. Smith and Miller (1980) reported rocket measurements that showed that the vertical density profile of an $E_s$ layer was determined largely by the vertical wind shear profile.

The effect of $E_s$ ionisation in the 95–105 km region on the night time radar winds and the subsequent optical/radar wind comparisons was investigated. Scaled hourly values of the ionogram $E_s$ parameters $f_oE_s$, $h'E_s$ and the $E_s$ type were obtained (Wilkinson pers. comm.). These were derived from measurements made by the Eyrewell ionosonde which is situated approximately 50 km northwest of Birdlings Flat. The parameter $f_oE_s$ is the highest o mode reflection frequency obtained from the $E_s$ layer and corresponds to the maximum plasma frequency of the layer. The parameter $h'E_s$ is the minimum virtual height of the ionogram trace used to obtain $f_oE_s$. The accuracy of the scaled $f_oE_s$ and $h'E_s$ values are $\pm 0.1$ MHz and $\pm 2$ km respectively (Piggott and Rawer 1972). These scaled values were available for 57 of the 103 nights and of these nights there were 32 (54%) during which $E_s$ was found to occur at or below 105 km for at least one hour of the night.

Figure 4.5 is a histogram of the frequency of occurrence of the scaled hourly $E_s$ virtual heights as a percentage of the total possible night time hours of the radar/optical

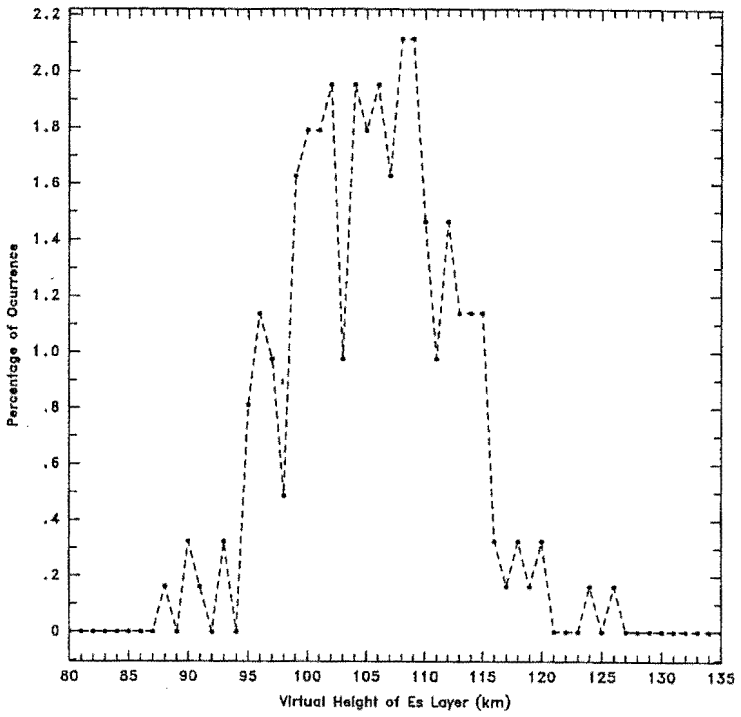


Figure 4.5: Histogram of the frequency of occurrence of the scaled hourly $E_s$ virtual heights as a percentage of the total possible night time hours of the radar/optical comparisons.

comparisons. It can be seen that about half of the heights occur at or below 105 km. The average night time virtual height of the $E_s$ layers was 105.6 km with a standard deviation of 6.6 km. The height values were corrected for delay in the ionosonde receiver which corresponded to a height overestimation of about 5 km (Tomlinson and Wilkinson pers. comm.).

Scaled values of $f_oE_s$ were available for all the corresponding $h'E_s$ hours and the distribution of the frequency of occurrence of $f_oE_s$ due to $E_s \leq 105$ km is shown in Figure 4.6 as a percentage the total numbers of night time $E_s \leq 105$ km. From this figure the most frequent value of $f_oE_s$ for night time $E_s \leq 105$ km is about 2.6 MHz. The mean value of $f_oE_s$ is 3.1 MHz with a standard deviation of 0.9 MHz. The median value is 3.0 MHz and this has a quartile range of 1.2 MHz respectively. The median value is probably more reliable because of the asymmetric shape of the distribution.

The presence of night time $E_s$ in the 90–105 km region with ionisation densities corresponding to an average plasma frequency of 2–3 MHz would be expected to produce strong reflections of the 2.4 MHz radar pulse. The majority of daytime $E_s$ layers are only 1–2 km thick and little or no pulse retardation would be expected. Night time $E_s$ may have thicknesses of 5 km and so pulse retardation may occur leading to an over-estimation of the height of the radar wind by 5 km or more (Namboothiri et al. 1993).

The absorption of MF/HF radar echoes from altitudes above the height of the $E_s$

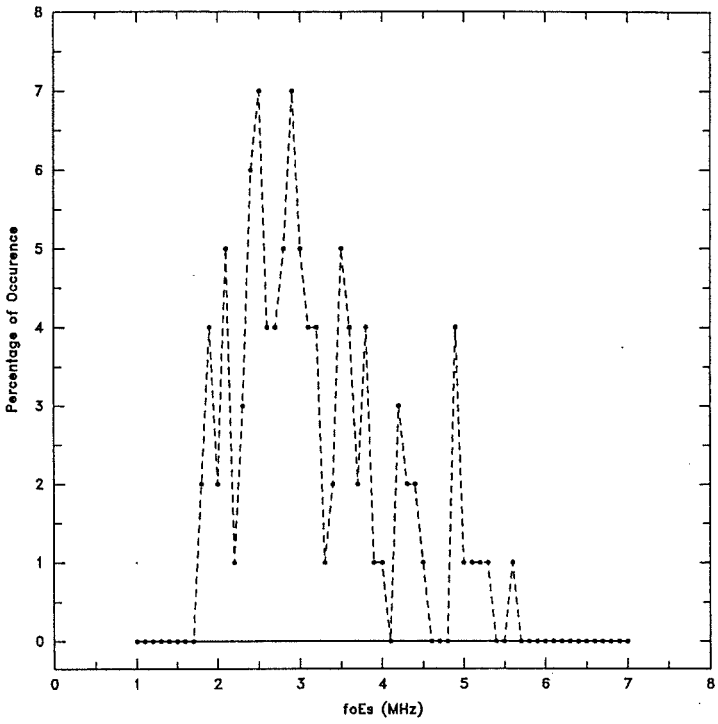


Figure 4.6: Histogram of the frequency of occurrence of the value of $f_oE_s$ of night time $E_s \leq 105$ km during the nights of the optical/radar wind comparisons as a percentage of the total number of night time occurrence $E_s \leq 105$ km.

layer, known as blanketing, occurs relatively frequently but this behaviour is variable (Smith 1966). During such times, the yield of radar wind values from heights above the $E_s$ height would be expected to be lower than from similar heights when the $E_s$ layer is not present. No significant difference was found in the yields of radar winds at heights above and below the scaled $E_s$ layers. The level of RF noise and interference associated with the radar winds may have contributed to this result.

It was therefore not possible to conclusively determine the effect of night time $E_s$ occurring below 105 km on the radar winds and, for the same reason, on the radar/optical wind comparison results.

## 4.2 The Birdlings Flat Medium-Frequency Radar

The medium-frequency (MF) partial-reflection radar used in this project is sited at Birdlings Flat near Christchurch, New Zealand (43°.83 S, 170°.68 E geographic). The radar operates in a pulse mode at vertical incidence using a frequency of 2.4 MHz. Partial reflections from the entire the 80–110 km height region, with a sampling interval of 1 km, are acquired in about 82 seconds. Raw radar winds are obtained every 2 to 10 minutes, depending on the data quality. The radar has been routinely producing MALT wind measurements by the Spaced Antenna (SA) method since 1964 (Fraser 1965, 1968).

Figure 4.7 shows the layout of radar station at Birdlings Flat. The transmitting array is labeled as "A" and the three receiving arrays are labeled as "C", "D" and "F". The dipoles are aligned approximately 8° south of the east-west line, i.e. the azimuth angle when looking eastward through the dipoles, measured clockwise from north, is 97°. This alignment is accounted for in the raw wind determinations.

The deterioration in the performance of the Birdlings Flat MF radar has been of concern. Measurements by Drs. G.J. Fraser and R.G.T. Bennett, of transmitter power, transmitting array phasing and impedance, receiving array phasing and impedance, receiver sensitivity and noise levels have not revealed any possible causes of the decreased performance.

### 4.2.1 The Transmitter

The transmitter produces a short radio pulse by modulating and amplifying a 2.4 MHz carrier wave which is fed into the transmitting array. The final stage of the transmitter consists of a push-pull tetrode amplifier with a measured output of ~80 kW ±10% (Fraser and Bennett pers. comm.). The harmonic content of the pulse was reduced by using a pulse shape with rounded leading and trailing edges. The pulse width was set to 30 $\mu$s which corresponds to a height resolution of 4.5 km (FWHM power measured at the receiver output) (Fraser 1989). A shorter pulse width would increase the height resolution but it would also

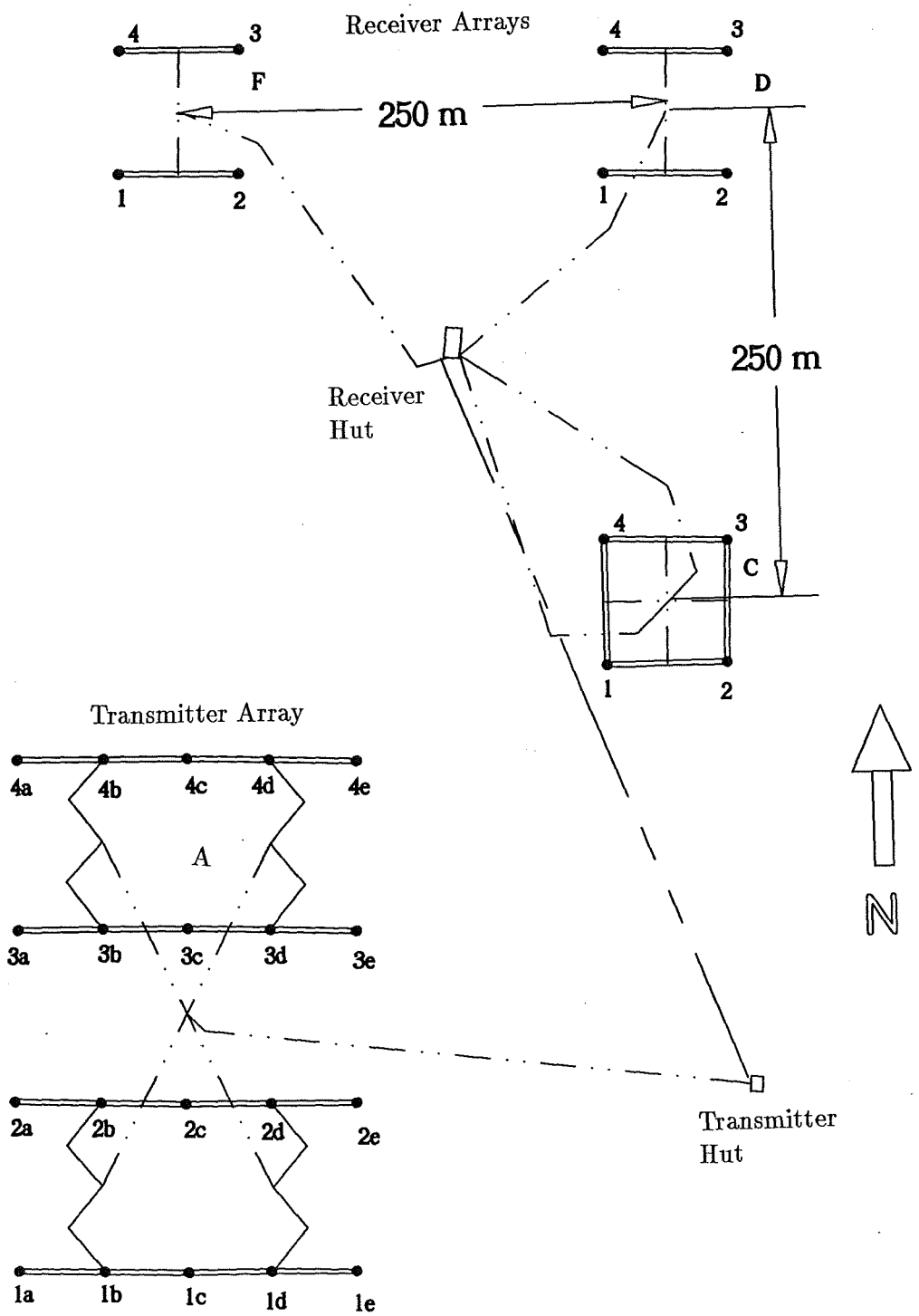


Figure 4.7: The layout of the partial-reflections drifts radar experiment at Birdlings Flat.

result in an increased amount of RF noise and interference received by the requisite larger bandwidth receivers.

A master oscillator operating at 9.6 MHz generated the carrier wave and also a millisecond counter. The transmitter operation is triggered by the millisecond counter. The counter was also used to synchronise the transmitter trigger and the beginning of the Analogue-to-Digital (A-D) conversion cycle of the received radar echoes.

The transmitter array (denoted as "A" in Figure 4.7) consists of a linearly polarised array of four rows of two colinear three-wire dipole aerials each 59 m in length (Krenek 1977). A carrier wave is pulse-modulated and then amplified to deliver approximately 100 kW of peak power to the array during each pulse. The dipoles are fed in-phase to produce a broadside array. The pulse is linearly-polarised in the east-west direction (Krenek 1977) and the radiation field is directed predominantly upwards.

Prior to May 1993, probing involved transmitting 256 30$\mu$s pulses at 230 ms intervals (4.35 Hz) into the MALT region (Fraser 1989). During April 1993, the computer system was replaced. The new probing regime involves transmitting 512 30$\mu$s pulses at 160 ms intervals (6.25 Hz). This also increased the probing time from 64 to 82 seconds (Fraser, pers. comm.). There was no pre- or post-detection integration.

### 4.2.2 The Receivers

The receiving array consists of three receiving antennas each 20m above the ground. The antennas (denoted as "F", "D" and "C" in Figure 4.7) each consist of a pair of parallel dipoles spaced $\lambda/2$ apart, and are arranged in a right-angled triangle with sides $2\lambda$ (250 m), $2\lambda$ and $2.8\lambda$. Like the transmitter array, the receiving array is fed in-phase to produce a broadside array (Fraser 1965) and the direction of reception is predominantly vertical.

The range or virtual height of the received signals is derived from the time delay between transmission and reception of backscattered signals. The signal returns are gated into 1 km heights. Since the transmitter pulse width at half-power (FWHP) is 4.5 km, the 1-km gated radar winds are not independent but are a weighted mean over this height interval.

Each received echo occurs from a volume of space which is determined by the height resolution and the aspect sensitivity of the polar diagram of the radar antenna system. Brown (1992) calculated the combined far field radiation pattern of the Birdlings Flat transmitting and receiving arrays as a function of zenith angle. The combined arrays have a half-power full-beam width of $32^o$ by $18^o$, perpendicular and parallel, respectively, to the dipoles (Brown 1992).

The polar diagram of the radar beam can be described (Hocking 1988b)

$$P_r(\theta) \sim \exp[-(\frac{\sin^2\theta}{\sin^2\theta_0})] \tag{4.22}$$

where $\theta_0$ is the zenith angle at which the polar diagram has fallen to 37% (1/e) of the maximum power. The radar polar diagram is dependent on the azimuth direction, $\phi$. For vertical probing, this equation has the form (Hocking 1988b):

$$P_r(\theta,\phi) \sim \exp[-\frac{(\sin\theta\sin\phi)^2 + (\sin\theta\cos\phi)^2}{\sin^2\theta_0}] \tag{4.23}$$

The probing at 95–100 km will be the product of the polar diagrams of the radar and the aspect sensitivity of the scatterers. The aspect sensitivity of the scatters above 80 km has been reported to be about 15–20$^o$ (Vincent and Belrose 1978, Hocking 1979, Hocking and Vincent 1982) which is comparable to the radar antenna beam size in the meridional direction but smaller by a factor of nearly three in the zonal direction.

The polar diagram of the backscatter from the scatterers can similarly be described as (Hocking 1988b)

$$P_s(\theta) \sim \exp[-(\frac{\sin^2\theta}{\sin^2\theta_s})] \tag{4.24}$$

where $\theta_s$ is the measure of the drop-off rate of backscatter power as a function of zenith angle and it characterises the nature of the scatterers. If $\theta_s \sim 90^o$ then the scatter is mainly isotropic. If $\theta_s \sim 0^o$ the scatter is mainly anisotropic and the scatterers are highly aspect sensitive.

The effective polar diagram of the radar and scatterers is the product of equations (4.23) and (4.24) (Hocking 1988b)

$$P_{eff}(\theta,\phi) \sim \exp[-\frac{(\sin\theta\sin\phi)^2 + (\sin\theta\cos\phi)^2}{\sin^2\theta_0} + \frac{\sin^2\theta}{\sin^2\theta_s}] \tag{4.25}$$

The effective FWHP beam width can be derived by finding the values of $\theta$ and $\phi$ where Equation (4.25) has fallen to a value of 0.5. The value of $\theta_s$ is taken to be 20$^o$ (35 km at 95–100 km), from the results of Vincent and Belrose (1978). In the zonal direction, $\theta_0 = 32^o$ and $\phi = 90^o$, and so the effective beam width in the EW direction is 28$^o$, which corresponds to ~48 km. In the meridional direction, $\theta_0 = 18^o$ and $\phi = 0^o$, and the effective beam width in the NS direction is 22$^o$, which corresponds to ~37 km. Hence, the radar wind measurements from 95–100 km are obtained from a horizontal elliptical area 48 x 37 km aligned in the EW direction. The 30% elongation in the EW direction and would result in lower correlations from drift motions in the zonal direction and may explain the greater variability in the zonal winds compared to the meridional (see section 5.7). The radar gain towards the zenith is ~10 dB (Brown 1992).

The BF radar operated in incoherent mode during the observation period of this project. That is, only the signal amplitude is recorded. The dynamic range of the receivers is increased by using logarithmic video amplifiers. When the input S/N >1 the output S/N power ratio is related to input S/N ratio by the relationship (Panter 1965)

$$(\frac{S}{N})_o = 2(\frac{S}{N})_i \tag{4.26}$$

When the S/N <1, i.e. noise dominates the signal, the non-linearity of the incoherent detectors and logarithmic amplifiers results in cross-modulation of the noise and signal components. The output S/N power ratio is then related to input S/N ratio by the relationship (Panter 1965)

$$(\frac{S}{N})_o = 0.92(\frac{S}{N})_i^2 \tag{4.27}$$

In phase-coherent reception, the phase as well as amplitude is obtained. This is achieved by comparing the phase of the received signals with the local oscillator producing the original transmitter pulse. The output consists of in-phase and quadrature components which can be treated as the real and imaginary part of a complex function. If the received signals occur at a different frequency to the original transmitted frequency (say due to Doppler shifting) then the in-phase and quadrature outputs will include an oscillating component in the complex signal amplitude with a frequency equal to the difference between the original transmitted frequency and the Doppler frequency. The S/N power ratio of the input and output signals are similar in size and so for low S/N signals coherent detection is preferable.

### 4.2.3 Analogue-to-Digital (A-D) Conversion

The three receiver outputs pass into three post-detector logarithmic amplifiers and then into the A-D convertors (Fraser 1984). Each A-D converter samples the input in 1-km range intervals and then stores the digitised output in its internal memory buffer.

The analogue signals from the three receivers are independently sampled and digitised at 256 points by a parallel eight-channel multiple A-D system (Brown 1992). Only three of the channels are required for this operation. Each channel consists of a 12-bit DATEL EH12B3 A-D converter with 2 kB of internal memory. The operating range of all three A-D converters is 0–10 V with a quantisation step of 2.4 mV. The minimum noise level from the receiver outputs is usually two to three times larger than the quantisation level (Brown 1992). Each A-D converter digitises the analogue input from the receiver once every 6.67 $\mu$s, when the transmitter pulse is triggered.

The cycle of sample-and-hold and digitisation is repeated every 6.67 $\mu$s until a predetermined number of range gates have been sampled, usually from 70–110 km. The

digitised data is transferred from the internal memories of the three A-D converters to the computer's memory. The A-D cycle is controlled by the external height reference pulses to which the transmitter pulse is synchronised (Fraser 1984). The result is a raw time-series of received signal amplitude variations. FCA is then performed on the raw data, which takes from 2–10 minutes, depending on the data quality. The raw data is then discarded and another pulsing run is initiated.

The zero height calibration was achieved by noting the time position and amplitude of the pulse using the suitably-attenuated receivers (Fraser 1984). This method has the advantage that it is independent of the receiver bandwidth. The unattenuated received transmitter pulse is saturated at the top of the pulse. The saturation is due to the delayed overload response of the receivers to the transmitter pulse. The nominal position of the transmitter pulse maximum is therefore taken to be halfway along the saturated top of the pulse. If the receiver were not overloaded, the position of the unloaded transmitter ground pulse maximum would be 3.5 km lower in height. Hence, the raw heights of winds determined by the BF radar are underestimated by 3.5 km. This was corrected for during the analysis procedure prior to the optical/radar comparisons.

### 4.2.4 The Computer and Data Acquisition

The partial-reflection drifts radar experiment at BF is controlled by a fully-automatic, on-line dedicated computer system which is responsible for transmitter and receiver control, data acquisition and storage. The partial-reflection records were also analysed on-site using FCA in real-time. The computer is also capable of re-starting the system after a power failure. Prior to May 1993, the data logging and acquisition was done using a DEC Micro LSI 11/23 mini-computer. This computer had a 16-bit microprocessor, 512 kb of RAM and a 22-bit Q-bus for connections to peripherals such as a hard disc and a magnetic tape drive. The date and time was supplied by an independent clock system attached to the LSI 11/23. During April 1993, the LSI-11/23 was replaced with a 386 IBM-compatible PC which enables a greater rate of data acquisition. The date and time is provided by the internal clock of the PC which was periodically checked for accuracy.

After each sampling run, FCA is performed on the digital data (Briggs et al. 1950, Brown and Chapman 1972, Briggs 1984). The auto- and cross-correlation functions between antennas are calculated, and used to derive the zonal and meridional wind velocities. These, together with other parameters are then written to magnetic media for subsequent collection and analysis.

The number of independent points associated with each raw radar record is about 210–280 times less than that the number of independent points associated with each raw FPS

measurement. For the Birdlings Flat radar, the number of independent points obtained at each sampled height during every 82 second run is about 60 to 80, because the number of independent radar points is determined by the ratio of the observation time to the fading time of the mean auto-correlation function. The fading time was calculated after the noise spike was removed and was typically 1–2 seconds.

### 4.2.5 Acceptance Criteria During Radar Wind Determination

Several test criteria (Briggs 1984, Fraser 1989, Hocking et al. 1989) were employed on the raw data prior to, and after, FCA to ensure the quality of the wind data was acceptable. The following criteria listed here are based on Briggs (1984) and the specific details are based on Brown (1992).

**The Auto-Correlation Functions**

**Signal to Noise Ratio** The S/N ratio of the raw data as determined from the de-spiked auto-correlation function, as discussed in section 4.1.3, had to exceed -6 dB.

**Fading Time** Signals with a fading time of $\tau_{fad}$>10 seconds were rejected.

**The Cross-Correlation Functions**

**Cross-correlation Maxima** Each cross-correlation function had to have a maximum value of not less than 0.2, which corresponds to being within 7 dB of the mean signal. Cross-correlation functions exhibiting oscillatory behaviour were rejected because the correct maxima are impossible to determine.

**Time Lags** Cross-correlation maxima which exhibited time lags ($\tau_{ij}^{'}$) of greater than 6 seconds were rejected. The data length of the cross-correlation function dictated the ability to find a fit and no fit was possible greater than 6 seconds.

**Normalised Time Discrepancy (NTD)** The sum of the three time delays around an array of three spaced antennae had sum to zero i.e. $\tau_{12}^{'} + \tau_{23}^{'} + \tau_{13}^{'} = 0$. This indicates the level of internal consistency of the data. The NTD (Gregory et al. 1979) is defined as

$$NTD = \frac{| \tau_{12}^{'} + \tau_{23}^{'} + \tau_{13}^{'} |}{| \tau_{12}^{'} | + | \tau_{23}^{'} | + | \tau_{13}^{'} |} \tag{4.28}$$

The result was rejected if NTD > 0.9 (Fraser pers. comm.) This value of NTD was chosen because May (1988) reported that a "considerable proportion" of the records will exhibit NTD values of 0.3 due to purely random errors. So this allows for a generous margin of error.

**The FCA Procedure**

**Apparent and True Velocity Magnitudes** The magnitude of the true velocity could be no less than one-third the magnitude of the apparent velocity. This removed cases of extreme elongation of the diffraction pattern and large time lags.

**Correlation Ellipse Ratio and Size** The axial ratio of the correlation ellipse had to be less than 5.0 and if the ratio was greater than 1.0 then the minor axis had to be greater than 50 metres.

**Apparent and True Velocity Directions** The directions of the apparent and true velocity vectors had to be within $90^o$ of each other for the same reason as above.

**True Velocity Magnitude** The result was rejected if the magnitude of the true velocity exceeded 300 $ms^{-1}$ for the same reason as above. It is also the speed of sound.

**Random Velocity Parameter** Values of $(V_c)_v$ (see Appendix C) which are more negative than 30 $ms^{-1}$ were rejected. Such values indicated excessively large uncertainties in the FCA parameters.

### 4.2.6 Triangle Size Effect

The size and configuration of the receiving antenna array is an important factor in determining the true velocity of the sampled ground diffraction pattern. The magnitude of the true velocity is found to be dependent on the antenna spacing (Golley and Rossiter 1970). This systematic error is known as the triangle size effect. The true velocity increases towards a limiting value as the antenna spacing is increased. Golley and Rossiter (1970) investigated the drift parameters derived from various spacings and configurations of triangular arrays of a 1-km diameter array of 89 equally-spaced antennas at Buckland Park (Briggs et al. 1969). The limiting value was assumed to be the correct drift velocity because it agreed with an independent method. This method (Briggs 1968, 1993) involved the spatial correlation of the 89 spaced antennae so that the ground diffraction pattern was oversampled over a very large area. Golley and Rossiter (1970) concluded that the optimum array configuration is an equilateral triangle with antenna spacings which give a cross-correlation of about 0.5 at zero lags i.e. $\rho(\epsilon_{i,j},\eta_{i,j},0) = 0.5$. This corresponds to an array spacing of slightly larger than $1\lambda$ for partial-reflections drifts in the MALT. Arrays which are smaller than this result in a higher correlation but an underestimation of the true velocity. Larger arrays tend to produce lower correlations which can cause FCA to frequently fail. No dependence on array spacing was found for the drift direction.

Golley and Rossiter (1970) concluded that the triangle size effect was partly due to a reduction in the cross-correlation functions between antenna pairs as a result of instrumental

differences between the receivers or the A-D converters. No significant difference in the shapes of the spatial and temporal auto-correlation functions was reported. The r.m.s deviation of the drift parameters was found to decrease with increasing array size and tended to a limit as the array size became comparable with the scale of the diffraction pattern. Antenna coupling at small spacings was suggested by Fedor and Plywaski (1972) as the cause of this effect but they found that it did not appear to be very important. Meek (1990), in a recent study, found a similar result. He suggested that the triangle–size effect was due mainly to the effect of random noise associated with the diffraction pattern and should be removed by de-spiking the auto-correlation functions (Goldstein 1950) prior to FCA (as described in section 4.1.1). Furthermore, he suggested that the noise tends to increase the elongation of the diffraction pattern in the direction of the hypotenuse of a right–angled triangular array. However, de-spiking was applied to the BF radar data in this present project, prior to the FCA procedure, and there is noticeable elongation of the radar wind vectors along the direction of the array hypotenuse (discussed later in this section), a behaviour related to the triangle-size effect. Therefore the presence of noise cannot be the sole reason for the triangle-size effect and related behaviour.

Hocking et al. (1989) suggested that the frequency of negative $V_c^2$ values is less for widely-spaced antenna pairs since the cross-correlation maxima occur at greater lag values and hence have less relative error. A very long fading time results in a broad auto-correlation function and consequently a negative $V_c^2$ value.

Related to the triangle size effect is the hypotenuse bias effect. This effect was first reported by Beynon and Wright (1969) and was also investigated by Golley and Rossiter (1970). It was also reported by Fraser and Kochanski (1970) from radar wind observations with the BF radar. It is the tendency for the major axis of the characteristic ellipse (see Appendix C) to be aligned along the hypotenuse when a right-angled antenna array is used. An array in the shape of an equilateral triangle would obviously eliminate this bias. Beynon and Wright (1969) suggested that the reason for the bias effect was because the contours of maximum amplitude were curved instead of straight, but no evidence for this was found by Felgate and Golley (1971) using the Buckland Park array complex.

The antenna spacing used at Birdlings Flat was larger than the optimum size found by Golley and Rossiter (1970). The array is also a right-angle triangle in which the antenna spacing along the hypotenuse is nearly 3 $\lambda$. The antenna spacing along the two short sides is $2\lambda$. The larger-than-optimum spacing will result in low cross-correlation values (less than 0.5 on average) which will increase the susceptibilty of the FCA procedure to noise. As a result, this spacing will lead to a larger variance associated with the radar wind values and this is precisely what is found for BF radar winds (Fraser pers. comm.). The number of rejected runs would also be higher than for a smaller array for the same reason.

In addition to larger-than-optimum spacing of the BF receiving array, there was evidence that another orientation effect is exhibited in the radar winds obtained by the BF radar in this project. This effect is exhibited in both the daily and monthly radar winds for both the original and reconstructed winds, including the simultaneous night time winds.

Figure 4.8 is a polar plot of the radar daily mean wind vectors for the FPS-simultaneous days in the project. Each filled circle represents the head of each daily mean wind vector. The slope of best fit through the distribution is shown on each plot, together with the associated 95% confidence interval. The major axis of the radar wind distribution of the daily mean radar winds in the 85–105 km height region lies at an angle of approximately $20^o$ to the EW direction. The orientation is close to orientation of the hypotenuse of the Birdlings Flat ground receiving array but the two do not exactly coincide. The distribution is, within the uncertainties of the slope, aligned perpendicular to the geomagnetic meridian line, which was $\sim 25.7^o$ in 1993 (Hydrographic Office, 1946). This infers that there is possibly some degree of geomagnetic control of the radar wind velocities at Birdlings Flat. As mentioned earlier, Stubbs (1977) reported evidence of geomagnetic control of partial reflection winds above 100 km, and the tendency for the characteristic ellipse associated with the winds, to be aligned along the geomagnetic meridian. The direction of the radar wind velocity is biased towards the perpendicular of the characteristic ellipse (Phillips and Spencer 1955).

This orientation effect exhibited in the BF radar winds may be partly a result of the rejection criteria used on the raw drifts determinations. The antenna spacing along the hypotenuse is almost 50% longer than the other two sides and so for wind drifts occurring along this direction only high correlations would be accepted, producing a bias for winds along this direction. The hypotenuse bias effect is however symmetrical in direction in the sense that it would tend to bias both zonal and meridional components equally and the elongation would be at $45^o$ to the EW direction.

For completeness, the plots in Figure 4.8 can be compared to the corresponding polar plot of the FPS daily mean winds in Figure 6.6, where there is no statistically significant elongation at the 95% level.

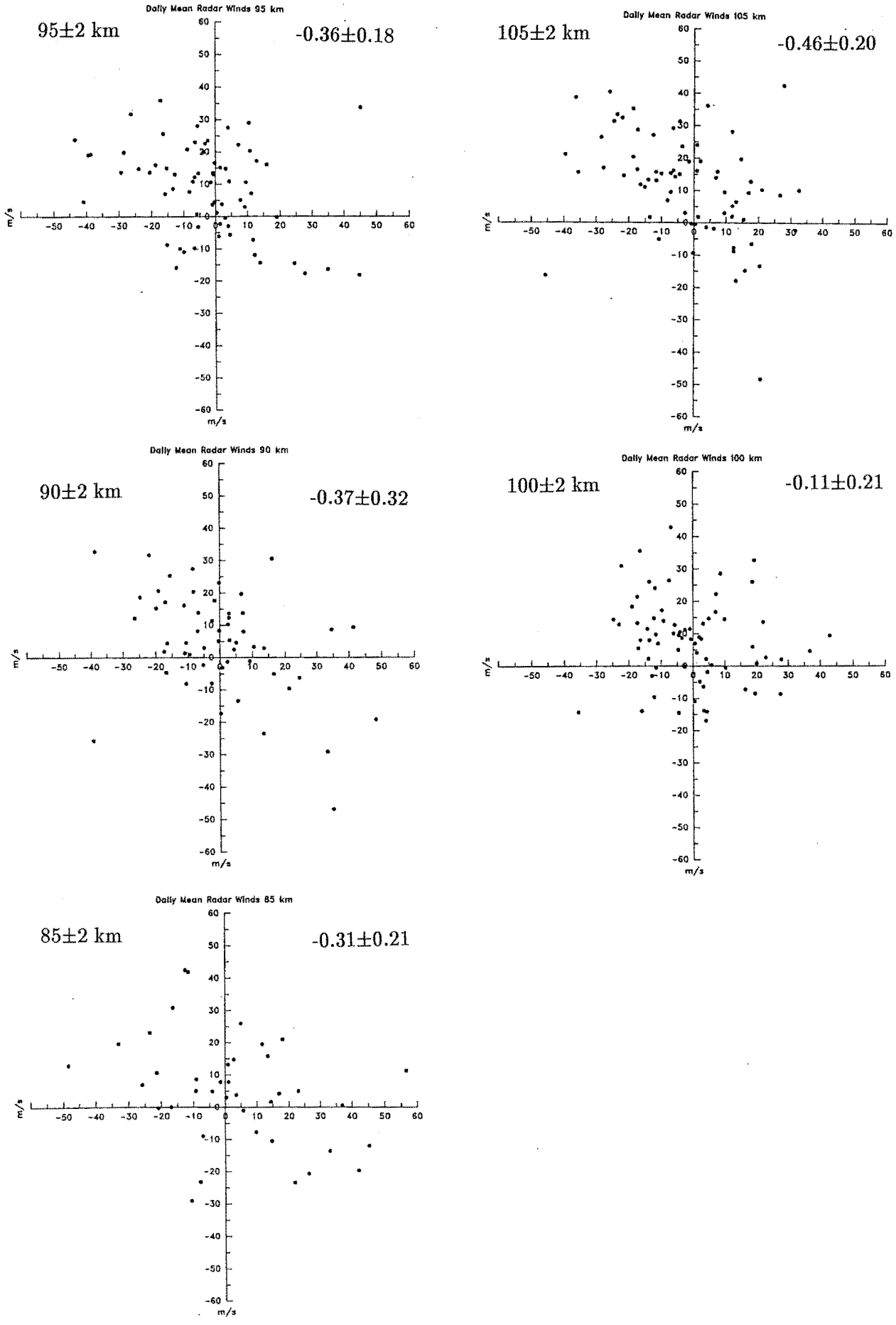


Figure 4.8: Polar plot of the daily mean radar wind vectors for the FPS-simultaneous days. The fitted slope values together with the associated 95% confidence level is also indicated.

# Chapter 5

# Data Reduction and Analysis

## 5.1 Wind Data Acquisition

During normal operation the two instruments do not probe/sample continuously or simultaneously the same volume of space. It is therefore desirable that these differences are minimised before any useful comparisons can be made.

There were, however, several reasons why the data from the two techniques could not be treated in exactly the same way. The main reason was that the yield of night time radar winds is less than during the day time due to the high level of RF noise and interference associated with the radar wind measurements. As a result, the optical and radar winds are not directly comparable.

The paucity of night time radar wind values necessitated, prior to time-averaging into 1-hour time bins, the grouping of the raw radar winds in 5-km height bins (see Section 5.5.1). Simultaneous raw radar winds which were separated by heights of $\sim$5 km or less were not independent, although raw winds from different times within the hour are independent. This averaging reduced the influence of the RF noise and oblique echoes. The estimated area probed by the effective polar diagram of the radar and scatterers (discussed in Chapter 4) may allow a contribution of oblique echoes from heights 5–6 km lower than the nominal vertical height of probing.

Because the hourly mean radar winds are partially independent over height and fully independent over time, the number of degrees of freedom will range from N/5 to N, where the factor of 5 would apply to the vertical bin size if all points were completely dependent. The sample variances of the radar hourly mean winds will therefore be underestimated by up to a factor of $\sqrt{5}$.

The two techniques observed the dynamics of two different mediums albeit in the same region; neutral gas (FPS) and ionisation (radar). The FPS samples emission from neutral atomic oxygen near 95 km and the winds are determined directly from the Doppler-

shifted fringe records. The radar winds are determined indirectly from the sampling of the ground diffraction pattern which is produced by radio-wave scatter from electron density variations in the MALT region. The effect of the geomagnetic and/or electric fields on the radar winds may become important at heights above about 95 km (see Section 4.1.2). The optical winds are derived from emission from a neutral species and so will not be directly affected by such fields.

The nature of the spatial averaging achieved by the two techniques is different. The horizontal extent of probing by the radar is governed by the product of the radar's radiation pattern and the scatterers' aspect sensitivity, as discussed in the previous chapter. The radar probes the MALT region from 80 to 110 km and obtains measurements from heights at 1 km intervals, which are weighted over the 4.5 km transmitter pulse width.

The FPS obliquely samples the 557.7 nm emission at an elevation of $20^o$ above the horizon. The sampling volume is a cylinder $\sim$30 km long and 3 km in diameter. The FPS winds are a line-of-sight average which are vertically-weighted by the 557.7 nm emission height profile (FWHM intensity $\sim$ 12 km (Shepherd et al. 1995)) which is centred near 95 km (Hernandez et al. 1995). The volume of space sampled by the FPS during each measurement is smaller than that probed by the radar but the raw FPS winds that are measured in opposite directions were combined into the corresponding zonal and meridional winds. Hence, for the comparisons, the hourly mean optical wind is the average of the two points separated by $\sim$500 km, the diameter of the observing area.

The nature of the temporal averaging achieved by the two techniques is also different. The radar probing time of the 80–110 km region required about 82 seconds and wind measurements were obtained every 2 to 8 minutes, depending on the data quality. By comparison, a single FPS wind measurement required about 12 minutes. The time of a raw FPS wind measurement was taken to be the mid-time of the measurement.

In order to minimise the operating and sampling differences between the two techniques the comparisons were made between the hourly mean optical and radar winds. An attempt was also made to vertically bin or weight the radar winds (Bevington and Robinson 1992) in order to approximate the 557.7 nm emission height profile. This is described later in Section 5.5.1.

## 5.2 Time-Averaged Wind Definitions

Each data set was time-averaged over several time-scales and these averages are defined below.

1. Individual Hourly Mean Winds.

The hourly mean FPS winds were calculated from the individual raw FPS winds. The raw values were weighted by their associated uncertainties. Approximately 7 to 14 hourly mean FPS wind values for each night were available, depending on the seasonal night-time duration.

The hourly mean radar winds were calculated from the individual raw radar winds for the same time period during the night as the FPS measurements. Because the uncertainties of noise-free observations were unknown, the raw radar winds were equally-weighted in order to derive the hourly means and their associated variances. There was a paucity of night time raw winds at the lower heights, especially below about 85 km, so the wind values there must be treated with caution.

The procedure of hourly averaging resulted in the reduction of variations which were not coherent over the period of 1 hour from the FPS and radar wind data sets. This was especially important for the radar winds because RF noise and interference resulted in large variations in the raw radar winds on time-scales of minutes.

2. Daily Mean Wind.

   The daily mean FPS wind was estimated from a least-squares fit of a 12-hr sinusoid function (discussed in section 5.8.1) to the individual hourly mean FPS wind data.

   The daily mean radar wind for each night was estimated from a least-squares fit of 12- and 24-hr sinusoid function (discussed in section 5.8.1) to the individual hourly mean radar wind data. The data from the entire 24-hour period centred on the night time was used.

3. Daily Vector Mean Winds.

   The average value of the FPS wind for each night was calculated from the individual hourly mean FPS wind values for each component of the wind vector. The individual hourly mean winds were weighted by their uncertainties.

   The average value of the night time radar winds was determined from the individual night time radar hourly mean wind values for each component of the wind vector which were simultaneous with the FPS winds. The vector mean winds were derived from the individual hourly mean winds and not the raw radar winds in order to remove any bias due to the diurnal variation in the number of raw radar wind values (more during the day, less at night).

   These simultaneous vector mean winds were more useful for the comparisons because they were concerned only with the simultaneous night time radar and FPS wind measurements and were independent of tidal estimates, etc. Therefore, any differences

between the FPS and radar wind measurements could be expected to be due solely to the FPS and radar techniques themselves.

Equal weighting was used to derive the daily radar vector mean winds because of the amount of RF noise and interference associated with the radar wind measurements. The level of RF noise and interference resulted in large and fluctuating sample variance values from hour to hour associated with the hourly mean radar wind values. The procedure of weighting the radar winds by the corresponding sample variances therefore produced erratic variations in the radar wind height profile and so the expected coherency over the 5-km binning interval was lost. Wind variations of 50 $ms^{-1}$ between adjacent 1-km heights were frequently exhibited, which is inconsistent with the 5-km binning interval used. The wind height profiles obtained by not weighting by the sample variances exhibited more consistency and coherence over the 5-km binning interval. This is clearly illustrated in Figures 5.1a and b which show the night time mean radar wind height profiles for 13 May 1994 obtained (a) by equal weighting the hourly mean wind values and (b) by weighting the hourly mean radar winds by their corresponding sample variances. The error bars in Figure 5.1a correspond to the standard deviation of the mean values. The error bars in Figure 5.1b were derived by weighting the hourly winds error values by the corresponding hourly sample variances. The differences due to weighting the hourly mean winds are clearly evident and it illustrates how significant the RF noise and interference was in the radar wind data. In Figure 5.1a, equal-weighted averaging minimises the effect of spurious points on the values of the mean winds. The mean zonal and meridional radar wind profiles for 13 May 1994 during the daytime are, within the uncertainties of the wind values, similar to the night time winds.

4. Monthly Hourly Mean Winds. For each month the corresponding hourly mean FPS winds from the selected nights were combined to obtain the mean diurnal variation for each month. The individual hourly mean optical winds were weighted by their uncertainties in order to derive the monthly hourly mean winds.

   The individual hourly mean radar winds from the FPS-simultaneous days during each month were similarly combined and the mean hourly winds for the monthly period were derived. These mean radar winds were calculated by equally weighting each individual daily hourly mean wind value for two reasons: (i) as in the case of the daily hourly mean winds, it reduced the diurnal bias due to the variable number of raw data points per hour. As a result, the variance of the mean values varied diurnally; (ii) the variances associated with the daily hourly mean winds, together with the hourly mean values themselves, were found to be large as a result of the presence of noise in the data. This was especially important for the radar winds because RF noise and interference caused

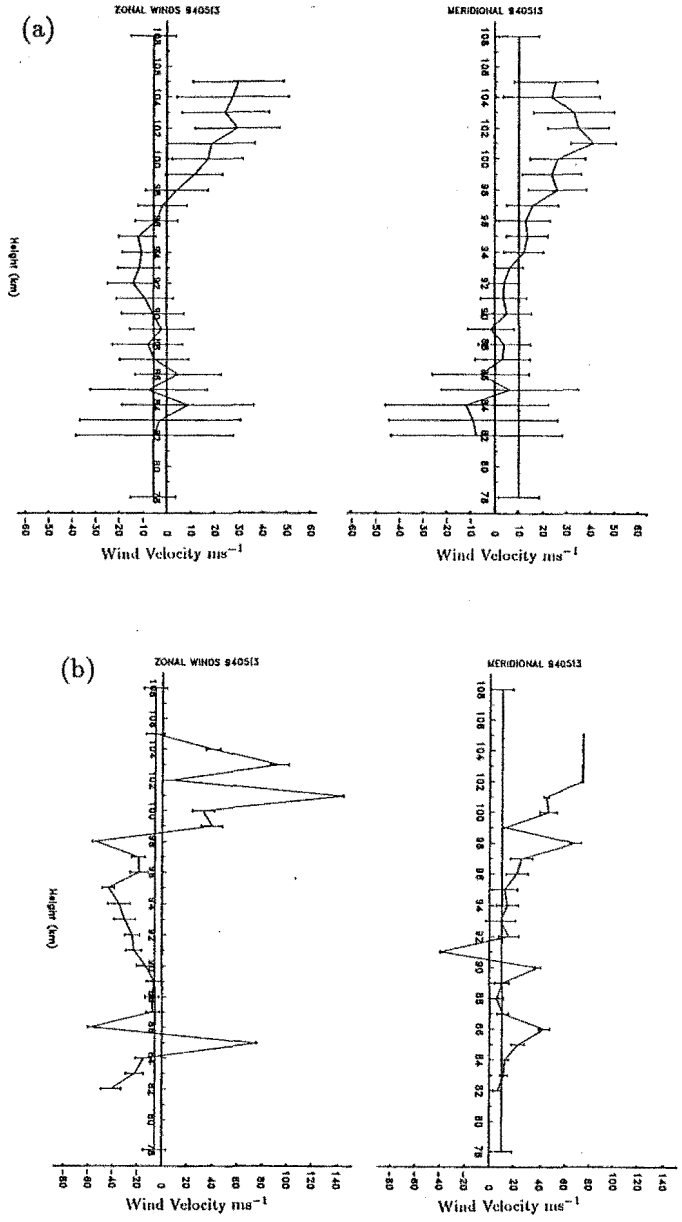


Figure 5.1: The night time mean radar wind height profiles for 13 May 1994 obtained by (a) equally-weighting the individual hourly mean wind values and (b) weighting the individual hourly mean wind values by their associated sample variances. The error bars correspond to the standard deviation of the mean values. The effect of noise on the weighting procedure is clearly evident.

large variations in the raw radar winds on time-scales of minutes. The amount of scatter exhibited by the monthly hourly mean winds was less than for the daily hourly mean winds but differences of $\sim$50ms$^{-1}$ from one hour to the next sometimes occurred.

5. Monthly Mean Wind. The monthly mean radar wind value was determined from the least-squares fit to the hourly mean wind data as discussed in Section 5.7.2. The data from the entire 24-hour period centred on the night time was used.

6. Monthly Vector Mean Winds. The average FPS wind value for each month was calculated by weighting the individual monthly hourly mean winds, for each component of the wind vector, from each particular monthly period by their associated uncertainties. Similarly, the average radar wind value for each month was calculated from the individual monthly hourly mean winds, for each component of the wind vector, from each particular monthly period.

A method to minimise the effect of outliers in the raw radar wind data, prior to the calculation of the hourly statistics, was investigated. Hourly median radar wind values were calculated from the raw data from several individual days and these were compared with the corresponding hourly mean radar wind values. The inter–quartile range was calculated for each median value as a measure of the scatter of the raw data. The differences between the corresponding sets of hourly mean and hourly median wind values were, for over 95% of the time, within the uncertainties of the hourly wind values, i.e. the standard deviation of the hourly means or the inter–quartile range of the hourly median values. Since there was no clear difference between either statistic the raw radar and the raw optical winds were time–averaged using hourly mean values.

## 5.3 FPS Data Reduction

### 5.3.1 Night Selection Criteria

The number of suitable nights was variable and dependent upon the weather conditions, magnetic activity and the operational status of the FPS and radar. The FPS winds were sensitive to cloud cover and so only clear nights within 10 nights centred around the new moon were selected. The nights were also selected to be during magnetically quiet ($K_p$<3) times in order to reduce any possible auroral 557.7 nm emission originating above 100 km. The level of magnetic activity was determined using the published planetary magnetic index, $K_p$ for the particular measurement period. Contamination by auroral 557.7 emission from above 100 km would result in a contribution from winds above the height of the 95–100 km layer (Hernandez and Killeen 1988, Lloyd et al. 1990, Manson et al. 1991, Phillips et al.

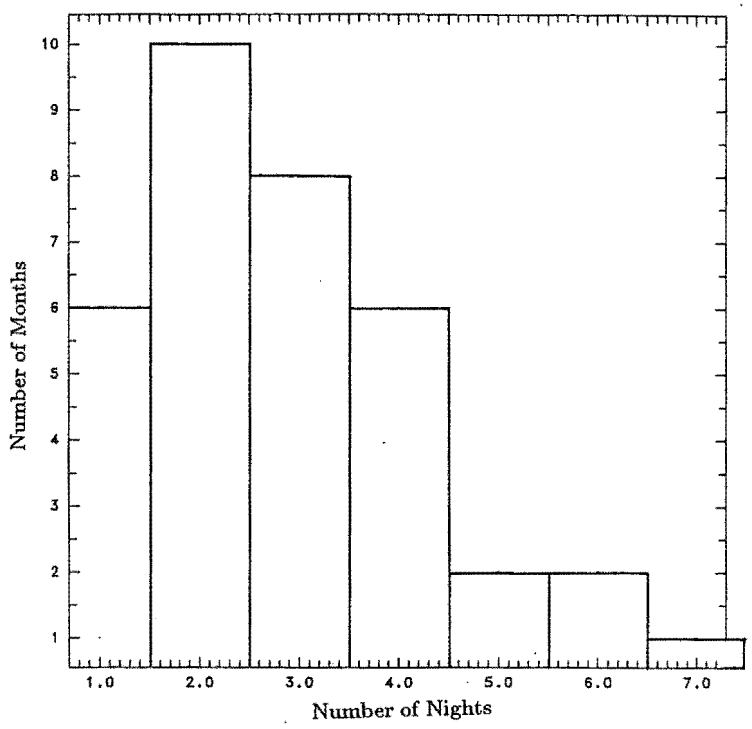


Figure 5.2: Histogram of the distribution of the number of nights comprising the monthly winds.

1994). The probability of auroral 557.7 nm emission at mid-latitudes originating from above 100 km increases during moderate to high magnetic activity ($K_p$>3) (Roach 1960, Silverman et al. 1962, Sanford 1959, 1964).

During the period February 1991 to July 1994, 103 clear, low $K_p$ ($K_p \leq 3$) nights were selected as suitable for comparison with the radar winds – about 10% of the total number of nights. The nights are grouped according to month in Table 5.1. The optical winds for these nights were derived and subsequently compared with the radar winds on various time-scales ranging from hours to several days.

Unless otherwise stated, the dates and times of the data discussed in this project are in UT and the dates are denoted either as a standard date or as a six-digit representation. For example, 4 March 1994 or 940304.

Figure 5.2 is a histogram of the distribution of the number of available nights during each month. For the 35 months investigated, there was an average of 3 suitable nights per month. Several of these months contained nights which were consecutive. Six of the 35 months contained only a single night, which left 29 months for which means over the monthly period were derived.

The presence of cloud was determined from the quality of the 557.7 nm emission

| Jan | Feb | Mar | Apr | May | Jun | Jul | Aug | Sep | Oct | Nov | Dec |
|---|---|---|---|---|---|---|---|---|---|---|---|
| | | | | | **1991** | | | | | | |
| | 19 | 10 | 12 | 10 | | | | | 13 | 24 | 9 |
| | 21 | 11 | 13 | 20 | | | | | 14 | 26 | |
| | 22 | 12 | 16 | 21 | | | | | | | |
| | | 15 | | 22 | | | | | | | |
| | | 16 | | | | | | | | | |
| | | 17 | | | | | | | | | |
| | | | | | **1992** | | | | | | |
| 9 | 6 | 3 | 15 | 26 | | | 19 | 12 | 3 | 25 | 3 |
| 26 | | 4 | 21 | 30 | | | | 26 | 4 | 27 | |
| | | 5 | | 31 | | | | | | 28 | |
| | | 7 | | | | | | | | | |
| | | 8 | | | | | | | | | |
| | | | | | **1993** | | | | | | |
| | 14 | 23 | 1 | 1 | 16 | 15 | 8 | 8 | 15 | 13 | 9 |
| | 15 | 26 | 11 | 2 | 20 | 24 | 10 | 12 | 16 | 14 | 10 |
| | 18 | 27 | 28 | 5 | 26 | 28 | 12 | 16 | 17 | 16 | 11 |
| | 19 | 28 | | 12 | 29 | | 20 | | 21 | 22 | |
| | | | | 13 | | | 24 | | | | |
| | | | | 19 | | | | | | | |
| | | | | 20 | | | | | | | |
| | | | | | **1994** | | | | | | |
| 9 | 15 | 4 | 27 | 13 | 22 | 12 | | | | | |
| 13 | 16 | 26 | 28 | | | 13 | | | | | |
| | | 27 | | | | | | | | | |
| | | 28 | | | | | | | | | |
| | | 29 | | | | | | | | | |
| | | 31 | | | | | | | | | |

Table 5.1: The dates of the 103 suitable nights used for the radar/optical wind comparisons.

fringe records and a nightly meteorological log, which was kept by the resident superintendent at Mt. John, Mr. M. Clark. The log provided a general indication of the sky conditions during each night and if cloud was present, the night was rejected.

Fringe records of the $P_1(2)$ line at 840.0 nm in the OH(6-2) Meinel hydroxyl band were obtained at the same time with the 557.7 nm records. This emission line was useful because it was more sensitive to the presence of cloud than the 557.7 nm records. The Meinel bands occur from about 500 nm through into the near-infrared and, in total, are the brightest emissions of airglow anywhere in the spectrum. The 840.0 nm line emission originates at 88.6±1.4 km (Hernandez et al. 1995) and has a vertical width of ~10 km (Baker and Stair 1988). The emission is a result of transitions from vibrationally-excited levels of ground-state OH radicals and is produced via the replacement reaction between H and $O_3$ (Bates and Nicolet 1950):

$$H + O_3 \rightarrow OH^* + O_2 \tag{5.1}$$

The determination of cloud cover was based on the assumption that the 840.0 and 557.7 nm emission were spatially and temporally homogeneous. It is however well documented that both emissions are frequently not homogeneous and that large intensity variations may occur (Peterson and Kieffaber 1973, Moreels and Herse 1977, Herse et al. 1980, Armstrong 1982, 1986, Taylor et al. 1987, 1991, 1995, Taylor and Hapgood 1990). The non-homogenous nature of the emission on the FPS measurements was minimised by using the method of equidistant equal-noise sampling during data acquisition (see Section 3.2.7) (Hernandez et al. 1984).

The presence of cloud-cover reduced the S/N of both the 840.0 nm and 557.7 nm emissions by causing absorption and scattering of the emissions. For each fringe record, the ratio of the sample variance of the counts to the mean number of counts provided a qualitative measure of the S/N. An emission fringe produced from a dark cloudless sky had a low baseline (of about 15–25 counts) and a large mean and sample variance due the well-defined fringe profile. Conversely, an emission fringe obtained during cloud-cover would have a higher baseline and a reduced mean and sample variance due to degradation of the fringe profile.

Using differences in wind values between opposing observing directions to determine the presence of cloud was not deemed an effective method because previous studies (Abreu et al. 1983, Cogger et al. 1985, Price et al. 1995) have indicated that horizontal MALT wind gradients across the observing area may occur.

Ideally, it would be advantageous to have a direct record of the sky conditions throughout each entire night's observations. An infrared detector system is currently being

developed by a member of the research group, Mr. M. Plagmann, which will provide a comprehensive and direct monitoring system of the presence of cloud over the FPS observing area.

## 5.4 FPS 557.7 nm Wind Determination

Other workers have employed various techniques to derive winds from FPS fringes records. Hays and Roble (1971) describe a method of fitting the Fourier transform coefficients of an observed sky profile to Fourier coefficients of a model profile from an ideal instrument via a non-linear least-squares fitting routine. Hernandez (1966, 1970, 1986) uses a least-squares method of fitting the Fourier transform coefficients of an observed sky profile which has been de-convolved from the FPS instrument function. Hernandez et al. (1992) and Conner et al. (1993) devised a direct fit method whereby an analytical model of the observed profile is derived by optimising trial values of parameters such as peak position, temperature, background noise, etc using the Levenberg-Marquardt method. Hines et al. (1993) also used a non-linear least-squares Gaussian fit to derive line-of-sight wind, line intensity and temperature measurements.

In this project, FPS Doppler winds were determined from the 557.7 nm fringe peak positions using a non-linear weighted least-squares fitting algorithm (Press et al. 1992) which employed the Levenberg-Marquardt method (Levenberg 1944, Marquardt 1963). A Gaussian function was fitted to the raw 557.7 nm fringe profiles in order to determine the maxima positions. The uncertainty of the fit was obtained from the diagonal elements of the covariance matrix and were typically of the order of 0.01 bin. Records with fringe baseline values which were equal to or greater than the fringe amplitude were indicative of scattered light by cloud and were rejected. Records were also rejected if the sample variance/mean ratio of the fringe record was less than 10.0.

The maxima of the raw fringes were unequally-spaced in position, with subsequent orders occurring closer and closer together as the scanning voltage was increased. This non-linearity was the result of the non-linear scanning behaviour of the piezo-electric crystals and has been described by Hernandez (1978). Prior to calculating the Doppler shifts, the non-linearity is removed numerically from the raw fringe records.

If the position of the $x_{i+1}$th peak maxima position is plotted as a function of the $x_i$th peak position, a linear relationship $x_{i+1} = x_i b + a$, is obtained, where the y-intercept, a, and the slope, b, are the linearisation coefficients (Hernandez 1978). The slope, b, describes the amount of non-linearity present in a fringe record and the y-intercept, a, determines the peak position of the lowest order. Linear scanning would produce equally-spaced fringes resulting in a linear relationship with unity slope i.e. $b = 1.0$. Once obtained, the linearisation

constants can be used to remove the non-linearity that is present in the raw fringes using the following relationship. The position of the nth peak maxima in orders from an arbitrary reference point can be described by the relationship (Hernandez 1978)

$$\nu_i = \frac{1}{\ln(b)} \ln[1 - (\frac{x_n - x_0}{\frac{a}{1-b} - x_0})] \tag{5.2}$$

where a and b are the linearisation coefficients, $x_n$ is a displacement quantity proportional to the driving voltage and $x_0$ is a displacement quantity proportional to the driving voltage at an arbitrary reference point. In this case it is taken to be the fringe peak of lowest bin value.

The nightly average values of the two linearisation coefficients were determined and used to linearise that particular night's fringe records (see Appendix B). The uncertainties of a and b were the sample standard deviations of the mean values of a and b during the night. The validity of the linearisation was checked by comparing adjacent free spectral ranges in each fringe record. If the free spectral ranges were of the same value within the uncertainties of maxima positions then the linearisation was valid. Fringe records which failed this criterion were discarded and the linearisation coefficients were recalculated.

The value of the nightly average slope coefficient decreased slightly over the period of this project by about 0.2±0.1% year$^{-1}$. The cause of the decrease was possibly due to a drift in the characteristics of the piezoelectric scanning stacks.

After the linearisation procedure was completed, the degree of linearisation was checked using the free spectral range (FSR) (see Chapter 3) between subsequent orders of the fringe records. Two values of the FSR were determined from two pairs of maxima from each record. Records in which one or both FSR values were not within 1% of the night's mean FSR value were discarded.

The maxima positions of the linearised fringe records were determined using the same non-linear least-squares fitting method and algorithm (Levenberg 1944, Marquardt 1963, Press et al. 1992) used on the unlinearised fringe profiles. The raw FPS winds were calculated from the relative shifts between the maxima of the sky fringes and the night's zero velocity reference. The zero wind reference was obtained from the night's average zenith fringe maxima positions. The standard deviation of the zenith fringe maxima positions during each night corresponded to an uncertainty in the zenith zero reference velocity of typically 5–7 ms$^{-1}$.

The equation for the horizontal component of the line-of-sight Doppler velocity is:

$$V = \frac{\text{shift}}{\text{fsr}} (\frac{25.0c}{cos(22.2^o)\sigma_0}) \tag{5.3}$$

where shift is the relative phase, measured in bin numbers, between the fringe record

and the night's zenith average, fsr is the free spectral range, also measured in bin numbers. The factor of 25.0 converts the shift from bin numbers into wavenumbers and the cosine factor converts the line-of-sight velocity into a horizontal one by assuming that the layer is concentric with the Earth's spherical surface.

The raw FPS winds were determined by deriving the wind values using two orders of the fringe records. The final raw wind value was taken to be the average of the two values. The fit uncertainty associated with the raw FPS wind values was the combined fit uncertainties of the fringe positions of the zero wind reference, the sky fringes and the free spectral range.

The final uncertainty ($\sigma_r$), of the raw FPS winds was a combination of (i) the fitting error of the sky fringes ($\sigma_f$), (ii) the uncertainty of the zero velocity reference position ($\sigma_z$), and (iii) the stability of the FPS etalon ($\sigma_e$). The raw wind uncertainty was taken to be the square root of the sums of the squares of these three contributing uncertainties and was typically 10–12 $ms^{-1}$.

$$\sigma_r = \sqrt{\sigma_f^2 + \sigma_z^2 + \sigma_e^2} \tag{5.4}$$

These derived FPS wind uncertainty values are probably over-estimated by a factor of approximately 2 due to the simplified analysis which was used and which neglected effects due to the FPS instrumental function and the deadtime of the PMTs (Hernandez pers. comm). This did not alter the results of the optical/radar wind comparisons, however.

The hourly mean zonal FPS winds for each night were derived by combining together the raw east- and west-looking FPS winds. Similarly, the hourly mean FPS meridional winds for each night were derived by combining together the raw north- and south-looking FPS winds. The distance between the two oppositely-directed sampled zonal or meridional volumes was ~500 km and so the wind fields were spatially averaged over this distance. The hourly mean zonal and meridional winds for each night were derived from the raw winds which were weighted by their associated uncertainties.

## 5.5 MF Radar Data Reduction and Analysis

Wind data records from the MF radar at Birdlings Flat were provided by Dr. G.J. Fraser in the form of raw zonal and meridional wind values at 1-km height intervals ranging from below 75 km up to ~110 km. The height range of the radar winds used in this project was 80 to 105 km. The radar days used were governed by the suitable FPS nights. The radar wind times were converted from New Zealand Standard Time (NZST) to Universal Time (UT) (UT = NZST - 12.0 hrs) in accordance with the FPS data.

### 5.5.1 Radar Wind Weighting Schemes

The mean radar winds used in this comparison project were derived from raw radar winds which were grouped together from adjacent 5-km heights. The height, h, of the hourly mean radar winds is therefore equal to h±2 km, inclusive. Therefore winds at heights separated by 4.5 km are partially correlated i.e., not fully independent, because of the 4.5 km transmitter pulse-width, but they are fully independent in time as discussed at the beginning of this chapter. The degree of dependence with respect to height is difficult to ascertain due to the differences in the time of measurements from heights within 5 km of each other and also because of the presence of oblique echoes.

Two other weighting schemes were initially tried on the radar hourly mean winds in order to weight them in the vertical direction. The reason for doing this was twofold: (i) it increased the number of wind values in each hourly bin. This was important because during the night there were fewer wind values, especially below about 90 km. (ii) to attempt to approximate the vertical 557.7 nm emission profile.

As discussed earlier, the grouped winds with heights within 1–5 km were not fully independent but they were independent in time. Furthermore, the binning process reduced the influence of noise and oblique echoes. The weighting schemes that were tried are listed below:

**1. Straight Binning**

The raw radar winds were binned together from adjacent height bins using an arbitrary number of bins. Several binning intervals were attempted such as 1, 3, 5, 9 and 17 km. For example, the 5-km binned winds at 100 km would include the raw winds from 100±2 km (98–102 km, inclusive). This was definitely the most useful of the three methods.

**2. Gaussian Function**

The hourly mean radar winds were weighted using a Gaussian function of arbitrary width. Profiles of FWHM widths = 2, 4, 6, and 8 km were investigated. The number of adjacent height bins utilised in this weighting scheme was equal to (2*FWHM + 1). For example, the Gaussian-weighted radar winds centred at 100 km with a FWHM = 4 km, incorporated winds at heights from 96 to 104 km inclusive, i.e. 9 km in extent.

One advantage of Gaussian weighting over straight binning was that heights used away from the central Gaussian peak did not affect the final wind value as much as those heights near the central peak. For example, Gaussian weighting with a FWHM of 5 km would utilise the same number of height bins as a 9-km straight-binning regime but the central 4 or 5 heights would be weighted more heavily than the others. The outlying heights would still be important to bolster the number of radar wind values during the night.

**3. Rocket Profile**

The hourly mean radar winds were also weighted according to a vertical profile of the 557.7 nm emission as determined by a mid-latitude rocket flight (O'Brien et al. 1965). This method used 20 adjacent height bins at a time. The 80–105 km height range of the radar winds investigated in this project resulted from the radar sampling only part of the height range of the rocket profile.

### 5.5.2 Comparison of Weighting Schemes

Figure 5.3 shows the optical/radar hourly mean wind cross-correlations, as a function of height, resulting from the various weighting schemes attempted with the radar winds during the night of 10 May 1991. There was no significant difference at any particular height, within the 95% confidence limits between the resulting cross correlation coefficients of either the straight binning or the Gaussian-weighting schemes which utilised the same number of heights.

As the number of heights used in each scheme was increased the resulting height correlogram became smoother in profile and the magnitude of the correlation for a given height tended to decrease. The correlation magnitude decreased because of the number of winds from more disparate heights, especially greater than 5 km apart where the winds would be largely independent, was increased. In each height correlogram, the amount of variance in the correlation coefficient decreased as the number of available hourly mean wind values used in the cross-correlation calculation was increased. There was significant scatter in the cross correlation coefficients values between the various schemes for winds below 88–90 km. This was due to the lower S/N ratio of the returned echoes and hence greater scatter in the wind values compared to echoes received from a higher altitude.

Since there was no significant difference between the resulting cross-correlation coefficients for a given height the choice of the optimum weighting scheme became a trade-off between a suitable height-resolution, to localise the height of maximum agreement between the two wind data sets, and a sufficient number of hourly mean radar wind values. Combining several heights or weighting over several heights therefore reduced this problem but it also reduced the height resolution. An empirical study of several days' and months' hourly mean winds found little difference in the optical/radar wind correlations between the method using straight binning 5 km of adjacent bins and one using Gaussian weighting with a FWHM of 2 or 4 km, or even by weighting with the rocket profile. The former however was chosen for its greater utility.

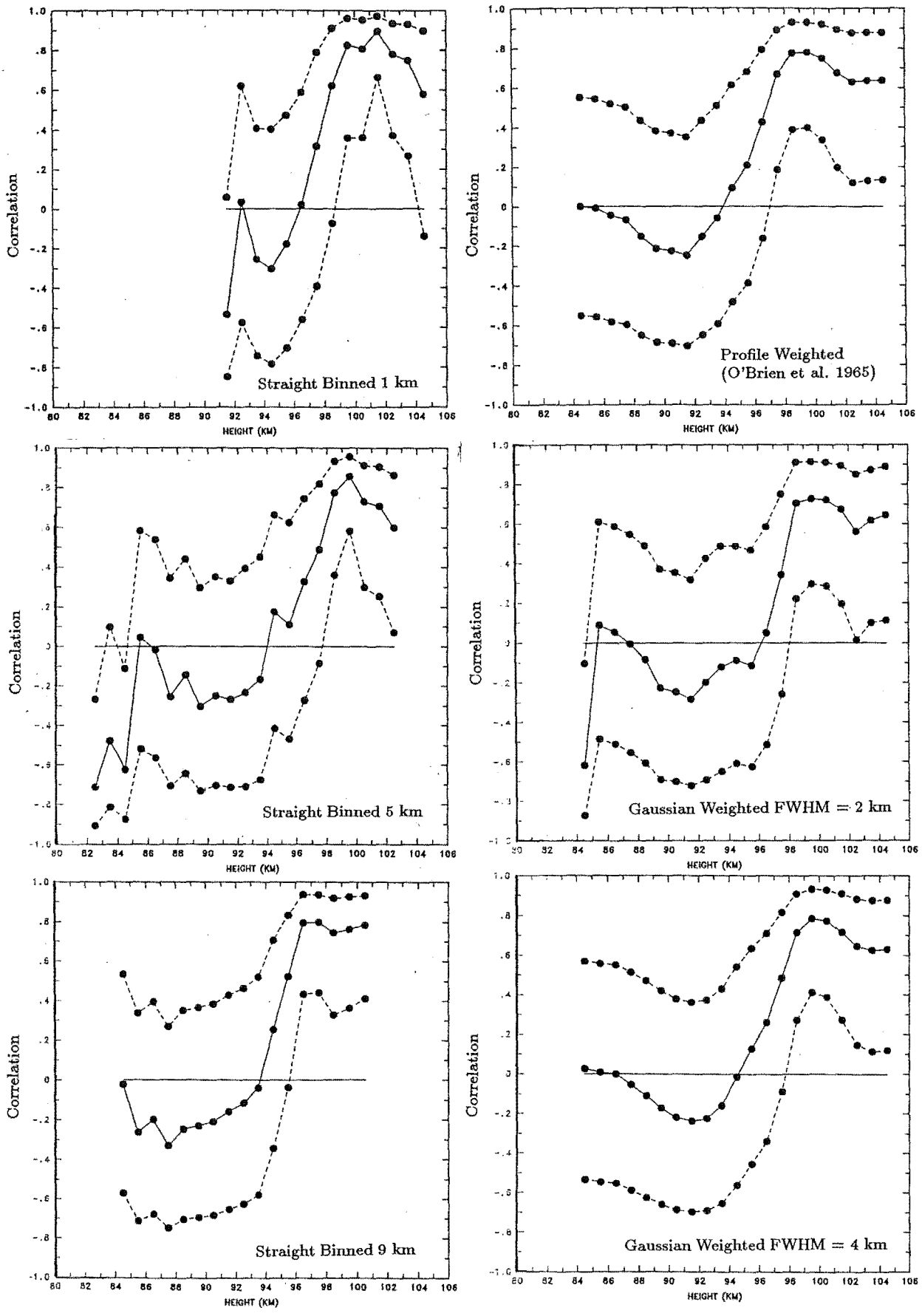


Figure 5.3: Height correlograms of the night time optical and radar winds on 10 May 1991 for the various radar wind weighting regimes. The bands are the 95% confidence limits of the correlation coefficients.

## 5.6 Optical/Radar Data Quality

### 5.6.1 Radar Data Quality

The raw MF radar winds possessed a large amount of scatter compared to the raw optical winds. A quantitative estimate of the scatter in the raw radar wind measurements was obtained by calculating the sample standard deviation of the night time hourly mean winds. At 95 km, this ranged from 15–65 $ms^{-1}$. The sample standard deviation of the combined day and night hourly radar winds at 95 km ranged from 15–60 $ms^{-1}$. Fraser (1989) reported that the sample standard deviation of the 1983–84 monthly mean radar winds at 80 km at Birdlings Flat was about 20–40 $ms^{-1}$, for the day and night winds combined. May (1988), using a statistical analysis, estimated the wind errors associated with the spaced antenna method to be 10–20 $ms^{-1}$. He also found that the wind errors may be overestimated by 10–20% due to acceptance criteria employed by the FCA procedure.

The BF receivers have a dynamic range of 40–50 dB and receiver saturation occurs at about 8.8 V. Prior to saturation, the logarithmic receiver response as measured at the receiver outputs is 5.15 dB $V^{-1}$ (Fraser, pers. comm.).

An estimate of the level of external RF noise was measured and recorded from each of the three receivers during each radar probing run. This is obtained from a range of 40 km where no radar echos or clutter are normally observed and this measurement is known as N40. N40 provides a qualitative lower-limit estimation of the amount of RF noise because the receivers saturate on the peaks of strong echo signals. The value of N40 generally increases after sunset, reaching a maximum around local midnight. There is a rapid reduction around sunrise. The night-time increase in the value of N40 can be explained by the absence of the D region during this time which results in interference from distant skywave propagation. The reduction in the level of ionisation, and hence absorption, also contributes by resulting in lower S/N of signal echoes.

Figure 5.4 shows the typical diurnal variation in the value of N40, in this case, the hourly mean N40 values for March 1994. It can be seen that during the night, the increase in noise power reaches nearly 20 dB around local midnight and values of 15–25 dB during the night are not uncommon.

This behaviour is consistent with results obtained from the radar polarimeter experiment operating at Birdlings Flat and discussed in chapter 4. Measurements from this instrument indicate that the amount of ionospheric noise increases by 20–30 dB during the night, thus severely hindering the operation of that instrument (von Biel pers. comm.).

Fraser (1989) reported that excessive RF noise occurred at night during the summer months as a result of thunderstorm activity in the tropics. This produced lower night time data rates compared to other times of the year. The finding is supported by the monthly night

time N40 values which are highest during the summer months. During this time, hourly N40 values corresponding to a noise power increases of 25 dB are not uncommon. By comparison, the noise power increase during the winter night time typically reaches values of about 15 dB.

Anthropogenic RF interference is another possible factor. One source during certain times was the marine-band weather broadcasts to coastal shipping. The most powerful of these originated from a transmitter at Awarua (Station ZLB), near Invercargill. The warnings were broadcast at numerous times throughout the day and night at 2.423 MHz, which was inside the passband of the radar receivers. This station was closed down in late 1991 but several other stations broadcasting near 2.4 MHz are still operating around the New Zealand coast on irregular schedules (Maritime Safety Authority pers. comm.). The broadcasts by this and other stations do not, in general, appear to be the dominant cause of the poor radar wind data quality since there is no correspondence between the broadcast schedule and the radar wind data quality. Sporadic periods of interference due to marine transmissions from fishing boats operating off the Canterbury coast also occur (Fraser pers. comm.) but these do not account for the significant level of RF noise.

A proportion of the fluctuations will also be due to the uncertainty in the sampling of the diffraction pattern by the aerial array. For the Birdlings Flat radar, the number of independent points obtained at each sampled height during every 82 second run is about 60 to 80.

### 5.6.2 Wind Data Autocorrelations

In order to quantify the level of correlation in the radar and optical wind data, the auto-correlation functions of the hourly mean winds were derived. The auto-correlation function describes the level of correlation of a data series as a function of time lag. Each radar time series consisted of 24 hourly mean wind values although, in keeping with the optical winds, only the night time hourly mean wind values were auto-correlated. On some nights there were a large number of gaps, especially below 90 km. The number of gaps decreased with increasing height. The gaps were not used during the calculation of the correlation coefficient at each lag. The correlation of the winds over 12 hours, corresponding to the semi-diurnal tidal variation, could therefore not be ascertained by this method because of the short night-time data length but it did provide an indication of the level of short-period (1-2 hours) coherence in the radar winds. The entire number of points in the time-series were used in the calculation of the auto-correlation function as described in Jenkins and Watt (1968).

Figure 5.5 shows the auto-correlograms for the night time optical and radar hourly mean winds at 95 and 100 km for 4 March 1994 and these are typical of the data set. Because

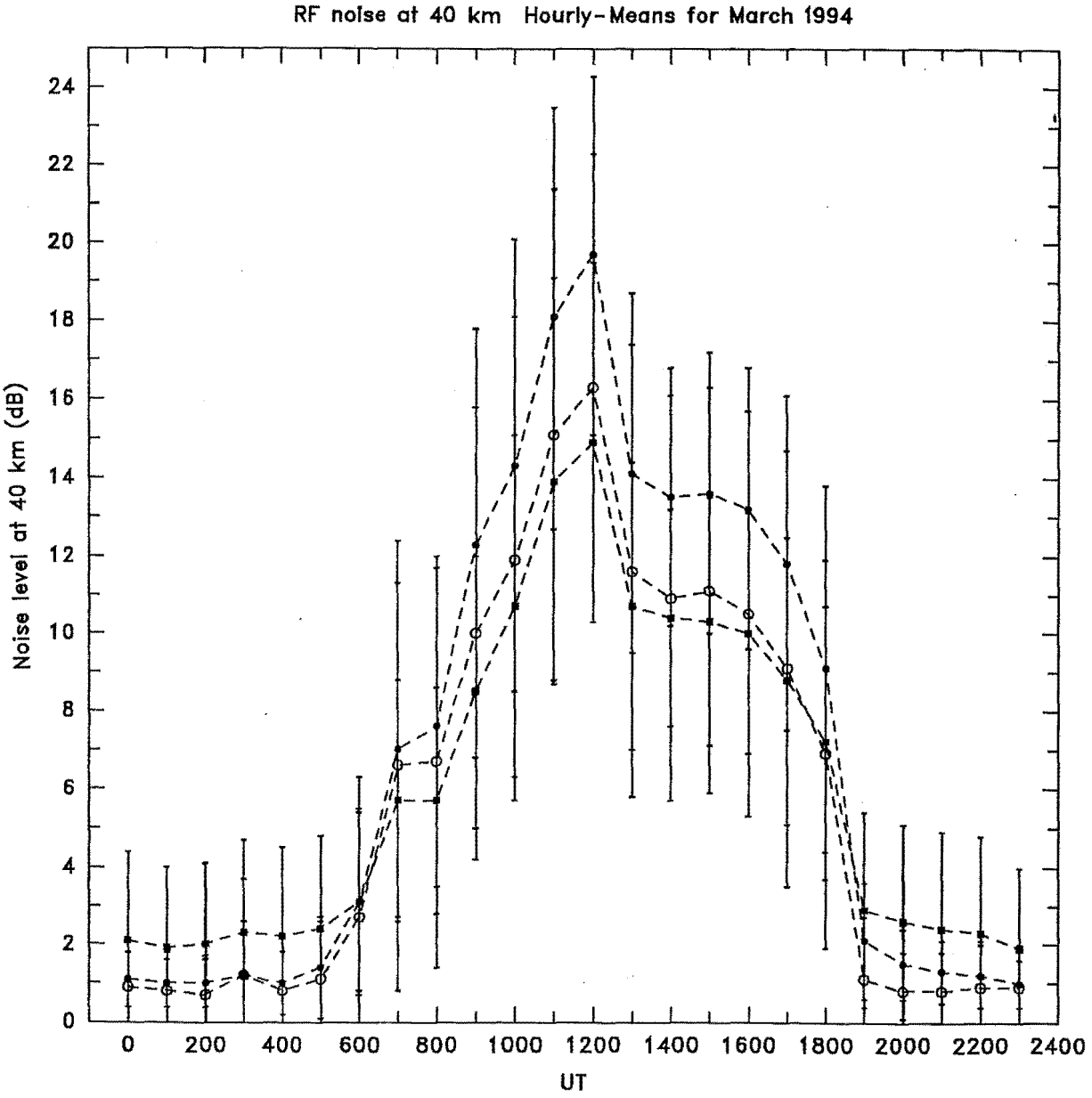


Figure 5.4: The diurnal variation in the hourly mean values of N40 for March 1994. The dark circles, open circles and closed squares correspond to receivers 1 to 3 (RX-1 to RX-3), respectively. The error bars are the standard deviations of the mean values.

of the short length of the optical time series only three hourly time lags were calculated. The dashed lines are the 95% confidence intervals of the auto-correlation function. The most noticeable feature of the radar wind auto-correlograms is the large peak or spike at zero lag. The function then rapidly falls to zero at a time lag of one hour. This indicates that the majority of power in the hourly mean radar wind time series is associated with uncorrelated high-frequency fluctuations with periods of less than one hour. The nature of these fluctuations is mainly due to RF noise and interference, which completely dominates the radar winds on such time scales. Typically, there is essentially no correlation exhibited in the radar winds on time scales of one hour or more.

The form of the FPS auto-correlograms is clearly quite different from those of the radar winds. The auto-correlation functions for both the zonal and meridional components fall to a value of zero at 2–3 hours indicating that the level of correlation in the FPS winds is much higher than in the radar winds. The auto-correlation function of a sinusoid variation, such as a single mode tidal oscillation is a cosine function of the time lag. The auto-correlation function of a 12-hour sinusoid variation, for example, would be zero-valued at a time lag of $\pm 3$ hours.

The night time hourly mean optical winds typically exhibited correlation from hour to hour which was statistically significant at better than the 95% confidence level for virtually all of the zonal and meridional winds. This was also evident from a simple visual inspection of the optical winds themselves which exhibit much less scatter than the corresponding radar winds. The lack of continuous 24-hour data was a limitation to the analysis of the optical wind data. Because of the short time series of the optical winds a value for each auto-correlation function at a lag of 12 hours was not possible. Also the auto-correlation of hourly mean optical wind data from consecutive nights by concatenation was also not possible because of the absence of day time optical wind data. However, it is clear the individual optical winds exhibit a much higher S/N than the corresponding radar winds. Such a large difference in the coherence between the optical and radar data sets makes the comparisons between the two methods difficult.

Figure 5.6 shows the auto-correlograms of the combined day and night time hourly mean radar winds for the entire month of October 1993 at $95 \pm 2$ km. Similar to the auto-correlograms of the daily hourly mean winds, there is a large peak at zero lag in both wind components indicating that the radar winds are dominated by fluctuations with time scales of less than one hour. Both components exhibit correlation over only 1 hour which is statistically significant at the 95% level. This is higher than exhibited in the hourly mean winds of a single night and so, on time scales of one month, the effect of the RF noise on the radar winds is reduced. One reason for this is the increased number of hourly mean wind values. The individual night time auto-correlograms in Figure 5.5 are derived from 10 hourly mean wind

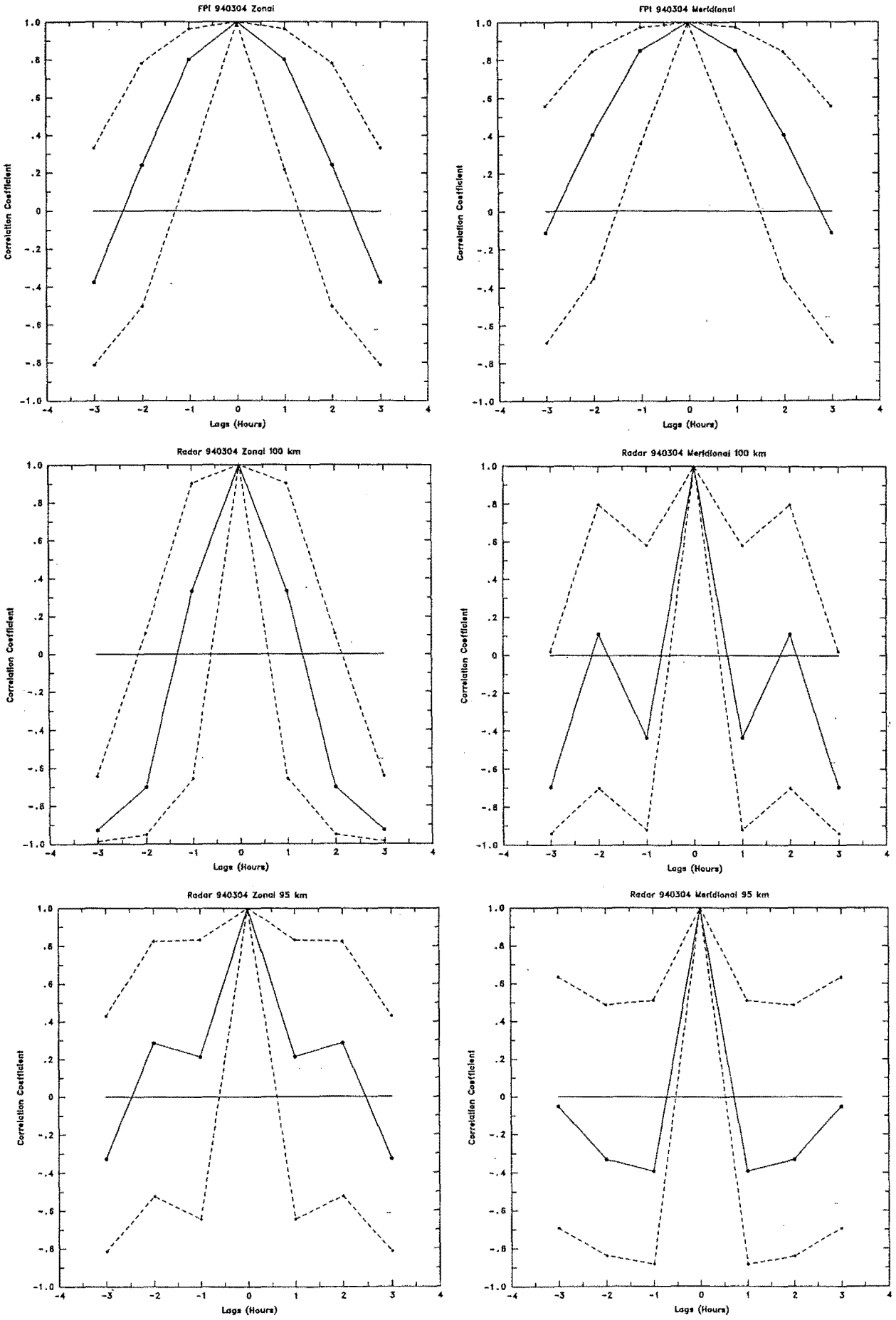


Figure 5.5: Auto-correlation functions of night time optical and radar hourly mean winds at 95 and 100 km for 4 March 1994. There are clearly distinct differences in the time scales of each wind set with the radar winds exhibiting a large amount of power associated with uncorrelated short-period wind fluctuations with periods of less than one hour.

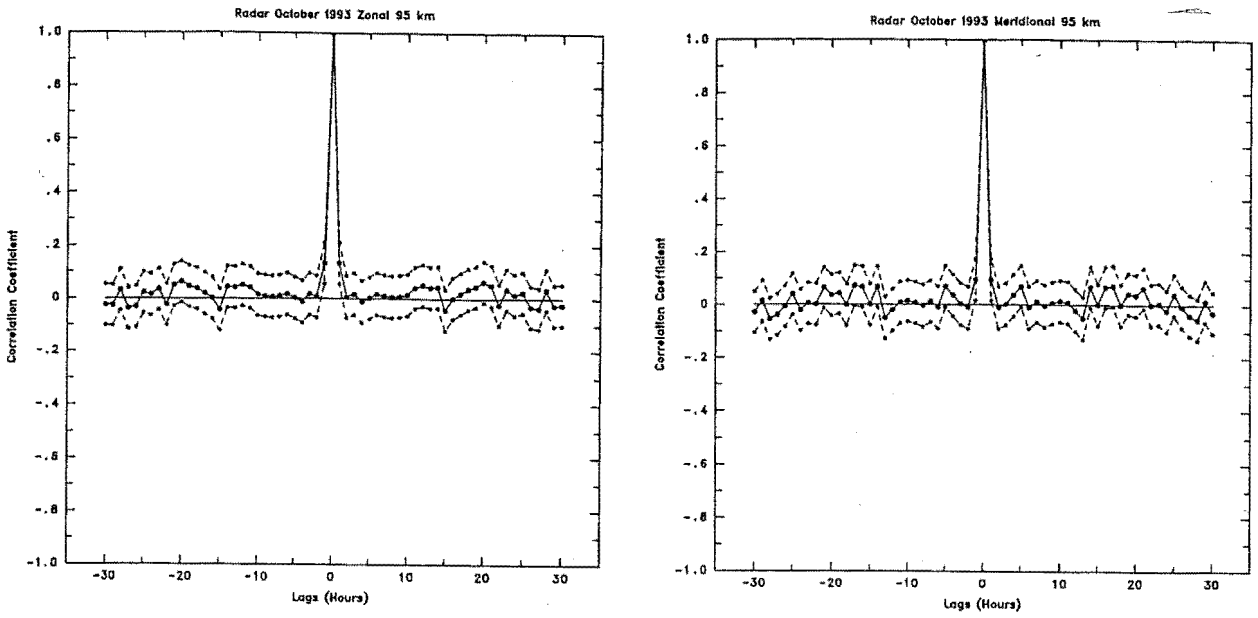


Figure 5.6: Auto-correlation function of daily hourly mean radar winds for October 1993 at 95±2 km. The large spike due to the presence of uncorrelated high-frequency noise dominates the autocorrelation function. The 95% confidence bands are also shown.

values whereas the auto-correlograms in Figure 5.6 are derived from 31 consecutive days of hourly mean values. There does not appear to be any statistically significant (to the 95% level) signal near 12 or 24 hours which would correspond to the semi-diurnal and diurnal tides in the correlograms in Figure 5.6. Hence, even on time-scales of days the effect of RF noise/interference severely limits the optical/radar comparisons. The high-frequency (T<1 hour) fluctuations exhibited in the auto-correlation functions dominate the radar winds and are clearly the greatest limitation in the optical/radar wind comparisons.

The S/N power ratio can be estimated from the auto-correlograms by measuring the ratio of the interpolated value of the auto-correlation function at zero lag to the spike less the interpolated value (Goldstein, 1951). The S/N power ratio of the monthly radar wind data for October 1993 in Figure 5.6 is clearly less than 5%. The S/N of the hourly mean radar wind data for the individual nights on which Figure 5.5 is based, also appears to be very small. Hence, the high-frequency noise dominates the signal on time-scales ranging from hours to weeks, making radar/optical wind comparisons difficult.

Despite the high level of RF noise and interference we know *a priori* that a 12-hour tidal variation must occur in the radar wind data. The diurnal variation in radar echo signal strength and noise power results in missing hourly data, especially during the night. There are three ways of dealing with the problem of missing data:

1. The data may be least-squares fitted to individual frequencies (Bloomfield 1976).

2. The power spectrum of the data can be obtained by calculating the auto-correlation

function with missing data points ignored (Chatfield 1983).

3. Linear interpolation may be applied to the original time series (Hamming 1989).

Procedure (1) was performed on each entire month's individual hourly mean radar winds using an algorithm written by Dr. G.J. Fraser (Fraser pers. comm.). This algorithm also subjected the hourly mean radar winds to a low pass filter of varying bandwidth. Auto-correlograms were produced of the winds subjected to the filtering process and these were compared with those obtained via the same procedure but applied to the randomly-generated wind data (procedure 2). The algorithm for procedure (2) was written by the author. Both procedures (1) and (2) involved several steps:

1. The individual hourly mean winds were calculated from the raw wind data to give a time series of hourly means.

2. The mean value of this time series was subtracted from the individual hourly mean winds.

3. A least-squares fit was then applied to the hourly mean data by varying the frequency in steps from the fundamental through to the Nyquist frequency.

4. A low–pass filter with a cosine taper was then applied in the frequency domain to the results of step 3.

5. The radar winds were then reconstructed from the filtered results of step 4 by using a Fourier series.

6. Using the results of step 5, the auto-correlation function was calculated.

The cosine filter taper boundaries were varied over the frequency region of interest. Random wind data, having a mean and standard deviation the same as the original radar wind data, was generated using a random number generator algorithm (Press et al. 1992). This data was then subjected to the same procedure as the radar wind data. Both sets of data were of the same length.

Auto-correlograms of the October 1993 radar winds at 95±2 km, which were reconstructed from the fit parameters, are shown in the left-hand side panels of Figure 5.7 for various filter pass-bands. Auto-correlograms of the random wind data are shown in the right-hand side panel of Figure 5.7 for the same filter pass-bands. The start and cutoff frequencies of the cosine taper shown here are (top to bottom) 3–12, 2–4 and 1.5–2.4 cycles $day^{-1}$, respectively. These correspond to oscillation periods of (top to bottom) 8–2, 12–6 and 16–10 hours, respectively.

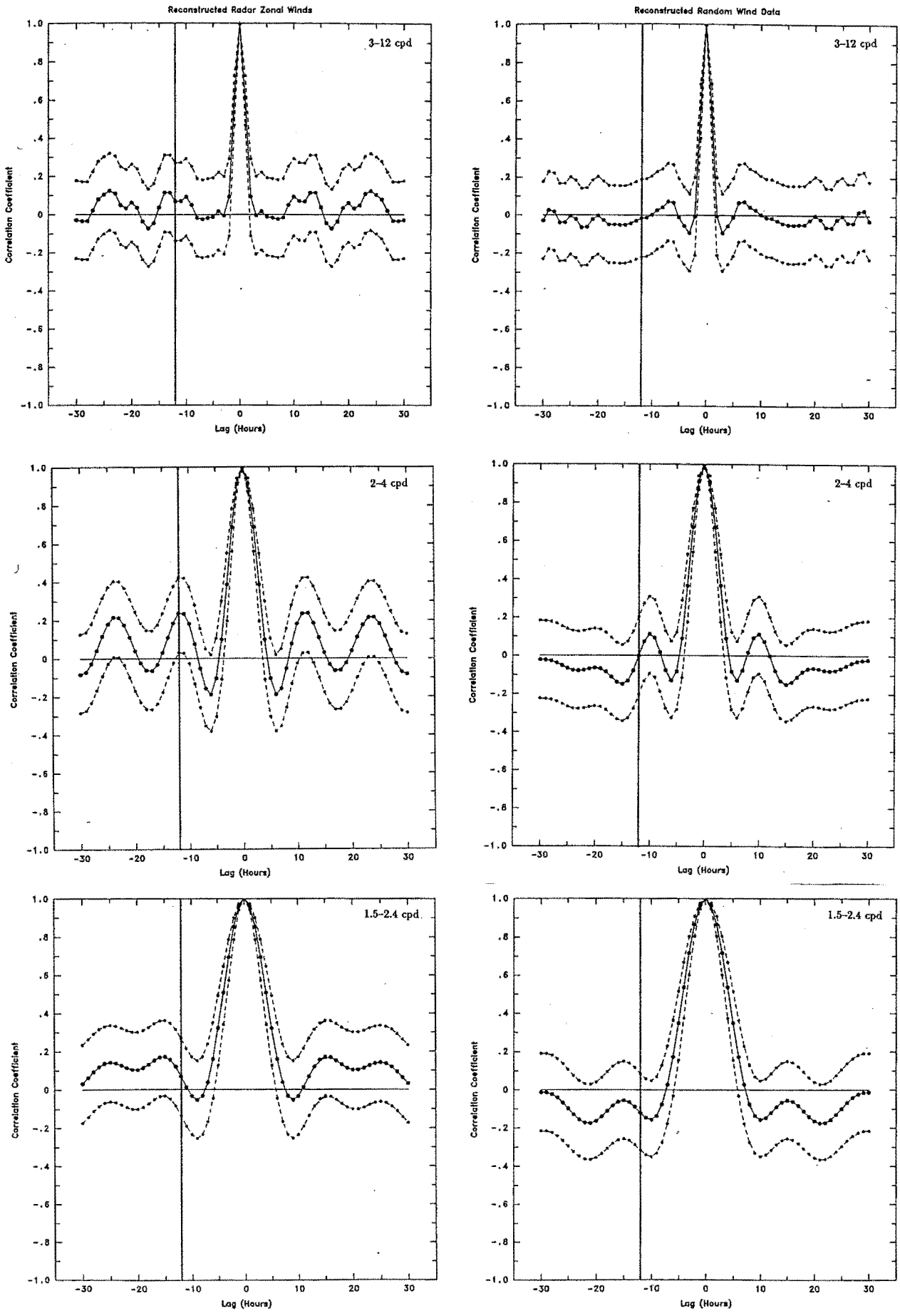


Figure 5.7: Auto-correlation functions of the reconstructed filtered zonal hourly mean radar winds at 95±2 km for October 1993 and of randomly-generated data for various filter pass-bands with a cosine taper of (start–cutoff) 3–12, 2–4 and 1.5–2.4 cycles day$^{-1}$ (top to bottom). The solid vertical bars correspond to a period of 12 hours.

In the top panels of Figure 5.7, there is no statistically significant 12-hour variation in the radar winds (left-hand panel) or the random data (right-hand panel). The correlation coefficients at 12 lags are +0.07 and -0.02, respectively, both are not statistically significant to the 95% confidence level.

There is evidence of a 12-hour variation in the middle panel of the October 1993 radar wind auto-correlogram. At 12 hours, the correlation coefficient is +0.24 and it is barely statistically significant to the 95% confidence level. In the corresponding random data auto-correlogram (middle-panel, right-hand-side), at 12 hours the correlation coefficient is 0.0. The S/N of the of the 12-hour signal in the radar data in the middle panel of Figure 5.7 is 0.30 (-5.0 dB). The auto-correlogram was derived from 744 hourly wind values. The central peak indicates a correlation which is statistically significant at the 95% level. The number of independent points can be deduced from the filtered spectrum. Each sampled frequency has 2 degrees of freedom; the phase and amplitude. From 0 to 12 cpd (the Nyquist frequency) the number of sampled frequencies is 360. In the middle panels of Figure 5.7, the filter passband allowed frequencies from 0 to 3 cpd, which is 1/4 of the total number of sampled frequencies. The number of independent points is therefore $360/4 = 90$.

There is no evidence of a 12-hour variation in the bottom-most panels of Figure 5.7 in both data sets. At 12 hours, the correlation coefficient corresponding to the radar winds is +0.07 and it is not statistically significant. The correlation coefficient corresponding to the random data is -0.12 and also also not significant. This is because the filter pass band cuts off at 10 hours and so some of the spectral power corresponding to a 12-hour period has been removed.

These plots indicate that the semi-diurnal tidal variation is present in the radar wind data but that it is dominated by the presence of large amounts of scatter due to RF noise and interference.

### 5.6.3 Optical/Radar Wind Variances

One notable feature of the FPS wind fields is that they usually exhibit a smooth variation with a 12-hour period, presumably the semi-diurnal tide, with little or no evidence of short-period wind variations (T$\sim$1–6 hours). This apparent lack of short-period variations is puzzling because there is a large body of literature reporting the presence of gravity waves in MALT radar wind measurements (Vincent and Stubbs 1977, Vincent and Reid 1983, Vincent 1984a, 1984b, Manson et al. 1979, Meek et al. 1985, Vincent and Fritts, for example).

The optical and radar techniques average over nearly similar vertical heights, $\sim$10 km and $\sim$5 km, respectively; therefore if gravity wave activity is a significant factor, then there should be little difference in the hourly variances between the raw FPS and radar winds.

An attempt was made to use the hourly variances of the raw FPS and radar winds as an estimate of the scatter of the radar winds within each hourly period. There were 1085 possible FPS-simultaneous hours. Both data sets have low numbers (only ~1–2) of raw wind values during each hour at night so the analysis of such hourly variance values would be incorrect.

The large variances associated with the hourly radar winds compared to the optical winds is mainly due to RF noise and interference. Gravity wave activity is also expected to contribute to the variance of the radar winds observed in the MALT region (Fritts 1984, 1985, 1990, Fritts and Rastogi 1985, Meek et al. 1985). MF radar observations in the southern hemisphere indicate that the mean square variance of wind variations with periods between 1–8 hours at a height of 95 km is ~600–800 $m^2s^{-2}$ (Vincent and Fritts 1987).

The lack of short-period variations in the optical winds is possibly due to the observing geometry of the FPS measurements. The observing geometry of the FPS will place a lower limit on the horizontal and vertical resolution available from the FPS measurements, as well as place a lower limit on the temporal resolution.

The FPS obliquely samples a 30-km long, 3.2 km diameter pencil of emission along the line of sight. The FPS spatially averages the emission measurements because of the vertical thickness (FWHM intensity of ~10–12 km) (Shepherd et al. 1995) of the emission layer and the observational geometry employed by the method. Wind oscillations with vertical wavelengths of the order of 15–20 km would effectively be filtered out because the measured FPS wind is a weighted mean of the vertical emission profile. The amplitudes of wind oscillations with vertical wavelengths comparable in size to the vertical emission profile will be considerably reduced.

The vertical wavelengths of gravity waves in the MALT have been reported by several workers. Vincent (1984a) found from partial reflection radar measurements at Adelaide (35°S) that gravity wave activity at 85 km had vertical wavelengths which ranged from 5–30 km with an average of about 12 km. The horizontal wavelengths ranged from 50–4000 km. Manson et al. (1979) reported the mean vertical wavelength associated with gravity wave activity to be ~20 km. Similarly, Meek et al. (1985) reported vertical wavelengths predominately in the 3–25 km range at heights of 80–110 km. These results indicate that the vertical wavelengths associated with gravity waves occurring in the 95–100 km region are less than or comparable to the vertical distance over which the FPS samples the 557.7 nm emission. It is therefore possible that much gravity wave activity in the MALT is not detectable by the FPS measurements.

These results indicate that the vertical wavelengths associated with gravity waves occurring in the 95–100 km region are less than or comparable to the vertical distance over which the FPS samples the 557.7 nm emission and so such variations are considerably reduced.

The vertical wavelength of the semi-diurnal tide is usually greater than 25 km and so is easily observed in the FPS winds. Hernandez et al. (1995) studied the FPS winds derived from two independent emission layers at 89 and 95 km above Mt. John and deduced vertical wavelengths of mainly 30–50 km for the semi-diurnal tide during the year.

The zonal (meridional) FPS wind fields were obtained by combining the opposite east and west (north and south) winds for each night. The sampled airglow volumes for two opposite directions, eg. north and south, are separated by ~500 km. This further spatially averages the optical wind fields. In order to do this it was assumed that there was little or no velocity gradient across the sky between the two opposing directions. Since the semi-diurnal tide was the dominant feature of the raw FPS winds and because this oscillation possessed a horizontal scale size which was much larger than the diameter of the observing area such an assumption could be used to a first approximation. In Section 6.3, it is shown that there was little difference in the behaviour between the zonal and east-looking optical winds and so this assumption, to the first approximation, can be made. The time resolution in the combined east/west optical winds is effectively halved compared to the east-looking optical winds.

Wind oscillations with horizontal wavelengths equal to diameter of the observing area (~500 km) would be selectively detected. Wavelengths of smaller scale-sizes would tend to produce differences in the measured wind between opposite observing directions due to aliasing of the wave. The differences in the optical wind between opposite directions was typically smaller than the uncertainty of the wind values (~10–15 $ms^{-1}$).

The instruments essentially shared a common sampling volume when the FPS observed in the direction of Birdlings Flat with only a 60–70 km separation (Figure 3.3). Differences in the wind field due to this small separation were expected to be negligible considering the 500-km diameter of the FPS observing area. The spatial averaging due to the radar measurements was different in nature to that employed by the FPS. The radar vertically probes a horizontal elliptical area approximately 48 km by 37 km aligned in the east-west direction. This area was much smaller than the dimensions enclosing the FPS observing cycle but was larger than the area sampled by each individual FPS measurement.

Different amounts of temporal averaging were employed by the two instruments. The sampling time for each FPS measurement was about 12 minutes compared to about 80 seconds for a radar measurement, a factor of 9, and ~60 minutes were required for an entire FPS observing cycle. The precise amount of time could vary because it was dependent upon the intrinsic intensity of the airglow emission. FPS measurements obtained from opposite directions can be separated by about 30 minutes in time and so wind variations with periods comparable to or less than this will not be observed by the FPS except as variance in the winds. Therefore, wind oscillations with periods of ~60 minutes or less would not be detected by the FPS measurements, but would still contribute to the FPS wind variance.

The results of several MALT wind studies indicate that the periods of the majority of gravity waves occurring in the 95–100 km region are less than ~1 hour. Meek and Manson (1983) reported intensity variations of 5–10% with periods of 15–20 minutes superimposed on variations with periods of several hours and the former variations were attributed to gravity waves propagating through the emission layer and producing the intensity fluctuations (Meek and Manson 1983). Intensity variations of 5–10% were also reported by Freund and Jacka (1979). These exhibited period of tens of minutes and were also attributed to gravity wave activity. Direct imaging of the emission by Armstrong (1982, 1986), Taylor et al. (1987, 1988, 1990, 1991, 1993) and Taylor and Garcia (1995) has produced similar results, but unlike the measurements of Freund and Jacka (1979) and Meek and Manson (1983), these imaging studies were similar to the FPS method in this project in that the 557.7 nm emission was obliquely sampled.

During the nights of 8–9 February, 1995, FPS measurements at Mt. John were made exclusively towards the east and zenith, in order to increase the time resolution of the FPS wind measurements. High magnetic activity and heavy cloud during each night however, prevented any conclusions being made about the presence of short-period (T~1–8 hours) wind variations during these nights.

There is strong observational evidence that the specific technique of measurement of the 557.7 nm emission has an important bearing on the interpretation of the wind velocity measurements. Freund and Jacka (1979) compared drift motions derived from 557.7 nm emission observations using a four-field photometer with simultaneous Doppler winds from FPS 557.7 nm emission observations. The FPS measures Doppler shifts of the neutral OI emission which directly indicates line-of-sight motion of the emitting gas. The photometer had a field of view of $5^o$ and the three sampling spots formed an equilateral triangle with sides 13 km in length at 95 km. Cross-spectral analysis was performed on the three sets of 557.7 nm intensity variations and a drift velocity was inferred from the temporal intensity variations across the photometer field of view.

The FPS wind vectors exhibited an anti-clockwise rotation during the each night which was consistent with neutral wind motion under the influence of a semi-diurnal tide. The photometric drift velocities did not exhibit this temporal behaviour but tended to be larger in magnitude and remain in one general direction, southwards, throughout the night. It was concluded that these were the result of gravity wave propagation through the layer causing intensity fluctuations within the emission layer (Freund and Jacka 1979).

Meek and Manson (1983) measured horizontal motions of 557.7 nm intensity fluctuations with a scanning field photometer and these were compared to simultaneously obtained MF radar winds. A similar study was made by Bruce et al. (1992) using a three-field photometer. In both studies the photometer drifts tended to move in the same general direction

during the night, which is similar to that found by Freund and Jacka (1979) (Meek and Manson 1983, Bruce et al. 1992). The radar wind vectors were seen in both studies to exhibit a rotation during the nights which is consistent with the behaviour of the semi-diurnal tide. It was concluded that the 557.7 nm emission drifts were due to the phase-front motion of gravity waves propagating through the emission layer and that the winds derived from the spaced-antenna radar measurements were due to the bulk motion of the neutral wind (Meek and Manson 1983, Bruce et al. 1992).

The FPS Doppler shift measurements measure the bulk physical motions of the emitters. The temporal airglow observations of intensity variations tend to detect wavefront motion. The spaced-antenna radar measurements also measure the bulk motion of the neutral air. The difference between the intensity and radar spaced-sensor measurements is that the partial-reflection radar echoes originate from regions of turbulence which move along closely with the neutral air motion (Hines 1991), as discussed in Chapter 4. The intensity variations arise from propagating gravity wave perturbations within the medium which alter the emission rate.

## 5.7 Optical/Radar Comparative Analysis

### 5.7.1 Cross-Correlation Analysis

One method used to compare the optical and radar winds was by cross-correlating the simultaneous radar and optical night time hourly mean winds. This method does not assume that any particular variation, tidal or otherwise, is present in the hourly mean wind data. Three pairs of wind components were cross-correlated: (i) the radar and optical zonal winds (zonal) (ii) the radar and optical meridional winds (meridional) and (iii) the radar zonal and the east-looking optical winds. The last comparison was made because when the FPS was looking towards the east it sampled a similar volume region to the radar above Birdlings Flat (~60 km separation). Because only night time winds were used any possible effect on the radar wind heights above 95–100 km due to pulse retardation (Fraser and Kochanski 1970; Namboothiri et al. 1993) was negligible.

The optical hourly mean winds were cross-correlated at zero time lag with the radar hourly mean winds at each height from 80 to 105 km. The correlation coefficients were then arranged as a function of height to produce a height-correlogram. A typical height-correlogram is shown in Figure 5.8 for the night time FPS/radar winds on 13 May 1994. The dashed lines indicate the 95% confidence level. The large width of the limits reflects the relatively small number of wind values available for the correlation. There is a large negative correlation between the optical and radar zonal winds above 97 km. The reason for

this behaviour is not clear and is not observed in the meridional correlogram where a weak significant positive correlation is apparent near 93 km, which is consistent with the 557.7 nm emission height results reported by Hernandez et al. (1995). A large negative correlation is also exhibited in the meridional winds below 88 km.

The number of available optical/radar night time wind pairs used in the correlation ranged from 4 to 14 and was dependent on the length of FPS night time conditions and on the availability of hourly mean radar wind values (fewer radar winds at lower heights).

The mean values calculated from each time-series were not subtracted during the correlation calculation in order to account for any variation in the mean wind flow of the radar winds with height. Otherwise the level of correlation would merely be determined by the phase and amplitude of the tidal variations.

The correlations were equally-weighted (see Section 5.2). Figure 5.9 is the height-correlogram for the night time winds in Figure 5.8, but in which the correlation was weighted by the sample variances associated with the optical and radar hourly mean winds. The large negative correlation above 97 km between the zonal optical and radar winds is still apparent but there is no significant positive correlation between the meridional optical and radar winds near 93 km which was observed in Figure 5.8. The effect of the RF noise and interference on the correlation coefficients is clearly evident with large and sudden variations in the correlation with height such as in the meridional correlogram at 99 km of Figure 5.9.

### 5.7.2 Comparisons Using the Semi-Diurnal Tide

Several comprehensive radar wind studies at Birdlings Flat and other sites (Smith 1981, Manson et al. 1979, 1981, 1985, 1988, 1989, 1990, Meek and Manson 1985, Franke and Thorsen 1993, Stening et al. 1995) indicate that the semi-diurnal tide is the dominant tidal variation in the 80–100 km region at mid-latitudes. This is also found from optical 557.7 nm wind studies at mid-latitudes (Hernandez and Roper 1979, Lloyd et al. 1990, Manson et al. 1991, Phillips et al. 1994, Fauliot et al. 1995, Hernandez et al. 1995) and supported by theoretical studies (Chapman and Lindzen 1970, Lindzen 1979, Forbes and Garret 1979, Forbes 1982b). In particular, Hernandez et al. (1995) explicitly showed that the dominant variation exhibited in the 557.7 nm Doppler emission winds above Mt. John, New Zealand has a period of 12 hours. The diurnal tide generally occurs less regularly and exhibits smaller spectral power (Smith 1981, Manson et al. 1985, 1989b).

A quantitative measure of the variations in the FPS and radar wind data was obtained by fitting the data to a function consisting of a constant and a sinusoidal function using singular value decomposition algorithm (Press et al. 1992). The raw FPS wind data were least-squares fitted to a sinusoid of unknown amplitude and phase and a period of 12

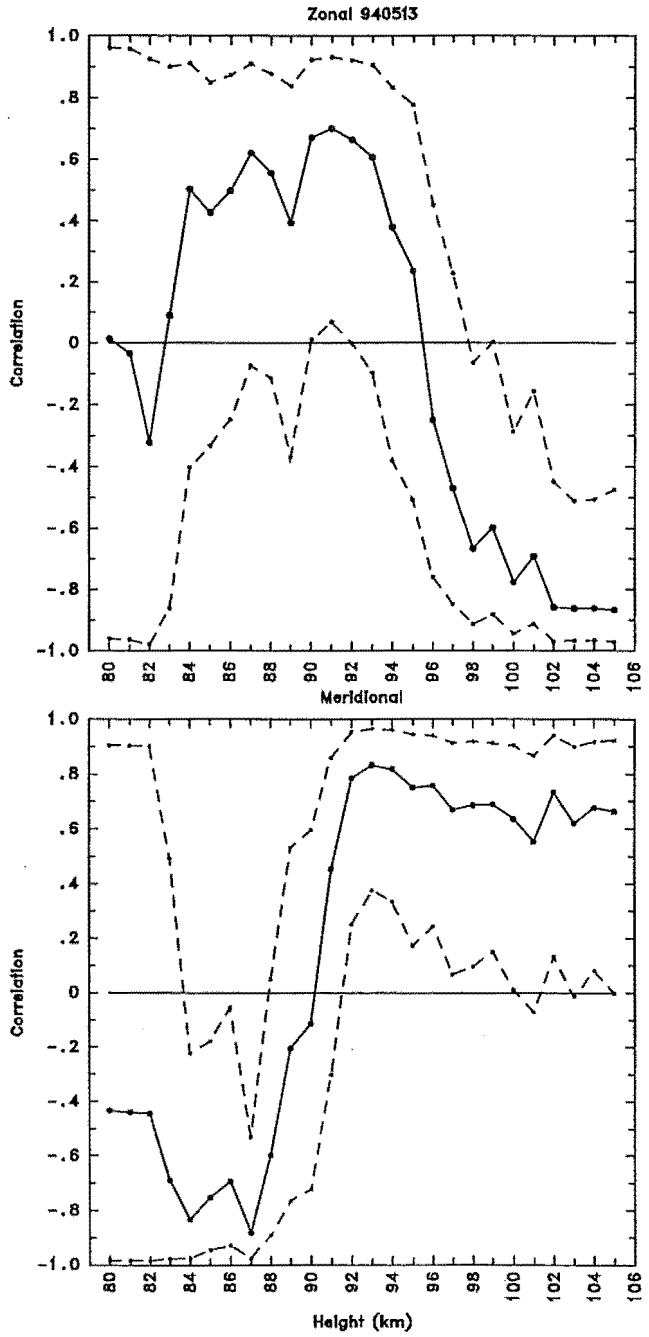


Figure 5.8: The height correlogram for the night of 13 May 1994. The dashed lines indicate the 95% level of the correlation. There is a significant negative correlation between the zonal optical and radar winds above 97 km.

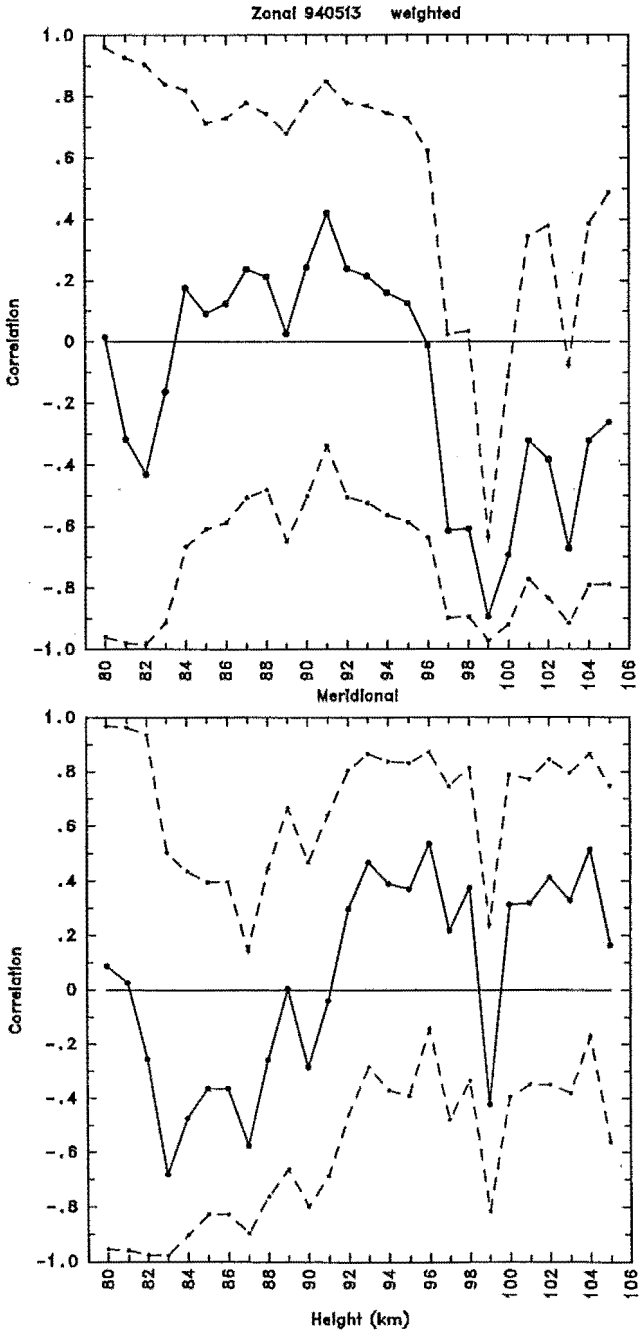


Figure 5.9: Height correlograms for the night of 13 May 1994 which were obtained by weighting by the associated uncertainties of the optical and radar winds. The effect of the noise on the weighting procedure is clearly evident.

hours. The exclusively night time operation of the FPS precluded the possibility of obtaining information about the phase and amplitude of the diurnal tide from the FPS wind data. If the amplitude of the diurnal tide was comparable to that of the semi-diurnal tide then the fitted values of the 12-hour amplitude and phase would be erroneous because the FPS wind field does not contain a full diurnal cycle. The fitted mean wind value would also be erroneous for the same reason. Hines (1966) described a method involving vector decomposition which enabled an estimate of the amplitude and phase of the diurnal tide to be obtained from wind data of at least 12 hours in length.

There were at least 12 hours of wind data on the nights during the months of April to August centred on winter. About 55% of the 103 nights had 12 or more hours of data. During the summer months, there was less than 12 hours of available nightly wind data. Hernandez et al. (1995) determined that the 12-hour wind oscillation present the winter months in the Mt. John FPS wind fields was also present during the summer months.

A weighted fit was made of the raw FPS winds for each night, the weighting according to the uncertainties of the raw wind values. Similarly, a weighted fit was performed on the hourly mean FPS winds using the uncertainties of the hourly mean winds. The differences between the values of the fit parameters for the raw wind fits and the hourly mean wind fits were less than or comparable to the uncertainties of the fit parameters. The weighted raw FPS wind fits were used for the optical/radar wind comparison.

The results of the auto-correlograms of month-long hourly mean radar wind time-series indicate that a 12-hour tidal oscillation is present in the radar winds, despite the presence of RF noise/interference. The daily hourly mean radar winds consisting of 24 hours centred on the FPS night were least-squares fitted with a 12- and 24-hour sinusoid of unknown amplitude, phase and mean.

Forbes (1985) recommended that, in order to make meaningful comparisons, tidal parameters should be derived from radar wind measurements which have been averaged over a least 6 days. This present project is concerned with the comparison of simultaneous optical and radar winds and, for this reason, necessitated making tidal measurements using low S/N radar winds consisting of only 24-hour long measurements.

The high level of RF noise and interference and the paucity of night time wind values, necessitated the use of the daytime, as well as the night, winds in the fitting procedure. The raw radar winds were not used for the fitting because there were greater numbers of raw wind values during the daytime and this would bias an equally-weighted fit (since the uncertainties of noise-free raw radar winds measurements were unknown) towards the daytime wind values, which was considered undesirable. An estimate of the amplitude of the diurnal tide could also be obtained by this method.

The radar wind least squares fits were obtained by equally weighting the hourly

mean radar winds. Weighting the fit according to the individual sample variances of the hourly mean radar winds resulted in clearly erroneous fit parameters and also the radar wind height profiles contained large variations in the fitted mean, amplitude and phase values over height intervals of 1–2 km, less than the 5-km binning interval. The lack of consistency at adjacent heights resulted from the large amount of RF noise and interference associated with the radar wind data which produced large and variable hourly sample variance values which grossly affected the tidal fits of the radar winds.

Wind values greater than $2\sigma$ away from the mean fit, called outliers, were not used in the fit. Such outliers, in some cases, grossly affected the reliability of the fit. Outliers were removed from the raw optical winds after an initial fit and a subsequent weighted fit was made. The occurrence of outliers in the raw optical winds was not frequent. If the reason for outliers were due to some mechanism other than cloud, such as a horizontal wind gradient across the observing area, then one would expect to observe the behaviour in both pairs of opposite-direction measurements (east-west or north-south) which was not generally the case.

Outliers were removed after an initial equally-weighted fit of the hourly mean radar winds and then a second fit was made. The second fit was weighted according to the sample standard deviations of the remaining hourly mean wind values. However the resulting second fit was frequently significantly different from the first fit to such a degree that new outliers would appear in the second fit or, more commonly, the outliers discarded from the first fit would now not be outliers if they had remained and used in the second fit (The first fit however would not have been obtained had these outliers remained). The fit parameters generally exhibited large changes over height intervals of 1–2 km so there was sometimes little internal consistency. By equally-weighting both the first and second fits any variations in the fit parameters with height were self-consistent with generally no large changes occurring within the 5-km binning interval.

The fit uncertainties were obtained from the diagonal elements of the covariance matrix which are the variances of the fitted parameters. The fit uncertainties in phase, amplitude and the mean wind for the FPS zonal and meridional winds were much smaller than for the radar winds and were typically 0.1 hours, 1.0 $ms^{-1}$ and 3.0 $ms^{-1}$ in phase, amplitude and the mean wind, respectively. For the FPS winds in the east observing direction the uncertainties were typically 0.2 hours, 1.5 $ms^{-1}$ and 4.2 $ms^{-1}$, respectively. The east-looking FPS uncertainties are larger than the zonal FPS uncertainties because during the night there were only approximately half the number of east winds compared to the number of zonal winds, which are the east- and west-looking FPS wind combined.

The radar wind fit uncertainties in phase, amplitude and the mean wind were typically about 0.8 hours, 7.0 $ms^{-1}$ and 12.0 $ms^{-1}$ respectively. These are similar to the results of a study by Smith (1981) of radar winds obtained at Birdlings Flat. He used the method

of linear regression and obtained least squares fit errors of 5–10 $ms^{-1}$ in wind velocity and 0.5–1.5 hours in the phase of the daily semi-diurnal tide.

Modulation from non-tidal frequencies such as variations in the prevailing wind, gravity wave and planetary wave activity will also contribute to the variance of the fit parameters of both the FPS and radar winds.

The goodness-of-fit of both sets of wind data was initially estimated by calculating the chi square ($\chi^2$) value associated with the fit (Bevington and Robinson 1992). The $\chi^2$ value however was not a particularly useful measure because of the large variances associated with the hourly mean radar winds. A more useful estimate of the goodness-of-fit was determined by calculating the correlation of the least squares fit with the original time series.

The number of optical nights for which the correlation of fit was statistically significant to the 95% level or better was 99 (zonal), 89 (meridional) and 89 (east-looking). The nights on which the optical winds exhibited fit correlations which were not significant to the 95% confidence level were those which exhibited wind amplitudes which were small compared to the wind uncertainties themselves (0–10 $ms^{-1}$) or they had a low number of wind values during the night.

The number of radar nights for which the correlation of fit was statistically significant to 95% level or higher was lower at the lower heights; 61 nights (zonal) and 55 nights (meridional) at 85 km and increased to ~85 nights for both components at 90 km or higher. There was no significant difference in the yield of significant fits between the zonal and meridional radar wind components. The nights on which low fit correlations were obtained usually exhibited low numbers of wind values or the hourly wind values exhibited a large amount of scatter from one hour to the next (50-100 $ms^{-1}$).

The results were similar for the radar monthly hourly mean wind fit comparisons. Of the 29 months investigated, the number of optical monthly mean nights for which the correlation of fit was statistically significant to the 95% confidence level or higher was 28 (zonal), 27 (meridional) and 28 (east-looking). For the radar winds, the yield was between 21–27, slightly less than obtained from the optical fits, with no apparent height trend and the yield was similar between the two wind components. There was no apparent trend in the yield of significant fits with increasing height. The effect of averaging several days during each monthly period did not increase the percentage yield of 95% level significance fits from those obtained from the daily fits.

The comparisons of the optical/radar tidal wind fits were only made on those nights for which the correlation of the least squares fits for both data sets was statistically significant at the 95% level or higher (Brooks and Carruthers 1953, Crow et al. 1960).

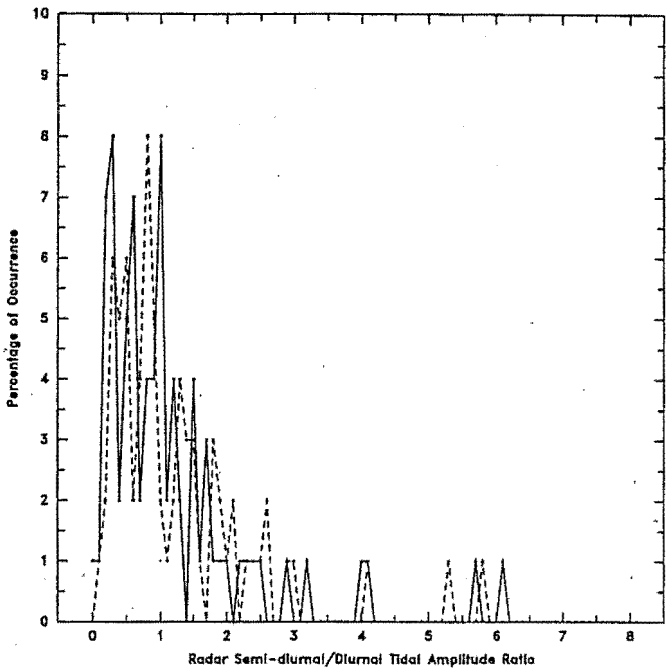


Figure 5.10: The distribution of radar semi-diurnal/diurnal tidal amplitude ratio values at 95 km. The median value is 0.9 for both components (zonal - solid, meridional - dashed) with an associated quartile range of 1.3.

### 5.7.3 The Diurnal Tide

Radar wind measurements indicate that the diurnal tide is generally weaker than the semi-diurnal in the mesosphere but is highly variable (Smith 1981, Manson et al. 1985, 1989b). The frequency distribution of the ratio of the radar amplitudes of the semi-diurnal tide to the diurnal tide was derived at 5-km intervals in the 85–105 km height region. The ratio distributions were characterised by a large narrow peak centered in the 0 to 1.0 region with a weak tail extending to ratio values of 5–6. There was no significant difference between the zonal and meridional amplitude ratio distributions. The medians of the distributions were relatively constant with height in the 85–105 km region, ranging from 0.7 at 85 km to 0.9–1.0 in the 90–105 km. The median differences between heights are probably not significant because the lower and upper quartile values are typically 0.6 and 1.6, respectively. There was no significant seasonal variation in the amplitude ratio of the semi-diurnal and diurnal tide.

The semi-diurnal/diurnal amplitude ratio distributions for the zonal (solid) and meridional (dashed) radar winds at the height of 95 km are shown in Figure 5.10. The medians of the distributions were both 0.9, which infers that the semi-diurnal tidal amplitude was, in general, only slightly larger than the amplitude of the diurnal tide at this height. The lower and upper quartile values were 0.5 and 1.8, respectively.

The presence of a diurnal oscillation would be expected to introduce a modulation into the night time optical wind wind field and, as a result, the semi-diurnal tidal fits would be expected to be poor. However, on the majority of nights (90 to 100), the correlation of the semi-diurnal tidal fits with the hourly optical winds was high. The mean correlation coefficient was 0.86 with a standard deviation of 0.08. These correlations were all statistically significant to the 95% confidence level. Such correlation infers that any modulation of the optical wind field due to a diurnal tide was usually smaller than $\sim$10–15 $ms^{-1}$, the typical uncertainty of the optical wind measurements. There was no significant seasonal variation in the correlation values.

# Chapter 6

# Optical Wind Results

## 6.1 Daily Winds

Figure 6.1 depicts a typical night's neutral winds obtained from the FPS measurements. The wind field is clearly dominated by a variation with a period of about 12 hours which is consistent with the behaviour of the semi-diurnal solar tide. The amplitude of the variation is about 30 $ms^{-1}$ and this varied slightly ($\sim$10 $ms^{-1}$) from night to night. The uncertainty in the raw optical wind values was typically about 10–15 $ms^{-1}$ (see Section 5.4), which is similar to that found by Lloyd et al. (1990), Manson et al. (1991), Hines et al. (1993) and Phillips et al. (1994). The uncertainty was consistent from one night to the next although it ranged from 8–20 $ms^{-1}$ depending on the count rate of the 557.7 nm fringe records.

Harmonic analysis of the wind fields, discussed in Chapter 5, yielded the phase and amplitude of the semi-diurnal tide from each night's raw optical winds together with the mean wind flow. Figure 6.2 shows the annual variation of the semi-diurnal phase and amplitude and the mean wind flow exhibited by the raw zonal and meridional FPS winds during the period of this study. The fit uncertainties in phase, amplitude and the mean wind were derived from the diagonal elements of the covariance matrix during the least-squares fitting procedure (Press et al. 1992). The uncertainties for the zonal and meridional winds were typically 0.1 hours, 1.0 $ms^{-1}$ and 3.0 $ms^{-1}$, respectively. The fit uncertainties in phase, amplitude and the mean wind for the FPS winds in the east-pointing direction were typically 0.2 hours, 1.5 $ms^{-1}$ and 4.2 $ms^{-1}$, respectively. These uncertainties are larger because there were approximately half the number of east winds during the night than zonal winds, which are east and west combined.

There is a very clear seasonal variation in the phase of the semi-diurnal tide (top panels) which varies over a range of about 7 to 8 hours during year. This variation is similar to that reported by Vincent et al. (1988) from radar wind measurements and by Fauliot

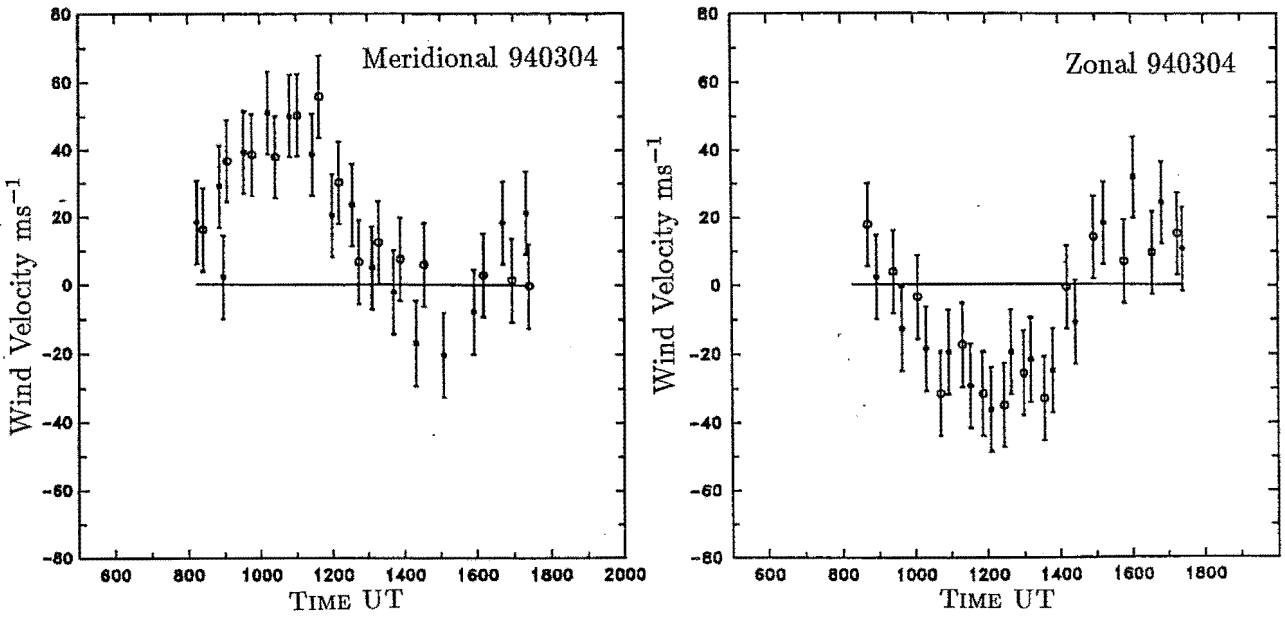


Figure 6.1: The raw optical winds derived from the FPS observations for the night of 4 March, 1994.

et al. (1995) from optical wind measurements, especially the sudden phase increase which occurs 3–4 weeks after the southern autumn equinox (Hernandez et al. 1995). The variation in phase on consecutive days within the same year has been attributed to the daily variability of the semi-diurnal tide as described by Fellous et al. (1974) and Walterscheid (1981).

The zonal winds exhibit a maximum eastward wind at approximately 7 hours UT during autumn. There is a clear transition in the phase of the semi-diurnal tide at about one month after the autumn equinox. During this time, the phase jumps about 2–3 hours from 7 hours UT to about 11 hours UT. During winter, the phase gradually moves from 11 hours UT to 1–2 hours UT at mid-winter. During spring, the phase gradually moves back through to 11 hours UT at the spring equinox. During mid-summer, the phase reaches 9 hours UT. There appears to be no rapid phase transition during the southern spring equinox. This is due to the lack of data during this time (Hernandez pers. comm.)

Similar behaviour is seen in the meridional optical winds. The sudden phase change during autumn is also clearly evident. At the onset of autumn, the meridional winds exhibit a maximum northward wind at approximately 10 hours UT. At approximately one month after the autumn equinox, there is a shift in the semi-diurnal tidal phase of about 2–3 hours to about 0–1 hours UT. During winter, the phase gradually increases to 4 hours UT at mid-winter. During spring, the phase gradually moves back through 1 hours UT at the southern spring equinox. At mid-summer, the phase occurs at about 0 hours UT. As with the zonal winds there appears to be no sudden transition in the tidal phase of the meridional winds during the southern spring equinox.

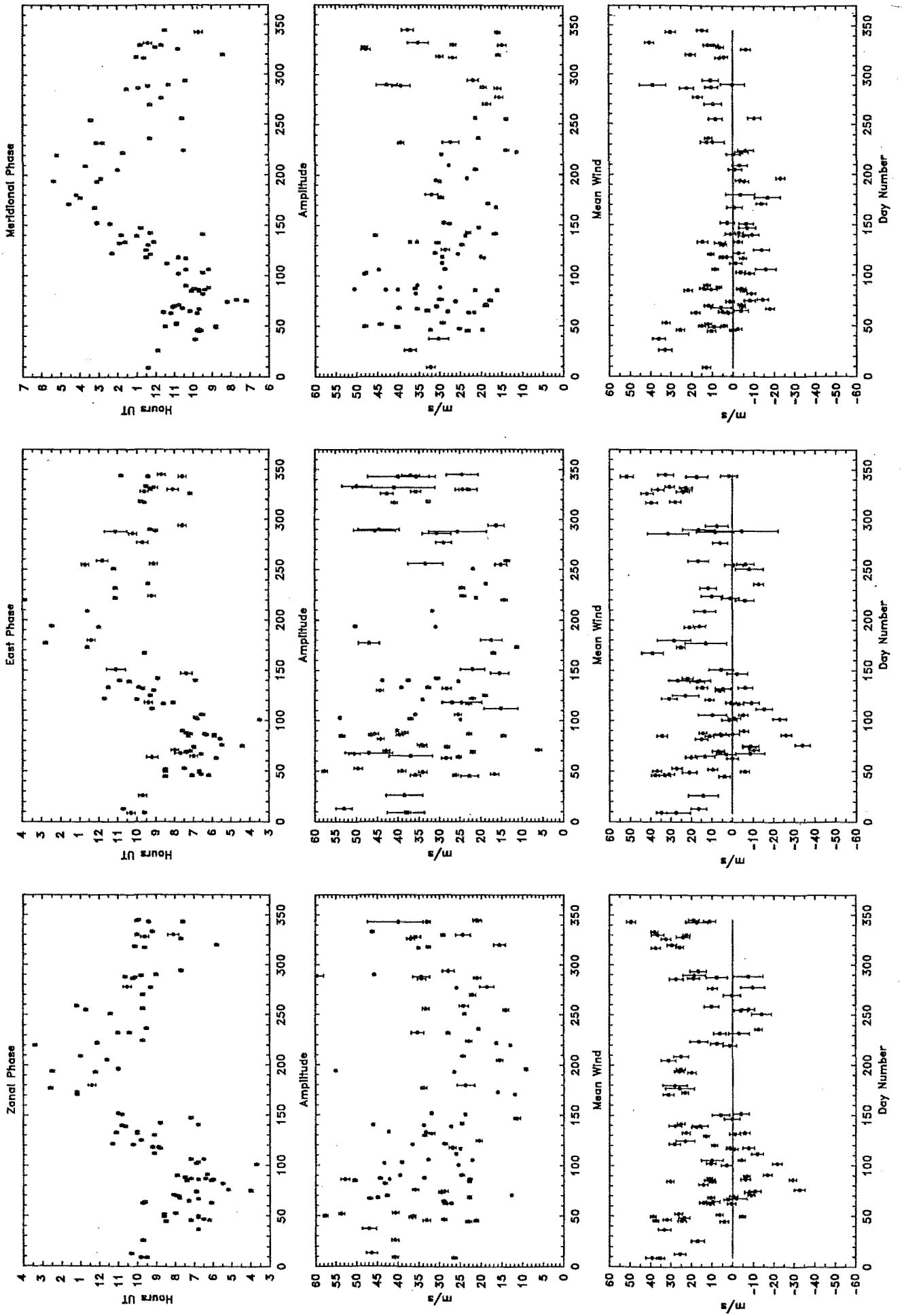


Figure 6.2: The daily semi-diurnal phase, amplitude and mean wind exhibited by the raw zonal and meridional daily FPS winds.

The rate of variation in the phase of the semi-diurnal tide in the optical winds exhibits an asymmetric pattern throughout the year. After the autumn equinox through to winter solstice (~110 days) the phase increases at an average rate of 2.2 hours month$^{-1}$. A subsequent decline in phase at the rate of 1.0 hour month$^{-1}$ then occurs from the time of winter solstice, through the summer solstice, to the southern autumn (~255 days).

The seasonal phase variations are generally consistent with the behaviour of the semi-diurnal tide as derived from radar measurements at Birdlings Flat during 1978–79 by Smith (1981) and during 1979–80 as reported by Manson et al. (1985, 1989 and 1990). In the case of the meridional winds in particular, the seasonal phase variations agree very well with those found for the Birdlings Flat radar winds at 95–100 km during 1983, as reported by Stening et al. (1995). The major difference was that there was no sudden phase transition observed in the optical winds at the spring equinox, unlike the radar winds at 90–100 km.

The seasonal variation in the phase of the semi-diurnal tide is due largely to changes in the contribution from symmetric and antisymmetric tidal modes as a result of seasonal variations in the amount of ozone and water vapour. During the equinoxes, antisymmetric modes are excited due to a decrease in the amount of ozone in the southern hemisphere as a result of northward transport (Aso and Vincent 1982, Vincent et al. 1989, Forbes 1990). Marked differences in tidal structure exist between the two hemispheres, especially with regard to the semi-diurnal tide (Vincent et al. 1989).

Figure 6.3 is a histogram of the phase difference between the zonal and meridional FPS winds. The average phase difference is 2.7±1.2 hours which is equivalent to 81°±36°. This indicates that the phase of the zonal wind leads the meridional by this amount and that the two wind components are in time quadrature (the phase of one time-series leads the other by 90°). Two equal-amplitude components in time quadrature produces an essentially circular wind variation during the night if the wind components are plotted on a polar diagram. Departure from quadrature and unequal amplitudes would produce and elliptically-shaped variation.

The amplitude of the semi-diurnal tide exhibited by the raw zonal and meridional FPS winds during the year was similar in both wind components (Figure 6.2 central panels) and a seasonal variation is clearly apparent. The zonal wind amplitudes are greatest during the period after summer solstice through to the autumn equinox, with amplitudes typically being 40 ms$^{-1}$ with a spread of about 15 ms$^{-1}$. The greatest amplitudes are exhibited about a month prior to the autumn equinox. During the winter and spring, the tidal amplitudes are smallest, with 20 ms$^{-1}$ being typical, a reduction by a factor of two compared to the autumn. The smallest amplitudes are exhibited a week or so after the winter equinox. The spread in amplitude during this time is about 10–15 ms$^{-1}$.

A similar seasonal variation in tidal amplitude is also evident in the meridional

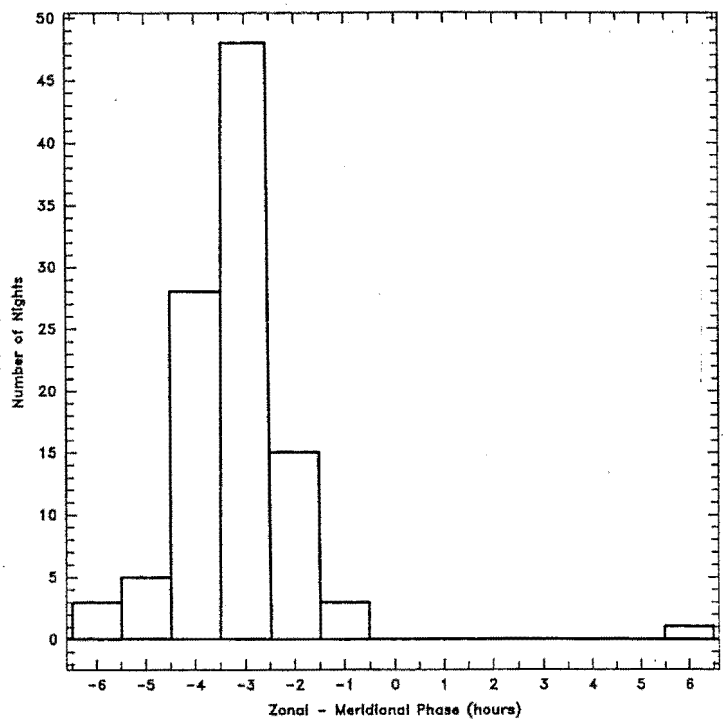


Figure 6.3: Histogram of the phase difference in the semi-diurnal tide exhibited in the raw zonal and meridional winds. The histogram wraps around at 6 hours.

winds. The tidal amplitudes during late spring through to late autumn are typically 35 $ms^{-1}$. The maximum in tidal amplitude appears to occur at about the time of the autumn equinox, which is about a month after the zonal maximum. The tidal amplitudes during winter through to the spring equinox are typically 15 $ms^{-1}$. The minimum appears to occur at about the time of the spring equinox, which is about two months after the zonal minimum.

A seasonal variation is also clearly apparent in both components of the nightly mean FPS winds derived from the tidal analysis procedure (Figure 6.2 bottom panels). The zonal mean wind exhibits a strong semi-annual variation which ranges from about 30 $ms^{-1}$ to -10 $ms^{-1}$. Strong eastward flow is seen to occur during the summer with a maximum flow of $\sim$30 $ms^{-1}$ around the summer solstice. During late summer–early autumn, the mean wind flow decreases and turns westward, reaching a maximum westward flow of 10 $ms^{-1}$ at the autumn equinox. During the winter, the zonal mean wind flow is 25 $ms^{-1}$ eastward, with maximum flow occurring at the winter solstice. As winter progresses the eastward flow decreases and finally becomes westward at about one month before the spring equinox. Maximum westward flow of about 10 $ms^{-1}$ occurs just before spring equinox. In late spring, the mean zonal flow becomes eastward and increases as summer approaches.

The short duration of night time conditions during summer would tend result in erroneous mean wind estimates. This would occur because the amplitude of the diurnal tide,

although irregular, is greatest (~20–25 $ms^{-1}$) during the summer months (Manson et al. 1989) and so biasing of the mean wind due to the diurnal tide will be greatest during the summer.

Unlike the zonal mean flow, the meridional mean flow exhibits a strong annual variation which ranges from about -10 $ms^{-1}$ to 20 $ms^{-1}$. The meridional mean flow is northwards during the six months centred on the summer solstice and the flow reaches a maximum of 20 $ms^{-1}$ around mid-summer. The onset of the northward flow occurs at the spring equinox and continues through to the autumnal equinox. After the autumnal equinox, the mean flow becomes southward reaching a maximum of ~15 $ms^{-1}$ at ~2 weeks after the winter solstice. Figure 6.2 (bottom panel) indicates that there is an apparent net eastward mean flow throughout the year of about 12 $ms^{-1}$. The standard deviation of this value is 16 $ms^{-1}$. In the meridional direction there is a net northward flow of about 5 $ms^{-1}$, although the standard deviation of this value is 13 $ms^{-1}$ and so is not significant.

The behaviour of the zonal mean flow is consistent with radar mean winds obtained near 95 km above Birdlings Flat during 1979–early 1980 by Smith (1981). The seasonal variation of -10 to 20 $ms^{-1}$ in the zonal mean wind flow was also very similar. In the meridional direction, however, there were differences. During the summer, the daily radar mean wind was southward (Smith 1981), opposite in direction that exhibited in the optical daily mean winds (Figure 6.2 bottom panel). Furthermore, during the winter, the radar mean wind flow was northward, again opposite to that exhibited by the optical mean winds, although the overall mean wind magnitudes were similar.

Figure 6.2 (bottom panel) indicates that the optical meridional mean flow is usually between -10 and 10 $ms^{-1}$, which is generally smaller than the corresponding zonal mean flow, and so the seasonal mean flow pattern can vary drastically from year-to-year. This variability is further illustrated in that the meridional mean flow during the 1983–84 summer, as measured by the Birdlings Flat radar, was northward, which is opposite to that exhibited in 1981 (Fraser pers. comm.).

Figure 6.4 shows the zonal and meridional vector mean FPS winds exhibited during the year. The error bars are the standard deviations of the mean values. The cross-correlation coefficients between the vector mean winds and the mean winds derived from the tidal analysis (lower panels of Figure 6.2) were 0.87 and 0.78 in the zonal and meridional directions, respectively, and these were significant to the 95% confidence level. This result indicates that, for the majority of the 103 nights investigated, any daily variations in the phase of the semi-diurnal tide did not grossly affect the vector mean wind value.

Figures 6.5a and b show the magnitudes and directions of the nightly mean wind vectors exhibited during the year. There is a clear seasonal variation in the magnitude of the mean wind vector during the year which is similar to that exhibited by the zonal mean

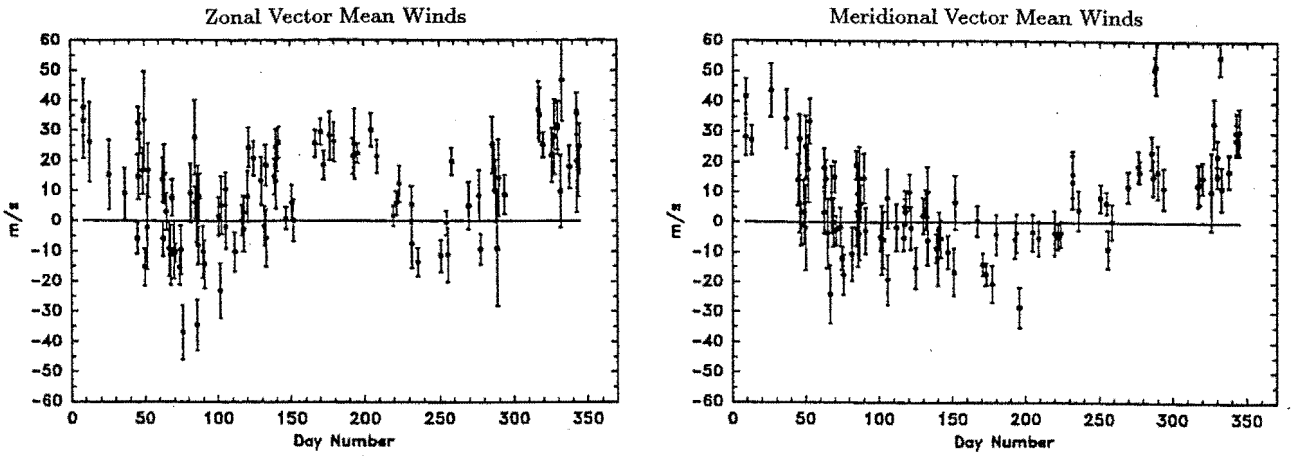


Figure 6.4: The nighttime vector mean zonal and meridional FPS winds derived from the nighttime hourly mean winds. The error bars are the standard deviations of the mean value.

winds. This is because both the zonal and meridional mean winds were similar in magnitude during the six-month period centred on the summer solstice and, during the rest of the year, the zonal winds were generally much larger than the meridional winds. The direction of the mean wind vectors varies seasonally in a similar way to the seasonal phase variation of the semi-diurnal tide in the FPS winds.

The FPS daily mean wind vectors for all 103 nights discussed above are shown as a polar plot in Figure 6.6. The mean wind flow is north-eastward with a magnitude of $\sim$20 $ms^{-1}$ for over half of the nights. This is consistent with the findings of radar winds studies in the southern hemisphere such as Fraser (1968), Smith (1981), Manson et al. (1985) and Phillips and Vincent (1989) which indicate that at 95–100 km the prevailing zonal mean wind is $\sim$10 $ms^{-1}$ and predominantly eastward.

Unlike the plots of the corresponding radar mean wind vectors in Figure 4.8, there is no statistically significant elongation in the distribution (to the 95% confidence level) exhibited in the FPS mean wind plot of Figure 6.6. Similar behaviour was evident in the FPS wind vectors on several time-scales, ranging from daily to monthly mean winds.

## 6.2 Monthly Winds

Figure 6.7 depicts a typical month's hourly mean neutral winds obtained from the FPS measurements. The wind field of the monthly hourly mean winds is clearly dominated by the semi-diurnal tide with an amplitude of about 30 $ms^{-1}$, as with the daily winds. This indicates that the phase of the semi-diurnal tide is usually quite stable on time scales of

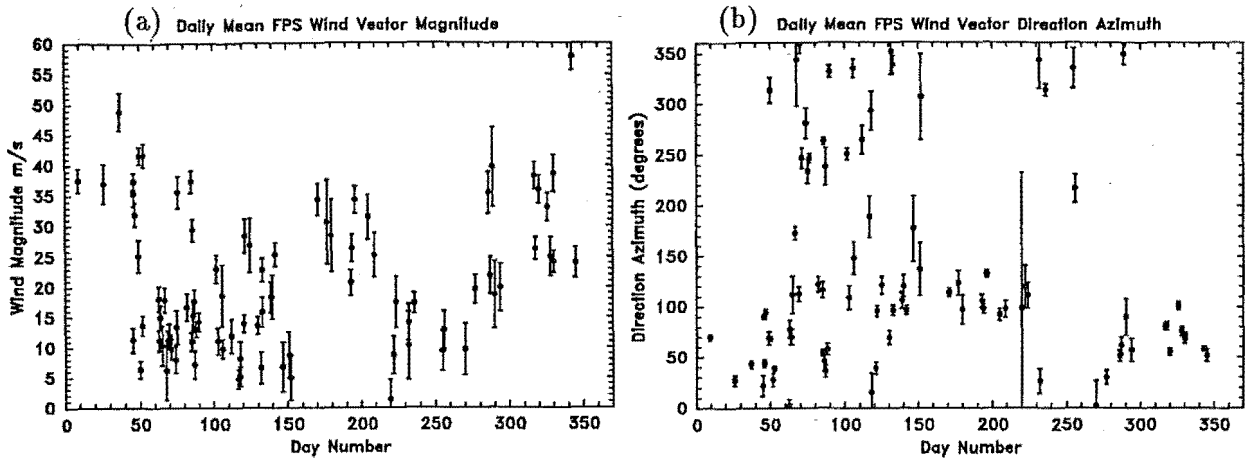


Figure 6.5: The (a) magnitudes and (b) direction azimuths with of the daily FPS mean wind vectors to show the seasonal variation exhibited. The error bars are the standard deviations of the mean values.

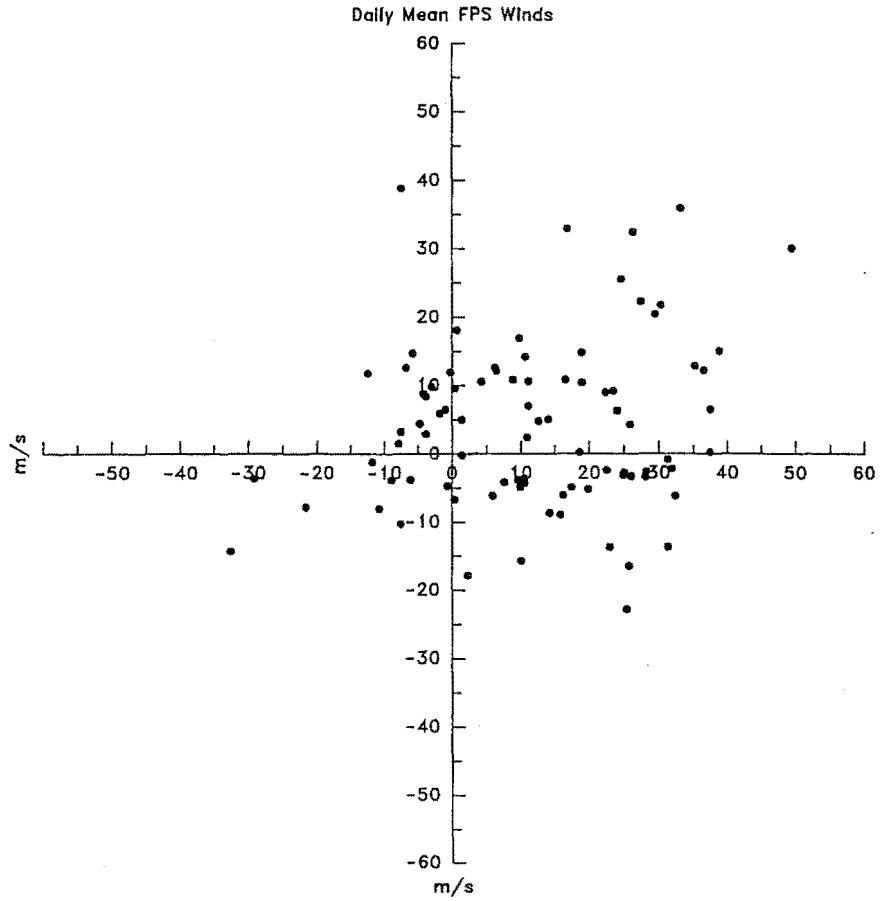


Figure 6.6: Polar plot of the daily FPS mean wind vectors. The uncertainties associated with these winds are typically $\sim$10 ms$^{-1}$ for both components.

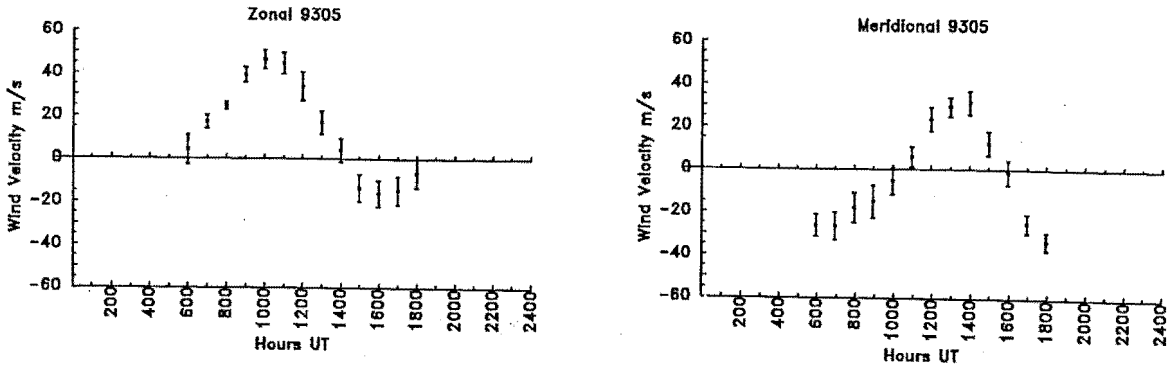


Figure 6.7: A typical FPS monthly hourly mean winds for May 1993. The semi-diurnal tidal variation is clearly dominant.

several days during the year except, perhaps, around the autumn equinox.

As expected, the seasonal variation in the phase and amplitude of the semi-diurnal tide exhibited in the monthly optical winds is very similar to that exhibited in the monthly radar winds. The results are consistent with other FPS monthly wind studies such as Lloyd et al. (1990), Manson et al. (1991) and Phillips et al. (1994) which reported similar behaviour in the monthly mean FPS winds from Saskatoon, Canada (52°N).

The monthly mean zonal and meridional winds for each month also exhibit similar behaviour as the daily optical winds discussed earlier. The monthly vector mean winds were also very similar to the monthly mean winds derived from the tidal analysis, indicating that, for the majority of the 29 months investigated, the vector mean wind values are not significantly affected by the variability of the semi-diurnal tide.

## 6.3 FPS Winds Measured in Opposite Directions

### 6.3.1 Individual Hourly Mean Winds

The raw zonal and meridional FPS winds were obtained by combining the east- and west-pointing and the north- and south-pointing FPS winds, respectively. The sky distance between opposing FPS sampling directions is about 500 km. Hence, the diameter of the observing area, is small compared to the horizontal scale size of the semi-diurnal tide, clearly the most dominant feature of the raw FPS wind field.

Combining the optical winds from opposite directions provides a good estimate of the horizontal wind directly above the Mt. John observatory. It also minimises the effect of any horizontal wind gradient that may be present in the wind field. Combining the winds also reduces the effect of any error in the zero wind reference because if an equal number of

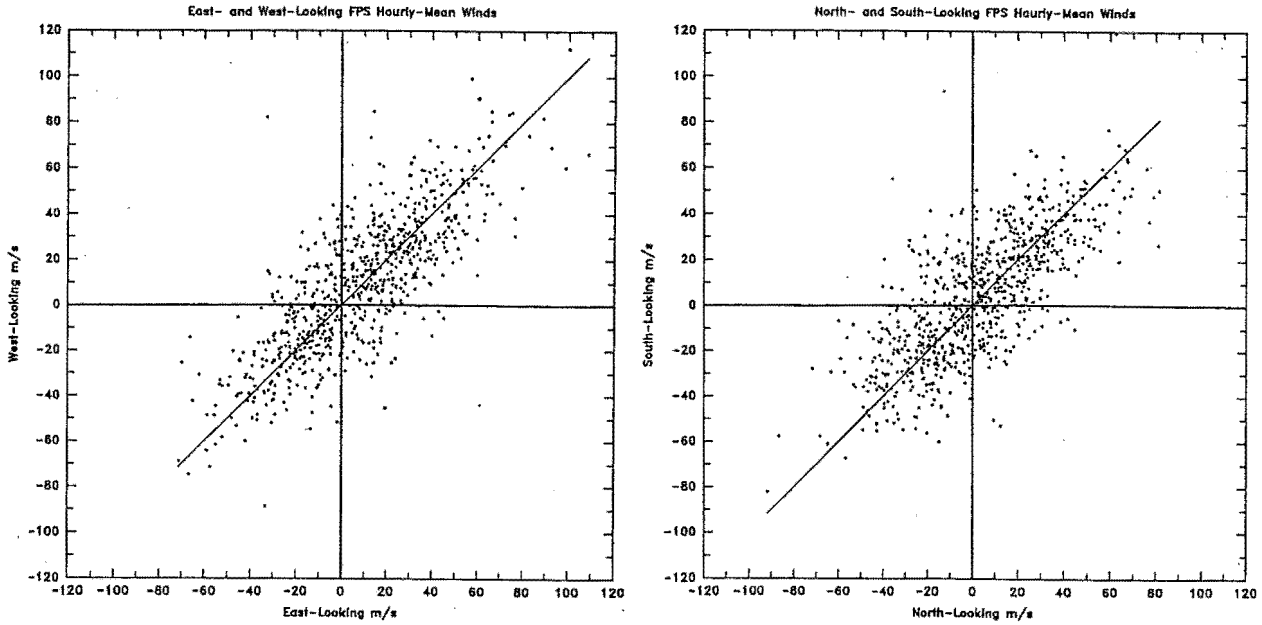


Figure 6.8: Scatter plots of the east- and west-pointing FPS hourly mean winds and north- and south-pointing FPS hourly mean winds for the entire 103 days. The straight line denotes 1:1 correspondence.

measurements were obtained in each direction then a positive error in one direction will be canceled out by a equally-valued negative error in the opposite pointing direction.

Care was taken to remove FPS measurements which occurred during twilight conditions. During this period the daytime 557.7 nm emission, which originates from regions higher up in the thermosphere near 115-120 km (Hunten 1971, Shepherd et al. 1993), is still possibly present and so the wind values may be unreliable. Significant differences in the FPS winds between opposite pointing directions occurred most frequently during this period.

Figure 6.8 shows scatter plots of the corresponding east- and west-pointing hourly-mean winds and the corresponding north- and south-pointing hourly-mean winds for the entire 103 nights. The uncertainties associated with these wind values was typically about 10–12 $ms^{-1}$.

The cross correlation coefficients were 0.80 for the east/west winds and 0.75 for the north/south winds. These are both statistically significant to the 95% level.

The average difference between the east- and west-pointing hourly mean winds was 1 $ms^{-1}$ with a standard deviation of 19 $ms^{-1}$. The standard deviation of the means was less than 1 $ms^{-1}$. The average difference between the north- and south-pointing hourly-mean winds was 1 $ms^{-1}$ with a standard deviation of 20 $ms^{-1}$. The standard deviation of the means were both less than 1 $ms^{-1}$, hence there was no significant systematic difference between the hourly mean FPS wind values in opposite observing directions.

Wind differences of $\sim$10 $ms^{-1}$ or more between opposite observing directions on

time scales of 2–3 hours or more were also occasionally observed. These were possibly due to the presence of a horizontal wind gradients across the observing area. Such a gradient may be the result of the FPS sampling a short period (T~1–2 hours) gravity wave with a horizontal wavelength comparable in size to the diameter of the observing area (~500 km). The gravity wave would be sampled at different points and the winds measured in opposite directions may therefore be large.

Another possibility is related to the way the wind field is sampled by the FPS. FPS wind measurements obtained in opposite directions are separated by about 30 minutes. The raw FPS winds are binned into hourly bins and so the time resolution of the FPS winds is reduced from about 30 to 60 minutes. If, during one hour, only one measurement is made in the north, but two are made in the south, for example, then the hourly mean north and south wind values will differ, although the difference would be expected to be less than or, at least comparable to, the uncertainty of the hourly mean values. Half-hourly binning of the raw winds would maximise the time resolution but was not practicable because of the lack of measurements per hour.

Comparisons between the east- and west-pointing FPS wind measurements were made for the summer and winter months and no significant difference was found between the opposite directions during either season. During the summer, there was no systematic difference between the east- and west-pointing FPS wind measurements although the spread of the individual differences was relatively large. The average difference (east minus west) was -1.4 $ms^{-1}$, with a standard deviation of 17.3 $ms^{-1}$. During the winter, a similar result was found, with the average difference (east minus west) being -4.3, $ms^{-1}$ with a standard deviation of 23.6 $ms^{-1}$.

### 6.3.2 Daily Mean Winds

The behaviour of the nightly raw FPS winds between each pair of opposite pointing directions was investigated. Small differences were exhibited between the fitted phase and amplitude of the semi-diurnal tide and between the estimated mean winds. The mean differences, together with their associated sample standard deviations (in parentheses), are shown in Table 6.1. The standard deviation of the mean value of the phase, amplitude and mean wind difference was 0.01 hours, 0.1 $ms^{-1}$ and 0.6 $ms^{-1}$, respectively.

The average phase differences between both direction pairs are comparable with the fit uncertainty (~0.1–0.2 hours). Figure 6.9 shows the east/west and north/south phase differences. There is no apparent seasonal variation in the east/west phase differences.

The sign and magnitude of the mean phase difference exhibited between the east and west-pointing tidal phases and indicated in Table 6.1 is consistent with the westward

| Direction Pair | Phase Difference (Hrs) | Amplitude Difference ($ms^{-1}$) | Mean Wind Difference ($ms^{-1}$) |
|---|---|---|---|
| East/West | −0.20 (0.81) | +1.5 (11.1) | −0.01 (10.5) |
| North/South | +0.10 (0.85) | −0.5 (13.0) | −2.2 (10.0) |

Table 6.1: Table of the mean differences exhibited between the phase and amplitude of the semi-diurnal tide between each opposite direction pairs of the nightly raw winds. The associated sample standard deviations are given in parentheses.

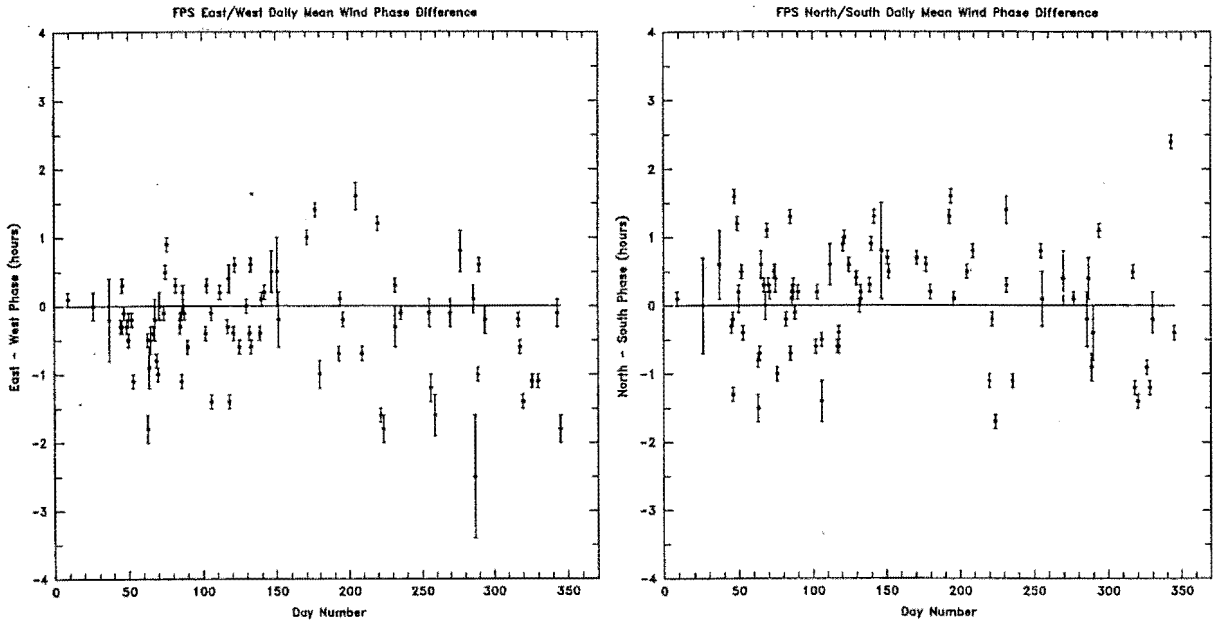


Figure 6.9: The phase differences in the semi-diurnal tide as exhibited by the east- and west-pointing and the north- and south-pointing raw nightly FPS winds.

migration of the semi-diurnal tide. A consequence of the 500-km horizontal diameter of the FPS observing area is that the phase of the semi-diurnal tide in the FPS wind field, as measured in the east-pointing direction, will lead the phase measured in the west-pointing direction by 0.3 hours. The sample standard deviation of the east-west phase differences (0.81) is larger than this value and so this explanation is not conclusive.

A weak but significant annual variation is exhibited in the north/south wind phase differences in Figure 6.9. The north/south phase differences are smallest during the equinoxes and the maximum positive and negative differences occur at the winter and summer solstices, respectively. From May until early August, the semi-diurnal tidal phase exhibited by the north-looking optical winds is consistently larger than that exhibited in the south-looking optical winds by ∼0.5–1.0 hour. This behaviour indicates that the semi-diurnal phase, as observed towards the south, occurred earlier than towards the north. The sign of the phase difference appears to reverse during early summer.

There were no significant systematic differences exhibited in the amplitude of the semi-diurnal tide between each opposite observing direction pair of the nightly winds. No seasonal variation was exhibited by the differences. The standard deviation of the mean semi-diurnal tidal amplitude difference was 0.1 $ms^{-1}$. No significant differences were exhibited in the fitted mean wind between each opposite observing direction pair of the nightly raw winds and no seasonal variation was exhibited.

# Chapter 7

# Radar Wind Results

## 7.1 Daily Winds

Figure 7.1 shows the raw winds of a typical 24 hour period obtained from the Birdlings Flat radar from the 90–105 km height region. As, discussed in Chapter 5, there is a significant amount of RF noise and interference associated with the radar wind measurements. The noise results in a significant amount of short-period variations exhibited in the radar wind values on time scales of less than one hour. The variations can be rather large, sometimes 50–100 $ms^{-1}$, on time-scales of 10 minutes. The data distribution in this height region for this period is shown in Figure 7.2 and it indicates the marked reduction in the number of acceptable wind returns obtained from above 90 km during the night.

Harmonic analysis of each day's hourly-mean radar winds yielded the daily phase and amplitude of the semi-diurnal tide. On most days, the phase of the semi-diurnal tide presents a relatively smooth variation with height as seen in Figure 7.3 and on consecutive days the phase is usually seen to be stable. The height interval between independent wind measurements is the convolution of the 5-km binning interval used with the 4-km transmitter pulse width and is 6–7 km. The high level of RF noise and interferences associated with the radar winds is evident from the sudden variations in the phase over height intervals smaller than 5 km.

If one assumes that only tidal mode is present in the phase plots in Figure 7.3 then a least-squares fit of the phase progression to a straight line can be made. The slope of the line will provide an estimate of the phase progression of the semi-diurnal tide with increasing height. Table 7.1 presents the least-squares fitted phase progression of the semi-diurnal tide for the days of 26–29 March, 1994 (see figure 7.3). The slope was calculated using phase values at heights which were separated by more than the 4.5 km pulse width of the radar, so they are largely independent. The slope uncertainty is the 95% confidence interval of the slope determination.

| Date | Height Region (km) | Slope hrs $km^{-1}$ | $\lambda_z$ (km) |
|---|---|---|---|
| 940326 | merid 80–100 | -0.57 ± 0.10 | 21 ± 5 |
| 940327 | merid 84–105 | -0.31 ± 0.09 | 39 ± 12 |
| 940328 | zonal 80–97 | -0.28 ± 0.08 | 43 ± 14 |
| 940329 | zonal 80–105 | -0.30 ± 0.11 | 40 ± 17 |
| | merid 80–105 | -0.39 ± 0.08 | 31 ± 7 |

Table 7.1: Least-squares fitted phase height progressions of the semi-diurnal tide for the radar winds for 26–29 March, 1994.

If the semi-diurnal tide was not present in the radar winds then the determined phase of the semi-diurnal tide would to exhibit a random variation with height. The slope estimates illustrate that the phase progression with height does not exhibit random behaviour but a statistically significant linear height variation.

Figure 7.4 shows the daily semi-diurnal phase and amplitude and the mean wind flow exhibited at a height of 95 km by the daily hourly mean zonal and meridional radar winds during the year. These fits involved 24 hours of hourly mean radar wind data. These values were derived from the least-squares fits of the original hourly mean radar winds to a 12- and 24-hour sinusoid. The scale is similar to that used for the corresponding optical winds in Figure 6.2. The uncertainties in phase, amplitude and the mean winds are typically, 0.8 hours, 7.0 $ms^{-1}$ and 12.0 $ms^{-1}$, respectively and were derived during the least-squares fitting procedure. There is a large amount of daily scatter in the phase and amplitude of the semi-diurnal tide exhibited by the daily hourly mean radar winds. The variability of the phase of the semi-diurnal tide seen here in Figure 7.4 is much greater than in the corresponding optical winds (Figure 6.2). This is possibly due to the large amount of noise affecting the radar wind measurements as well as any geophysical mechanism such as gravity wave activity.

No clear seasonal pattern is apparent in phase of the semi-diurnal tide (Figure 7.4 top panels). The phase is scattered over a wide range of hours. During the period from day numbers 160 to 260, just prior to the winter solstice through to the spring equinox, the zonal phase of the semi-diurnal tide is found to occur predominantly between 7 and 11 hours UT. The phase of the semi-diurnal meridional tidal winds during the same period is found to occur predominantly between 0 and 6 hours UT. The meridional tidal phases during the winter are consistent with those exhibited in the BF radar winds at 95–100 km during 1979–80 (Manson et al. 1985, 1989) and 1983 (Stening et al. 1995).

Table 7.2 is a histogram of the phase difference between the zonal and meridional hourly mean radar winds. There is no clear evidence of the time-quadrature exhibited between the zonal and meridional FPS winds components. The phase of the meridional radar winds,

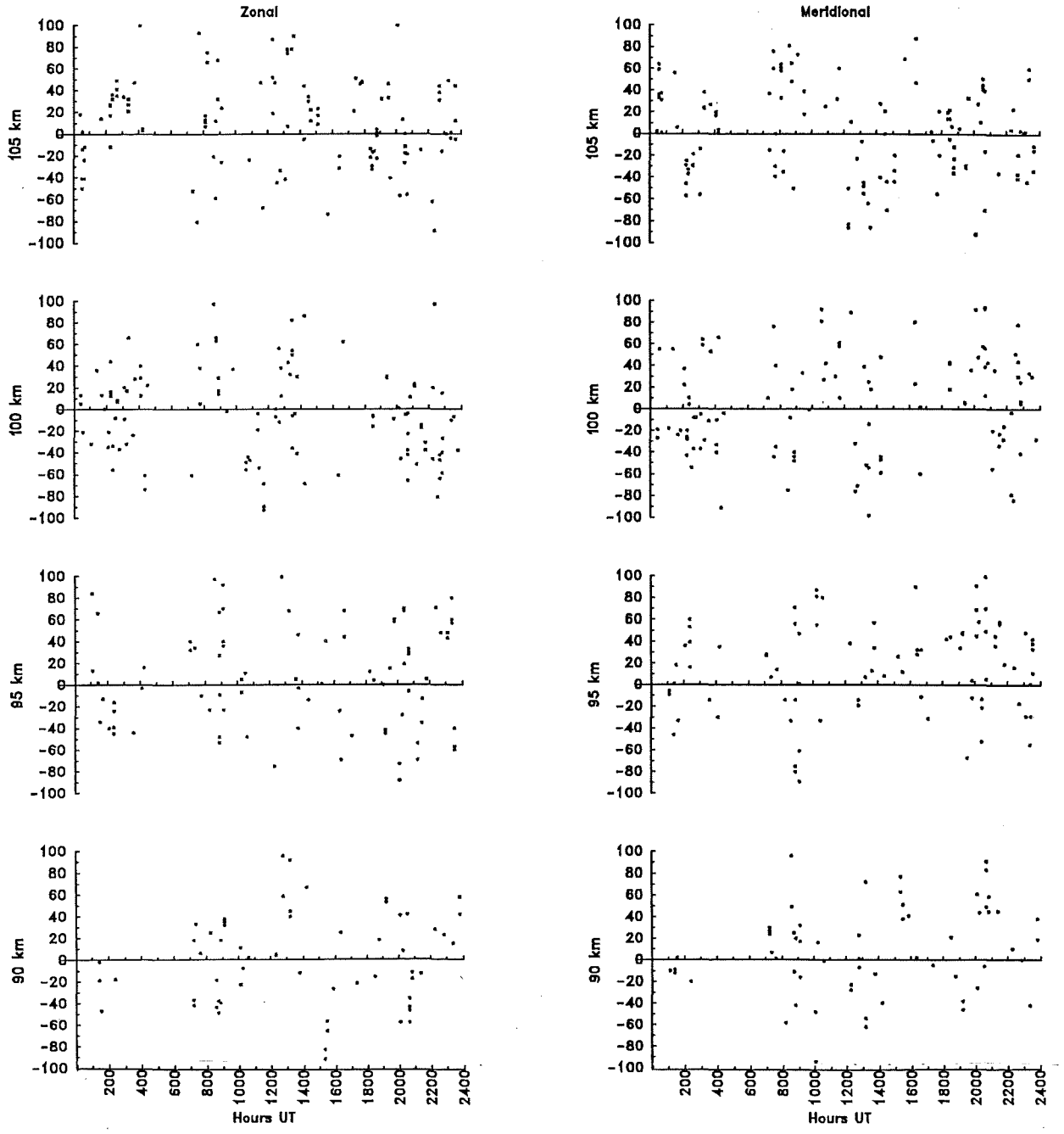


Figure 7.1: Typical raw radar winds at 90–105 km obtained from the Birdlings Flat radar during the 24 hour UT period of 4 March 1994.

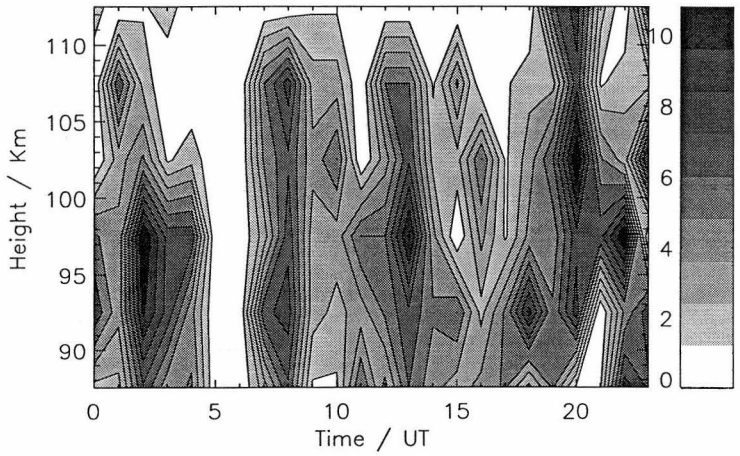


Figure 7.2: The data distribution of the usable raw radar winds shown in Figure 7.1. The contours range from 0 (white) to 10 (black) radar wind measurements per hour.

on average, lags the phase of the zonal winds by about 5 ± 2 hours, which corresponds to 150° ± 60°. Previous studies on the semi-diurnal tidal oscillation in BF radar wind data during 1979–80 (Smith 1981) and 1983 (Stening et al. 1995) have indicated that time-quadrature is exhibited between the zonal and meridional wind components. A much smaller radar data set was used in this present project, however. There were only 3 available days, on average, during each month, which is less than 10% of the total possible days the three-and-a-half year period. Smith (1981) and Stening et al. (1995) both used two years of monthly wind data.

The middle panels in Figure 7.4 show the amplitude of the semi-diurnal tide exhibited at 95 km by the daily hourly mean radar winds during the year. The amount of scatter is large, but some general features of the seasonal variations are apparent. The average tidal amplitude exhibited by the zonal winds at 95 km was 16 $ms^{-1}$ with a standard deviation of 24 $ms^{-1}$. The average tidal amplitude exhibited by the meridional winds at 95 km was 20 $ms^{-1}$ with a standard deviation of 24 $ms^{-1}$. Although these values are not significant they are similar to the reported (Manson et al. 1989) radar amplitudes of ~20 $ms^{-1}$ during the summer near 95 km for Christchurch during 1979–80.

A similar seasonal amplitude variation was exhibited by both wind components. The zonal wind amplitude was greatest during autumn, with amplitudes of 20–30 $ms^{-1}$, with

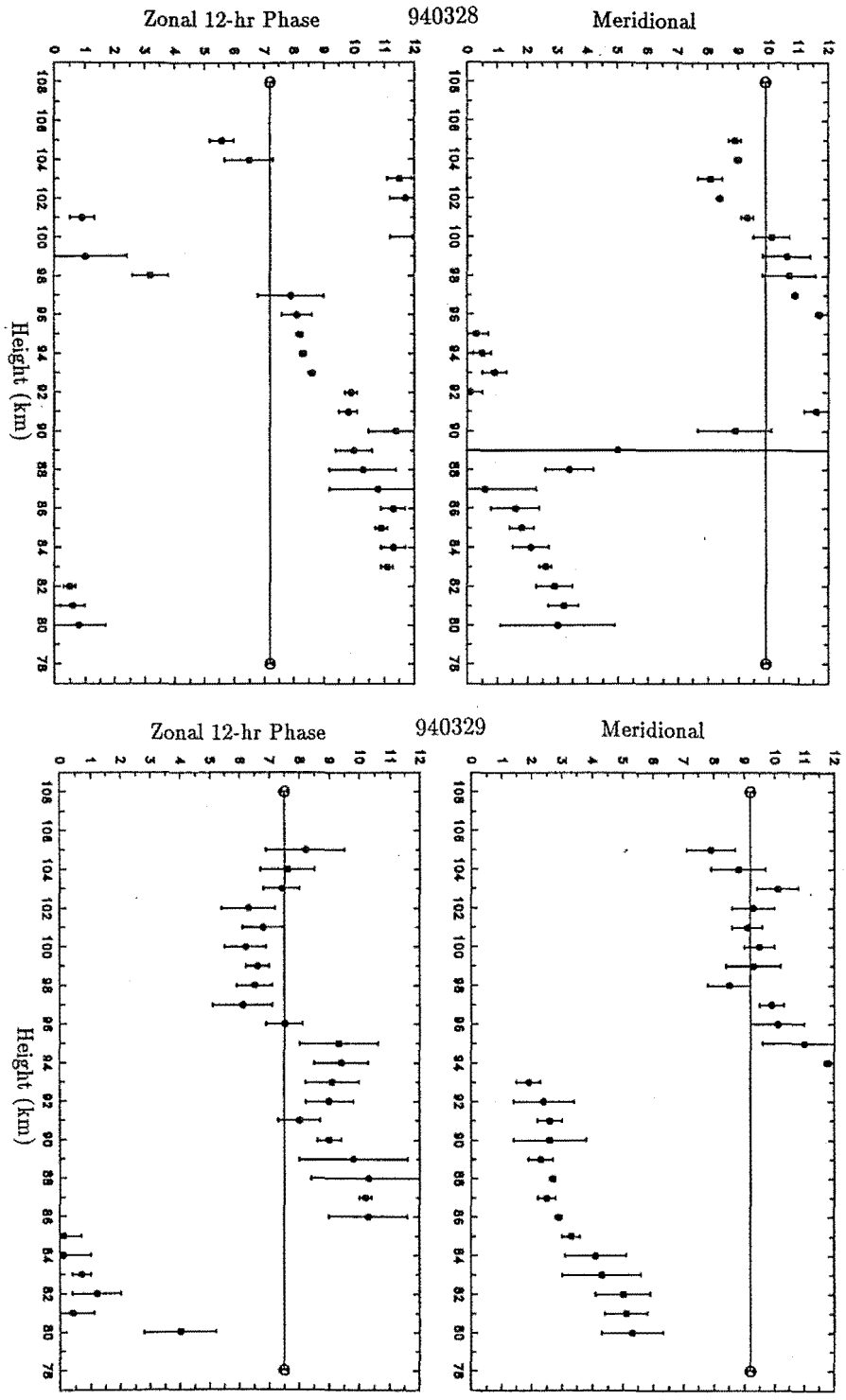


Figure 7.3: The height profiles of the daily semi-diurnal phase for the consecutive days of 28 and 29 March, 1994. The horizontal line in each plot is the corresponding daily FPS phase. Heights separated by more than 5 km are largely independent.

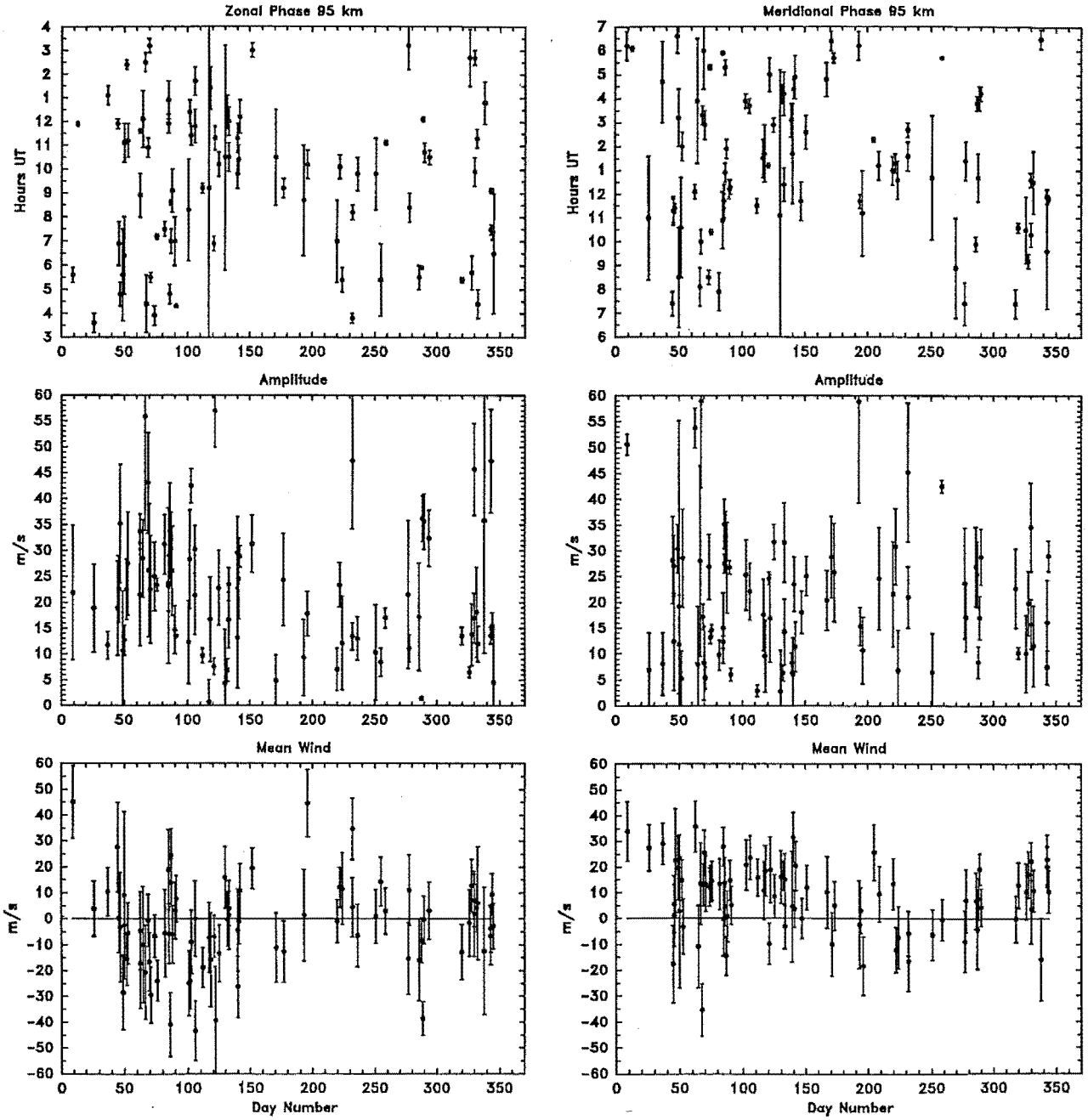


Figure 7.4: The daily semi-diurnal phase, amplitude and mean wind exhibited at 95 km by the daily hourly mean radar winds.

| Phase Diff (hrs) | 85 km | 90 km | 95 km | 100 km | 105 km |
|---|---|---|---|---|---|
| -6 | 7 | 6 | 9 | 9 | 15 |
| -5 | 9 | 11 | 13 | 12 | 8 |
| -4 | 9 | 13 | 9 | 5 | 13 |
| -3 | 4 | 3 | 8 | 4 | 1 |
| -2 | 1 | 4 | 4 | 4 | 5 |
| -1 | 1 | 1 | 3 | 5 | 4 |
| 1 | 2 | 0 | 0 | 3 | 4 |
| 2 | 4 | 0 | 2 | 2 | 1 |
| 3 | 2 | 1 | 4 | 3 | 1 |
| 4 | 1 | 4 | 2 | 8 | 6 |
| 5 | 1 | 3 | 7 | 8 | 9 |
| 6 | 8 | 12 | 9 | 8 | 6 |

Table 7.2: Histogram of the phase difference in the semi-diurnal tide exhibited between the daily hourly mean zonal and meridional radar winds.

a spread of $\sim$20 ms$^{-1}$. A minimum of 10–20 ms$^{-1}$ in amplitude occurs near the winter solstice for about six weeks, but the scatter of the amplitude values makes this difficult to ascertain. The seasonal variation of the meridional wind amplitudes is similar, being greatest during autumn, with amplitudes typically of 20–30 ms$^{-1}$, with a spread $\sim$20 ms$^{-1}$. A minimum of 10–15 ms$^{-1}$ in amplitude occurs at the winter solstice for about six weeks, but, again, the scatter of the amplitude values makes this difficult to ascertain. There were sometimes irregular nightly variations of 10–15 ms$^{-1}$ in the semi-diurnal amplitude in both components but these were not significant due to the uncertainty of the amplitude values, however similar irregular nightly variations was reported by Manson et al. (1991).

On any given night, the semi-diurnal tidal amplitude typically varied smoothly with increasing height, and the profile shape was usually consistent on consecutive days.

The bottom panels in Figure 7.4 show the daily mean zonal and meridional radar winds at 95 km. There is considerable scatter exhibited in the the zonal mean winds during the year. The average annual zonal mean wind at 95 km was 2 ms$^{-1}$ westwards, with a standard deviation of 24 ms$^{-1}$. The average annual meridional mean wind at 95 km was 10 ms$^{-1}$, with a standard deviation of 18 ms$^{-1}$.

The amount of scatter makes the interpretation of the mean wind variation difficult. The zonal mean wind appears to exhibit a weak semi-annual zonal variation which ranges from about -15 to 10 ms$^{-1}$. A weak eastward flow of $\sim$0–10 ms$^{-1}$ occurs during the summer and winter. Maximum westward flow of 10–20 ms$^{-1}$ occurs around the autumn equinox. There is a transition from a westward flow to a weak eastward flow during early winter. There is another a transition in the mean flow, from eastward to westward, during the spring

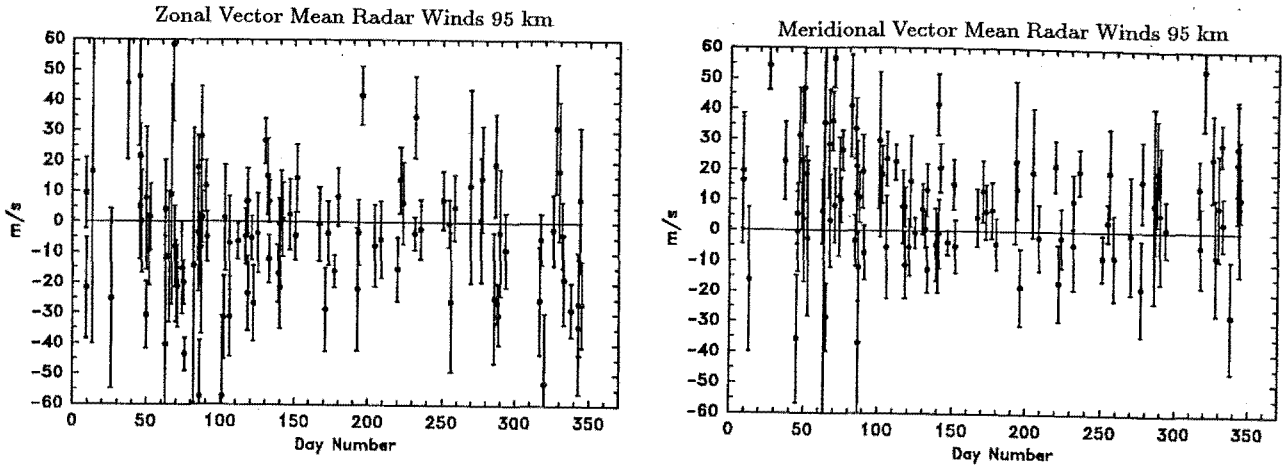


Figure 7.5: The nighttime vector mean radar winds at 95 km as a function of day number.

equinox. Another transition from westward to a weak eastward flow occurs about the time of the summer solstice.

No semi-annual variation is apparent in the meridional mean flow. There is, however, an apparent annual variation which ranges from about -10 $ms^{-1}$ to 20 $ms^{-1}$. The onset of northward flow occurs after the spring equinox and reaches a maximum of about 15–20 $ms^{-1}$ about a week before the autumn equinox. The transition to a southward flow occurs at winter solstice, reaching a maximum of about 10 $ms^{-1}$ a month later.

Higher up, at 105 km (not shown), the seasonal variations in the meridional mean wind flow occurs ~2–4 weeks later than at 90–100 km. The northward maximum occurs at about a week after the autumn equinox, reaching about 25 $ms^{-1}$ at this time. A weak southward flow occurs in late winter, with the onset of northward flow occurring in early summer, although the scatter of the mean wind values makes this difficult to determine precisely.

The daily vector mean radar winds at 95 km are shown in Figure 7.5. The error bars are the standard deviations of the mean values. The cross-correlation coefficients, for all 103 nights, between the vector mean winds in Figure 7.5 and the mean winds in Figure 7.4 for the 90, 95, 100 and 105 km are 0.44, 0.38, 0.51 and 0.34 for the zonal component, and 0.41, 0.21, -0.20 and 0.18 for the meridional component. These coefficients are all statistically significant to better than the 95% confidence level. The correlation between the vector mean winds and the mean wind winds are clearly much lower for the radar winds than for the optical winds in section 6.1. The effect of daily tidal variations on the determination of the vector mean winds would contribute to a reduced correlation between these two types of mean winds, but

the level of RF noise/interference associated with the radar winds will unavoidably reduce the correlation between the two sets of mean radar winds.

The mean radar wind flow for the days in which a correlation of fit better the 95% was obtained is shown as polar plots in Figure 4.8 in Chapter 4. These plots indicate that the mean wind flow was predominantly towards the north–west, with a magnitude of $\sim$20 $ms^{-1}$. Wind flow towards the north–east occurred on nearly half the days and towards the south–east, on about one–third of the time. North–eastward and south–westward flow occurred least often of all, each occurring only on about 10% of the nights.

## 7.2 Monthly Winds

### 7.2.1 Monthly mean radar and CIRA-86 zonal winds

The monthly mean BF radar winds over a period of nearly four years (January 1991 to July 1994, a total of 41 months) were derived from the daily hourly mean radar day and night winds for each entire month, not just the FPS-simultaneous nights, for the 80–105 km height region.

No allowance was made for group retardation of the radar transmitter pulse which could possibly occur, especially during the daytime in the summer months. In these cases, group retardation of up to 5 km or more may be present for BF wind values from above 95 km (Namboorthiri et al. 1993). The 4.5 km transmitter pulse width and the 5-km binning interval, means that the mean radar winds at 95 km, for instance, are partially correlated with those at 100 km. Hence, any group retardation occurring at 100 km will be smeared out to below 95 km. There is no significant difference in the agreement between the model and radar wind profiles of summer and winter so there is no evidence of group retardation affecting the summer radar wind profiles.

The monthly mean radar winds were found to typically exhibit a general consistency from year to year. Figure 7.6 shows the monthly mean radar wind height profiles for the months of January 1991, 1992 and 1994 over the period of this present project. No radar data were available during January 1993, for technical reasons. The error bars associated with each BF radar wind value is the standard deviation of the mean wind value.

The zonal radar wind profiles were compared to the CIRA-86 model monthly zonal wind profiles (Rees et al. 1990) for the latitude of 45°S. The latter were obtained by linearly interpolating the CIRA-86 monthly zonal mean model winds at latitudes 40°S and 50°S. The CIRA-86 model winds were originally obtained at 3.5 km intervals. These were linearly interpolated in height to obtain model winds at 1 km intervals in order to match those of the radar winds. The CIRA-86 model zonal wind height profile for January at 45°S latitude is

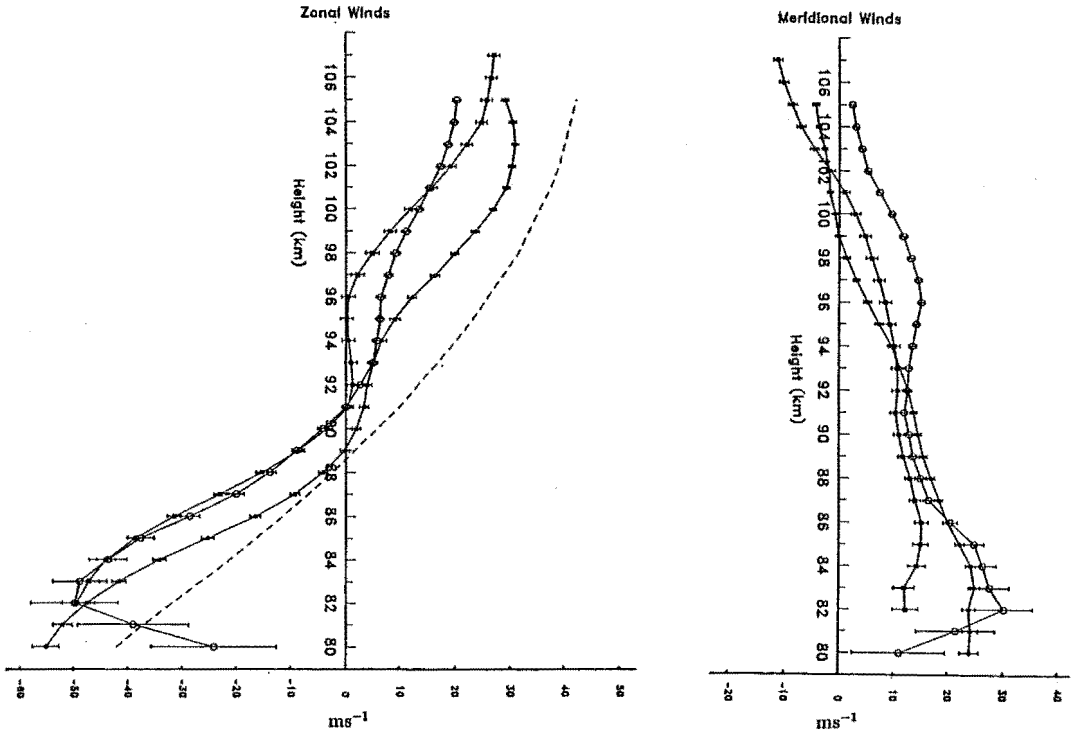


Figure 7.6: The monthly mean radar velocity height profiles for January for 1991 (filled circles), 1992 (open circles) and 1994 (filled squares). The error bars are the standard deviations of the mean values. The CIRA-86 monthly mean model zonal wind for January (dotted line) is also shown.

also shown in Figure 7.6.

There was generally good agreement between the model winds and the radar winds, especially in direction. Above 90 km, the model zonal winds tend to be $\sim$10 ms$^{-1}$ more eastward than the corresponding radar winds, as evident in Figure 7.6. Significant departures, of up to 30 ms$^{-1}$ and oppositely–directed flow, occurred above 90 km during the equinoctial months of March–April and September–October.

The monthly mean BF radar winds obtained during this present project are also generally consistent with those obtained during 1979–80 at Birdlings Flat by Smith (1981). There were some differences, but these could be attributed to the inter-annual variability of the mean wind flow. Figure 7.7 shows the radar wind height profiles for January 1980 (Smith 1981). The zonal profile is clearly very similar to the 1991–1994 January height profiles which indicates that the monthly BF radar winds are consistent annually over several years.

The monthly zonal BF radar wind profiles and the CIRA-86 zonal model wind profiles were cross–correlated and the results are shown in Figure 7.8. The deviation of the two wind sets during the equinoxes is also clearly evident. For the individual months, all but one produced statistically significant correlations. The number of points used in

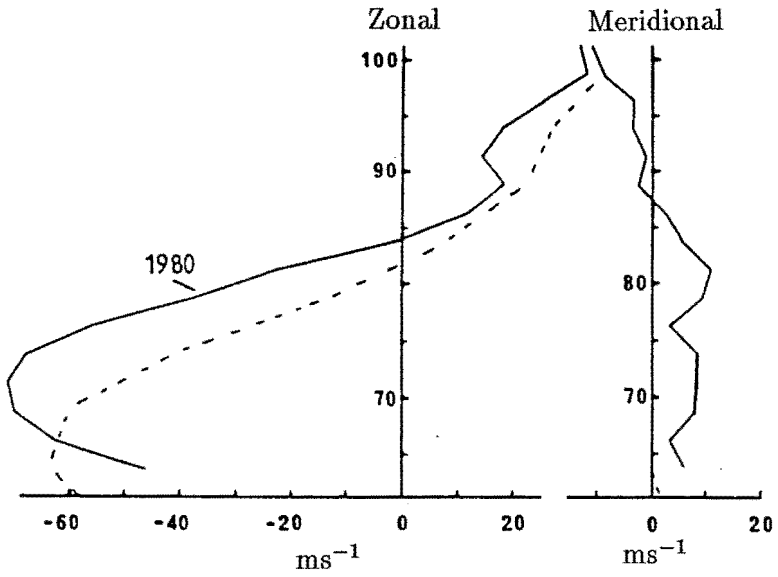


Figure 7.7: The monthly mean radar velocity height profiles for January 1980 as reported by Smith (1981). The dashed line is the CIRA 72 (1972) monthly zonal mean model wind for January.

the correlation calculations was 26, which corresponds to the number of heights. Of the 45 months investigated, significant correlations (95% confidence limits) were found for 42 of them. No significant correlation was found for September 1992, September and October 1993. Significant negative correlations were obtained for March and September 1991, March and October 1992, March 1993 and March and September 1994, inferring that the monthly mean winds during these months of the two data sets were in opposite directions.

Corresponding months from each of the four years show high congruity and this is even apparent for the equinoctial months. For example, the March winds of all four years are very similar, as are those of September. The correlation coefficients from one year to the next are also relatively similar, except perhaps for October.

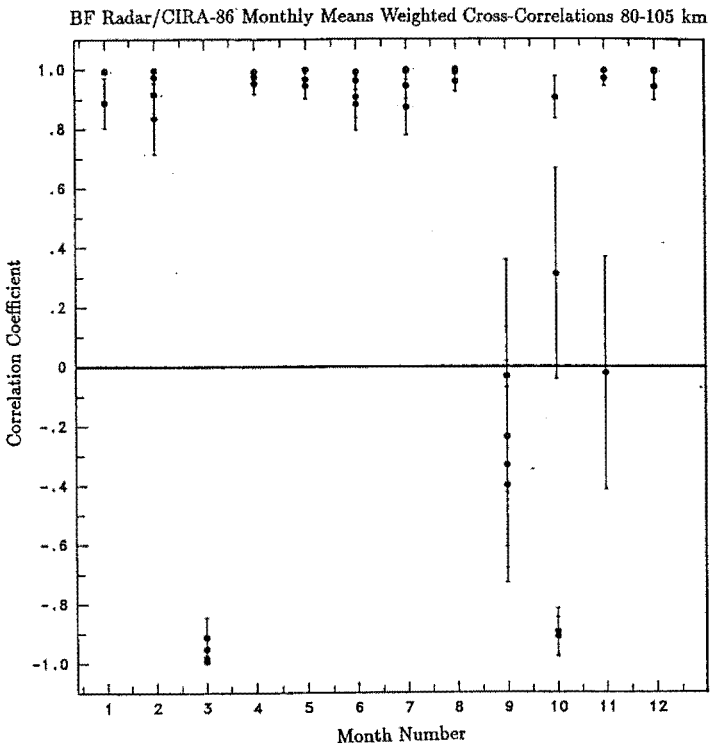


Figure 7.8: The cross-correlations between the monthly mean zonal radar winds and the CIRA-86 zonal monthly mean winds for each month. The agreement between the two winds is excellent for most of the year except for near the equinoxes.

# Chapter 8

# Optical/Radar Wind Comparisons

## 8.1 Daily Winds

The results of the comparisons between the optical and radar winds are presented and discussed in this chapter. Two methods of comparison were employed on the radar and optical wind data sets. The simultaneous night time hourly mean optical and radar winds were cross-correlated. A comparison was made of the fitted phase and amplitude of the semi-diurnal tide and the mean winds which were obtained from the least-squares fit of the optical and radar daily winds.

### 8.1.1 Daily Hourly-Mean Winds

#### Tidal Fit Comparisons

The hourly mean optical and radar winds in the 90–105 km region for 4 March 1994 are shown in Figure 8.1. The solid curves are the tidal fits determined by the least-squares procedure described in Chapter 5. This night is relatively typical of the nights used in this project although the number of night time radar winds is higher than typically seen. The number at the top right of each plot is the correlation coefficient of the fit. An asterisk next to the correlation coefficient denotes that the correlation of fit was not significant to the 95% level. This occurred for the meridional radar winds at 95 and 100 km.

The FPS winds appear to be dominated by a semi-diurnal oscillation with an amplitude of about 25 $ms^{-1}$. A similar amplitude is observed in the zonal radar wind field. The meridional radar winds are more scattered, as indicated by the lower correlations.

The phase of the radar winds can be seen to generally decrease in time with increasing height, as expected from semi-diurnal tidal theory. For a fixed ground station, the time of maximum wind of the semi-diurnal tide will decrease in time with increasing height. There is a large ($\sim$15–20 $ms^{-1}$) diurnal tidal contribution in the meridional wind field in the

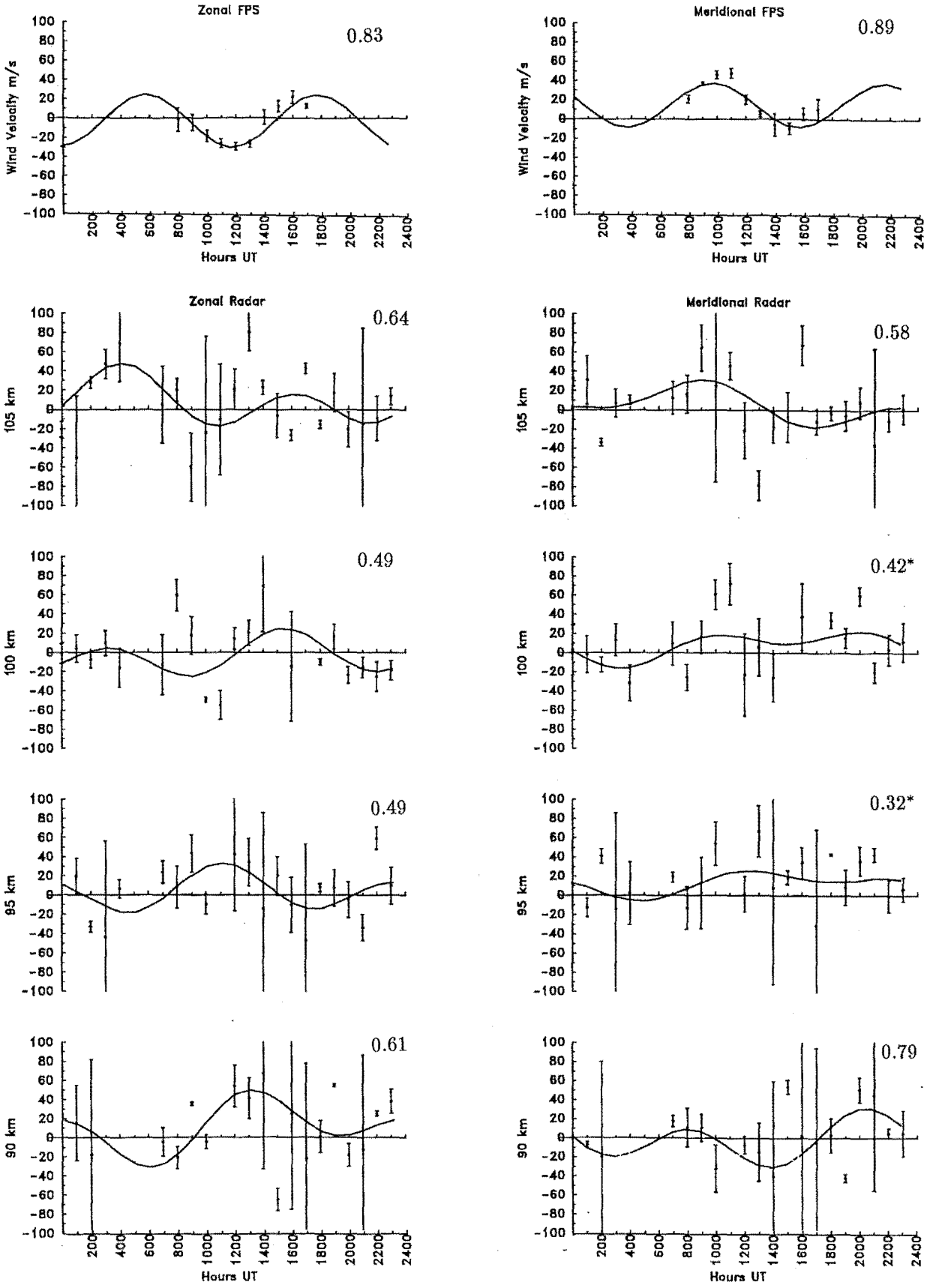


Figure 8.1: The hourly mean radar and optical winds for 4 March 1994. The least squares tidal fits together with their corresponding correlation coefficient of fit are also shown.

95–100 km height region but it is not seen in the zonal wind fields (Figure 8.1). The diurnal contribution produced the insignificant correlation of fit values, in the meridional winds in the 95–100 km region. A phase jump of 5–6 hours can be seen between 95–100 km in the zonal wind field. This may indicate the presence of several tidal modes in the wind fields. From an inspection of the phase of the tidal fits for both sets of winds there appears to be best agreement in the optical/radar wind fields near 100 and 105 km.

The differences (optical minus radar) in the values of the fit parameters between the optical and radar hourly mean winds for the 103 suitable nights in the 85–105 km height interval were investigated. Only those nights' winds whose fits exhibited a correlation of fit to 95% or better significance were used in the difference comparisons. The number of nights was dependent on the number of available radar winds and this was dependent mainly on the height, ranging from 48 nights at 85 km up to 73 nights at 105 km.

The optical/radar differences in the fitted phase of the semi-diurnal tide are shown as a series of height histograms in Table 8.1. Each point in the histogram is independent since each night contributes to only one point in the histogram. Their associated uncertainties are typically 0.6 hours or less. Each column corresponds one height range. For example, the 100 km column represents phase differences between the optical winds and the radar winds at 100 km. The differences (in this case, phase) are arranged in rows according to the magnitude and the sign of the difference. For example, the zonal winds at 100 km; in the row denoted "-5", there were 10 nights on which the optical-radar phase difference was between -4 and -5 hours. A positive difference indicates that the maximum eastward (in the zonal wind case) or northward (in the meridional wind case) optical wind occurred between 0 to 6 hours after the corresponding radar wind maximum. A negative difference indicates that the maximum eastward or northward optical wind occurred between 0 to 6 hours before the corresponding radar wind maximum.

All 103 nights are combined together and so the height histogram reveals only the vertical structure of the radar/optical tidal wind phase differences which are independent of season. At lower heights, negative differences occur more frequently than positive ones. As the height increases, the differences tend to become more positive. This is especially apparent in the histograms of the meridional phase differences and is consistent with the behaviour of the semi-diurnal tide which dominates the variation of the wind fields, especially in the case of the optical winds.

The meridional height histograms exhibit clearly more consistency with height than the corresponding zonal and east-looking histograms. The phase difference of the semi-diurnal tide between the optical and radar meridional winds tends to decrease from $\sim$-(1–5) hours near 90 km, to $\sim\pm$(1–2) hours at 100–105 km, where the differences in phase are smallest. This region is slightly higher than the 95–100 km region generally agreed as the origin of the

557.7 nm nightglow emission (Donahue et. al. 1973, Shepherd et al. 1995, Ward et al. 1995) but it is consistent with the findings of Phillips et al. (1994). The tidal fits used both day and night time radar data so the increased height discrepancy may be partly due to group retardation (Fraser and Kochanski 1970, Namboorthiri 1993).

The zonal and the east-looking histograms exhibit more scatter than the meridional histograms and the height variation seen in the meridional histograms is also less apparent. The scatter may be due to the larger amount of scatter associated with the zonal radar winds themselves since the FPS zonal and meridional winds have similar amounts of scatter associated with them. The larger amount of scatter associated with the zonal radar wind component is possibly the result of the beam pattern of the radar (as discussed in Chapter 4). The height histograms of the zonal and east-looking winds indicate that the phase difference of the semi-diurnal tide between the optical and radar winds is smallest at about 100–105 km, although it is not as clear as in the meridional winds.

Small differences are evident between the zonal and east-pointing histograms. Since the same radar winds are used for both histograms, the differences must be due to intrinsic differences between the zonal and east-pointing FPS wind fields. The least-squares fit routine was sensitive to noise, especially for sparse data series, and the number of east-looking FPS winds was approximately half the number of zonal FPS winds. Hence the east-looking wind fits were more susceptible to scatter. It is possible that the differences are due to gravity waves with horizontal wavelengths comparable to or less than the diameter of the observing area ($\sim$500 km) which produce wind gradients across the observing area between opposing directions. The gradients are not evident in the combined east-west FPS winds.

There was a large spread exhibited in the tidal phase differences between the optical and radar winds for all three components and there was no significant seasonal variation in the differences. The lack of seasonal variation is due mainly to the scatter in the hourly mean radar winds fits. A similar result was found in the tidal phase differences between the monthly optical and radar winds. For example, the scatter between the FPS/radar phase difference values for March for the years 1991 to 1994 was about 9 hours. This was not significantly different from the scatter in the daily differences at the 95% confidence level.

No consistent pattern was exhibited in height histograms of the monthly optical/radar zonal phase differences, unlike the daily winds (Table 8.1). This can be attributed to the small number of monthly differences available ($\sim$19–25) spread over the 12 hours (-6–+6 hours) of possible differences.

The differences in the amplitude of the semi-diurnal tide exhibited in the optical and radar winds are shown as height histograms in Table 8.2. Like the phase differences there was no apparent seasonal variation. The amplitude differences are typically 5–15 $ms^{-1}$ for both components and the optical wind amplitude is in general larger than the corresponding

| Phase Diff (hrs) | 85 km | 90 km | 95 km | 100 km | 105 km |
|---|---|---|---|---|---|
| | | Zonal | | | |
| -6 | 7 | 6 | 7 | 7 | 6 |
| -5 | 8 | 8 | 9 | 10 | 4 |
| -4 | 10 | 9 | 6 | 4 | 5 |
| -3 | 2 | 5 | 5 | 8 | 11 |
| -2 | 6 | 7 | 7 | 4 | 3 |
| -1 | 6 | 5 | 9 | 11 | 9 |
| 1 | 4 | 5 | 6 | 9 | 10 |
| 2 | 2 | 8 | 5 | 9 | 9 |
| 3 | 2 | 5 | 9 | 7 | 12 |
| 4 | 4 | 4 | 7 | 6 | 4 |
| 5 | 5 | 6 | 6 | 6 | 4 |
| 6 | 5 | 3 | 5 | 4 | 9 |
| | | Meridional | | | |
| -6 | 3 | 4 | 5 | 3 | 5 |
| -5 | 6 | 10 | 6 | 1 | 2 |
| -4 | 6 | 8 | 7 | 2 | 3 |
| -3 | 8 | 9 | 13 | 8 | 6 |
| -2 | 4 | 1 | 9 | 14 | 9 |
| -1 | 2 | 12 | 9 | 11 | 19 |
| 1 | 5 | 7 | 10 | 14 | 18 |
| 2 | 3 | 3 | 7 | 11 | 15 |
| 3 | 2 | 5 | 6 | 7 | 7 |
| 4 | 5 | 6 | 3 | 6 | 1 |
| 5 | 6 | 4 | 4 | 2 | 3 |
| 6 | 5 | 5 | 6 | 2 | 2 |
| | | East | | | |
| -6 | 5 | 8 | 9 | 7 | 4 |
| -5 | 11 | 6 | 5 | 10 | 4 |
| -4 | 6 | 9 | 6 | 4 | 3 |
| -3 | 3 | 3 | 4 | 7 | 8 |
| -2 | 6 | 7 | 9 | 6 | 5 |
| -1 | 3 | 3 | 8 | 6 | 10 |
| 1 | 1 | 7 | 5 | 11 | 7 |
| 2 | 2 | 4 | 6 | 9 | 9 |
| 3 | 2 | 4 | 4 | 4 | 12 |
| 4 | 2 | 4 | 7 | 5 | 6 |
| 5 | 6 | 4 | 6 | 6 | 5 |
| 6 | 6 | 5 | 4 | 2 | 7 |

Table 8.1: Histogram of the height variation of the differences in the phase of the semi-diurnal tide between the daily optical and radar winds for the zonal, meridional and east-looking winds. The associated uncertainties were typically ~0.6 hrs or less.

radar wind amplitude. It is also apparent from Table 8.2 that the distribution of the optical/radar wind amplitude differences in the 90 to 105 km region is independent of height. The uncertainties of the amplitude differences were typically $\sim$6–10 $ms^{-1}$.

There were several nights, indicated in Table 8.2, on which the radar wind amplitudes were greater than the corresponding optical amplitudes by over 55 $ms^{-1}$, resulting in negative amplitude differences. The frequency of occurrence of these differences was greater at the lower heights (80–90 km) and are a result of the decrease in the S/N ratio of the radar winds at lower altitudes.

The ratios of the semi-diurnal optical/radar wind amplitudes provide a relative comparison of the amplitudes as measured by each technique. In the 85–105 km region, the optical semi-diurnal amplitude was found to be between 1–1.4$\times$ greater than the amplitude of the radar semi-diurnal tide. The amplitude difference appeared to be largest near 95 km. The heights quoted here are the heights of the radar winds. Figure 8.2 presents the distribution of the optical/radar wind amplitude ratio values at 95 km as a percentage of the total number of available nights. The distribution is clearly asymmetric which exhibits a peak at $\sim$1–1.4 and a weak tail which extends to ratio values of 5–6. There is no significant difference exhibited between the zonal (solid) and meridional (dashed) wind components. The median values of the zonal and meridional distributions at 95 km are both 1.4 and their associated quartile ranges are 1.5. There was no significant seasonal variation in the ratio values.

There was an apparent decrease in the median optical/radar amplitude ratio above and below above 95 km but these were not significant given the large standard deviations associated with the distributions. At 85 km, the median of zonal and meridional optical/radar amplitude ratios were 0.9 and 0.8, respectively, inferring that the radar wind amplitudes were comparable if not slightly larger than the optical wind amplitudes. This particular result however is very probably affected by the lower S/N ratio of the radar winds at this lower height.

These results are consistent with the findings of Burrage et al. (1996) who reported that the amplitudes of horizontal Doppler optical winds obtained from the High Resolution Doppler Interferometer (HRDI) instrument, an FPS aboard the orbiting NASA Upper Atmosphere Research Satellite (UARS) (Hays et al. 1993) were twice that of corresponding MF radar winds from Saskatoon, Canada. A similar wind amplitude discrepancy was found between comparisons of southern hemisphere MF radar winds and horizontal Doppler optical winds obtained from the WINDII instrument (Shepherd et al. 1993) aboard UARS (Gault et al. 1996).

Measurements obtained from the MU radar (an MST radar) operated by the Radio Atmospheric Science Center of the University of Kyoto, Japan were used by Dunford (pers. comm.) to derive horizontal radar wind velocities. The velocities were derived using the

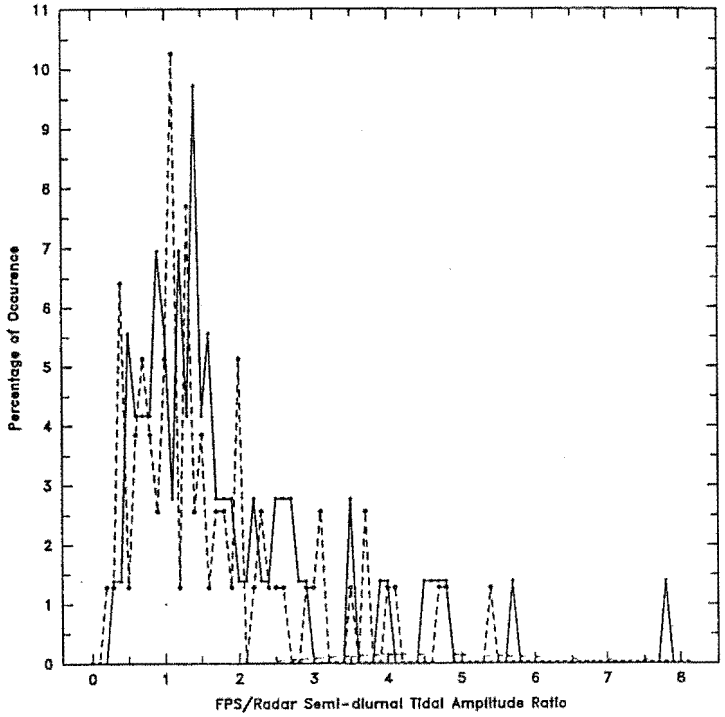


Figure 8.2: The distribution of optical/radar semi-diurnal tidal amplitude ratio values at 95 km. The median value is 1.4 for both components (zonal - solid, meridional - dashed) with an associated quartile range of 1.5.

Briggs (Briggs et al. 1950, Briggs 1984) and Brown and Chapman (1972) methods (Dunford pers. comm.) and then compared. The Brown and Chapman (1972) method was used in the determination of the raw radar winds used in the FPS/radar comparisons. The median ratio of the over 7000 wind velocities by the Briggs to the Chapman and Brown method was 1.2 with a standard deviation of 0.3 (Dunford pers. comm.). This is comparable to the FPS/radar semi-diurnal tidal amplitude ratio found in this project. The Brown and Chapman method therefore appears to one possible reason for the FPS/radar wind amplitude discrepancy found in this project.

The observed amplitude of the semi-diurnal tide exhibited in the radar (or FPS) winds is a consequence of the convolution of radar pulse width (or vertical 557.7 nm emission profile) and with the vertical wind profile of the semi-diurnal tide. The 4.5 km transmitter pulse width (radar) and the 10–12 km width (FWHM intensity) of the 557.7 nm emission profile at 45°S (Shepherd et al. 1995) (FPS) (see Figure 8.12) would produce a reduction in the tidal wind amplitudes in both methods.

If the above process is responsible for the amplitude discrepancy then during periods when the semi-diurnal tide exhibits a vertical wavelength which is large compared to the radar pulse width and vertical scale of the 557.7 nm emission the FPS/radar tidal amplitude ratio

will be near unity. Hernandez et al. (1995) used FPS wind measurements from Mt. John and reported that the vertical wavelength of the semi-diurnal tide has values typically less than 50 km during the period from October through to February and about a month after the autumn equinox in April. Around the time of the autumn equinox the semi-diurnal tide exhibits a vertical wavelength of between 50–100 km. If the optical/radar amplitude differences are due mainly to undersampling of the vertical wind structure one would expect that to observe near-unity FPS/radar semi-diurnal amplitude ratio values during the autumn equinox. The FPS/radar tidal amplitude ratios during the autumn equinox were not significantly different from those occurring during the rest of the year, when the vertical wavelength was less than 50 km.

The differences (optical minus radar) between the optical and radar daily mean winds are shown in Figure 8.3. The uncertainties associated with the differences are typically about 12 $ms^{-1}$. A semi-annual variation is apparent in the zonal optical/radar mean wind differences. The differences between FPS and radar mean winds at 95–100 km are greatest during 50–100 days centred on the winter solstice and at about six weeks prior to the summer solstice. During this period, the FPS mean winds are typically 20–40 $ms^{-1}$ larger than the radar winds. The differences are smallest, and not significantly different from zero, for a similar time period during the equinoxes. The seasonal variation of the optical/radar mean zonal wind differences coincides almost exactly with the seasonal variation of the zonal daily mean optical winds shown in lower panel of Figure 6.2. No semi-annual variation is apparent in the meridional mean wind differences at 95–100 km but a weak annual variation is possibly present. The optical/radar mean wind differences in Figure 8.3 are greatest when the optical mean wind is at its seasonal maximum. The reason for the differences is unclear but it possibly due to the same reasons responsible for the FPS/radar tidal amplitude differences discussed above.

Table 8.3 shows the optical/radar mean wind differences as height histograms. The heights being those of the radar winds. There is clearly a large spread in the mean wind differences between the optical and radar winds. Over the 85–105 km region the mean zonal optical wind flow was consistently larger than the corresponding radar winds by 10–20 $ms^{-1}$ despite the large amount of scatter in the histograms. The zonal and east-looking height histograms are similar and the apparent differences between them are smaller or comparable to the uncertainties, typically $\sim$12 $ms^{-1}$, associated with the differences. The mean meridional radar wind flow was consistently larger than the corresponding optical mean wind by 5–15 $ms^{-1}$.

The ratios of the optical/radar mean wind flow, unlike the semi-diurnal tide amplitude ratios, were different for each wind component. In the 90–100 km region the FPS mean zonal wind was generally larger than the corresponding radar mean wind with the median

| Amp Diff ($ms^{-1}$) | Zon 85 | 90 | 95 | 100 | 105 | Mer 85 | 90 | 95 | 100 | 105 | Eas 85 | 90 | 95 | 100 | 105 |
|---|---|---|---|---|---|---|---|---|---|---|---|---|---|---|---|
| -105 | 2 | 0 | 1 | 0 | 1 | 5 | 0 | 0 | 0 | 1 | 2 | 0 | 1 | 0 | 0 |
| -100 | 0 | 0 | 0 | 0 | 0 | 0 | 0 | 0 | 0 | 0 | 0 | 0 | 0 | 0 | 0 |
| -95 | 0 | 0 | 0 | 0 | 0 | 1 | 0 | 0 | 0 | 0 | 0 | 0 | 0 | 0 | 0 |
| -90 | 0 | 0 | 0 | 0 | 0 | 0 | 0 | 0 | 0 | 0 | 0 | 0 | 0 | 0 | 0 |
| -85 | 0 | 1 | 0 | 0 | 0 | 1 | 0 | 0 | 0 | 0 | 0 | 0 | 0 | 0 | 0 |
| -80 | 0 | 0 | 0 | 1 | 0 | 0 | 0 | 0 | 0 | 0 | 0 | 0 | 0 | 1 | 0 |
| -75 | 0 | 0 | 0 | 0 | 0 | 0 | 0 | 0 | 0 | 0 | 0 | 1 | 0 | 1 | 0 |
| -70 | 0 | 0 | 0 | 0 | 0 | 0 | 0 | 0 | 0 | 0 | 0 | 0 | 0 | 0 | 1 |
| -65 | 1 | 0 | 0 | 1 | 1 | 0 | 0 | 1 | 0 | 0 | 0 | 0 | 0 | 0 | 0 |
| -60 | 0 | 0 | 0 | 0 | 0 | 1 | 1 | 0 | 0 | 0 | 1 | 0 | 0 | 0 | 0 |
| -55 | 1 | 1 | 1 | 0 | 0 | 1 | 0 | 0 | 0 | 0 | 1 | 1 | 0 | 0 | 1 |
| -50 | 0 | 0 | 1 | 0 | 0 | 0 | 0 | 0 | 0 | 0 | 1 | 0 | 1 | 0 | 0 |
| -45 | 2 | 0 | 0 | 0 | 1 | 0 | 0 | 2 | 0 | 1 | 1 | 0 | 0 | 0 | 0 |
| -40 | 0 | 2 | 0 | 0 | 2 | 0 | 1 | 0 | 0 | 0 | 0 | 1 | 2 | 0 | 1 |
| -35 | 2 | 0 | 0 | 0 | 0 | 0 | 0 | 1 | 0 | 1 | 1 | 0 | 0 | 0 | 1 |
| -30 | 4 | 0 | 1 | 2 | 2 | 2 | 2 | 1 | 0 | 0 | 4 | 1 | 0 | 1 | 1 |
| -25 | 1 | 3 | 1 | 1 | 5 | 0 | 0 | 0 | 0 | 4 | 1 | 2 | 3 | 1 | 6 |
| -20 | 4 | 4 | 2 | 4 | 7 | 1 | 3 | 5 | 8 | 4 | 2 | 3 | 3 | 1 | 9 |
| -15 | 4 | 7 | 1 | 3 | 8 | 2 | 7 | 2 | 2 | 7 | 5 | 3 | 1 | 5 | 2 |
| -10 | 7 | 3 | 7 | 7 | 4 | 7 | 2 | 5 | 6 | 8 | 3 | 5 | 4 | 5 | 8 |
| -5 | 6 | 7 | 6 | 9 | 9 | 6 | 3 | 5 | 8 | 4 | 3 | 8 | 3 | 9 | 5 |
| 5 | 4 | 8 | 9 | 10 | 8 | 5 | 8 | 11 | 14 | 13 | 7 | 8 | 5 | 10 | 5 |
| 10 | 10 | 8 | 13 | 11 | 9 | 4 | 10 | 11 | 4 | 8 | 8 | 8 | 13 | 7 | 9 |
| 15 | 6 | 7 | 10 | 10 | 9 | 2 | 9 | 8 | 8 | 6 | 5 | 6 | 11 | 9 | 7 |
| 20 | 2 | 6 | 7 | 8 | 5 | 5 | 6 | 7 | 8 | 6 | 3 | 5 | 3 | 8 | 4 |
| 25 | 2 | 3 | 6 | 8 | 2 | 0 | 5 | 7 | 3 | 8 | 2 | 4 | 12 | 12 | 5 |
| 30 | 1 | 5 | 7 | 7 | 5 | 0 | 2 | 4 | 2 | 2 | 2 | 4 | 3 | 4 | 3 |
| 35 | 0 | 3 | 5 | 0 | 6 | 2 | 3 | 1 | 3 | 1 | 1 | 3 | 2 | 1 | 5 |
| 40 | 0 | 1 | 1 | 1 | 1 | 0 | 2 | 3 | 1 | 0 | 0 | 2 | 2 | 0 | 4 |
| 45 | 0 | 1 | 1 | 0 | 0 | 0 | 0 | 1 | 1 | 0 | 0 | 0 | 2 | 0 | 0 |
| 50 | 1 | 0 | 0 | 1 | 0 | 0 | 0 | 0 | 1 | 0 | 0 | 0 | 1 | 1 | 1 |
| 55 | 0 | 1 | 0 | 0 | 0 | 1 | 0 | 0 | 0 | 0 | 0 | 1 | 0 | 1 | 0 |

Table 8.2: Histogram of the height variation of the differences in the amplitude of the semi-diurnal tide between the daily optical and radar winds. The associated uncertainties were $\sim$10 $ms^{-1}$ or less.

ratio values of 1.3–1.5 being typical. The spread of the distributions was large with an inter-quartile range of ~1.5–2.0 being typical and there was no significant height dependency in the ratio values. The FPS mean meridional wind was generally less than the corresponding radar wind with median values of 0.7–1.0 being typical. The inter-quartile range for these median values was however ~0.6–0.8. One possible reason for the difference between the zonal and meridional wind components is the generally larger magnitudes exhibited by the zonal compared to the meridional winds and the greater variability of the zonal wind, as discussed in Chapter 5.

### Optical/Radar Wind Cross-Correlations

Only very low yields of significant correlations (to the 95% level) were obtained between the simultaneous optical/radar hourly night time winds in the 80–105 km region. There were however, statistically significant differences in the yields between each wind component when the sign of the correlation was considered.

The number of significant correlations obtained from the optical/radar night time zonal and the east-looking wind correlations was not significantly different from the correlation of two random distributions. This assumes that the probability of a significant correlation is uniform through the 80–105 km height region, although one might expect an increase in the occurrence of significant positive correlations in the 95–100 km region, the expected height of the 557.7 nm emission. The number of significant positive correlations obtained between the meridional optical/radar night time winds was the only correlation set that was significantly different from a random distribution. The meridional yield was over twice the number obtained from the zonal correlations.

Figure 8.4 shows the distribution of heights at which a significant correlation was obtained between the optical and radar night time hourly winds. Not all of these points are independent, but the calculations to test for statistical significance were performed using only the independent points. There are approximately equal numbers of positive and negative zonal correlation coefficients, which indicates that there is a large amount of variability in the zonal wind component compared to the meridional component. The meridional distribution exhibits significantly more positive correlations than negative, throughout the 85–105 km height region. A $\chi^2$ test on the independent points in Figure 8.4 indicates that there is no statistically significant difference in the numbers of positive and negative correlations. In the meridional distribution in Figure 8.4, the $\chi^2$ test indicates that there are significantly more (to better than 99.9%) positive correlations between the optical and radar winds and so the grouping is not random. The average height of the significant positive correlations between the meridional optical and radar hourly mean winds was 95.8 km with a standard deviation

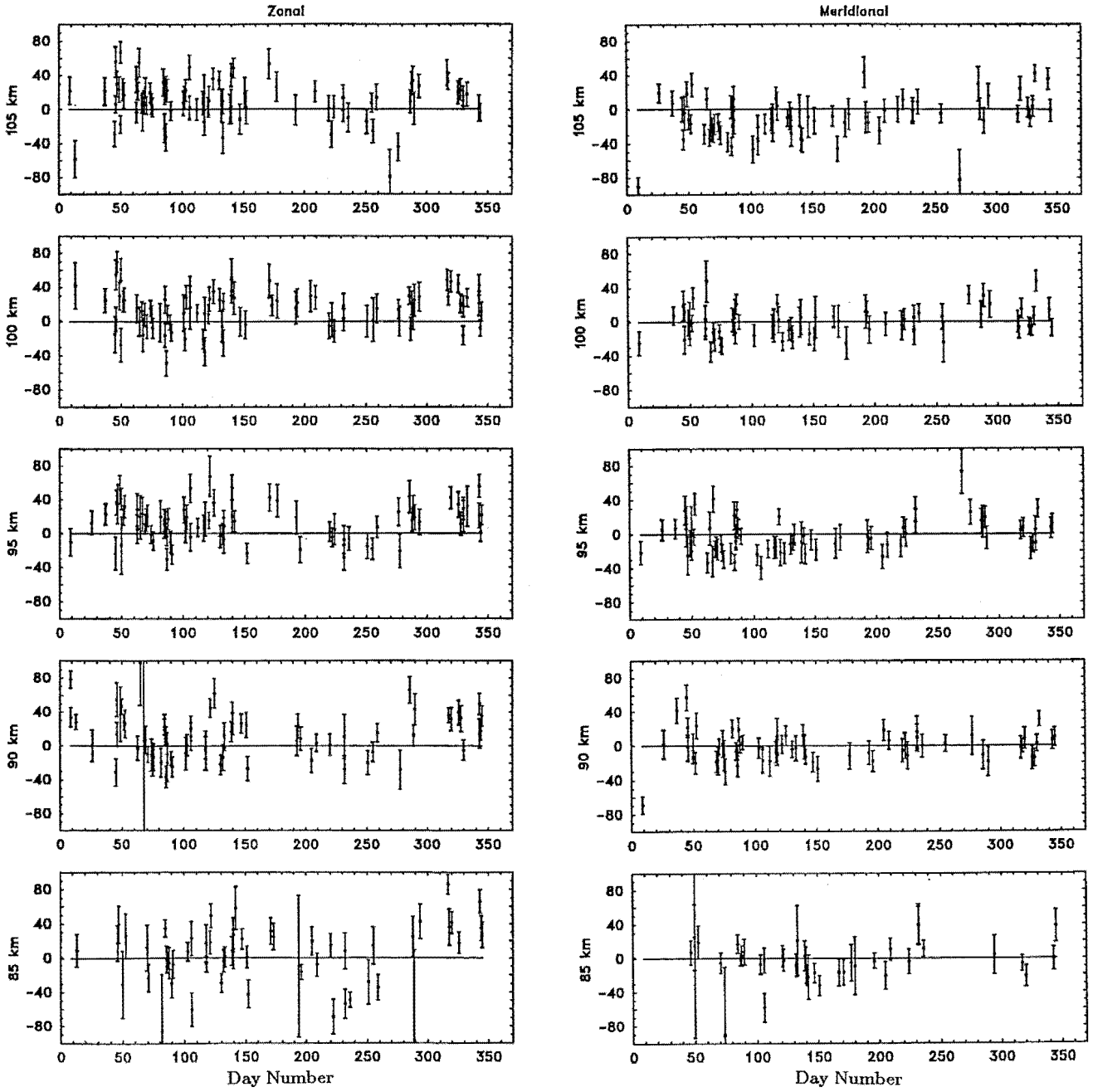


Figure 8.3: Differences in the mean wind flow (in $ms^{-1}$) between the daily optical and radar winds as a function of day number in the 85–105 km height region.

| Mean Diff ($ms^{-1}$) | Zon 85 | 90 | 95 | 100 | 105 | Mer 85 | 90 | 95 | 100 | 105 | Eas 85 | 90 | 95 | 100 | 105 |
|---|---|---|---|---|---|---|---|---|---|---|---|---|---|---|---|
| -105 | 3 | 0 | 1 | 0 | 0 | 4 | 1 | 0 | 0 | 0 | 3 | 0 | 1 | 0 | 0 |
| -100 | 1 | 0 | 0 | 0 | 0 | 0 | 0 | 0 | 0 | 0 | 0 | 0 | 0 | 0 | 0 |
| -95 | 0 | 0 | 0 | 0 | 0 | 1 | 0 | 0 | 0 | 1 | 1 | 0 | 0 | 0 | 0 |
| -90 | 1 | 0 | 0 | 0 | 0 | 0 | 0 | 0 | 0 | 0 | 0 | 0 | 0 | 0 | 0 |
| -85 | 0 | 0 | 0 | 0 | 0 | 0 | 0 | 0 | 0 | 1 | 1 | 0 | 0 | 0 | 0 |
| -80 | 0 | 0 | 0 | 0 | 1 | 0 | 0 | 0 | 0 | 0 | 1 | 0 | 0 | 0 | 0 |
| -75 | 0 | 0 | 0 | 0 | 0 | 0 | 0 | 0 | 0 | 0 | 0 | 0 | 0 | 0 | 0 |
| -70 | 1 | 0 | 0 | 0 | 0 | 0 | 1 | 0 | 0 | 0 | 0 | 0 | 0 | 0 | 1 |
| -65 | 1 | 0 | 0 | 0 | 0 | 0 | 0 | 0 | 0 | 0 | 1 | 0 | 0 | 0 | 0 |
| -60 | 0 | 0 | 0 | 0 | 1 | 1 | 0 | 0 | 0 | 0 | 0 | 0 | 0 | 0 | 0 |
| -55 | 1 | 0 | 0 | 0 | 0 | 0 | 0 | 0 | 0 | 0 | 0 | 0 | 0 | 0 | 0 |
| -50 | 1 | 0 | 0 | 1 | 0 | 0 | 0 | 0 | 0 | 2 | 2 | 0 | 0 | 0 | 1 |
| -45 | 1 | 0 | 0 | 0 | 1 | 0 | 0 | 0 | 0 | 1 | 0 | 0 | 0 | 1 | 0 |
| -40 | 0 | 1 | 0 | 1 | 0 | 0 | 0 | 1 | 1 | 4 | 1 | 0 | 0 | 1 | 1 |
| -35 | 2 | 1 | 1 | 0 | 2 | 1 | 0 | 3 | 0 | 2 | 1 | 2 | 0 | 0 | 1 |
| -30 | 3 | 3 | 1 | 2 | 3 | 0 | 2 | 2 | 3 | 5 | 2 | 1 | 0 | 2 | 2 |
| -25 | 1 | 2 | 4 | 2 | 1 | 3 | 1 | 8 | 6 | 3 | 2 | 0 | 3 | 3 | 1 |
| -20 | 1 | 5 | 3 | 4 | 1 | 4 | 9 | 7 | 3 | 9 | 2 | 1 | 2 | 4 | 3 |
| -15 | 1 | 4 | 2 | 2 | 3 | 0 | 8 | 10 | 7 | 6 | 0 | 8 | 2 | 2 | 2 |
| -10 | 4 | 4 | 5 | 6 | 1 | 7 | 6 | 5 | 8 | 9 | 4 | 5 | 10 | 2 | 5 |
| -5 | 3 | 3 | 6 | 6 | 7 | 6 | 9 | 10 | 10 | 8 | 3 | 7 | 2 | 5 | 4 |
| 5 | 2 | 5 | 4 | 7 | 11 | 4 | 9 | 4 | 8 | 8 | 2 | 2 | 5 | 4 | 9 |
| 10 | 4 | 4 | 4 | 8 | 10 | 2 | 4 | 8 | 7 | 2 | 2 | 4 | 3 | 6 | 7 |
| 15 | 4 | 8 | 7 | 4 | 5 | 3 | 5 | 3 | 6 | 4 | 1 | 4 | 5 | 9 | 9 |
| 20 | 5 | 4 | 12 | 7 | 5 | 2 | 3 | 4 | 2 | 3 | 5 | 4 | 10 | 9 | 9 |
| 25 | 4 | 3 | 8 | 9 | 13 | 1 | 3 | 2 | 3 | 1 | 2 | 7 | 10 | 9 | 3 |
| 30 | 3 | 6 | 4 | 13 | 3 | 1 | 0 | 5 | 1 | 1 | 6 | 3 | 4 | 5 | 6 |
| 35 | 3 | 3 | 4 | 2 | 6 | 0 | 1 | 0 | 2 | 1 | 1 | 3 | 3 | 6 | 2 |
| 40 | 2 | 5 | 4 | 1 | 2 | 3 | 0 | 1 | 0 | 1 | 3 | 3 | 4 | 1 | 5 |
| 45 | 2 | 1 | 4 | 3 | 2 | 0 | 1 | 1 | 0 | 2 | 1 | 1 | 1 | 1 | 0 |
| 50 | 1 | 3 | 0 | 3 | 2 | 0 | 0 | 0 | 2 | 0 | 0 | 4 | 2 | 0 | 3 |
| 55 | 0 | 1 | 3 | 2 | 1 | 0 | 0 | 0 | 0 | 0 | 1 | 1 | 2 | 3 | 0 |
| 60 | 1 | 0 | 1 | 0 | 2 | 0 | 1 | 0 | 0 | 0 | 1 | 1 | 1 | 2 | 2 |
| 65 | 0 | 1 | 0 | 1 | 0 | 0 | 0 | 0 | 0 | 0 | 0 | 1 | 0 | 0 | 0 |
| 70 | 1 | 1 | 1 | 1 | 1 | 0 | 0 | 0 | 0 | 0 | 1 | 0 | 0 | 1 | 1 |
| 75 | 0 | 0 | 0 | 0 | 0 | 0 | 0 | 1 | 0 | 0 | 0 | 1 | 1 | 0 | 0 |
| 80 | 0 | 1 | 0 | 0 | 0 | 0 | 0 | 0 | 0 | 0 | 0 | 1 | 0 | 0 | 0 |
| 85 | 0 | 0 | 0 | 0 | 0 | 0 | 0 | 0 | 0 | 0 | 0 | 0 | 0 | 0 | 0 |
| 90 | 1 | 0 | 0 | 0 | 0 | 0 | 0 | 0 | 0 | 0 | 1 | 0 | 0 | 0 | 0 |
| 95 | 0 | 0 | 0 | 0 | 0 | 0 | 0 | 0 | 0 | 0 | 0 | 0 | 0 | 0 | 0 |
| 100 | 0 | 1 | 0 | 0 | 0 | 0 | 0 | 0 | 0 | 0 | 0 | 0 | 0 | 0 | 0 |
| 105 | 2 | 0 | 1 | 1 | 1 | 3 | 0 | 0 | 0 | 0 | 2 | 1 | 1 | 1 | 1 |

Table 8.3: Histogram of the height variation of the differences in the mean wind flow between the daily optical and radar winds. The associated uncertainties were typically ~12 $ms^{-1}$.

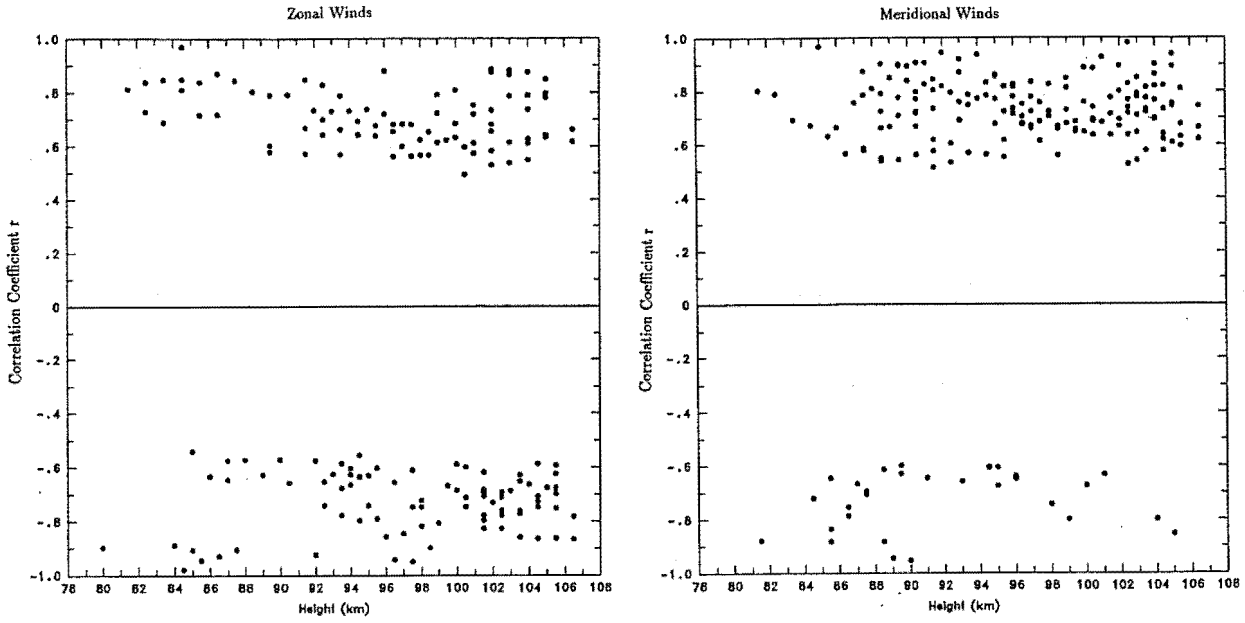


Figure 8.4: The heights and values of the correlations between the night time optical and radar hourly mean winds in the 80–105 km region which were statistically significant to better than the 95% confidence level.

of 6.4 km.

The differences found between the zonal and meridional distributions indicate that there are important differences between the radar and optical winds with respect to the wind component. The greater degree of variability in the zonal wind comparisons may be due to the larger sampling area of the radar in the zonal direction (48 km compared to 37 km in the meridional direction). The larger zonal sampling area arises because the horizontal area probed by the radar is the product of the polar diagram of the radar and the aspect sensitivity of the scatterers (see Section 4.2.2). Because the beam is wider in the zonal direction, a wider range of scattering angles will be received. Consequently, the spatial correlation function in the zonal direction will be narrower and so, for a given antenna spacing, a smaller cross-correlation will be obtained and will therefore be more susceptible to noise and interference problems. This will also result in a greater variance in the zonal wind values compared to the corresponding meridional winds. The distribution of the east-looking FPS/zonal radar wind comparisons is very similar to the FPS/radar zonal winds with no significant differences occurring between two distributions.

The yield of significant correlations between the monthly optical and radar hourly mean winds was similar to the daily wind results. Between 8 to 10% of the total number of

possible correlations were significant. This yield is slightly higher than for the daily correlations, possibly because of the effect of averaging the radar wind data over several days. The yield of either positive or negative correlations for a particular wind component was similar to the daily result. The meridional optical/radar wind correlations yielded about 3 times as many significant positive correlations as the zonal correlations. The yield of significant positive or negative correlations between the zonal and east-looking optical/radar winds was not significantly different from that of two random distributions. The average height of the significant positive correlations between the monthly meridional optical and radar hourly mean winds was 96.2 km with a standard deviation of 6.6 km.

As well as the correlating the superposed hourly mean winds for each month, correlations were also calculated between the concatenated individual FPS and radar hourly mean winds for the selected nights during each month. Although this method provided a larger number of points for the correlation calculation this advantage was negated by the individual random variations in each time series so that there was no significant increase in the yield of significant correlations.

The mesospheric 557.7 nm emission originates near 95–100 km in height (Hernandez et al. 1995). If the FPS and radar are simultaneously sampling similar volume regions and if the 557.7 nm emission height maximum remains constant during the night then one would expect to obtain a high yield or, at least, a grouping of significant positive optical/radar wind correlations in the 95–100 km height region, in particular, when the optical winds are derived from east-looking observations almost directly above the radar station. The night time optical/radar wind correlation yields are however much less than expected. A grouping of significant correlations in the 90–100 km is indicated for the meridional winds but no such grouping is indicated for the zonal wind components.

The low yield of significant correlations between the individual hourly optical and radar winds is contrary to the results obtained by earlier optical/radar wind comparison studies such as by Lloyd et al. (1990), Manson et al. (1991) and Phillips et al. (1994) which all reported generally good, and sometimes excellent, agreement was found between the nightly optical and radar winds. The high level of RF noise and interference and the small number of night time hourly values contributed significantly to the low yields.

On occasions, statistically significant positive and negative correlations occurred at different heights during the same night which may indicate the presence of vertical structure in the radar or optical winds. There is evidence from results obtained by Shepherd et al. (1995) of variability in the height of the airglow layer of about 5 km over a period of several hours at mid-latitudes. Furthermore, Hernandez et al. (1995) reported daily height variations of about 2 km of the 557.7 nm layer above New Zealand. The range of heights was about 5 km in total (Hernandez et al. 1995).

### 8.1.2 Daily Mean Winds

Comparisons of the daily mean optical and radar wind vectors yielded similar results to those of the tidal fits and the correlations. The magnitude of optical wind vector is generally 5–15 $ms^{-1}$ larger than the corresponding radar winds at heights above 90 km, with the differences being generally less than 25 $ms^{-1}$. There was also no apparent seasonal dependency in the direction differences between the optical and radar wind vectors. The direction differences are shown as height histograms in Table 8.4. Only a weak pattern is evident due to the small number of nights on which the correlation of fit for both the optical and radar winds was significant to the 95% level or better (39–60 nights depending on the height, as discussed earlier). However, there appears to be a consistent difference of 0–30$^o$ between the optical and radar wind directions with no apparent systematic variation with height. There is also a group of nights with direction differences of $\sim$120$^o$ at 95–100 km which appears to be related to the systematic NW-SE direction alignment of the daily mean radar wind vectors, as discussed in chapter 4.

If one assumes that the RF noise is purely random then its effect upon the radar winds would be reduced by increasing the number of days. Table 8.5 shows the height histograms of the daily wind vector differences for all 103 days, independent of their goodness-of-fit. The histograms (Tables 8.4 and 8.5) are relatively consistent with each other and it illustrates the necessity for a large number of nights in order to obtain a clear understanding of the wind vector differences. The weak pattern exhibited in Table 8.4 is now more clearly evident in Table 8.5. In the 90–105 km region, there are a large number of nights (20–30) on which the optical and radar wind vectors differ by less than 60$^o$ and there are a similar number of nights on which the wind vectors differ by $\sim$120$^o$. The average difference in the directions of the optical and radar wind vectors was 30–50$^o$ with a standard deviation of 90–100$^o$.

The velocity height profiles (solid curve) of the mean radar winds on the night of 4 March 1994, a typical night, are shown in Figure 8.5 together with mean FPS wind (vertical line). The mean winds were derived from simultaneous hourly winds and the error bars are the standard deviations of the mean values.

The heights of agreement between the simultaneous optical and radar night time vector mean winds are presented as histograms in Figure 8.6. The histograms of the zonal (closed circles) and east-looking FPS (open circles) daily mean wind agreements exhibit a similar form with an increase in the number of agreement heights with height. In general, these two distributions exhibit a peak at about 98–100 km. The median height of agreement between the daily mean zonal radar and optical wind was 94.0 km with an inter-quartile range of 12.0 km km from 1356 values. The median height of agreement between the daily mean

| Dir | | Ht | km | | |
|---|---|---|---|---|---|
| **Diff (°)** | **85** | **90** | **95** | **100** | **105** |
| -180 | 2 | 2 | 3 | 5 | 2 |
| -150 | 4 | 3 | 3 | 3 | 3 |
| -120 | 3 | 4 | 5 | 5 | 2 |
| -90 | 1 | 3 | 1 | 5 | 6 |
| -60 | 1 | 1 | 8 | 2 | 9 |
| -30 | 6 | 7 | 5 | 7 | 8 |
| 30 | 2 | 6 | 6 | 5 | 7 |
| 60 | 1 | 3 | 5 | 5 | 8 |
| 90 | 5 | 6 | 5 | 2 | 2 |
| 120 | 5 | 6 | 9 | 11 | 7 |
| 150 | 4 | 4 | 6 | 4 | 4 |
| 180 | 5 | 5 | 3 | 3 | 2 |

Table 8.4: Histogram of the height variation of the differences in the direction of the mean wind vector between the daily optical and radar winds for days on which the optical and radar correlations of fit were significant to 95% or better.

| Dir | | Ht | km | | |
|---|---|---|---|---|---|
| **Diff (°)** | **85** | **90** | **95** | **100** | **105** |
| -180 | 4 | 3 | 6 | 6 | 3 |
| -150 | 4 | 4 | 6 | 6 | 3 |
| -120 | 5 | 8 | 8 | 7 | 4 |
| -90 | 3 | 7 | 2 | 8 | 11 |
| -60 | 4 | 4 | 10 | 6 | 13 |
| -30 | 12 | 13 | 11 | 12 | 15 |
| 30 | 5 | 10 | 8 | 12 | 10 |
| 60 | 5 | 11 | 8 | 9 | 10 |
| 90 | 7 | 9 | 10 | 8 | 6 |
| 120 | 9 | 12 | 12 | 14 | 9 |
| 150 | 6 | 9 | 9 | 8 | 7 |
| 180 | 7 | 7 | 11 | 7 | 12 |

Table 8.5: Histogram of the height variation of the differences in the direction of the mean wind vector between the daily optical and radar winds for all 103 days.

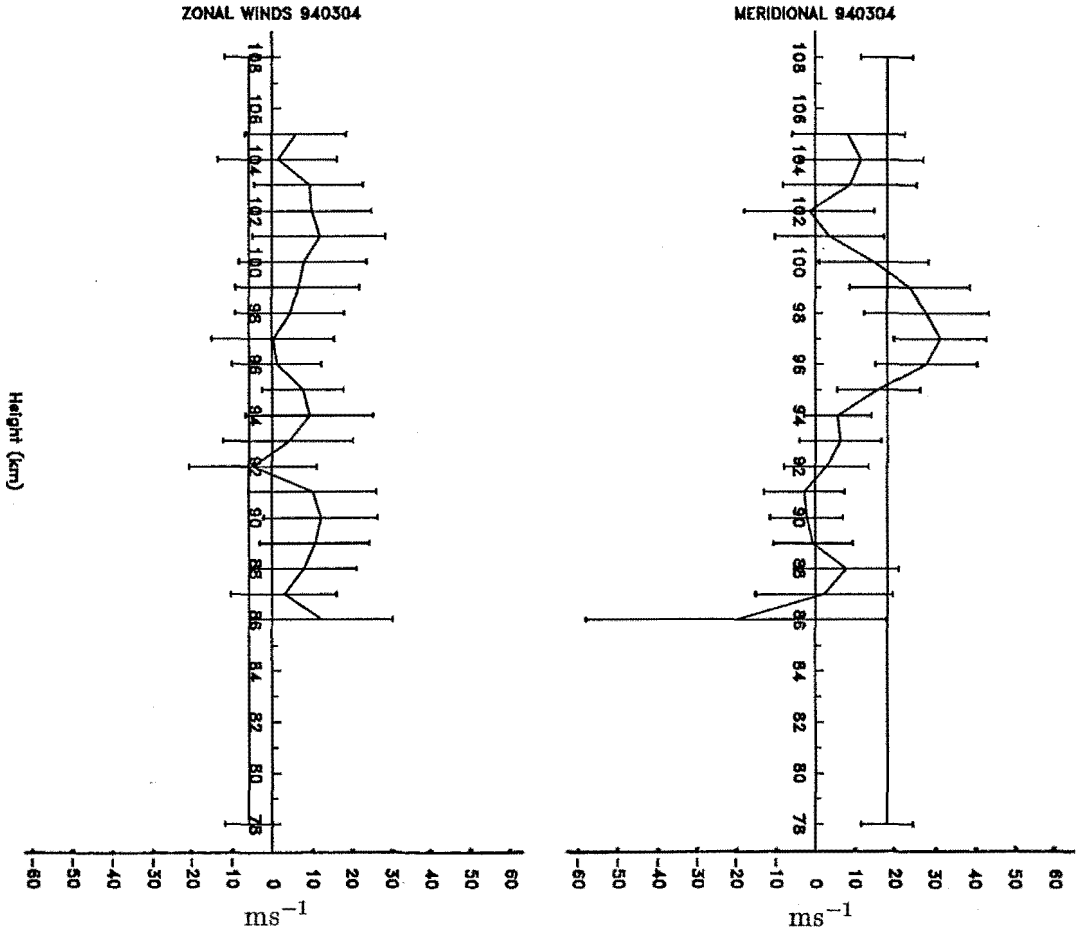


Figure 8.5: Velocity height profiles of the night time vector mean radar (curves) and FPS winds (vertical lines) for 4 March 1994.

east-looking optical winds and the zonal radar winds was also 94.0 km with an inter-quartile range of 12.0 from 1420 values.

The distribution of the meridional mean wind agreements is much flatter than the two zonal distributions and exhibits a peak near about 100 km. The flattening of the distribution is most probably due to a large number of meridional wind agreements below 90 km. This is a consequence of the small meridional mean wind values occurring there and the increase in the uncertainty of the wind values with decreasing height. This effect tended to reduce the average height of agreement between the two sets of mean winds. The average height of agreement between the daily mean meridional optical and radar winds was 94.0 km with an inter-quartile range of 13 km from 1578 values.

It must be noted that the three histograms in Figure 8.6 comprise heights of agreement which are not all independent because of the 5-km binning interval used and the 4.5 km width of the transmitter pulse. This effect will tend to increase the yield of heights at which the optical and radar mean winds agree and it will cause a smearing of the height distribution of agreements, but the specific shape of the distribution will remain essentially unaltered.

A similar yield of agreements was obtained from comparing the monthly optical and radar mean night time wind values but will not be shown for reasons of brevity. The zonal and meridional distributions were both slightly flatter for a similar reason to daily night winds.

## 8.2 Monthly Winds

### 8.2.1 Monthly Hourly Mean Winds

Figures 8.7 and 8.8 are contour plots of the simultaneous optical and radar hourly mean winds for each month for the period of this project. These figures essentially summarise the comparisons of the radar and optical hourly mean winds and they consist of the 103 days of simultaneous optical and radar wind data. The data presented in these figures have been treated in the same manner in order to produce hourly mean wind values for each month. Each contour corresponds to a velocity change of 10 $ms^{-1}$ with white corresponding to maximum positive zonal (eastward) or meridional (northward) wind velocity and black corresponding to maximum negative zonal (westward) or meridional (southward) wind velocity.

Figures 8.7a–c show the zonal, meridional and east-looking FPS monthly hourly mean winds. The FPS winds exhibit a smooth variation throughout the night. The semi-diurnal tide and the seasonal variation of its phase is clearly evident in the optical wind fields. The total seasonal variation in phase is about 7 hours with the rate of phase change being

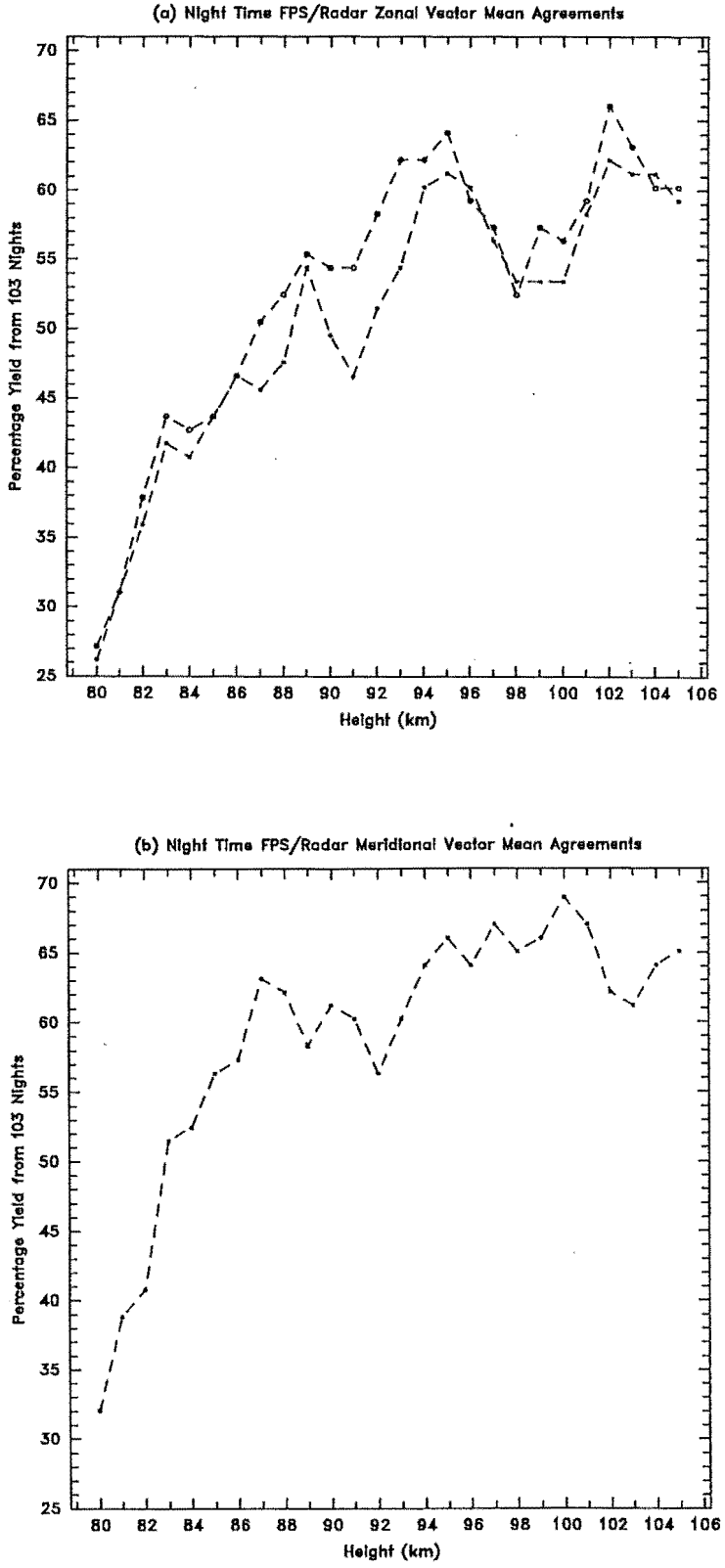


Figure 8.6: Histogram of the yield of heights of agreement between the night time vector mean optical winds. (a) Zonal (filled circles) and East-looking FPS (open circles) (b) Meridional.

greatest at about 3 weeks after the autumn equinox during April/May. Maximum westward wind flow occurs during the autumn equinox at about 13:00 UT. The east-looking FPS winds are very similar to the FPS zonal winds although there are some small differences. The duration of maximum eastward flow appears to be slightly longer in the zonal winds compared to the east-looking winds. During the next 2–3 months the night time wind flow has reversed to maximum eastward flow. Another cell of eastward flow also occurs from October through to March prior to midnight (12:00 UT). A weak westward flow occurs centred near 16:00 UT around September in both the zonal and east-looking winds.

In the meridional optical wind field there is a strong northward flow centred near 90:00 UT during January. A small cell of strong southward flow is seen near 17:00 UT during March/April and another cell of strong southward flow occurs near 10:00 UT during winter. This is gradually replaced by a northward flow centred near midnight (0:00 UT) after spring equinox. The time of maximum northward flow gradually decreases after summer solstice to be centred near 10:00 UT in January.

Figure 8.8a–d show the zonal and meridional radar monthly hourly mean winds at 100 km and 95 km, respectively, for the same days presented in Figure 8.7a–c. This region is the generally accepted height region of occurrence of the 557.7 nm emission (Hernandez et al. 1995). The radar wind fields at 95 and 100 km are characterised by the presence of short time-scale ($\sim$ 1 hour) variations. There is no smooth night time wind variation as seen in the optical winds. It is apparent that, on the time-scale of hours, no obvious correspondence exists between the optical and radar wind fields. This is because RF noise dominates the radar wind values (Figure 5.6) and so no useful radar/optical wind comparison can be made on this time scale. Figure 8.8a–d comprise simultaneous hourly winds, therefore any inter-annual wind variability would be expected to be similar for both sets.

Figures 8.9a–d are contour plots derived from the hourly mean radar winds at 95 and 100 km for the entire term of this project, a total of 1246 days. Each contour corresponds to a velocity change of 10 $ms^{-1}$ with white corresponding to maximum positive zonal (eastward) or meridional (northward) wind velocity and black corresponding to maximum negative zonal (westward) or meridional (southward) wind velocity. The time scales of the wind variations exhibited in these plots are similar to those in the FPS plots of Figure 8.7a–c but, despite the increased amount of radar data utilised, there is still no correspondence between the radar and optical plots.

### Tidal Fit Comparisons

Above 90 km, for the majority of the year, the amplitude of the semi-diurnal tide exhibited by the monthly optical winds is generally larger than the corresponding radar tidal

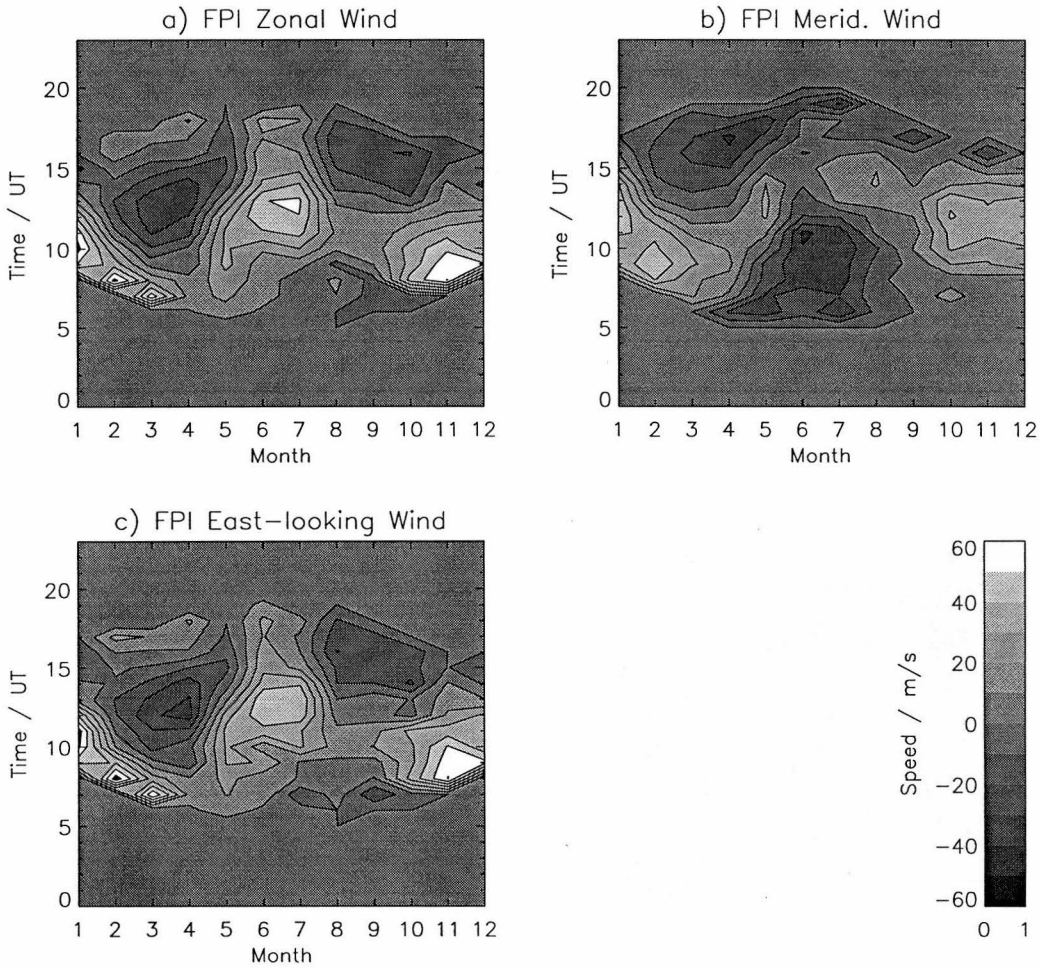


Figure 8.7: Contour plot of the (a) zonal, (b) meridional and (c) east-looking monthly hourly mean FPS winds for the 103 nights.

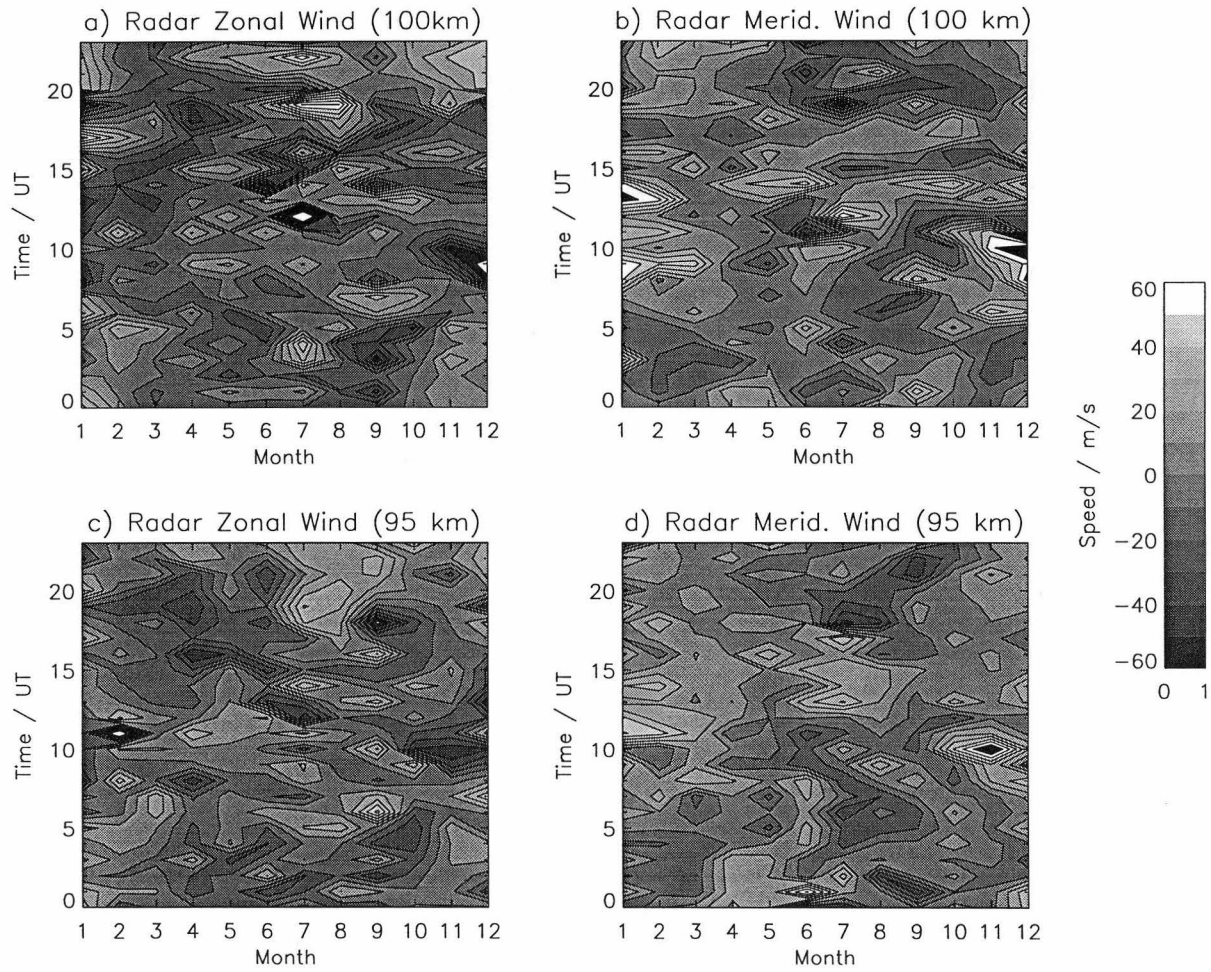


Figure 8.8: Contour plots of the FPS-simultaneous zonal and meridional monthly hourly mean radar winds for the 103 nights at 95 km (a and b) and 100 km (c and d)

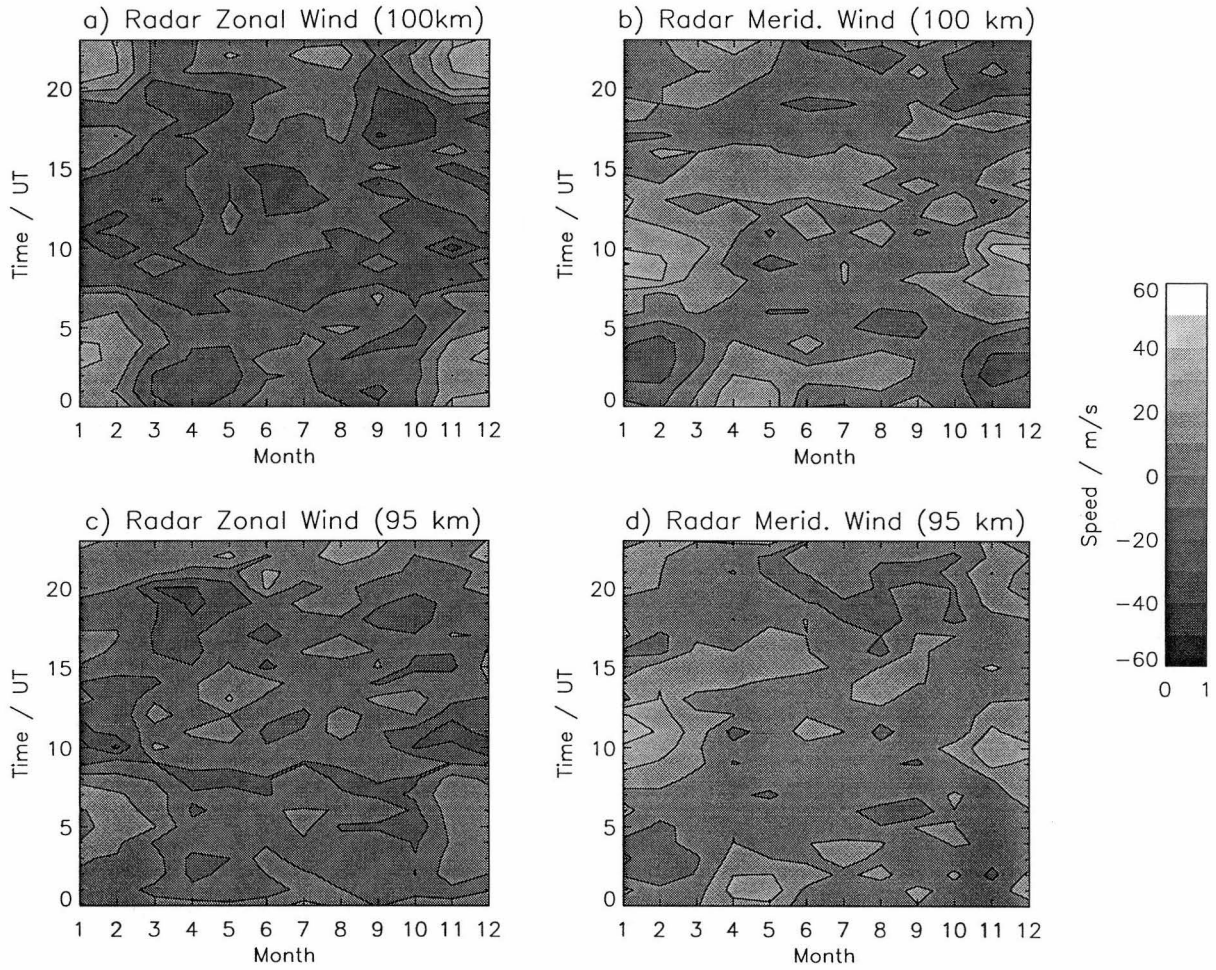


Figure 8.9: Contour plots of the zonal and meridional monthly hourly mean radar winds at 95 km (a and b) and 100 km (c and d) derived from the entire set of data for the term of this project.

amplitude. The zonal amplitude differences exhibit a quasi-annual variation which are largest ($\sim$15–25 ms$^{-1}$) from about one month prior to the summer solstice through to April. During the winter and the spring equinox only small differences ($\leq$10 ms$^{-1}$) are exhibited. The meridional winds exhibit a similar quasi-annual variation but the time of occurrence of the difference maximum occurs about one month later than the corresponding zonal winds with the maximum amplitude of about 10–20 ms$^{-1}$. There are small differences of up to 0–5 ms$^{-1}$ occurring from June until September. The differences increase again in October towards the summer maximum. The inter-annual variability of the semi-diurnal tide contributed $\sim$20 ms$^{-1}$ to the spread in the amplitude differences from year to year for a particular month.

The differences in the mean wind between the zonal and meridional optical/radar hourly mean winds for each month are presented in Figure 8.11. A semi-annual variation in the difference is apparent. The zonal mean wind differences are greatest around 2–3 months centred on the summer and winter solstices. During this time the optical winds are 30–40 ms$^{-1}$ larger than the corresponding radar winds. The differences are smallest (0–10 ms$^{-1}$) around the equinoxes. The meridional mean optical/radar wind differences exhibit a weak annual variation, although the uncertainties of the differences are large compared to the variation. The radar winds are generally larger than the optical winds by $\sim$15 ms$^{-1}$ during 2–3 months centred on the autumn equinox and less eastward than the optical winds during 2–3 months centred on the spring equinox. During the summer and winter solstices, the optical/radar mean wind differences are negligible. The inter-annual variability of the mean wind differences of both components is $\sim$15–20 ms$^{-1}$.

The seasonal variation in the optical/radar mean wind differences seen in Figure 8.11 are similar to the daily mean wind differences in Figure 8.3, but are smoother due to the averaging of the monthly winds. The mean wind differences are greatest when the optical mean winds are at their seasonal maximum. The reason for the differences is unclear but is it possibly due to the same reasons responsible for the FPS/radar tidal amplitude differences.

## 8.3 Optical/Radar Winds Comparisons and UARS Observations

Figure 8.12 shows the zonally-averaged volume emission rate height profiles of the 557.7 nm emission at 4 hours local time (16:00 UT) for the two-month period of March/April 1993. The 557.7 nm emission maximum is centred near 93 km and the height uncertainty of the profile is $\pm$1 km (Hernandez et al. 1995). These data were derived from measurements made by the WINDII instrument aboard the UARS satellite (Shepherd et al. 1995) for the latitude corresponding to Mt. John and Birdlings Flat (44°S). The WINDII data provided an excellent way of ascertaining the meaning of the results of the optical/radar wind comparisons

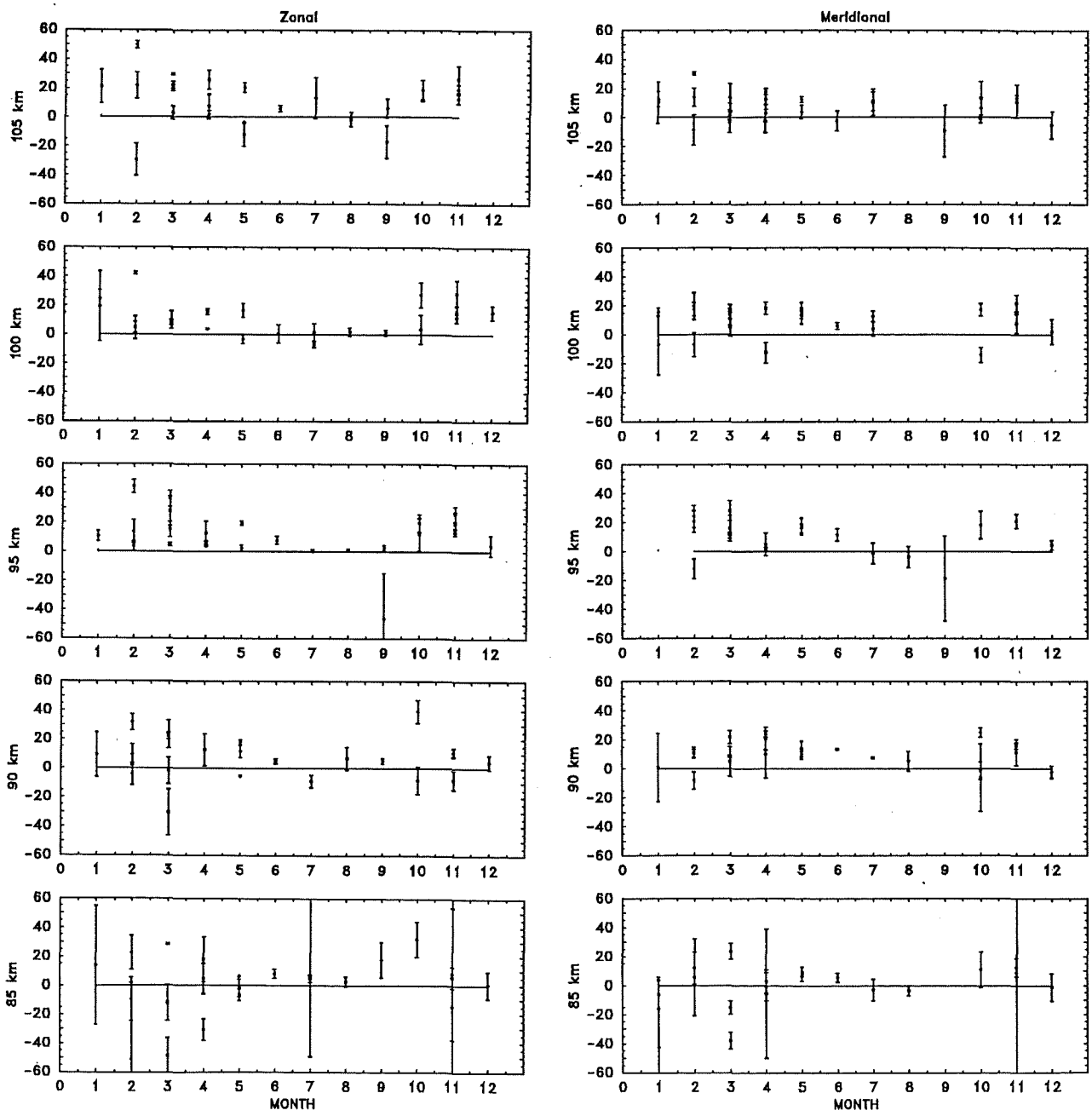


Figure 8.10: Differences in the amplitude of the semi-diurnal tide between the monthly optical and radar winds as a function of month.

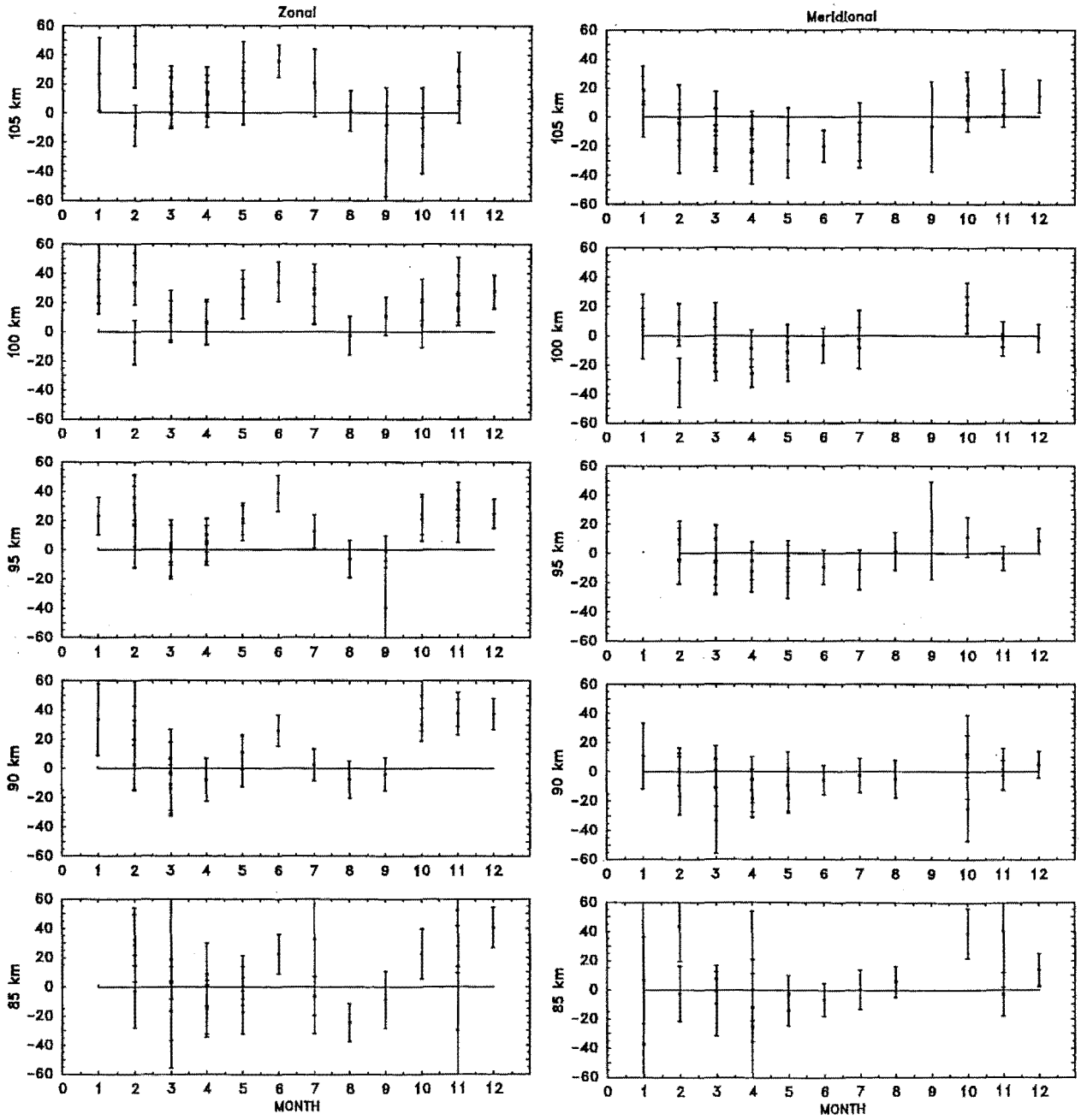


Figure 8.11: Optical/radar daily mean wind differences as a function of month.

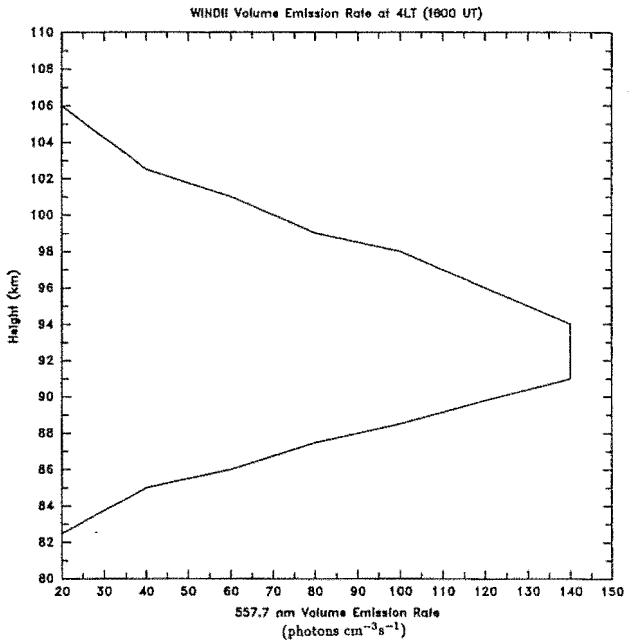


Figure 8.12: Zonally-averaged volume emission rate height profile of the 557.7 nm emission at 44°S at 4 hours local time (16:00 UT) from March/April 1993. (Adapted from Shepherd et al. 1995).

obtained in this present project. The longitudinal extent of the observations associated with the emission profile was not stated.

Only seven (12%) suitable FPS nights were available during the March/April 1993 period. These were 930323, 26–28, 930401, 11, 28. The hourly winds for the mean diurnal variation of these nights were calculated from the raw FPS and radar winds. The radar winds were (i) straight binned over 5 km as in previous sections and (ii) vertically weighted according to the 557.7 nm emission profile at the corresponding hourly period in order to approximate the 557.7 nm emission profiles. The amplitude of the semi-diurnal wind exhibited in the hourly mean time series for both the optical and the radar winds was reduced by a factor of about 2 in the profile-weighted winds compared to the 5-km binned winds. The observed amplitude of the semi-diurnal tide will decrease as a consequence of increasing the heights over which the wind are averaged. The semi-diurnal tidal amplitude of the profile-weighted winds was small ($\sim$10–15 ms$^{-1}$), whereas the amplitude of the 5-km binned winds was comparable to the optical winds ($\sim$20–25 ms$^{-1}$). Therefore the 5-km binned radar winds were used in the comparison.

Figure 8.13 shows the hourly zonal and meridional radar wind height profiles centred at 16:00 hours UT (4 hours LT) for March/April 1993 coincident with the WINDII 557.7 nm emission distribution in Figure 8.12. The solid vertical bar is the FPS hourly mean wind and the error bars for both wind sets correspond to the standard deviation of the mean values. There is very good agreement between the optical and radar winds, especially in the 86–94 km

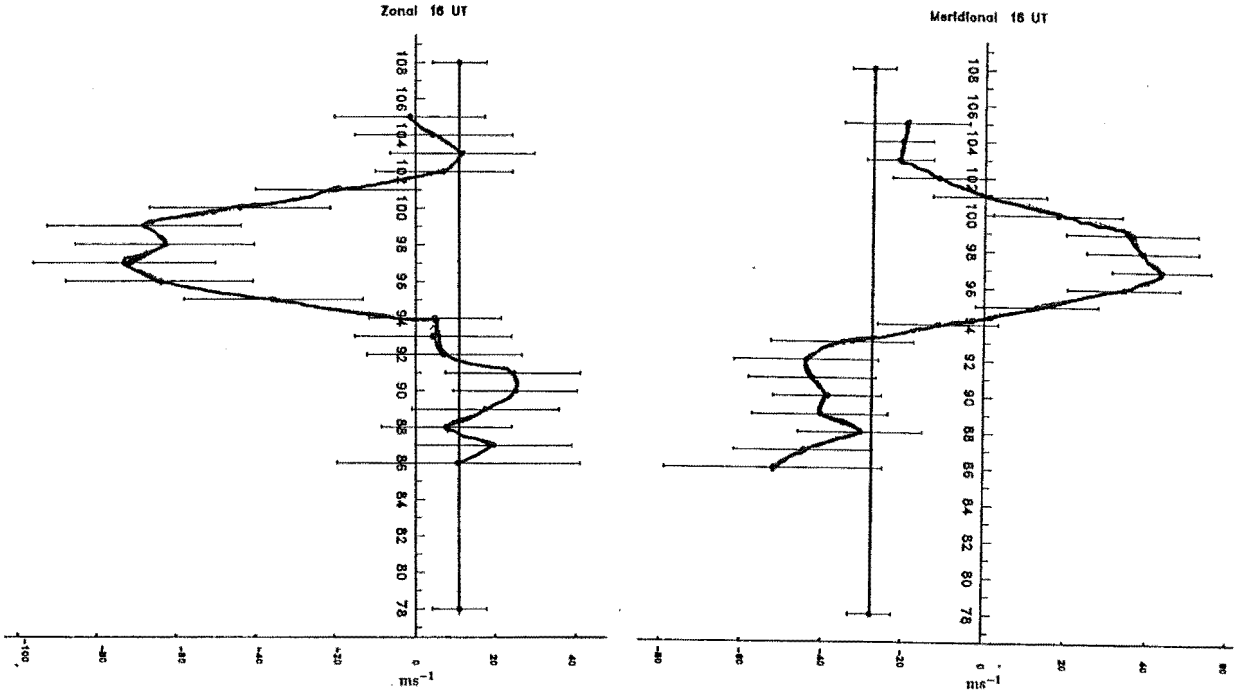


Figure 8.13: Hourly vector mean zonal and meridional radar and FPS wind height profiles centred at 16:00 hours UT (4 hours LT) for March/April 1993.

height region which is consistent with the height of the 557.7 nm emission from the WINDII profile in Figure 8.12. Both the optical and radar winds are in agreement in the 104–107 km region also, in both components. A wind shear of $\sim$10–15 $ms^{-1}km^{-1}$ is exhibited in the radar zonal winds which results in the optical and radar winds being in opposite directions in the 95–100 km region during this hour.

The heights of agreement between the hourly mean FPS and radar winds during the mean night for March/April 1993 are shown in Figure 8.14. The heights of best agreement are shown by filled circles (zonal winds) and open circles (meridional winds). From early evening through to 14:00 UT (02:00 hours LT), there is agreement between the two winds in the 95–105 km region. Two hours later, at 16:00 UT (04:00 hours LT), there is a marked bifurcation in the heights of agreement of nearly 10 km (Figure 8.13).

Correlations of the winds for the period do not indicate any statistically significant agreement between the hourly night time optical and radar winds in the 80–105 km region. The radar and optical hourly night time winds were cross-correlated with the assumption that the 557.7 nm emission layer remained at a fixed height during the night. It is possible that the lack of agreement between the optical and radar night time winds is due to the height variations of the 557.7 nm emission during the mean night for March/April. The level of RF noise associated with the radar winds was however a very significant factor.

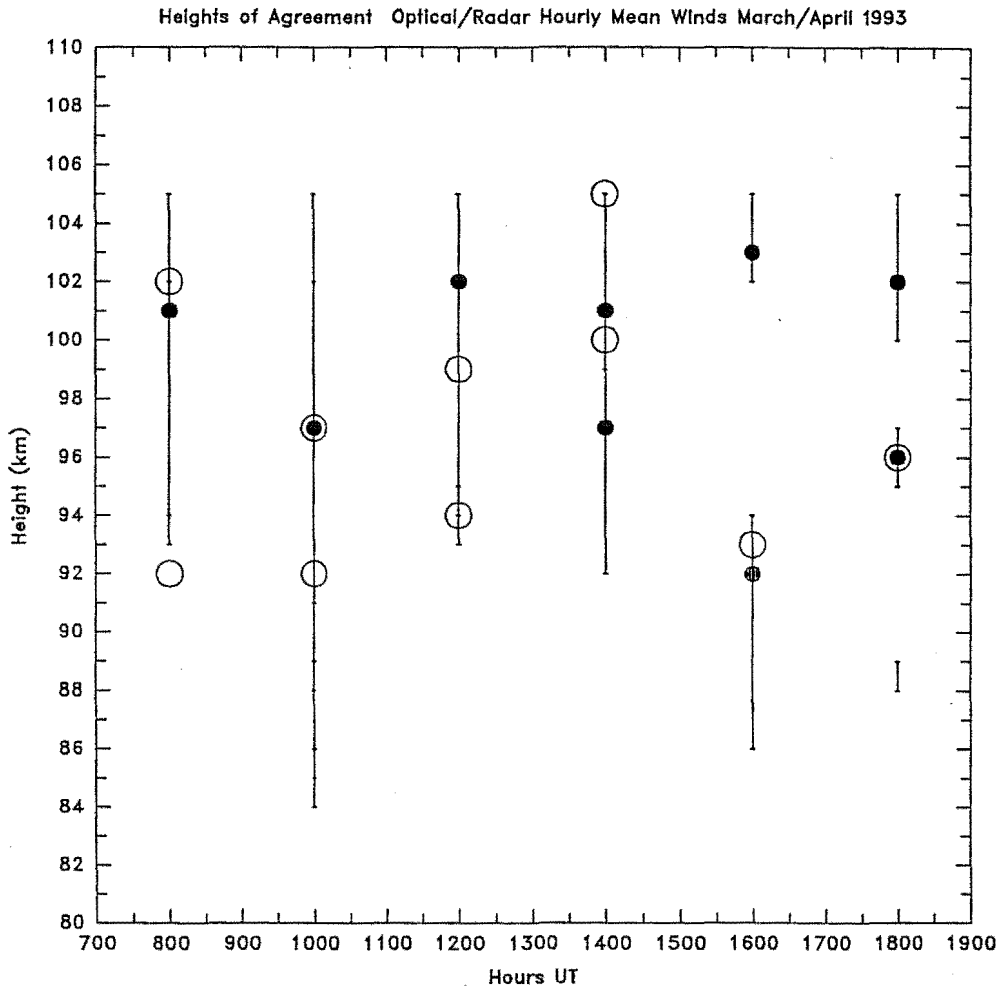


Figure 8.14: Heights of agreement between the optical and radar hourly mean winds during the mean night of March/April 1993 (Best agreements are shown as filled circles (zonal) and open circles (meridional).

Height variations of the emission layer may explain the low yield of significant correlations between the optical and radar winds on the 103 nights. Evidence of large and rapid variations 557.7 nm emission distribution, both vertically and horizontally, has been reported by several rocket and satellite workers. Donahue et al. (1973) and Wasser and Donahue (1979) used on board satellite photometer limb data and found large variations in the vertical and horizontal 557.7 nm emission distribution. Swenson et al. (1989) also found evidence of large variations in the peak tangent height of the 557.7 nm emission from limb observations made aboard the shuttle orbiter Spacelab 1 mission of December 1983. Observations of the 557.7 nm emission layer were made along an orbit track centred at about 45°S indicated the height of maximum 557.7 nm emission at 22:25 LT to occur near 90 km (Swenson et al. 1989). These three studies, using tangent peak height measurements, were made under the assumption that any horizontal variations were negligible.

# Chapter 9

# Conclusions

## 9.1 Introduction

This project involved the comparison of horizontal winds in the upper mesosphere at 80–105 km which were obtained by two different techniques. Optical Doppler winds were derived from night time observations of the mesospheric 557.7 nm airglow emission near 95 km (FWHM intensity ~10-12 km) (Shepherd et al. 1995) using a Fabry-Perot Spectrometer (FPS) during the period February 1991 to July 1994. These were compared to simultaneous radar winds obtained using a partial-reflection MF (2.4 MHz) wind–profiling radar. The comparisons were made on 103 nights considered suitable by exhibiting no cloud and low magnetic activity (low $K_p$) in order to eliminate the possibility of auroral contamination in the FPS measurements.

The two techniques appear to record different physical phenomena in the atmosphere over differing spatial and temporal scales. The FPS samples a cylindrical volume of emission approximately 30 km long and 3 km in diameter at 95–100 km. Each FPS wind observation requires 10–15 minutes. The FPS observations consist of a repeating sequence of observations towards the four cardinal points (N, E, S, W) at an elevation of 20° above the horizon and in the zenith. Observations in opposite directions are approximately 500 km apart. The optical measurements obtained from opposite directions are combined into zonal and meridional winds and so the optical wind field is further averaged over a horizontal distance of 500 km. When the FPS was observing towards the east during its observing sequence the instruments sampled volumes separated by only 60 km.

The radar winds are derived from vertical probings which take about 80 s to complete. The transmitter pulse-width at half-power (FWHP) corresponds to a vertical height of 4.5 km. The radar probes an elliptical area approximately 48×37 km in horizontal extent at 95–100 km which is elongated EW. The horizontal extent of the radar probing is determined by the product of the radar polar diagram and the aspect sensitivity of the scatterers. Scat-

terers above 80 km have been reported to exhibit an aspect sensitivity of 15–20$^o$ (25–35 km at 95–100 km) (Vincent and Belrose 1978, Hocking 1979, Hocking and Vincent 1982). The EW elongation of the sampled area will result in lower FCA correlations in the zonal direction compared to the meridional direction. The resulting zonal winds will therefore exhibit a larger variance than the corresponding meridional winds.

## 9.2 Data Reduction and Quality

The optical and radar wind were not directly comparable because there were several differences between the optical and radar data acquisition techniques, but these differences were minimised by comparing time–averaged wind data. More importantly, the data from the two techniques could not be treated in exactly the same way. The main reason was because the yield of night time radar winds is less than during the day time due to the higher level (20–25 dB) of RF noise and interference associated with the radar wind measurements, while there were no optical wind measurements during the day.

The paucity of night time radar wind values necessitated, prior to time-averaging into 1-hour time bins, the grouping of the raw radar winds in 5-km height bins. Simultaneous raw radar winds which were separated by heights of $\sim$5 km or less were not independent, although raw winds from different times within the hour were independent. This averaging reduced the influence of the RF noise, and of oblique echoes which may allow a contribution from heights 5–6 km below the nominal vertical height of probing.

Because the hourly mean radar winds are partially independent over height and fully independent over time, the number of degrees of freedom will range from N/5 to N, where the factor of 5 would arise from the vertical bin size of 5 km if all points in the bin were completely dependent. The sample variances of the radar hourly mean winds will therefore be underestimated by up to a factor of $\sqrt{5}$, because all the binned values in one bin are assumed to be independent.

The amount of noise/interference was measured by the radar and found be similar to with the mean RF noise power measured independently in this region of the globe (Davies 1992). The noise power was greatest during the summer when the night time noise power enhancement could reach $\sim$25 dB and lowest during the winter when maximum values of $\sim$15-20 dB were typical.

The RF noise and interference arose for several reasons. The absence of a night time D region (and hence less absorption) enables MF radio signals to propagate large distances, resulting in interference. The paucity of night time radar echoes was further compounded by the size of the receiving array used in this project, which was larger than the optimum size (Golley and Rossiter 1970) by nearly a factor of two. As a result, the FCA procedure was

more susceptible to noise and hence the resulting radar winds exhibited large variances.

The optical winds clearly exhibit an oscillation with a period of 12 hours and whose behaviour is consistent with the semi-diurnal tide. The radar winds exhibited a larger amount of scatter than the optical winds and the semi-diurnal tidal oscillation was not as evident in the radar winds. A quantitative comparison of the quality of the two data sets was achieved by calculating the auto-correlation functions of the individual optical and radar hourly mean winds. The night time hourly mean radar winds were dominated by high-frequency variations which were uncorrelated over time-scales of 1 hour or less. Hourly mean radar wind values separated by more than 1 hour were not correlated at the 95% confidence level. In contrast to this, the optical winds exhibited a significant correlation over 1–2 hours, which would be expected from the relatively smooth semi-diurnal sinusoidal wind variation exhibited by the night time optical winds.

On monthly time scales, the radar winds were still dominated by uncorrelated high-frequency variations and the presence of a tidal oscillation was not found to occur at a level which was statistically significant to the 95% confidence level. A low–pass filter was applied to the radar wind data. The auto-correlation functions of the filtered radar wind data exhibited a statistically significant peak at the period corresponding to the semi-diurnal tide. The peak position was independent of the filter bandwidth. When random noise was passed through the same filter 12 hour peak was not present.

## 9.3 Optical/Radar Wind Comparison Results

### 9.3.1 Daily Winds

Cross-correlations between the simultaneous night time hourly mean optical and radar winds produced low yields of significant correlations but despite this, there were statistically significant differences between the zonal and meridional wind components in the results. The zonal wind correlations yielded relatively equal numbers of positive and negative correlations which were uniformly scattered between in height 80–105 km. The meridional wind correlations yielded more positive significant correlations than negative and a $\chi^2$ test indicated that this was statistically significant. The majority of positive significant meridional wind correlations tended to occur in the 90–105 km range.

The distribution of the significant positive correlations between the optical and radar winds enabled an estimate of the height of the 557.7 nm emission layer to be made. The average height of the significant positive correlations between the night time meridional FPS and radar hourly mean winds was 95.8 km with a standard deviation of 6.4 km. This height is agrees closely with the average height of 95.2 km obtained by Hernandez et al. (1995) from

studies of WINDII 557.7 nm emission data obtained above Mt. John during 1992–93. Only a very small number of negative significant correlations occurred in this height region, but mostly tending to occur in the 80–90 km region.

The zonal and meridional optical/radar wind comparison results indicate that there are important differences between the optical and radar winds with respect to comparison of the zonal and meridional wind components. The greater amount of variability in the zonal winds is the result of the larger sampling area of the radar in the zonal direction (48 km compared to 37 km in the meridional direction). The larger zonal sampling area arises because the horizontal area probed by the radar is the product of the polar diagram of the radar and the aspect sensitivity of the scatterers (see Section 4.2.2). Because the beam is wider in the zonal direction, a wider range of scattering angles will be received. Consequently, the spatial correlation function in the zonal direction will be narrower and so, for a given antenna spacing, a smaller cross-correlation will be obtained and will therefore be more susceptible to noise and interference problems.

The low yield of significant correlations between the individual hourly optical and radar winds is contrary to the results obtained by earlier optical/radar wind comparison studies such as by Lloyd et al. (1990), Manson et al. (1991) and Phillips et al. (1994) which all reported generally good, and sometimes excellent, agreement was found between the nightly optical and radar winds.

The distribution of daily mean radar wind vectors for all 103 days was aligned perpendicular to the direction of the magnetic meridian. This indicates that the radar winds at 85–105 km are possibly under partial geomagnetic control. This is consistent with the findings of Stubbs (1977) who reported evidence of geomagnetic control of partial reflection winds above 100 km, and the tendency for the characteristic ellipse associated with the winds, to be aligned along the geomagnetic meridian. The direction of the radar wind velocity is biased towards the perpendicular of the characteristic ellipse (Phillips and Spencer 1955). There was no statistically significant elongation in the distribution of the corresponding FPS wind vectors.

As well as the zonal optical/radar and meridional optical/radar wind comparisons, a comparison was made of the east-pointing FPS winds and the zonal radar winds. The similar sampling volume would be expected to minimise any possible comparison differences which may arise due to the combination of the east- and west-pointing FPS into the FPS zonal winds. There was, however, no significant difference between the results of the east-pointing FPS/zonal radar wind comparisons and the zonal optical/radar wind comparisons.

### 9.3.2 Tides

The optical and radar winds were least-squares fitted to 12-hour and a combination of 12- and 24-hour sinusoidal functions, respectively. The fit parameters were then compared. The paucity of night time radar wind data necessitated using the daytime winds in the radar wind fits.

Height histograms of the differences in the fitted phase of the semi-diurnal tide in the optical and radar winds indicated, like the night time cross-correlation results, that there were significant differences in the zonal and meridional comparisons. The phase differences of the zonal optical and radar winds were quite evenly scattered over the 12 possible hours. The meridional height histograms were more consistent and showed that the optical/radar phase differences tended to decrease from $\sim$-(1–5) hours near 90 km to $\sim\pm$(1–2) hours at 100–105 km, where the differences were smallest. The zonal histograms, although more scattered, indicated that the phase differences were also smallest in this height region.

The amplitudes of the semi-diurnal tide as exhibited in the optical and radar wind fields were investigated and the optical tidal amplitudes were generally slightly larger than the corresponding radar amplitudes. The median optical/radar semi-diurnal amplitude at a height of 95 km was 1.4 with a lower and upper quartile values of 1.0 and 2.5, respectively. The amplitude discrepancy was largest near 95 km. Discrepancies between the amplitudes of optical and radar winds have been reported by Phillips et al (1994) and Burrage et al. (1996).

Measurements obtained from the MU radar (an MST radar) operated by the Radio Atmospheric Science Center of the University of Kyoto, Japan were used by Dunford (pers. comm.) to derive over 7000 horizontal radar wind velocities by the Briggs (Briggs et al. 1950, Briggs 1984) and the Brown and Chapman (1972) methods. His results indicate that the latter method under-estimates the wind amplitude by about 1.2 times. This may be one reason for the FPS/radar wind amplitude discrepancy found in this present project.

The diurnal tide did not appear to have a significant effect on the least-squares fits of the optical winds. This was indicated by the large number of nights for which a high and significant correlation was obtained between the fit and the original FPS winds. Since the uncertainty of the hourly optical winds was typically 10–15 $ms^{-1}$, any modulation of the optical wind field by the diurnal tide would be less than this magnitude. An estimate of the relative amplitudes of the semi-diurnal and diurnal tides were obtained from the radar wind fits. In the 95–100 km height region, the semi-diurnal amplitude tended to be greater than the diurnal amplitude. The semi-diurnal/diurnal tidal amplitude ratio was 0.9 with lower and upper quartile values of 0.5 and 1.8, respectively.

### 9.3.3 Monthly Winds

Comparisons were made between the hourly mean night time FPS and radar winds for each month, averaged over the entire $3\frac{1}{2}$-year observing period. On this time-scale, the effects of wind variations which are not coherent on time scales of 12 hours or less, will be minimal. There was clearly no agreement between the optical/radar wind fields. The optical wind exhibited a smooth semi-diurnal variation, whose phase varied smoothly throughout the year. The radar wind field, despite a similar time-averaging, exhibited only short-period ($\sim$1 hour), apparently random, variations.

Comparisons of simultaneous hourly FPS and radar wind averaged over several nights during March/April 1993 were made in conjunction with a mean 557.7 nm emission height profile at 44°S from WINDII data for March/April (Shepherd et al. 1995). There was good agreement between the FPS and radar hourly winds height in the 86–94 km height region, with best agreement at 92 km. This agrees well with the height of 93 km for the emission maximum from the WINDII profile (Shepherd et al. 1995). The low height of the WINDII 557.7 nm emission has been reported to be lower than average during the autumn equinox (Hernandez et al. 1995).

## 9.4 Gravity Waves and Optical Winds

The FPS observing geometry and the vertical distribution of the 557.7 nm emission (FWHM intensity is 10–12 km) (Shepherd et al. 1995), place a lower limit on the optical detection of gravity wave propagation in the 95–100 km region. Wind oscillations with vertical wavelengths of the order of 15–20 km would be reduced because the measured FPS wind is a weighted mean of the vertical emission profile. Wind oscillations with horizontal wavelengths equal to the diameter of the observing area ($\sim$500 km) would be selectively detected. Wavelengths of smaller scale-sizes would tend to produce differences in the measured wind between opposite observing directions. Vincent (1984a) found from partial reflection radar measurements at Adelaide (35°S) that the average vertical wavelength of gravity wave activity at 85 km ranged from 5–30 km with an average of about 12 km with horizontal wavelengths ranging from 50–4000 km. Manson et al. (1979) reported gravity wave activity to be dominated by vertical scales of about 20 km. Similarly, Meek et al. (1985) reported vertical wavelengths predominantly in the 3–25 km range at heights of 80–110 km. Hence, it is possible that much gravity wave activity is not detectable by the FPS.

In addition to the FPS observing geometry, the FPS and radar employed different amounts of temporal averaging during wind measurements. The sampling time for each FPS measurement was about 12 minutes compared to about 80 seconds for a radar measurement,

a factor of 9, and ~60 minutes were required for an entire FPS observing cycle. FPS measurements obtained from opposite directions can be separated by about 30 minutes in time and so wind variations with periods comparable to or less than this will only be observed as variance in the winds.

## 9.5 Summary

The results of the FPS/radar wind comparisons were of limited success due to the significant effect of RF noise associated with the radar wind measurements. The meridional optical/radar wind comparisons produced more consistent results than the zonal wind comparisons. This was mainly due to the greater variability associated with the zonal radar winds as a result of the radar probing pattern.

The mean height of best agreement from the cross-correlations between the night time FPS and radar hourly mean winds was 95.8 km with a standard deviation of 6.4 km. This height is agrees closely with the generally accepted height of the 557.7 nm emission layer of ~95 km (O'Brien et al. 1965, Donahue et al 1973, Thomas and Young 1981, Shepherd et al. 1993b, 1995, Ward et al. 1995, Hernandez et al. (1995)). Hernandez et al. (1995) reported average height of 95.2 km from studies of WINDII 557.7 nm emission data obtained near Mt. John during 1992–93. The height of best agreement obtained from the comparison of the phase of the semi-diurnal tide fitted to the optical and radar winds was found to occur in the 100–105 km height region. This is ~5 km higher than the height obtained from the night time wind cross-correlations, but it is consistent with the results of Phillips et al. (1994). The tidal estimates used both day and night time radar data so the height discrepancy may be due to group retardation of the radar measurements (Fraser and Kochanski 1970, Namboothiri 1993).

In order to clarify the differences exhibited between the optical and radar wind fields the effect of the RF noise needs to be reduced. The installation of a new transmitter and coherent receivers has recently been completed and this has already increased the radar data yield and quality. The size of the radar receiving antenna array is soon to be reduced and transformed into an equilateral triangle configuration with sides of $\sim 1.5\lambda$. This configuration will also remove any possible bias in the radar wind directions along the hypotenuse of an array.

# Appendix A

# FPS Technical Details

## A.1 Etalon Reflectivity

The reflectivity, R, of the etalon coatings at the wavelengths investigated was determined by Hernandez and Smith (pers. comm.) using the technique described by Giacomo (1952). This technqiue involves the measurement of the transmission of light through the FPS with the etalon in place, and then, with the etalon removed. There are several advantages afforded by this method. It requires only the etalon and a standard broadline source and the entire etalon is sampled at once. Also, the results are independent of the surface quality of the mirror flats (Giacomo 1952). The etalon's absorption coefficient, A, due to losses such as caused by absorption and forward and backward scatter by the etalon coatings is small - only about 0.5% (Hernandez 1986), since R + T + A = 1, where R and T are the reflection and transmission coefficients, respectively. From Chapter 2, the response of an etalon to a very broad line is (Hernandez 1986)

$$Y = \frac{1-R}{1+R}[1 - \frac{A}{1-R}]^2 = \frac{T^2}{1-R^2} \tag{A.1}$$

Since Y and T can be measured directly, the reflectivity can easily be determined. It can be seen from Equation (A.1) that the reflectivity is independent of the surface quality of the mirror. The reflection coefficients of the etalon coatings for the Mt. John FPS are shown in Table A.1.

## A.2 Sign Convention of FPS Winds

Thoughout this project the meteorological convention was used to describe the optical and radar wind velocities. The wind velocity is positive if directed eastward or northward, and negative if directed westward or southward.

| Wavelength (nm) | R (%) |
|---|---|
| 557.7 | 79.4 |
| 632.8 | 76.8 |
| 840.0 | 79.0 |

Table A.1: Reflectivity of the etalon as determined by the Giacomo (1952) method (Hernandez and Smith pers. comm.).

The correct sign convention for the FPS winds was determined from first principles in the following manner. The intensity of the fringe pattern is recorded at the centre during scanning. This is known as central point scanning. If one considers the scanning setup in which the etalon gap distance decreases during the scan then the recorded fringes exhibit an increase in order with increasing bin number.

For normal incidence ($\cos\theta = 1.0$) Equation (3.2) becomes

$$n\lambda = 2d \tag{A.2}$$

The refractive index $\mu$ is taken to be $\sim$1.0 and so n $\propto \lambda^{-1}$. For a stationary source, the wavelength transmitted at maximum intensity is $\lambda$ and, for a given order $\lambda \propto$ d. If $\delta\lambda$ is the smallest resolvable wavelength then

$$\delta\lambda = \frac{2}{n}\delta d \tag{A.3}$$

So as $d$ increases by $\delta d$, $\lambda$ increases by $\delta\lambda$. As $d$ increases towards the right (increasing bin number), $\lambda$ also increases towards the right (redshift). As d decreases towards the left (decreasing bin number), $\lambda$ also decreases towards the left (blueshift). An approaching emission source will produce a fringe centred towards the left of a stationary source and a receding emission source would produce a fringe centred to the right.

If the FPS is observing in the north direction and a northward wind is blowing, the fringe maxima will be red-shifted to a higher bin number. If the wavelength shift relative to the zenith zero reference is calculated as direction minus zenith reference then a positive shift is obtained and so the sign of the wind is positive. This is in the correct meteorological convention. If a southward wind is blowing, then the fringe maxima will be blue-shifted to a lower bin number. The wind is approaching from the north so the wavelength shift relative to the zenith zero reference will be negative and so the sign of the wind will be negative.

If the FPS is observing in the south direction and a northward wind is blowing, the fringe maxima are blue-shifted to a lower bin number. The shift relative to the zenith zero

| Time Period | Pinhole size (mK) |
|---|---|
| Feb 1992 – May 1991 | 45.0 |
| May 1991 – Sep 1991 | 57.0 |
| 23 Sep 1991 – 11 Jan 1993 | 27.0 |
| 11 Jan 1993 – Present | 45.0 |

Table A.2: The time periods of the various sizes of the main pinhole employed in the FPS at Mt. John.

reference in this case is calculated as zenith reference minus direction and a positive shift is obtained. The change of order in the wavelength shift calculation allows for the meteorological convention. If the FPS is observing in the south direction and a southward wind is blowing, the fringe maxima are red-shifted to a higher bin number. If the shift relative to the zenith zero reference in this case is negative and so the sign of the wind is negative.

## A.3 Main Pinhole Aperture Size

The diameter, a, of the central pinhole aperture affects the resolving and light-gathering power of the FPS. For a fixed etalon gap distance, the aperture will sample a finite amount of a fringe order across its diameter, namely, n + $\epsilon/2\pi$ at the aperture centre, to n + $\epsilon/2\pi$ - k/$2\pi$ at the edge. The fraction of the order sampled by the aperture is therefore k/$2\pi$ (Vaughan 1989).

If the fringes, consisting of light of wavelength, $\lambda_0$, are formed on the aperture by a lens of focal length, f, the wavenumber interval sampled by the aperture is determined by (Vaughan 1989)

$$\Delta\sigma_k = \frac{a}{8\lambda_0 f^2} \tag{A.4}$$

It can be seen that the fraction of orders sampled by the aperture increases as the square of the aperture diameter increases. Therefore, a larger diameter aperture reduces the resolving power of the FPS.

During this project, various sizes of central pinhole apertures were employed in the FPS, corresponding to sampled wavenumber intervals ranging from 27.0 to 57.0 mK. A milli–Kayser (mK) is a unit of inverse length. For example, 57 mK = 57 $\times$ $10^{-3}$ $cm^{-1}$ or 57 $\times$ $10^{-3}$ wavenumbers. This was done in order to determine the optimum size, in terms of maximising the resolving power and count rate, for the two emission wavelengths that were simultaneously measured during FPS operation. The time–periods during which each aperture size was employed are listed in Table A.2.

# Appendix B

# FPS Non-linear Scanning

## B.1 FPS Piezoelectric Scanning

The scanning behaviour of piezoelectric material with regard to the FPS's has been described by Hernandez (1978) and their use has been reviewed by Vaughan (1989). A voltage change applied to piezoelectric material induces a strain upon the material causing it to increase in length parallel to the direction of the applied voltage. The amount of incremental length increase, $\Delta$L, is proportional to the voltage increment, $\Delta$V, which is applied across the material. For a stack of piezoelectric discs of thickness, t, and total length, l, this is described by the equation

$$\Delta l = d_{33}\frac{l}{t}\Delta V \tag{B.1}$$

where $d_{33}$ is the strain constant for the particular material (Vaughan 1989). Piezo-electric materials with large strain constants are desirable in order to obtain a larger length increase for a given voltage increment (Basedow and Cocks 1980). For piezoelectric discs, the strain constant parallel to the z-plane ($d_{33}$) is twice as large as the strain constant for tubes ($d_{31}$) and stacking also increases the amount of scanning that can be achieved.

The strain constant, $d_{33}$, for the piezoelectric material in the Mt. John etalon was calculated to be $(320 \pm 50) \times 10^{-12}\mathrm{mV}^{-1}$. This infers that the material was probably PZT-4 or PZT-5A (Vaughan 1989), although this is not certain. The material was originally believed to be PZT-8 but the amount of non-linearity exhibited by the piezoelectric crystals ($\sim$8–9%) is much greater than expected for PZT-8 ($\sim$1%). If the material is PZT-8, then it is possible that non-linearity is a result of the shape and construction of the spacers themselves. The individual piezo-electric crystals comprising each stack are flat, washer-shaped discs epoxied together. It is possible that when a voltage is applied to the stack, strains are induced which are directed radially outwards so that the stack dimensions not only vary longitudinally as intended, but also perpendicularly to the major axis of the stack. Being contact glued, the

perpendicular expansion is inhibited so strain occurs, which increases with increasing ramp voltage. The glue itself may also have become slightly electrically conductive. It is possible that impact knocks, possibly experienced during the etalon's shipment to New Zealand, may have also contributed to the larger-than-expected non-linear behaviour.

## B.2 FPS Record Linearisation

The linearisation coefficients, a and b, described in section 5.4, are wavelength-dependent and the following formulae allow for the conversion of coefficients from one wavelength to another:

$$b_2 = b_1^{\frac{\lambda_2}{\lambda_1}} \tag{B.2}$$

$$a_2 = \frac{a_1}{(1 + b_1^{\frac{\lambda_2}{\lambda_1}})} \tag{B.3}$$

The amount of non-linearity present in scanning operation of the piezo-electric crystals was initially determined in the following way. Fringe profile records, consisting of five 557.7 nm maxima instead of the usual three fringe maxima, were obtained. The two additional fringes were obtained by increasing the voltage range applied to the piezoelectric stacks and this would provide a more accurate determination of the linearisation coefficients than that obtained from the three-maxima fringe 557.7 nm data.

Three 557.7 nm five-fringe records from December 1990 were analysed. The linearisation coefficients were determined from the average of a least-squares fit to the fringe maxima. This procedure was repeated on nine sets of five-fringe records from a 632.8 nm frequency-stabilised He-Ne laser from September 1991 after the piezo stacks were interchanged. These possessed a much much higher S/N than the 557.7 nm fringe records and allowed a more accurate determination of the linearisation coefficients.

Table B.1 shows the slope coefficients (bold face) which were obtained in December 1990, when the inside set of piezo-electric crystals were used for scanning, and in September 1991, when the outside set were used for scanning, together with the coefficients for the other wavelength derived using Equations B.2 and B.3. The uncertainties expressed are the standard deviation of the mean value. It can be seen that there is a clear difference in the amount of non-linearity between the two sets amounting to about 0.45% for the 557.7 nm fringes and 0.51% for the 632.8 nm fringes.

Initially, the linearisation of a particular night's fringes was done using the value of b, derived from the five-maxima 557.7 nm fringes of December 1990 together with the particular night's average 557.7 nm value for a. Early on in the project, it was discovered

| Date | 557.7 nm | 632.8 nm |
|---|---|---|
| 901202 | **0.9336±0.0016** | 0.9250±0.0019 |
| 910921 | 0.9291±0.0003 | **0.9199±0.0003** |

Table B.1: Slope coefficients that were obtained in December 1990 and in September 1991 after the etalon scanning operation was reversed.

that the nightly average 557.7 nm slope coefficient, which was determined from the normal three-peak fringe records, was significantly lower than that obtained from the five-maxima fringes of December 1990. For example, the value of b for the night of 16 April 1991 was 0.9161 ± 0.0134. In addition to this, the linearised fringes possessed significant residual non-linearity which was indicated by successive free spectral range values within each record differing by 2–3%.

The difference in the linearisation slope coefficient between the three- and five-maxima fringe data is most probably due to the different behavioural characteristics in the piezoelectric stacks at different ramp gain settings of voltage ramp. The five-fringe records required a larger ramp voltage range than the three-fringe records. The non-linear behaviour of the piezoelectric stacks therefore appears to be dependent on the scanning voltage range used. The linearisation of the raw fringes to within 1% of the night time mean FSR (see Section 5.4) indicates that the first-order approximation is sufficient enough for the ~750 V ramp used in the scanning operation, but for larger ramp voltages a higher-order polynomial of the form $x_{i+1} = a + bx_i + cx_i^2$ would be required.

## B.3 Ramp Generator Linearity

The ramp generator controls the servo process of scanning the etalon. The output of the ramp generator was checked to determine whether it contributed to the observed non-linearity of the fringe data. The voltage, measured by a digital multimeter, was found for increasing gate values (0–377 octal or 0–256 decimal) and can be seen in Figure B.1. This plot is clearly linear within the limits of the uncertainty in the voltage measurement (0.01 V) and so the ramp generator did not significantly contribute to the non-linearity of the fringe records.

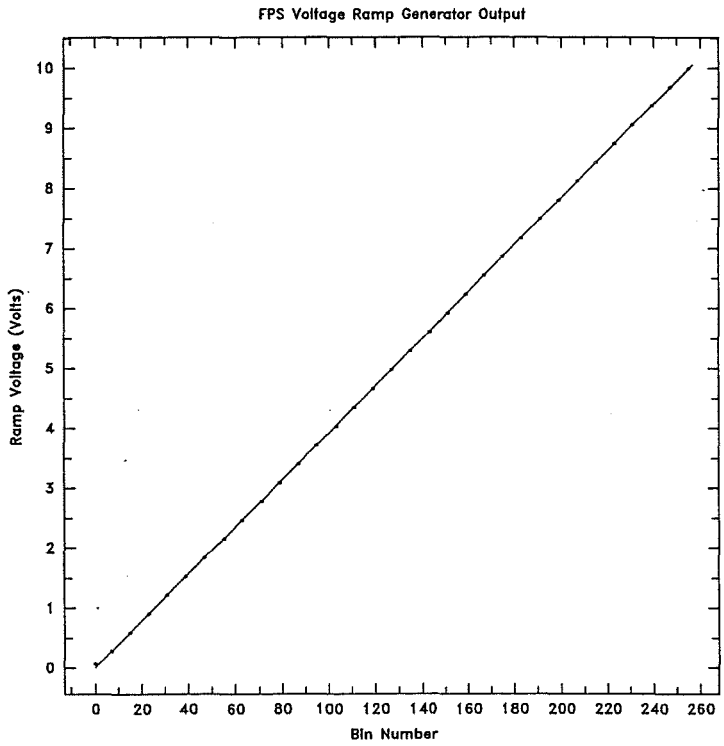


Figure B.1: The output of the ramp generator. The plot is linear to within 0.01 V.

# Appendix C

# Other FCA Parameters

There are several other parameters which are derived from the FCA procedure and some of these shown below.

The characteristic ellipse is defined as $\rho(0,0,\tau_{fad}) = \rho(C\tau_{fad}^2) = 0.5$ using Equation (4.11) and can be described as

$$\frac{A}{C}\epsilon^2 + \frac{B}{C}\eta^2 + \frac{2H}{C}\epsilon\eta = \tau_{fad}^2 \tag{C.1}$$

Another spatial parameter is $d_{0.5}$. This is the distance in which the spatial correlation drops to a half in the wind direction. In terms of the wind direction

$$\epsilon = \frac{d_{0.5}}{V}V_\epsilon \tag{C.2}$$

and

$$\eta = \frac{d_{0.5}}{V}V_\eta \tag{C.3}$$

If this is substituted into Equation (4.11), one obtains

$$[\frac{A}{C}V_{\epsilon^2} + \frac{B}{C}V_{\eta^2} + 2\frac{H}{C}V_\epsilon V_\eta]\frac{d_{0.5}^2}{V^2} = \tau_{fad}^2 \tag{C.4}$$

The fading time as seen by an observer moving with the drifting pattern is known as $T_{0.5}$. Therefore, from Equation (4.17)

$$\rho(0,0,T_{0.5}) = \rho(KT_{0.5}^2) = 0.5 \tag{C.5}$$

Using this result and the definition of the characteristic ellipse, given at the beginning of this discussion, it can be shown that the fading time observed by the moving observer is related to the fading time observed on the ground as

$$T_{0.5}^2 = \frac{C}{K}\tau_{fad}^2 \tag{C.6}$$

Another parameter which is important with respect to quantifying the random motion exhibited by the diffraction pattern is the random velocity parameter $(V_c)_v$. This is defined as the ratio of the scale size parameter $d_{0.5}$ to the time scale parameter $T_{0.5}$ and is a description of the amount of random change undergone by the pattern. However, it is not directly a physical measurement of the random motion (Briggs 1984).

$$(V_c)_v = \frac{d_{0.5}}{T_{0.5}} \tag{C.7}$$

This parameter is obtained by using the spatial correlation function of equation (4.13) and the relationships of Equations (C.4) and (C.6). As a result

$$(V_c)_v^2 = \frac{K}{C}\frac{d_{0.5}^2}{\tau_{fad}^2} = \frac{AV_x^2 + BV_y^2 + 2H[V_xV_y]}{C}\frac{d_{0.5}^2}{\tau_{fad}^2} \tag{C.8}$$

The value of $(V_c)_v^2$ can be determined because A/C, B/C and H/C are known. The $(V_c)_v^2$ may become negative as a result of statistical fluctuations when the random velocity associated with the pattern is near-zero. In this case the square root of the absolute value of $(V_c)_v{}^2$ is determined.

# References


Abbott, W.N., 1964, *Possible Correlations Between Sporadic-E and Low-Altitude Airglow Emission of 5577 Å in the Median Latitudes*, J. Atmos. Terr. Phys., **26**, 776–780.

Abreu, V.J., Schmitt, G.A., Hays, P.B., Meriwether, J.W., Tepley, C.A. and Cogger, L.L., 1983, *Atmospheric Scattering Effects on Ground-based Measurements of Thermospheric Winds*, Planet. Space Sci., **31**, No. 3, 303–310.

Akasofu, S.I., *Polar and Magnetospheric Substorms*, D. Reidel, Dordrecht, Holland, 1968.

Appleton, E.V., 1927, *The Influence of the Earth's Magnetic Field on Wireless Transmission*, U.R.S.I. Proceedings, Washington General Assembly.

Appleton, E.V. and M.A.F. Barnett, 1925, *Some Direct Evidence for Downward Atmospheric Reflection of Electric Rays*, Proc. Roy. Soc., **109A**, 621–641.

Andrews, D.G., J.R. Holton and C.B. Leovy, 1987 *Middle Atmosphere Dynamics*, Vol.40 International Geophysics Series, Academic Press Inc., 489 pp.

Armstrong, E.B., 1968, *Variations in the Width of the OI λ 5577 Line in the Night Airglow*, Planet. Space Sci., **16**, 211-229.

Armstrong, E.B., 1982, *The association of visible airglow features with a gravity wave*, J. Atmos. Terr. Phys., 44, No. 4, 325–336.

Armstrong, E.B., 1986, *Irregularities in the 80–100 km region: A Photographic Approach*, Radio Sci., **21**, No. 3, 313–318.

Aso, T. and Vincent, R.A., 1982, *Some Direct Comparisons of Mesospheric Winds Observed at Kyoto and Adelaide*, J. Atmos. Terr. Physics, 44, 267–280.

Axford, W.I., 1963, *The Formation and Vertical Movement of Dense Ionized Layers in the Ionosphere due to Neutral Wind Shears*, J. Geophys. Res., **68**, 769–779.

Babcock, H.D., 1923, *A study of the Green Auroral Line by the Interference Method*, Astrophys. J., **57**, 209–221.

Baker, D.J. and Stair A.T., 1988, *Rocket Measurements of the Altitude Distributions of the Hydroxyl Airglow*, Physica Scripta, **37**, 611–622.

Baker, D.J. and Waddoups, R.O., 1967, *Rocket Measurements of Midlatitude Night Airglow Emissions*, J. Geophys. Res., **72**, No. 19, 4881–4883.

Baker, D.J. and Waddoups, R.O., 1968, *Correction to paper by D. Baker and R. Waddoups, 'Rocket Measurements of Midlatitude Night Airglow Emissions'*, J. Geophys. Res., **73**, No.7, 2546–2547.

Barbier, D., 1959, *Sur les Variations Systematiques des Intensites des Prociples Radiations de la Luminere du Ciel Nocturne a l'Observatoire de Haute-Provence*, Ann. Geophys., **15**, 412–414.

Barth, C.A., 1964, *Three Body Reactions*, Ann. Geophys., **20**, 182–196.

Bates, D.R., 1979, *On the Proposals of Chapman and of Barth For $O(^1S)$ Formation in the Upper Atmosphere*, Planet. Space Sci., **27**, 717–718.

Bates, D.R., 1990, *Oxygen Green and Red Line Emission and $O_2^+$ Dissociative Recombination*, Planet. Space Sci., **38**, No. 7, 889–902.

Bates, D.R., 1992, *Nightglow Emissions from Oxygen in the Lower Thermosphere*, Planet. Space Sci., **40**, No. 2/3, 211–221.

Bates, D.R. and Nicolet, M., 1950, *The photochemistry of water vapour*, J. geophys. Res., **55**, 301–327.

Beer, T., *Atmospheric Waves*, Adam Hilger London, 1975, 300pp.

Belrose, J.S., 1970, *Radio wave probing of the ionosphere by the partial reflection of radio waves (from heights below 100 km)*, J. Atmos. and Terr. Phys., **32**, 567–596.

Benedetti-Michelangeli, G., G. Cappuccio, F. Congeduti and G. Fiocco, *Active and Passive Optical Doppler Techniques for the Determination of Atmospheric Temperature, 1: An Airglow Spectrophotometer with Internal Laser Reference*, in Structure and Dynamics of the Upper Atmosphere, Developments in Atmospheric Science, 1., Elsevier Scientific Publ. Co., 1974, pp205–210.

Beynon, W.J.G. and J.C. Wright, 1969, *The analysis of ionospheric drift data in the closely spaced receiver method*, J. Atmos. Terr. Phys., **31**, 593–596.

Best, G.T. and Armstrong, E.B., 1968, *Rocket Measurements of the Altitudes of the Layers Emitting the 5577 ÅLine of Oxygen and the Continuum in the Night Airglow*, Planet. Space Sci., **16**, 821–824.

Bevington, P.R. and D.K. Robinson, *Data Reduction and Error Analysis for the Physical Sciences*, 2nd ed., 1992, McGraw-Hill, 328pp.

von Biel, H.A., 1992, *Assessing the correlated signal power in D-region partial reflections*, J. Atmos. Terr. Phys., **54**, No. 11/12, 1523–1526.

Biondi, M.A. and W.A. Feibelman, 1968, *Twilight and nightglow emission spectral line shapes of oxygen λ6300 and λ5577 radiation*, Planet. Space Sci., **16**, 431–443.

Bowhill, S.A., 1966, *A Rocket Experiment on the Structure of Sporadic-E*, Rad. Sci., **1**, 187–190.

Bond, F.R. and I.L. Thomas, 1971, *The Southern Auroral Oval*, Aust. J. Phys., **24**, 97–102.

Blamont, J.E., 1963, *Turbulence in Atmospheric Motions Between 90 and 130 km of Altitude*, **10**, Planet. Space Sci., 89–101.

Bloomfield, P., 1976, *Fourier Analysis of Time Series: An Introduction*, John Wiley and Sons Inc., 258 pp.

Brenton, J.G. and Silverman, S.M., 1970, *A Study of The Diurnal Variation of the 5577 Å[OI] Airglow Emission at Selected IGY Stations*, Planet. Space Sci., **18**, 641–653.

Briggs, B.H., 1968, *On the Analysis of Moving Patterns in Geophysics – I. Correlation Analysis*, J. Atmos. Terr. Phys., **30**, 1777–1788.

Briggs, B.H., 1977, *Ionospheric Drifts*, J. Atmos. Terr. Phys., **39**, 1023–1033.

Briggs, B.H, 1984, *The Analysis of Spaced Sensor Records by Correlation Techniques*, Handbook for Middle Atmosphere Program, (ed. by R.A. Vincent), **13**, 166–186.

Briggs, B.H., 1993, *Observations of Atmospheric Dynamics using Radar Techniques*, Aust. J. Phys., **46**, 127–147.

Briggs, B.H., Phillips, G.J. and Shinn, D.H, 1950, *The Analysis of Observations on Spaced Receivers of the Fading of Radio Signals*, Proc. Phys. Soc., B, **63** , 106–121.

Briggs, B.H. and M. Spencer, 1954, *Horizontal Movements in the Ionosphere*, Rep. Prog. Phys., **17** , 245–280.

Briggs, B.H., Elford, W.G., Felgate, D.G., Golley, M.G., Rossiter, D.E. and Smith, J.W., 1969, *Buckland Park Aerial Array*, Nature, **223**, 1321–1325.

Briggs, B.H. and R.A. Vincent, 1973, *Some theoretical considerations on remote probing of weakly scattering irregularities*, Aust. J. Phys., **26**, 805–814.

Brooks, C.E.P. and N. Carruthers, *Handbook of Statistical Methods in Meteorology*, H.M. Stationary Office, London, 1953, 412pp.

Brown, T.L., 1973, *The Chemistry of Metallic Elements in the Ionosphere and Mesosphere*, Chem. Rev., **73**, 645–660.

Brown, W.O.J., 1992, *MF Radar Interferometry*, PhD Thesis, University of Canterbury, 312 pp.

Brown, G.M. and J.W. Chapman, 1972, *Full correlation ionospheric drift analysis for a general observing triangle*, Ann. Geophys., **28**, No.2, 349–356.

Bruce, I., Reid, I.M. and Briggs, B.H., 1992, *Comparison of Results From a Three-field Photometer and Spaced-Antenna Radar*, p45, Workshop on Multiple Receiver Radar Techniques, Aug. 6-7, 1992, Urbana-Champaign.

Budden, K.G, *The Propagation of Radio Waves: the theory of radio waves of low power in the ionosphere and magnetosphere*, Cambridge University Press, 1985, 669pp.

Burrage, M.D., W.R. Skinner, D.A. Gell, P.B. Hays, A.R. Marshall, D.A. Ortland, A.H. Manson, S.J. Franke, D.C. Fritts, P. Hoffman, C. McLandress, R. Niciejewski, F.J. Schmidlin, G.G. Shepherd, W. Singer, T. Tsuda and R.A. Vincent, 1996, *Validation of mesosphere and lower thermosphere winds from the high resolution Doppler imager on UARS*, J. Geophys. Res., **101**, No.D6, 10,365–10,392.

CCIR, 1988, *Characteristics and applications of atmospheric radio noise data*, CCIR Report 332–3, Int. Telecom. Union, Geneva.

Chamberlain, J.W., 1961, *Physics of the Aurora and Airglow*, Vol.2 International Geophysics Series, Academic Press Inc., 704 pp.

Chapman, S., 1931, *Some Phenomena of the Upper Atmosphere*, Proc. Royal Soc., Series A, No. A 820, **132**, 353–374.

Chapman, S. and Lindzen, R.S., *Atmospheric Tides – Thermal and Gravitational*, D. Reidel, Dordrecht, Holland, 1970, 200 pp.

Chatfield, C., 1983, *Statistics for Technology*, 3rd. ed., Chapman and Hall, London.

Chimonas, G. and W.I. Axford, 1968, *Vertical Movement of Temperate-zone Sporadic-E Layers*, J. Geophys. and Space Res., **73**, 111–117.

Chimonas, G., 1974, *Turbulent Diffusion as a controlling factor in Sporadic-E*, J. Atmos. and Terr. Physics, **36**, 235–244.

Cogger, L.L. and Anger, C.D., 1973, *The OI 5577 ÅAirglow Experiment on the ISIS 2 Satellite*, J. Terr. and Atmos. Phys., **35**, 2081–2084.

Cogger, L.L., R.D. Elphinstone and J.S. Murphee, 1981, *Temporal and Latitudinal 5577 ÅAirglow Variations*, Can. J. Phys., **59**, 1296–1307.

Cogger, L.L., Murphee, J.S., Tepley, C.A. and Meriwether, J.W., 1985, *Measurements of the E Region Neutral Wind Field*, Planet. Space Sci., **33**, No. 4, 373–379.

Cogger, L.L., R.D. Elphinstone and D.H. Giers, 1988, *Wave Characteristics Obtained From OH Rotational Temperatures and 557.7 nm Airglow Intensities*, J. Terr. and Atmos. Phys., **50**, 943–949.

Conner, J.F., Smith, R.W. and Hernandez, G., 1993, *Techniques for Deriving Doppler Temperatures From Multiple-Line Fabry-Perot Profiles: An Analysis*, Appl. Opt., **32**, No. 23, 4437–4444.

Constantinides, E. and J.F. Bedinger, 1971, *Observed redistribution of E-region ionisation by neutral winds*, J. Atmos. Terr. Phys., **36**, 461–471.

CIRA 72, *CIRA 72 - COSPAR International Reference Atmosphere 1971*, Akademie-Verlag, Berlin, 1972, 450 p.

Christophe-Glaume, J., 1965, *Etude de la Raie 5577 Åde l'Oxygene dans la Luminescence Atmospherique Nocturne*, Ann. Geophys., **21**, 1–57.

Crow, E.L., F.A. Davis and M.W. Maxfield, *Statistics Manual*, Dover NY, 1960, 288 pp.

Dandekar B.S. and Silverman, S.M., 1964, *The Effect of Solar Flares on the [OI] Green Line of the Nightglow*, Planet. Space Sci., **12**, 867–874.

Dandekar B.S. and Turtle, J.P., 1971, *Atomic Oxygen Concentration from the Measurement of the [OI] 5577 ÅEmission of the Airglow*, Planet. Space Sci., **19**, 949–957.

Davies, K., *Ionospheric Radio*, 1966, Inst. Elec. Eng., 580pp.

Davies, K., *Ionospheric Radio*, 1990, Inst. Elec. Eng., 580pp.

Derblom, H., 1981, *Non-Sporadic Properties of Sporadic-E*, Uppsala Ionospheric Obs. Rep., 75 pp.

Dewan E.M. and R.E. Good, 1986, *Saturation and the "Universal" Spectrum for Vertical Profiles of Horizontal Scalar Winds in the Atmosphere*, J. Geophys. Res., **91**, No.D2, 2742–2748.

Dickinson, P.H.G., Bolden, R.C. and Young, R.A., 1974, *Measurement of Atomic Oxygen in the Lower Ionosphere Using a Rocket-Borne Resonance Lamp*, Nature, **252**, 289–291.

Donahue, T.M., Guenther, B. and Thomas, R.J., 1973, *Distribution of Atomic Oxygen in the Upper Atmosphere Deduced from Ogo 6 Airglow Observations*, J. Geophys. Res., **78**, No.28, 6662–6689.

Dungey, J.W., 1959, *Effect of a Magnetic Field on Turbulence in an Ionized Gas*, J. Geophys. Res., **64**, 2188-2191.

Evans, W. F., Llewellyn, E. J. and Vallance Jones, A., 1972, *Altitude Distribution of the $O_2(^1\Delta)$ Airglow Emission*, J. Geophys. Res., **77**, No. 28, 4899-4901.

Evans, W. F., Llewellyn, E. J. and Vallance Jones, A., 1973, *Altitude Distribution of Hydroxyl Bands of the $\Delta\nu=2$ Sequence in the Nightglow*, Can. J. Phys., **51**, 1288–1292.

Fabry, Ch., and Perot (1896) *Mesure de Petites Epaisseurs en Valeur Absolue*, Compt. Rend., **123**, 802–805.

Fabry, Ch., and Perot (1897) *Sur les Franges des Lames Minces Argentees et Leur Application a la Mesure de Petites Epasseurs D'air*, Ann. Chim. Phys., **12**, 459–501.

Fauliot, V., G. Thuillier and M. Herse, 1995, *Observations of the E-region horizontal winds in the auroral zone and at mid-latitudes by a ground-based interferometer*, Ann. Geophys., **13**, 1172–1186.

Fedor, L.S. and Plywaski, W., 1972, *The Interpretation of Ionospheric Radio Drift Measurements – IV. The Effects of Signal Coupling Among Spaced Sensor Channels* J. Atmos. Terr. Phys., **34**, 1285–1303.

Felgate, D.G. and M.G. Golley, 1971, *Ionospheric irregularities and movements observed with a large aerial array*, J. Atmos. Terr. Phys., **33**, 1353–1369.

Fellous J.L., A. Spizzichino, M. Glass and M. Massebeuf, 1974, *Vertical propagation of tides at meteor heights*, J. Atmos. Terr. Phys., **36**, 385–396.

Fellous J.L., R. Bernard, M. Glass, M. Massebeuf and A. Spizzichino, 1975, *A study of the variations of atmospheric tides in the meteor zone*, J. Atmos. Terr. Phys., **37**, 1511–1524.

Forbes, J.M., 1982a, *Atmospheric Tides 1. Model Description and Results for the Solar Diurnal Component*, J. Geophys. Res., **87**, No.A7, 5222-5240.

Forbes, J.M., 1982b, *Atmospheric Tides 2. The Solar and Lunar semidiurnal Components*, J. Geophys. Res., **87**, No.A7, 5241–5252.

Forbes, J.M., 1984, *Middle Atmosphere Tides*, J. Atmos. and Terr. Phys., **46**, No. 11, 1049–1067.

Forbes, J.M., 1985, *Middle Atmosphere Tides*, Handbook for Middle Atmosphere Program, (ed. by S. Kato), **18**, 150–56.

Forbes, J.M., 1990, *Atmospheric Tides Between 80 km and 120 km*, Adv. Space Res., **10**, No. 12, (12)127–140.

Forbes, J.M. and Garrett, 1978, *Thermal excitation of atmospheric tides due to insolation absorption by $O_3$ and $H_2O$*, Geophys. Res. Lett., **5**, 1013–1016.

Forbes, J.M. and H.B. Garrett, 1979, *Theoretical Studies of Atmospheric Tides*, Rev. Geophys. and Space Phys., **17**, No.8, 1951–1981.

Forbes, J.M. and Vial, F., 1989, *Monthly simulations of the semidiurnal tide in the mesosphere and lower thermosphere*, J. Atmos. and Terr. Phys., **51**, No. 7/8, 649–661.

Forsyth, R.J. and Wraight, P.C., 1987, *A Survey of Research on Nightglow Variability*, Planet. Space Sci., **35**, No. 11, 1449–1461.

Franke, S.J. and D. Thorsen, 1993, *Mean Winds and Tides in the Upper Middle Atmosphere at Urbana (40°N, 88°W) During 1991-1992*, submitted to J. Geophys. Res.

Fraser, G.J., 1965, *The Measurement of Atmospheric Winds at Altitudes of 64–120 km Using Ground-based Radio Equipment*, J. Atmos. Sci., **22**, 217–218.

Fraser, G.J., 1968, *Seasonal Variation of Southern Hemisphere Mid-latitude Winds at Altitudes of 70–100 km*, J. Atmos. Terr. Phys., **30**, 707–719.

Fraser, G.J., 1984, *Partial Reflection Spaced Antenna Wind Measurements*, Handbook for Middle Atmosphere Program, (ed. by R.A. Vincent), **13**, 233–247.

Fraser, G.J., 1989, *Monthly Mean Winds in the Mesosphere at 44S and 78S* PAGEOPH, **30**, Nos. 2/3, 291–301

Fraser, G.J. and Kochanski, A., 1970, *Ionospheric Drifts from 64-100 km at Birdlings Flat*, Ann. de Geophys., **26**, 675–687.

Fraser, G.J. and Khan, U., 1990, *Semidiurnal variations in the time scale of irregularities near the Antarctic summer mesopause*, Rad. Sci., **25** no. 5, 997–1003.

Fraser, G.J. and Vincent, R.A., 1970, *A Study of D-region Irregularities*, J. Atmos and Terr. Phys., **32**, 1591–1607.

Fraser, G.J., Vincent, R.A., Manson, A.H., Meek, C.E. and Clark, R.R., 1989, *Inter-annual variability of tides in the mesosphere and lower thermosphere*, J. Atmos and Terr. Phys., **51**, No. 7/8, 555–567.

Fraser, G.J., Yu. I. Portnyagin, J.M. Forbes, R.A. Vincent, I.A. Lysenkop, and N.A. Makarov, 1995, *Diurnal tide in the Antarctic and Arctic mesosphere/lower thermosphere regions*, J. Atmos. Terr. Phys., **57**, No.4, 383–393.

Frederick, J.E., 1979, *Influence of Gravity Wave Activity on Lower Thermospheric Photochemistry and Composition*, Planet. Space. Sci., **27**, 1469–1477.

Freund, J.T. and Jacka, F., 1979, *Structure in the $\lambda$ 557.7 nm [OI] Airglow*, J. Terr. and Atmos. Physics, **41**, 25–31.

Fritts, D.C., 1984, *Gravity Wave Saturation in the Middle Atmosphere: A Review of Theory and Observations*, Rev. Geophys. and Space Phys., **22**, No.3, 275–308.

Fritts, D.C., 1989, *A review of Gravity Wave Saturation Processes, Effects, and Variability in the Middle Atmosphere*, PAGEOPH, **30**, Nos. 2/3, 343–371.

Fritts, D.C., 1990, *Gravity Waves in the Middle Atmosphere of the Southern Hemisphere*, in Dynamics, Transport and Photochemistry in the Middle Atmosphere of the Southern Hemisphere, Kluwer Academic Publishers, 171–189.

Fritts, D.C. and P.K. Rastogi, 1985, *Convective and Dynamical Instabilities due to Gravity Wave Motions in the Lower and Middle Atmosphere: Theory and Observations*, Rad. Sci., No.6, 1247–1277.

Gardner, F.F. and Pawsey, J.L., 1953, *Study of the Ionospheric D-region Using Partial Reflections*, J. Atmos and Terr. Phys., **3**, 321–344.

Gardner, C.S. and J.D. Shelton, 1985, *Density Response of Neutral Atmospheric Layers to Gravity Wave Perturbations*, J. Geophys. Res., **90**, No. A2, 1745–1754.

Gault, W.A, G. Thuillier, G.G. Shepherd, S.P. Zhang, R.H. Weins, W.E. Ward, C. Tai, B.H. Solheim, Y. Rochon, C. McLandress, C. Lathuillere, V. Fauliot, M. Herse, C.H. Hersom, R. Gattinger, L. Bourg, M.D. Burrage, S.J. Franke, G. Hernandez, A. Manson, R. Niciejewski and R.A. Vincent, 1996, *Validation of $O(^1S)$ Wind Measurements by WINDII: The WIND Imaging Interferometer on UARS*, J. Geophys. Res., **101**, No.D6, 10,405–10,430

Gerbier, N. and M. Berenger, 1961, *Experimental studies of lee waves in the French Alps*, Quart. J. Roy. Met. Soc., **87**, 13-23.

Giacomo, P., 1952, *Methode Directe de Mesure des Caracteristiques d'un Systeme Interferential de Fabry-Perot*, Compt. Rend, **235**, 1627–1629.

Gobbi, D., Takahashi, H., Clemesha, B.R. and Batista, P.P., 1992, *Equatorial Atomic Oxygen Profiles Derived From Rocket Observations of OI 557.7 nm Airglow Emission*, Planet. Space Sci., **40**, No. 6, 775–781.

Goldstein, H., 1951, *The Fluctuations of Cluster Echoes. Propagation of Short Radio Waves*, (ed. Kerr, D.E., McGraw-Hill).

Golley, M.G. and Rossiter, D.E., 1970, *Some Tests of methods of Analysis of Ionospheric Drift records Using An Array of 89 Aerials*, J. Atmos and Terr. Phys., **32**, 1215–1233.

Gonzalez, N., Hauchecorne, A., Kirkwood, S., Lübken, F.J., Manson, A.H., Mourier, A., Schmidlin, F.J., Schminder, R., Kürschner, D., Singer, W. and H.U. Widdel, 1994, *Intercomparisons of simultaneous remote and in situ wind measurements*, J. Atmos and Terr. Phys., **56**, Nos. 13/14, 1985–2001.

Greer, R.G.H, Murtagh, D.P., McDade, I.C., Dickinson, P.H.G., Thomas, L., Jenkins, D.B., Stegman, J., Llewellyn, E.J., Witt, G., Mackinnon, D.J. and Williams, E.R., 1986, *ETON 1: A Data Base Pertinent to the Study of Energy Transfer in the Oxygen Nightglow*, Planet. Space Sci., **34**, No. 9, 771–788.

Gregory, J.B., 1961, *Radio Wave Reflections from the Mesosphere*, J. Geophys. Res., **66**, No. 2, 429–445.

Gregory, J.B., Meek, C.E., Manson, A.H. and Stephenson, D.G., 1979, *Developments in the Radiowave Drifts Technique for Measurement of High-Altitude Winds*, J. Appl. Meteor., **18**, 682–691.

Greet, P.A. and Jacka, F., 1989, *Observations of the sodium layer using a Fabry-Perot spectrometer: twilight temperature variations*, J. Terr. and Atmos. Phys., **51**, 91–99.

Gulledge, I.S., Packer, M.D., Tilford, S.G. and Vanderslice, J.T., 1968, *Intensity Profiles of the 6300 Åand 5577 ÅOI Lines in the NIght Glow*, J. Geophys. Res., **73**, No. 17, 5535–5547.

Hamming, R.W., 1989, *Digital Filters*, 3rd. ed., Prentice-Hall, NJ.

Hargreaves, J.K., *The Solar Terrestrial Environment*, Cambridge Atmospheric and Space Science Series 5, 1992, 420 pp.

Hariharan, P., Basics of Interferometry, Academic Press, 1992, 213 pp.

Hartree, D.R., 1931, *Propagation of Electro-Magnetic Waves in a Refracting Medium in a Magnetic Field*, Proc. Camb. Phil. Soc., **27**, 143.

Hatfield, R., Tuan, T.F. and Silverman S.M., 1981, *On the Effects of Atmospheric Gravity Waves on Profiles of H, $0_3$, and OH Emission*, J. Geophys. Res., **86**, No. A4, 2429–2437.

Hays, P.B. and R.G. Roble, 1971, *A Technique for Recovering Doppler Line Profiles from Fabry-Perot Interferometer Fringes of Very Low Intensity*, Appl. Optics, **10**, No.1, 193–200.

Hays, P.B., Abreu, V.J., Dobbs, M.E., Gell, D.A., Grassl, H.J. and W.R. Skinner, 1993, *The High-Resolution Doppler Imager on the Upper Atmosphere Research Satellite*, J. Geophys. Res., **98**, No.D6, 10,713–10,723.

Hennes, J. and L Dunkelman, 1966, *Photographic Observations of Nightglow from Rockets*, J. Geophys. Res., **71**, No. 3, 755–762.

Hernandez, G., 1966, *Analytical Description of a Fabry-Perot Photoelectric Spectrometer*, Appl. Optics, **5**, No.11, 1745–1748.

Hernandez, G., 1970, *Analytical Description of a Fabry-Perot Photoelectric Spectrometer 2. Numerical Results*, Appl. Optics, **9**, No.7, 1591–1596.

Hernandez, G., 1971, *The Signature Profiles of $O(^1S)$ in the Airglow*, Planet. Space Sci., **19**, 467–476.

Hernandez, G., 1976, *Lower-Thermosphere Temperatures Determined From the Line Profiles of the O I 17,924-K (5577 Å) Emission in the Night Sky 1. Long-Term Behavior*, J. Geophys. Res., **81**, No. 28, 5165–5172.

Hernandez, G., 1978, *Piezoelectric Scanning of Fabry-Perot Spectrometers: Nonlinearities*, Appl. Opt., **17**, No.19, 3088–3095.

Hernandez, G., 1980, *Measurement of thermospheric temperatures and winds by remote Fabry-Perot spectrometry*, Opt. Eng., **19**, No.4, 518–531.

Hernandez, G., 1986, *Fabry-Perot Interferometers*, Cambridge Studies in Modern Optics 3, Cambridge University Press, 343 pp.

Hernandez, G. and Silverman, S.M., 1964, *A Reexamination of Lord Rayleigh's Data on the Airglow 5577 Å[OI] Emission*, Planet. Space Sci., **12**, 97–112.

Hernandez, G. and Mills, O.A., 1973, *Feedback Stabilised Fabry-Perot Interferometer*, Appl. Opt., **12**, No. 1, 126–130.

Hernandez, G. and Roper, R.G., 1979, *A Comparison between Radio Meteor and Airglow Winds*, J. Geomag. Geoelectr., **31**, 419–426.

Hernandez, G., Sica, R.J. and Romick, G.J., 1984, *Equal-noise Spectroscopic Measurement*, Appl. Opt., **23**, No. 6, 915–919.

Hernandez, G and T.L. Killeen, 1988, *Optical Measurements of Winds and Kinetic Temperatures in the Upper Atmosphere*, COSPAR Adv. Space Res., **8**, No.5–6, (5)149–(5)213.

Hernandez, G. and R.W. Smith, 1995, *Winds and vertical wavelengths deduced from the ground-based measurement of Doppler shifts of the* $O_2(b^1\Sigma_g^+ - X^3\Sigma_g^-)$, $OI(^1D_2 - ^1S_0)$, *and the* $X^2\Pi$ *OH(6-2) band* $P_1(2)_{c,d}$ *line emissions in the midlatitude upper middle atmosphere*, Geophys. Res. Lett., **22**, No.4, 369–372.

Hernandez, G., Weins, R., Lowe, R.P., Shepherd, G.G., Fraser, G.J., Smith, R.W., LeBlanc, L.M., and M. Clark, 1995, *Optical determination of the vertical wavelength of propagating 12-hour period upper atmosphere oscillations*, Geophys. Res. Lett., **22**, No.17, 2389–2392.

Herse′, M., Moreels, G. and Clairemidi, J., 1980, *Waves in the OH Emissive Layer: Photogrammetry and Topography*, Appl. Optics, **19**, No. 3, 355–362.

Hines, C.O., 1964, *Internal Atmospheric Gravity Waves at Ionospheric Heights*, Can. J. Phys., **38**, 1441–1481.

Hines, C.O., 1966, *Diurnal Tide in the Upper Atmosphere*, J. Geophys. Res., **71**, No.5, 1453–1459..

Hines, C.O., 1968, *Some Consequences of Gravity-wave critical layers in the Upper Atmosphere*, J. Atmos. Terr. Phys., **30**, 837–843.

Hines, C.O., 1991, *The Saturation of Gravity Waves in the Middle Atmosphere. Part III: Formation of the Turbopause and of Turbulent Layers beneath It*, J. Atmos. Sci., **48**, No.11, 1380–1385.

Hines, C.O. and D.W. Tarasick, 1987, *On the Detection and Utilization of Gravity Waves in Airglow Studies*, Planet. Space Sci., **35**, 851–866.

Hines, C.O., Adams, G.W., Brosnahan, J.W., Djuth, F.T., Sulzer, C.A., Tepley, C.A. and Van Baelen, J.S., 1993, *Multi-instrument observations of mesospheric motions over Arecibo: comparisons and interpretations*, J. Atmos. Terr. Phys., **55**, No. 3, 241–287.

Hocking, W.K., 1979, *Angular and Temporal Characteristics of Partial Reflections From the D-region of the Ionosphere*, J. Geophys. Res., **84**, No. A3, 845–851.

Hocking, W.K., 1983, *The Spaced Antenna Drift Method*, Handbook for Middle Atmosphere Program, (ed. by R.A. Vincent), **9**, 171–186.

Hocking, W.K., 1985, *Turbulence in the altitude region 80 to 120 km*, Handbook for Middle Atmosphere Program, (ed. by K. Labitzke, J.J. Barnett and B. Edwards), **16**, 290–304.

Hocking, W.K., 1988a, *Two Years of Continuous Measurements of Turbulence Parameters in the Upper Mesosphere and Lower Thermosphere made with a 2-MHz Radar*, J. Geophys. Res., **93**, No.D3, 2475–2491.

Hocking, W.K., 1988b, *Target Parameter Estimation*, Proc. International School on Atmospheric Radar, Kyoto, ed. S. Fukao, pp P7-1–P7-66.

Hocking, W.K. and Vincent, R.A., 1982, *A Comparison Between HF Partial Reflection Profiles from the D-region and Simultaneous Langmuir Probe Electron Density Measurements*, J. Atmos. Terr. Phys., 44, 843–854.

Hocking, W.K., May, P.T. and Rottger, J., 1989, *Interpretation, Reliability and Accuracies of Parameters Deduced by the Spaced Antenna Method in Middle Atmosphere Applications*, PAGEOPH, **130**, Nos. 2/3, 571–604.

Hodges, R.R., 1979, *Generation of turbulence in the upper atmosphere by internal gravity waves*, J. Geophys. Res., **72**, 3455–3458.

Holton, J.R., 1992, *An Introduction To Dynamic Meteorology*, International Geophysics Series **48**, Academic Press, 3rd ed., 507 pp.

Hooke, W.H., 1968, *Ionospheric Irregularities Produced by Internal Gravity Waves*, J. Terr. Atmos. Phys., **30**, 795–823.

Houghton, J.T., 1986, *The Physics of Atmospheres*, 2nd ed., Cambridge University Press, pp105–117.

Hunten D.M., Roach F.E. and Chamberlain, J.W, 1956, *A Photometric Unit for the Airglow and Aurora*, J. Terr. Atmos. Phys., **8**, 345–346.

Hydrographic Office, 1946, *Variation of the Compass for 1955*, Map prepared by the Department of the Navy, Washington, D.C.

Jacka, F., 1984, *Application of Fabry-Perot Spectrometers for Measurement of Upper Atmosphere Temperatures and Winds*, Handbook for Middle Atmosphere Program, 13 (ed. Vincent, R.A. SCOSTEP Secretariat), 19–40.

Jacka, F. and F.R., Bond, 1968, *Optical Auroral Morphology*, Ann. Geophys., **24**, No.2, 457–553.

Jenkins, G.M. and D.G. Watts, 1968, *Spectral Analysis and its Applications*, Holden-Day, San Fran., pp174–181.

Johnson, R.M. (ed), *Satellite Environment Handbook*, Stanford Univ. Press, 1961.

Kato S. and S. Matsushita, 1968, *Space charge waves and ionospheric irregularities*, J. Atmos. Terr. Phys., **30**, 857–869.

Kelley M.C. and R.A. Heelis, *The Earth's Ionosphere: Plasma Physics and Electrodynamics*, International Geophysical Series vol. 43., Academic Press, 1989, 487pp.

Kent, G.S., 1970, *Measurement of Ionospheric Movements*, Rev. Geophys. Space Phys., **8**, No. 2, 229–288.

Killeen, T.L. and Hays, P.B., 1981, *Nonthermal Line Profiles from $O(^1S)$ in the Thermospheric Airglow*, Appl. Opt., **20**, No. 19, 3314–3317.

Killeen, T.L. and Hays, P.B., 1983, *$O(^1S)$ From Dissociative Recombination of $O_2^+$: Nonthermal Line Profile Measurements From Dynamics Explorer*, J. Geophys. Res., **88**, No. A12, 10163–10169.

Kita, K., Iwagami, N., Ogawa, T., Miyashita, A. and Tanabe, H., 1988, *Height Distributions of the Night Airglow Emissions in the $O_2$ Herzberg I System and Oxygen Green Line from a Simultaneous Rocket Observation*, J. Geomag. Geoelectr., **40**, 1067–1084.

Lawson, J.L. and Uhlenbeck, G.E., *Threshold Signals*, MIT Radiation Laboratory Series, 1950, McGraw Hill, 388 pp.

Lindzen, R.S., *Tides and Internal Gravity Waves in the Atmosphere*, in Structure and Dynamics of the Upper Atmosphere, Developments in Atmospheric Science, 1., Elsevier Scientific Publ. Co., 1974, pp21–87.

Lindzen, R.S., 1976, *A modal decomposition of the semidiurnal tide in the lower thermosphere*, J. Geophys. Res., **81**, 1561–1571.

Lindzen, R.S., 1979, *Atmospheric Tides*, Ann. Rev. Earth Planet. Sci., **7**, 177–225.

Lindzen, R.S., 1981, *Turbulence and Stress Owing to Gravity Wave and Tidal Breakdown*, J. Geophys. Res., **86**, No. C10, 9707-9714.

Lindzen, R.S., *Dynamics in Atmospheric Physics*, Cambridge University Press, 1990, 310 pp.

Lindzen, R.S. and Hong, S, 1974, *Effects of Mean Winds and Horizontal Temperature Gradients on Solar and Lunar Semidiurnal Tides in the Atmosphere*, J. Atmos. Sci., **31**, 1421–1446.

Lloyd, N., A.H. Manson, D.J. McEwen and C.E. Meek, 1990, *A Comparison of Middle Atmospheric Dynamics at Saskatoon (52° N, 107° W) as Measured by a Medium-Frequency Radar and a Fabry-Perot Interferometer*, J. Geophys. Res., **95**, No. D6, 7653–7660.

Lomb, N.R., 1976, *Least-squares Frequency Analysis of Unequally Spaced Data*, Astrophys. Space Sci., **39**, 447–462.

Manson A. H., 1995, *Ann. Rep. Inst. Space and Atmos. Studies, University of Saskatoon*, p34–36.

Manson A. H., Merry, M.W.J. and Vincent R.A., 1969, *Relationship Between the Partial Reflection of Radio Waves from the Lower Ionosphere and Irregularities as Measured by Rocket Probes*, Radio Sci., **4**, No. 10, 955–958.

Manson A.H., Meek, C.E. and R.J. Stening, 1979 *The role of atmospheric waves (1.5 h–10 days) in the dynamics of the mesosphere and lower thermosphere at Saskatoon ((52° N, 107° W) during four seasons of 1976.*, J. Atmos. Terr. Physics, **41**, 325–335.

Manson A. H., Meek, C.E. and Gregory, J.B., 1981, *Winds and Waves (10 min - 30 days) in the Mesosphere and Lower Thermosphere at Saskatoon (52° N, 107° W, L=4.4) during the Year October 1979 to July 1980*, J. Geophys. Res., **86**, 1915.

Manson, A.H. and C.E. Meek, 1985, *Middle Atmosphere (60–110 km) tidal oscillations at Saskatoon, Canada (52° N, 107° W) during 1983–1984*, Rad. Sci., **20**, No.6, 1441–1451.

Manson A.H., Meek, C.E., Smith, M.J. and Fraser G.J., 1985, *Direct comparisons of prevailing winds and tidal winds (24-, 12-h) in the upper middle atmosphere (60–105 km) during 1978–80 at Saskatoon (52° N, 107° W) and Christchurch (44° S, 173° E)*,J. Atmos. Terr. Phys., **47**, No. 5, 463–476.

Manson A.H., Meek, C.E., Teitelbaum, H., Vial, F., Schminder, R., Kurschner, D., Smith, M.J., Fraser, G.J. and Clark, R.R., 1989, *Climatologies of Semi-diurnal and Diurnal Tides in the Middle Atmosphere (70–110 km) at Middle Latitudes (40–55°)*, Planet. Space Sci., **51**, No. 7/8, 579–593.

Manson A.H., Meek, C.E., Schminder, R., Kurschner, D., Clark, R.R., Muller, H.G., Vincent, R.A., Phillips, A., Fraser, G.J., Singer, W. and Kazimirovsky, E.S., 1990, *Tidal Winds From the MLT Global Radar Network During the First LTCS Campaign – September 1987*, J. Atmos. Terr. Physics, **52**, No. 3, 175–183.

Manson A.H., Meek, C.E., Lloyd, N. and McEwen, D.J., 1991, *Dynamics of the Lower Thermosphere at Saskatoon (52° N, 107° W) During 1988/1989: Comparisons of Measurements by a Medium-Frequency Radar and a Fabry-Perot Interferometer*, Planet. Space Sci., **39**, No. 11, 1511–1525.

May, P.T., 1988, *Statistical Errors in the Determination of Wind Velocities by the Spaced Antenna Method*, J. Atmos. Terr. Phys., **50**, No. 1, 21–32.

McCaulley, J.W., Roach, F.E. and Matsushita, S., 1960, *A Study of Local Geomagnetic Influence on the [OI] 5577 Nightglow Emission at Fritz Peak*, J. Geophys. Res., **65**, No. 5, 1499–1501.

McDade, I.C. and Llewellyn, E.J., 1984, *A Comment on Proposed Mechanisms For the Excitation of $O(^1S)$ in the Aurora*, Planet. Space Sci., **32**, 1195–1198.

McDade, I.C., Murtagh, D.P., Greer, R.G.H, Dickinson, P.H.G., Witt, G., Stegman, J., Llewellyn, E.J., Thomas, L. and Jenkins, D.B., 1986, *ETON 2: Quenching Parameters for the Proposed Precursors of $O_2(b^1\Sigma_g^+$ and $O(^1S)$ in the Terrestrial Nightglow*, Planet. Space Sci., **34**, 789–800.

McEwan, M.J. and L.J. Phillips, *Chemistry of the Atmosphere*, 1975, Arnold, 301pp.

Meek C.E., 1990, *Triangle size effect is spaced antenna wind measurements*, Radio Sci., **25**, No.4, 641–648.

Meek C.E. and A.H. Manson, 1983, *Measurements of the Structure and Drift Velocities of Airglow ($\lambda$ = 557.7 nm) Irregularities: Saskatoon (52° N, 107° W) Canada*, J. Atoms. Terr. Phys., **45**, 203–212.

Meek C.E., I.M. Reid and A.H. Manson, 1985, *Observations of Mesospheric Wind Velocities 2. Cross Sections of Power Spectral Density for 48–8 hours, 8–1 hours, and 1 hour to 10 min over 60–110 km for 1981*, Rad. Sci., **20**, 1383–1402.

Midgley, J.E. and Liemohn, H.B., 1966, *Gravity Waves in a Realistic Atmosphere*, J. Geophys. Res., **71**, 3729–3748.

Mitra, S.N., 1949, *A Radio Method of Measuring Winds in the Ionosphere*, Proc. Inst. Elect. Engrs., **96**, Part III, 441–446.

Moreels G. and Herse, M., 1977, *Photographic Evidence of waves Around the 85 km Level*, Planet. Space Sci., **25**, 265–273.

Namboothiri, S.P., A.H. Manson and C.E. Meek, 1993, *E-region real heights and their implications for MF radar-derived wind and tidal climatologies*, Rad. Sci., **28**, No.2, 187–202.

Namboothiri, S.P., Meek, C.E. and Manson, A.H., 1994, *Variations of Mean Winds and Solar Tides in the Mesosphere and Lower Thermosphere Over Time Scales Ranging From 6 Months to 11 Yr: Saskatoon, 52°N, 107°W*, J. Atoms. Terr. Phys., **56**, No. 10, 1313–1325.

Neff, S.H., 1965, *Observation of the OI 5577 ÅNightglow at Christchurch, New Zealand*, J. Geophys. Res., **70**, No. 7, 1743–48.

Noxon, J.F., 1978, *Effect of Internal Gravity waves Upon Airglow Temperatures*, Geophys. Res. Lett., **5**, No.1, 25–27.

Nygren, T., L Jalonen, J. Oskman and T. Turunen, 1984, *The Role of an Electric Field on Neutral Wind Direction in the Formation of Sporadic-E layers*, J. Atmos. Terr. Phys., **46**, 373-381.

O'Brien B.J., Allum, F.R. and Goldwire, H.C., 1965, *Rocket Measurements of Midlatitude Airglow and Particle Precipitation*, J. Geophys. Res., **70**, No. 1, 161–175.

Offermann, D. and Drescher, A., 1973, *Atomic Oxygen Densities in the Lower Thermosphere as Derived from In Situ 5577 ÅNightglow and Mass Spectrometer Measurements*, J. Geophys. Res., **78**, No. 28, 6690–6700.

Ogawa, T., Iwagami, N., Nakamura, M., Takano, M., Tanabe, H., Takechi, A., Miyashita, A. and Suzuki, K., 1987, *A Simultaneous Observation of the Height Profiles of the Night Airglow OI 5577 Å, $O_2$ Herzberg and Atmospheric Bands*, J. Geomag. Geoelectr., **39**, 211–228.

Packer, D.M., 1961, *Altitudes of the Night Airglow Radiations*, Ann. Geophys., **17**, 67–75.

Panter, P.F., *Modulation, Noise and Spectral Analysis*, McGraw-Hill Book Co., New York, 1965.

Peterson, A.W. and Kieffaber, L.M., 1973, *Infrared Photography of OH Airglow Structures*, Nature, **242**, 321–322.

Petitdidier, M. and H. Teitelbaum, 1977, *Lower Thermosphere Emissions and Tides*, Planet. Space Sci., **25**, 711–721.

Petitdidier, M. and H. Teitelbaum, 1979, *$O(^1S)$ Excitation Mechanism and Atmospheric Tides*, Planet. Space Sci., **27**, 1409–1419.

Phillips, G.J. and Spencer M., 1955, *The effects of anisometric amplitude patterns in the measurement of ionospheric drifts*, Proc. Phys. Soc. London, B68, 481–492.

Phillips, A. and Vincent, R.A., 1989, *Radar Observations of Prevailing Winds and Waves in the Southern Hemisphere Mesosphere and Lower Thermosphere*, PAGEOPH, **130**, Nos. 2/3, 303–318.

Phillips, A., Manson, A.H., Meek, C.H. and Llewellyn, E.J., 1994, *A Long-Term Comparison of Middle Atmosphere Winds Measured at Saskatoon (52°N 107° W) by a Medium-Frequency Radar and a Fabry-Perot Interferometer*, J. Geophys. Res., **99**, No.D6, 12923–12935.

Piggott, W.R. and K. Rawer (eds.), *URSI Handbook of Ionogram Interpretation and Reduction*, 2nd ed., World Data Center A, 1972, 135pp.

Press, W.H., S.A. Teukolsky, Vetterling, W.T. and Flannery, B.P., 1992, *Numerical Recipes: The Art of Scientific Computing*, 2nd ed., Cambridge, New York, 963 pp.

Price, G.D., R.W. Smith and G. Hernandez, 1995, *Simultaneous Measurements of large vertical winds in the upper and lower thermosphere*, J. Atmos. Terr. Phys., **57**, No.6, 631–643.

Rayleigh, Lord (Strutt, R.J.), 1928, , Mem. Commonw. Obs. Aust., **1**, 5.

Rathbone, A.J. and J.F.E. Johnson, 1985, *EISCAT Observations of a Sequential $E_s$ Layer*, J. Atmos. Terr. Phys., **47**, 1071–1074.

Rees, D., J.J. Barnett and K. Labitzke (eds.)., 1990, *COSPAR INTERNATIONAL REFERENCE ATMOSPHERE: 1986*, **10**, No.12, Pergamon Press, 517 pp.

Rees, M.H., 1989, *Physics and Chemistry of the Upper Atmosphere*, Cambridge Atmospheric and Space Science Series, 289 pp.

Reid, I.M., 1986, *Gravity wave motions in the upper middle atmosphere (60-110 km)*, J. Atmos. Terr. Phys., **48**, 1057–1072.

Reid, I.M. and R.A. Vincent, 1986, *Measurements of the horizontal scales and phase velocities of short period mesospheric gravity waves at Adelaide, Australia*, J. Atmos. Terr. Phys., **49**, 1033–1048.

Rishbeth, H. and Garriott, O.K., *Introduction to Ionospheric Physics*, International Geophysics Series **14**, Academic Press, 1969, 331pp.

Rishbeth, H. and J.C.G. Walker, 1982, *Directional currents in nocturnal E-region layers*, Planet. Space Sci., **30**, 209.

Roach, F.E., 1955, *A Review of Observational Results in Airglow Photometry*, Ann. Geophys., **11**, 214–231.

Roach, F.E., 1960, *The Intensity of [OI] 5577 in the Subauroral Region as a Function of Magnetic Activity*, J. Geophys. Res., **65**, No. 5, 1495–1497.

Roach, F.E., Tandberg-Hanssen, E. and Megill, L.R., 1958, *The Characteristic Size of Airglow Cells*, J. Atmos. Terr. Phys., **13**, 113–221.

Roach, F.E., Tandberg-Hanssen, E. and Megill, L.R., 1958, *Movements of Airglow Cells*, J. Atmos. Terr. Phys., **13**, 122-130.

Roach, F.E. and M.H. Rees, 1960, *The Absolute Zenith Intensity of [OI] 5577 at College, Alaska*, J. Geophys. Res., **65**, No. 5, 1489–1493.

Roach, F.E., McCaulley, J.W., Marovich, E. and Purdy, C.M, 1960, *A Comparative Study of Absolute Zenith Intensities of [OI] 5577*, J. Geophys. Res., **65**, No. 5, 1503–1511.

Rosenberg, N. and Zimmerman, S.P., 1967, *Correlation Between the 5577 Å[OI] Night Airglow Intensity and Solar Activity*, Planet. Space Sci., **15**, 863–872.

Rowe, J.F., 1974, *Downward Transport of Nighttime $E_s$-layers into the Lower E-region at Arecibo*, J. Atmos. Terr. Phys., **36**, 225–234.

Sanford, B.P., 1959, *Studies of the Upper Atmosphere from Invercargill, New Zealand*, Ann. Geophys., **15**, 445–452.

Sanford, B.P., 1964, *Aurora and Airglow Intensity Variations with Time and Magnetic Activity at Southern High Latitudes*, J. Atoms. Terr. Phys., **26**, 749–769.

Scargle, J.D., 1982, *Studies in Astronomical Time series Analysis. II. Statistical Aspects of Spectral Analysis of Unevenly Spaced Data*, Astrophys. J., **263**, 835–853.

Schubert, G., Walterscheid, R.L. and Hickey, M.P., 1991, *Gravity Wave-Driven Fluctuations in OH Airglow From an Extended, Dissipative Emission Region*, J. Geophys. Res., **96**, No. A8, 13869–13880.

Sharp, W.E. and Torr, D.G., 1979, *Determination of the Auroral $O(^1S)$ Production Sources from Coordinated Rocket and Satellite Measurements*, J. Geophys. Res., **84**, 5345–5348.

Shepherd, G.G., G. Thuillier, W.A. Gault, B.H. Solheim, C. Hersom, J.M. Alunni, J.F. Brun, S. Brune, P. Charlot, L.L. Cogger, D.L. Desaulniers, W.F.J. Evans, R.L. Gattinger, F. Girod, D. Harvie, R.H. Hum, D.J.W. Kendall, E.J. Llewellyn, R.P. Lowe, J. Ohrt, F. Pasternak, O. Peillet, I. Powell, Y. Rochon, W.E. Ward, R.H. Weins and J. Wimperis, 1993a, *WINDII, the Wind Imaging Interferometer on the Upper Atmosphere Research Satellite*, J. Geophys. Res., **98**, No.D6, 10,725–10,750.

Shepherd, G.G., G. Thuillier, B.H. Solheim, S. Chandra, L.L. Cogger, W.F.J. Evans, R.L. Gattinger, W.A. Gault, M. Herse', A. Hauchecorne, C. Lathuilliere, E.J. Llewellyn, R.P. Lowe, H. Teitelbaum, and F. Vial, 1993b, *Longitudinal Structure in Atomic Oxygen Concentrations Observed with WINDII on UARS*, Geophys. Res. Lett., **20**, No.12, 1303–1306.

Shepherd, G.G., McLandress, C. and B.H. Solheim, 1995, *Tidal influence on $O(^1S)$ airglow emission rate distributions at the geographic equator as observed by WINDII*, Geophys. Res. Lett., **22**, No.3, 275–278.

Shinn, D.H. and H.A. Whale, 1952, *Group velocities and group heights from the magneto-ionic theory*, J. Atmos. and Terr. Physics, **2**, 85.

Silverman, S.M., 1970, *Night Airglow Phenomenology*, Space Sci. Rev., **11**, 341–379.

Silverman, S.M., F. Ward and R. Shapiro, 1962, *The Correlation between the 5577 A Night Airglow Intensity and Geomagnetic Activity*, J. Geophys. Res., **67**, No.6, 2255–2264.

Silverman, S.M. and Bellew, W.F., 1966, *Magnetic Storm Enhancement of the 5577 Å[OI] Airglow Emission Intensity*, Ann. Geophys., **22**, 458–459.

Slanger, T.G. and G. Black, 1977, *$O(^1S)$ in the Lower Thermosphere – Chapman Vs Barth*, Planet. Space Sci., **25**, 79–88.

Smith, E.K. and S. Matsushita, (eds.), Ionospheric Sporadic E, Vol 2 in Electromagnetic Waves, Pergamon Press, Oxford, 1962, 391 pp.

Smith, L.G., 1966, *Rocket Observations of Sporadic-E and related Features of the E region*, Rad. Sci., **1**, 178–186.

Smith, M.J., 1981, *Upper Atmosphere Circulation and Wave Motion*, PhD thesis, University of Canterbury, 320 pp.

Smith, S.M., 1989, *Ionospheric Sporadic-E Dynamics*, MSc thesis, University of Canterbury, 142 pp.

Solheim B.H. and E.J. Llewellyn, 1979, *An indirect mechanism for the production of $O(^1S)$ in the aurora*, Planet. Space. Sci., **27**, 473–479.

Stening, R.J., Fleming, K. and Fraser, G.J., 1995, *Upper Atmospheric Semi-diurnal Tides at Christchurch (44°S) and Scott Base (78°S)*, J. Atmos. Terr. Physics, **57**, No. 8, 857-869.

Stubbs, T.J., 1973, *The Measurement of Winds in the D-region of the Ionosphere by use of Partially Reflected Radio Waves*, J. Atmos. Terr. Phys., **35**, 909–919.

Stubbs, T.J., 1977, *A study of ground diffraction pattern parameters associated with D-region partial reflections*, J. Atmos. Terr. Phys., **39**, 589–594.

Stubbs, T.J. and R.A. Vincent, *Studies of D-region Drifts During the Winters of 1970–72*, Aust, J. Phys., **26**, 645–660.

Swenson, G.R., Mende, S.B. and Llewellyn, E.J., 1989, *Imaging Observations of Lower Thermospheric $O(^1S)$ and $O(_2$ Airglow from STS 9: Implications of Height Variations*, J. Geophys. Res., **94**, No. A2, 1417–1429.

Takahashi, H., Batista, P.P., Clemesha, B.R., Simonich, D.M. and Sahai, Y., 1979, *Correlations Between OH, NaD and OI 5577 ÅEmissions in the Airglow*, Planet. Space Sci., **27**, 801–807.

Takahashi, H., Sahai, Y. and Batista, P.P., 1984, *Tidal and Solar Cycle Effects on the OI 5577 Å, NaD and OH(8,3) Airglow Emissions Observed at 23°S*, Planet. Space Sci., **32**, 897–902.

Takahashi, H., Batista, P.P., Sahai, Y. and Clemesha, B.R., 1985, *Atmospheric Wave Propagations in the Mesopause Region Observed by the OH(8,3) Band, NaD, $O_2A$(8645 Å) Band and OI 5577 ÅNightglow Emissions*, Planet. Space Sci., **33**, No. 4, 381–384.

Tanaka, T. and S.V. Venkateswaran, 1982, *Characteristics of field-aligned E-region irregularities over Iioka (36°N), Japan – I*, J. Atmos. Terr. Physics, 44, 381–393.

Tarasick, D.W. and Hines, C.O., 1990, *The Observable Effects of Gravity Waves on Airglow Emissions*, Planet. Space. Sci., **38**, No. 9, 1105–1119.

Taylor, M.J., Hapgood, M.A. and Rothwell, P., 1987, *Observations of Gravity Wave Propagation in the OI (557.7 nm), Na (589.2 nm) and the Near Infrared OH Airglow Emissions*, Planet. Space Sci., **35**, No. 4, 413–427.

Taylor, M.J. and Hapgood, M.A., 1988, *Identification of a Thunderstorm as a Source of Short Period Gravity Waves in the Upper Atmospheric Nightglow Emissions*, Planet. Space Sci., **36**, No. 10, 975–985.

Taylor, M.J. and Hapgood, M.A., 1990, *The Origin of Ripple-type Wave Structure in the OH Nightglow Emission*, Planet. Space Sci., **38**, No. 11, 1421–1430.

Taylor, M.J., Espy, P.J., Baker, D.J., Sica, R.J., Neal, P.C. and Pendleton, W.R., 1991, *Simultaneous Intensity, Temperature and Imaging Measurements of Short Period Wave Structure in the OH Nightglow Emission*, Planet. Space Sci., **39**, No. 8, 1171–1188.

Taylor, M.J., Ryan, E.H., Tuan, T.F. and Edwards, R., 1993, *Evidence for Preferential Directions for Gravity Wave Propagation Due to Wind Filtering in the Middle Atmosphere*, J. Geophys. Res., **98**, No. A4, 6047–6057.

Taylor, M.J. and F.J. Garcia, 1995, *A two-dimensional spectral analysis of short period gravity waves imaged in the OI(557.7 nm) and near infra red OH nightglow emissions over Arecibo, Puerto Rico*, Geophys. Res. Lett., **22**, No.18, 2473-2476.

Thomas. L., A.J. Gobson, and S.K. Bhattacharyya, 1977, *Lidar observations of a horizontal variation in the atmospheric sodium layer*, J. Atmos. Terr. Phys., **39**, 1405–1409.

Thomas. L., Greer, R.G.H. and P.H.G. Dickinson, 1979, *The Excitation of the 557.7 nm Line and the Herzberg Bands in the Nightglow*, Planet. Space Sci., **27**, 925–931.

Thomas. R.J., 1981, *Analyses of Atomic Oxygen, the Green Line, and the Herzberg Bands in the Lower Thermosphere*, J. Geophys. Res., **86**, No. A1, 206–210.

Thomas. R.J. and T.M. Donahue, 1971, *Analysis of Ogo 6 Observations of the 5577 ÅTropical Nightglow*, J. Geophys. Res., **77**, No. 19, 3557–3565.

Thomas. R.J. and R.A. Young, 1981, *Measurement of Atomic Oxygen and Related Airglows in the Lower Thermosphere*, J. Geophys. Res., **86**, No. C8, 7389-7393.

Thrane, E.V., Haug, A., Bjelland, B., Anastassiades, M. and Tsagakis, E., 1968, *Measurements of D-region electron densities during the International Quiet Sun Years*, J. Atmos. Terr. Phys., **30**, 135–.

Tolansky, S., *Multiple-Beam Interferometry of Surfaces and Films*, Oxford Press, 1948, 187pp.

Torr, M.R., Torr, D.G. and Laher, R.R., 1985, *The $O(_2$ Atmospheric O–O Band and Related Emissions at Night From Spacelab 1*, J. Geophys. Res., **90**, No. A9, 8525–8538.

Tsedelina, Y.Y., 1965, *Movements of inhomogeneities in plasma (ionosphere)*, Geomag. Aeron., **5**, 525–530.

Turek, R.S., K.L. Miller, R.G. Roper and J.W. Brosnahan, 1995, *Mesospheric wind studies during AIDA Act'89: morphology and comparison of various techniques*, J. Atmos. Terr. Phys., **57**, No.11, 1321–1343.

Turunen, T., T. Nygren, A. Huuskonen, and L. Jalonen, 1988, *Incoherent Scatter Studies of Sporadic-E using 300 m resolution*, **50**, 277-287.

Vallance Jones, A., Meier, R.R. and Shefov, N.N., 1985, *Atmospheric Quantal Emissions: A Review of Recent Results*, J. Atmos. Terr. Phys., **47**, No. 7, 623–642.

Vaughan, J.M., 1989, *The Fabry-Perot Interferometer: History, Theory, Practice and Applications*, Adam Hilger Series on Optics and Optoelectronics, Bristol and Philadelphia, 583 pp.

Vial, F. and Forbes, J.M., 1989, *Recent Progress in Tidal Modelling*, J. Atmos. Terr. Phys., **51**, No. 7/8, 663–671.

Villars, F. and H. Fesbach, 1963, *The effect of the earth's magnetic field on irregularities of ionization in the E layer*, J. Geophys. Res., **68**, 1303–1320.

Vincent, R.A., 1973, *The Interpretation of Some Observations of Radio Waves Scattered from the Lower Ionosphere* , Aust. J. Phys., **26**, 815–827.

Vincent, R.A., 1984a, *Gravity-wave motions in the mesosphere*, J. Atmos. Terr. Phys., **46**, No. 2, 119–128.

Vincent, R.A., 1984b, *MF/HF radar measurements of the dynamics of the mesopause region – A review*, J. Atmos. Terr. Phys., **46**, No. 11, 961–986.

Vincent, R.A., Stubbs, T.J., Pearson, P.H.O., Lloyd, K.H. and Low, C.H., 1977, *A Comparison of Partial-Reflection Drifts with Winds Determined by Rocket Techniques – 1*, J. Atmos. Terr. Phys., **39**, 813–821.

Vincent, R.A. and Belrose, J.S., 1978, *The angular distribution of radio waves partially reflected from the lower ionosphere*, J. Atmos. Terr. Phys., **40**, 35–47.

Vincent, R.A. and D.C. Fritts, 1987, *A Climatology of Gravity Wave Motions in the Mesopause region at Adelaide, Australia*, J. Atmos. Sci., 44, No.4, 748–760.

Vincent, R.A., Tsuda, T. and Kato, S., 1988, *A Comparative Study of Mesospheric Solar Tides at Adelaide and Kyoto*, J. geophys. Res., **93**, No.D1, 699–708.

Vincent, R.A., Tsuda, T. and Kato, S., 1989a, *Asymmetries in Mesospheric Tidal Structure*, J. Atmos. Terr. Phys., **51**, No. 7/8, 609–616.

Walterscheid R.L., 1981, *Inertio-Gravity Wave Induced Accelerations of Mean Flow Having an Imposed Periodic Component: Implications for Tidal Observations in the Meteor Region*, J. Geophys. Res., **86**, No. C10, 9698–9706.

Walterscheid R.L., J.G. DeVore and S.V. Venkateswaran, 1980, *Influence of Mean Zonal Motion and Meridional Temperature Gradients on the Solar Semidiurnal Atmospheric Tide: A Revised Spectral Study with Improved Heating Rates*, J. Atmos. Sci., **37**, 455–470.

Walterscheid R.L. and Schubert, G., 1987a, *A Dynamical-Chemical Model of Tidally Driven Fluctuations in the OH Nightglow*, J. Geophys. Res., **92**, No. A8, 8775–8780.

Walterscheid R.L., Schubert, G. and Straus, J.M., 1987b, *A Dynamical-Chemical Model of Wave–Driven Fluctuations in the OH Nightglow*, J. Geophys. Res., **92**, No. A2, 1241–1254.

Walterscheid R.L. and Schubert, G., 1993, *A Comparison of Theories For Gravity Wave Induced Fluctuations in Airglow Emissions*, submitted to J. Geophys. Res.

Ward, W.E., E.J. Llewellyn, Y. Rochon, C.C. Tai, W.S.C. Brooks, B.H. Solheim and G.G. Shepherd, 1995, *Spatial Variability in $O(^1S)$ and $O_2(b^1\Sigma_g^+)$ Emissions as Observed with the Wind Imaging Interferometer (WINDII) on UARS* in *The upper mesosphere and lower thermosphere: a review of experiment and theory*, Johnson, R.M. and T.L. Killeen (eds.), Geophysical Monograph 87, Amer. Geophys. Union, 323–328.

Ward, F. and Silverman, S.M., 1962, *Characteristics of the 5577 Å [OI] Night Airglow at Maruyama and its Relation to Magnetic Activity*, J. Geophys. Res., **67**, 5357–5360.

Wasser, B. and Donahue, T.M., 1979, *Atomic Oxygen Between 80 and 120 km: Evidence for a Latitudinal Variation in Vertical transport Near the Mesopause*, J. Geophys. Res., **84**, No. A4, 1297–1309.

Watanabe, T. and Nakamura, M., 1981, *Rocket Measurements of $O_2$ Atmospheric and OH Meinel Bands in the Airglow*, J. Geophys. Res., **86**, No. A7, 5768–5774.

Weins, R.H., G.G. Shepherd, W.A. Gault and P.R. Kosteniuk, 1988 *Optical Measurements of Winds in the Lower Thermosphere*, J. Geophys. Res., **93**, No. A6, 5973–5980.

Weins, R.H. and G.G. Shepherd, 1989, *Reply*, J. Geophys. Res., **94**, No. A2, 1553–1554.

Weinstock J., 1978, *Theory of the Interaction of Gravity waves with $O_2(^1\Sigma)$ Airglow*, J. Geophys. Res., **83**, No. A11, 5175–5185.

Whitehead, J.D., 1961, *The formation of the Sporadic-E layer in the temperate zones*, J. Atmos. Terr. Phys., **20**, 49–58.

Whitehead, J.D., 1970, *Survey of Sporadic-E Processes*, Space Research VII, North-Holland Publ. Co., 89–99.

Whitehead, J.D., 1972, *Some Recent Work on Sporadic-E Theory*, Rad. Sci., **7**, 381–384.

Whitehead, J.D., 1989, *Recent Work on Mid-latitude and Equatorial Sporadic-E*, J. Atmos. Terr. Phys., **51**, No.5, 401–424.

Widdel, H.U., M. Bittner and U.P. Hoppe, 1994, *Vertical velocities measured at Biscarrosse ($44^oN$) and by EISCAT at Tromso ($69.6^oN$) during the DYANA campaign*, J. Atmos. Terr. Phys., **56**, Nos.3/4, 1779–1796.

Witt. G., Stegman, J., Solheim, B.H. and Llewellyn, E.J., 1979, *A Measurement of the $O_2(b^1\Sigma_g{}^+ - X^3\Sigma_g{}^-)$ Atmospheric Band and the $OI(^1S)$ Green Line in the Nightglow*, Planet. Space Sci., **27**, 341–350.

Yee, J.H. and Abreu, V.J., 1978, *Mesospheric 5577 Å Green Line and Atmospheric Motions - Atmospheric Explorer Satellite Observations*, **35**, No. 11, 1389–1395.

vanZandt, T.E., 1982, *A universal spectrum of buoyancy waves in the atmosphere*, Geophys. Res. Lett., **9**, 575–578.

# Acknowledgements

There are many people who deserve my thanks for their help during this project. Without their help it would not have been possible.

I would like to express my deepest thanks to my principle supervisor Dr. Grahame Fraser for his help, patience, encouragement and hospitality during the these years. I would also like to greatly thank my associate supervisor Dr. Gonzalo Hernandez for his help and patience and also for the generosity and hospitality he and Donna showed me when I visited the US.

Similarly, I am extremely grateful to Gonzalo's colleague in the FPS program, Dr. Roger Smith for all his help and for the hospitality he and Isa showed me when I visited.

I am also very grateful to Mike Clark and John Baker who kept a watchful eye on the FPS, a.k.a Doris, and sent me packages of data. Also, thanks to Roger Govind for his expertise and humour during excursions down to Mt. John, a.k.a Club Tekapo.

To Dr. Harvey Cummack, who helped demystify some of the behaviour occurring in the upper atmosphere, I am most grateful. Thanks also to past and present students such as Drs. Bryan Lawrence, Bill Brown and Andrew Taylor, Manfred Plagmann, John Grant, Andy Reisinger, Adam Dunford and Dave Frame.

Thanks also to the New Zealand Vice-Chancellors' Committee (formerly the University Grants Committee) for awarding me a New Zealand Universities' Post-Graduate Scholarship and an Edward and Isabel Kidson Scholarship.

I would especially like to thank my mother and my sister for all their support and encouragement during my university career.

Finally, and most of all, I would like to thank Mary for her love and support during this project. I could not have done it without her.